Do fault-related folds follow the same scale law properties as their associated faults?

Eleanor Grace Pitcher

The scaling law distribution properties of fault-related folds were assessed in comparison to the distributions of their associated faults to determine whether or not they are governed by the same scaling law properties. The fault-related fold and fault data were collected from three-dimensional seismic data modelled in TrapTester and Petrel from the Gulf of Mexico (TrapTester), Gulf of Gabès (TrapTester) and the Inner Moray Firth (Petrel). They were sampled by one-dimensional multiline sampling (TrapTester) and two-dimensional (Petrel) fault and fold length sampling. To ensure the accuracy of this data collection method a comparative test of methodologies was carried out using the Gullfaks, North Sea data set and comparing it to the results published by Fossen and Rørnes (1995). By validating the methodologies (TrapTester) used the data sets were analysed using the Kolmogorov-Smirnov and Anderson-Darling test on a "moving window" in R to assess the scaling law distributions of the data. Based on previous findings from published work the power law distribution was tested first since fault populations are understood to follow this distribution. An exponential distribution and log-normal distribution were also tested. The results of this suggest that fault-related folds are not necessarily governed by the same distributions of the underlying fault population. It is proposed that fault-related folding is heavily controlled by the competence and thickness of the surrounding stratigraphic units, as well as the dip angle of the underlying faults. Incompetent beds will accommodate more folding compared to competent beds which are more likely to fault. A thinner stratigraphic unit will be unable to accommodate as much folding as a thicker stratigraphic unit. An underlying fault with a low dip angle will cause the overlying stratigraphic units to preferentially fault and won't propagate as large a fold throw in comparison to underlying faults with a high dip angle.

Do fault-related folds follow the same scale law properties as their associated faults?

Eleanor Grace Pitcher

Thesis presented for the degree of Master of Science by Research to the University of Durham, 2016

Under the Supervision of Dr Jonathan Imber and Professor Ken McCaffrey

Research conducted at:

Department of Earth Sciences

Durham University

Science Labs

Durham

DH1 3LE

Table of Contents

Table of Figures

Equation 8:$D_{n,n'} > c(\alpha)\sqrt{\frac{(n+n')}{(nn')}}$, $D_{n,n'}$; Kolmogorov-Smirnov statistic, $c(\alpha)$; critical value based on the α level it is tested at, n; size of sample one, n'; size of sample two

.....87

Equation 9: $n\int_{-\infty}^{\infty}(F_n(x)-F(x))^2 w(x)dF(x)$, $F_n(x)$; empirical distribution function, $F(x)$; hypothesised distribution function, $w(x)$; weighting function, n; number of observations

.....88

Equation 10: $A = n\int_{-\infty}^{\infty}\frac{\left(F_n(x)-F(x)\right)^2}{F(x)\left(1-F(x)\right)}dF(x)$, A; the distance which the Anderson-Darling test is based on, $F_n(x)$; empirical distribution function, $F(x)$; hypothesised distribution function, n; number of observations

.....88

Equation 11: $T.AD = \frac{(AD-\mu)}{\sigma}$, $T.AD$; Anderson-Darling test statistic, AD; Anderson-Darling criterion for k-samples, μ; mean of the data, σ; standard deviation of the data

.....89

Equation 12: $\alpha = \frac{dy}{dx} = \frac{\log y_1 - \log y_2}{\log x_1 - \log x_2}$, α; exponent value, y_1; y value at the lower end of the data (cumulative fault number), x_1; x value at the lower end of the data (fault size), y_2; y value at the upper end of the data (cumulative fault number), x_2; x value at the upper end of the data (fault size)

.....98

Equation 13: $\log y = \log C - \alpha \log(x)$, y; cumulative fault number, x; fault size, C; y-intercept, α; exponent value which is the gradient of the straight line

.....98

Equation 14: $D = \frac{TWTT}{2}v$, D; depth, $TWTT$; two-way travel time, v; velocity

.....102

Equation 15: $m = \frac{\log y - \log c}{\log x}$, y; cumulative fault number, x; fault size, c; y-intercept, m; exponent value which is the gradient of the straight line

.....150

Acknowledgements

For his dedicated supervision and guidance from undergraduate into postgraduate I'd like to think Dr Jonathan Imber, my primary supervisor for this project. He's constantly believed in me and supported my ideas, teaching me how to refine them and showing me that I can pursue a career in research. Thanks also go to Professor Ken McCaffrey for his continued support throughout the year and offering ideas and research methods to carry out.

I would also like to thank Dr Camila Caiado who became like a third supervisor throughout the project, for her help in learning and writing the code in R which has formed a significant part of this project. Without her incredible insight, help and time spent helping to learn the statistical methods and maths in R the project would not have gone as far as it has, or reached such comprehensive conclusions as it has managed to. As well as this the constant support from the Durham University Earth Sciences IT team for coming to the rescue when my computer had a meltdown, and for being on hand to download all the extra programs which were required for the project. And to the Earth Sciences postgraduates and staff for their continued support and guidance throughout the year, as well as providing guaranteed company for a break in the coffee room.

Thanks also go to Alexandru Lăpădat for sharing his Inner Moray Firth data and interpretations, as well as teaching me how to use Petrel and being constantly on hand for any seismic modelling related questions. Charlie must also be thanked for her constant reminders and letting me know about important emails and dates she knows I'll miss, which I'm sure will be continued into our PhDs.

A huge thank you must all be given to my parents and sister for their constant support throughout undergraduate and postgraduate in all forms. To my dad for proof reading my work, my mum for making sure I'm well fed and my sister for providing constant hilarity and reassurance. As well as to my housemates and extended house mates, Heather, Aislin, Hannah, Phil, Katharine, Liddie and Webby. For their reassurance and also making sure I'm well fed, the constant banter and guaranteed company for a chilled film night. With special thanks to Aislin for her proof reading and honest feedback.

1. Aim, hypothesis and introduction

Previous works by Yielding et al., (1996), Watterson et al., (1996), Nicol et al., (1996) and Fossen and Rørnes (1996) have provided strong evidence to suggest that fault size attributes (fault throw and fault length) follow a power law scaling distribution. It is hypothesised that the fault-related folds formed by an underlying fault population could be described by the same scaling distribution.

The aim of this study is to determine whether fault-related folds follow the same power law scaling properties as their associated faults, or if they follow a different scaling law. It is highly likely that the scaling law distribution which fault-related folds are governed by is highly variable depending on the tectonic setting. This means it will vary for extension or compression, if the bed type is ductile or brittle and the bed thickness, therefore making it difficult to define the scaling law distribution. A secondary aim of this study is to develop and test new statistical methods to discriminate between power-law and other (e.g. exponential, log-normal or normal) distributions.

Fault-related folding occurs at and adjacent to the tipline (volume of rock at and beyond the zero-displacement contour) of a fault plane, where the underlying deformation by fracturing has not propagated far enough to displace the overburden rock. The scaling properties of fault-related folds have been under examined and therefore the potential outcomes are difficult to predict.

The figure below illustrates the development of a fault-propagation fold, a specific type of fault-related fold that will form the basis of this study. In figure 1a it starts with an un-deformed host rock with a fracture within it; in figure 1b slip has occurred on the fracture and the overlying sediments have been folded but the fault has not propagated into them; in figure 1c the fault has begun to propagate into the overlying sediments; finally, in figure 1d the fault has propagated through all the overlying sediments and folding has ceased, although there is some folding preserved in the sediments around the fault. These processes are discussed further in chapter 1.4.

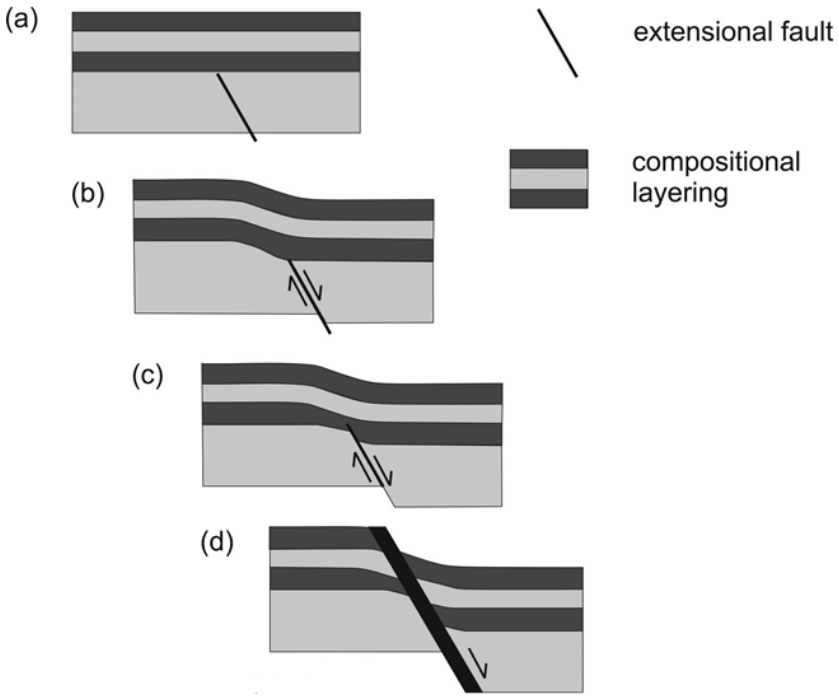

Figure 1: shows the propagation of a fault-related fold from an undeformed strata in a, to a fault-related fold in b and c, where it is completely faulted in d (modified, Schwerdtner et al., 2014)

The potential outcomes of this research are that it could improve the understanding of fold geometry which would be beneficial to the hydrocarbon industry. It could lead to a scaling relationship which could be applied to folds and make the discovery of new fault-related hydrocarbon traps easier to predict in the future.

This research focuses on one-dimensional multiline sampling, looking predominantly at fault-displacement (throw) and fold amplitude, but also looking briefly into fault-length (sampling along mapped, two-dimensional horizon surfaces). Three-dimensional seismic data were used to carry out one-dimensional multiline sampling where the resolution of seismic data at depths below 3km is typically 30m (although in favourable circumstances, 10m). This means that fault offsets of less than 30m are essentially “invisible” on most seismic reflection data (Yielding et al., 1996). Depending on the sampling methods used only faults above some limit can be resolved (Kim and Sanderson, 2005). Depth maps are also considered which are contoured to 20m, meaning that

any fault size smaller than 20m cannot be measured. The effect of this can be seen in our figures in chapter 4.5.1. Seismic reflection datasets and associated interpretations from the Gulf of Mexico study area have been depth converted; other interpretations derived from seismic reflection datasets are presented in two-way travel time unless depth converted by hand from well log data available.

1.2 Size distributions and power-law (fractal) scaling relationships

Fractal distributions are largely agreed to follow a power-law distribution by authors such as Turcotte (1989), Yielding et al., (1996), Needham et al., (1996), Nicol et al., (1996) and Watterson et al., (1996). The power law distribution satisfies a data set which is comprised of a large amount of small objects and a smaller amount of large objects (figure 2). Fractal distributions are defined by the number of objects with a characteristic size greater than a given value (Turcotte, 1989).

In detail, the form of this equation varies between authors;

i. $N \propto r^{-D}$, where N is the number of objects with a characteristic size greater than r which scales by the power-law exponent D (Turcotte, 1989).

ii. $N = aS^{-D}$, where N is the number of faults having a size greater or equal to S which denotes a "size" of the fault, a is a measure of the sample size and D the power-law exponent (Yielding et al., 1996; Needham et al., 1996).

iii. $N \propto S^{-C}$, where N is the number of faults with size greater than or equal to S, and C is the power-law exponent (Nicol et al., 1996, Watterson et al., 1996).

Nevertheless, all these equations are of the form

Equation 1: $\boldsymbol{F = aX^{-b}}$

(Hooker et al., 2014), and can be expressed as $\log F = \log a - b \log X$ to satisfy the equation of a straight line of the form $y = mx + c$ in log-log space. This transformation makes it much simpler to derive the power-law exponent which governs the scaling of the "fault size" population

because it will be the gradient of the straight-line or straight-line section of the graph when plotted on a log-log graph.

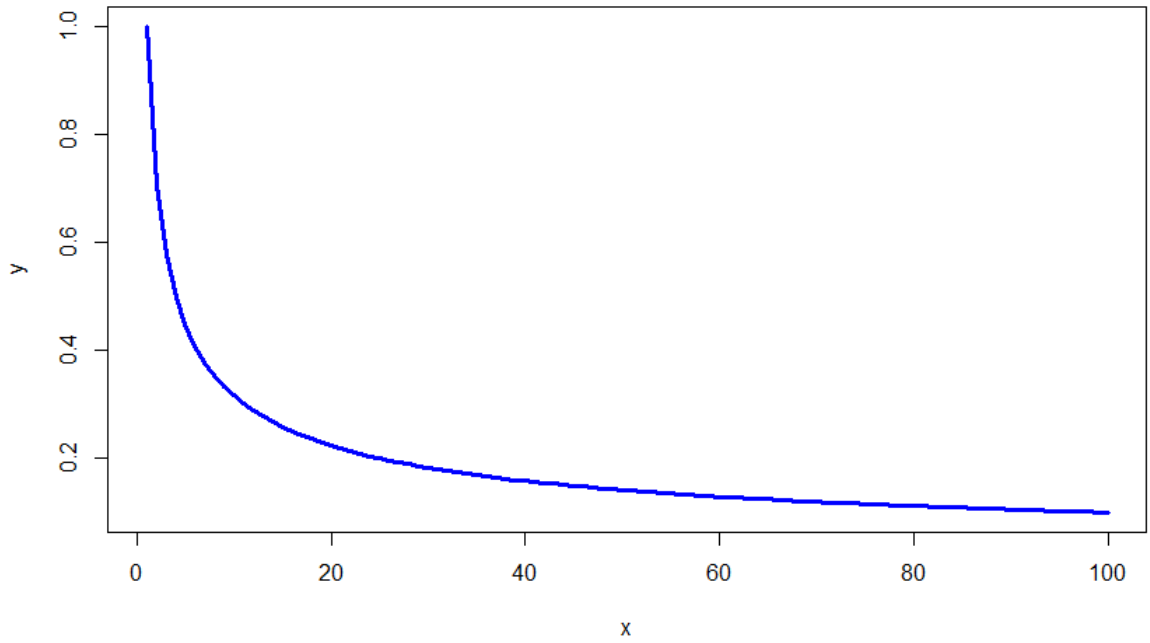

Figure 2: power law with arbitrary axis

The relationships expressed by equations (ii) and (iii) describe "fault size" which refers to trace-length or fault-displacement (or, more commonly, throw) (Yielding et al., 1996; Nicol et al., 1996; Needham et al., 1996), and can be used in a variety of data collection techniques and dimensions. The power-law exponent derived from each of these situations is summarised in table 1 below, and varies by which dimension the data has been collected in.

Geological Case	Exponent	Documented
Fault-trace lengths (two-dimensional samples)	-1.1 to -2.0	Yielding et al., 1996
Fault-trace maximum displacements (two-dimensional sample)	-1.1 to -1.5	Yielding et al., 1996
'Arbitrary' displacements (one-dimensional sample)	-0.5 to -1.0	Yielding et al., 1996
Line sample throw populations	-0.4 to -1.0	Nicol et al., 1996
Line sample throw populations (outcrop data)	-0.4 to -0.6	Nicol et al., 1996
Line sample throw populations (seismic data)	-0.8 to -1.0	Nicol et al., 1996
Line sample throw populations (coal-mine data)	-0.5 to -0.8	Nicol et al., 1996

Table 1: lists the expected exponent values published by various authors for a number of different sampling techniques (the exponent value can be dependent on populations size, with larger populations potentially leading to larger exponents and smaller populations smaller exponents).

Being able to identify these scaling properties provides a powerful tool for predicting the numbers of geological structures, such as small-scale faults in the brittle crust that are below the resolution of seismic reflection data (Scholz and Cowie, 1990; Walsh et al., 1991; Jackson and Sanderson, 1992; Marrett and Allmendinger, 1992). Understanding scaling properties also enables the constraint and testing of fault growth models (Walsh and Watterson 1987, 1992; Cowie and Scholz, 1992a, b). It also makes it possible to extrapolate for restricted parts of a fault population to predict the amount of unobserved faults in the same area. This allows their likely impact on hydrocarbon production to be constrained (Heffer and Bevan, 1990; Yielding et al., 1992; Gauthier and Lake, 1993).

It is important to note that changing the dimension of the scaling domain i.e. from one-dimensional to two-dimensional (line to plane), two-dimensional to three-dimensional (plane to volume), changes the power-law exponent for that data set (Yielding et al., 1996). It is generally suggested that this is by ±1 depending on which way the dimension has changed; so, moving from one dimension to two dimensions would increase the exponent for one, or reduce it by moving in the other direction.

Within all of these different types of data collection and dimension there is still variation between the scales of the fault system. Nicol et al (1996) proposed that although the existence of a systematic relationship is still uncertain, it appears that larger faults tend to have higher exponent values than those of smaller faults. However, in a single fault system the fault size could range up to eight orders of magnitude. Although the size range of an individual data set is rarely greater than two orders of magnitude (Nicol et al., 1996), i.e. a fault system ranging from 0.001m to 1000m, but the data set only includes values from 10s of meters to 100s of meters and is a subset (sample) of the whole population. It has previously been suggested that some fault populations are power-law over at least two and a half orders of magnitude (Watterson et al., 1996).

Work carried out by Fossen and Rørnes (1995) supports the idea that within a single dataset there may be smaller sub-populations which themselves are power-law distributions; supporting the ideas of Nicol et al (1996) that an individual power-law dataset is a subset of a larger fault system.

As previously stated, geological systems scale from micro- to macro-scale so present variable complexity and so are not necessarily believed to be scale invariant. More recent work by Kruhl (2013) looked into the important properties of the quantification of complex rock structures. He has highlighted three main areas which should be considered;

i. Different scaling behaviour on different scales
ii. Inhomogeneity
iii. Anisotropy

All these studies suggest that the scaling properties of fault systems are not usually constant over several orders of magnitude. It is well known that self-similarity varies over different scaling regimes for natural patterns and that this is standard, not the exception (Kruhl, 2013). These breaks in scaling can be identified when sampled populations (e.g. fault throw data) are plotted on a log-log graph, whereby there are multiple linear segments with varying slopes.

Kruhl (2013) presents two different reasons for the existence of different scaling regimes of rock structures on different scales. The first of these is that rock fabric and rock composition are different across different scales and will deform differently from micro- to macro-scale, therefore the same processes will act differently (Flook, 1979; Kaye, 1978, 1989; Suteanu and Kruhl, 2002). Secondly, processes will act with different intensities over different scales and two processes can act synchronously or subsequently on the formation of entities and agglomerates (Keulen et al., 2007). In addition, non-geological fracturing processes can result in different scaling regimes where the fault population has been influenced by non-geological stress/strain. This causes the scaling law distribution to be altered from what is expected of a naturally fractured population (Blenkinsop, 1994). Irrespective of this, some structures with self-similarity over several orders of magnitude do exist (e.g. fault relay zones; Peacock, 2003; Long and Imber, 2011).

Within rock structures, inhomogeneity is a dominant characteristic and is affected by scale. Inhomogeneity results from how various processes interact with each other over time, as well as the scale at which the rock is studied. It is inevitable that a pattern becomes more inhomogeneous at it has a lower resolution limit, i.e. crystals and pores viewed on a micro-scale will appear more inhomogeneous compared with being viewed on a macro-scale. According to Kruhl (2013), rock structures and the resulting patterns tend towards inhomogeneity on small scale and, vice versa, gain homogeneity with increasing size (Kruhl, 2013). As a result, care has to be taken when analysing natural datasets as irregular areas of analysis can lead to different lengths of scan-line. If carried out over different scales such sampling strategies may not provide representative samples of the population and its fractal distribution.

1.3 Alternative distributions

A possible alternative distribution is an exponential distribution, in this case it is a negative exponential as will be identified in equation 2, but for the duration of this thesis will be referred to as an exponential distribution.

Equation 2: $y = m^{-x}$

Exponential distribution would state that there be an exponentially larger amount of smaller faults than larger faults as can be seen in figure 3. This will plot as a straight-line on a linear against log plot (Franklin, 2013).

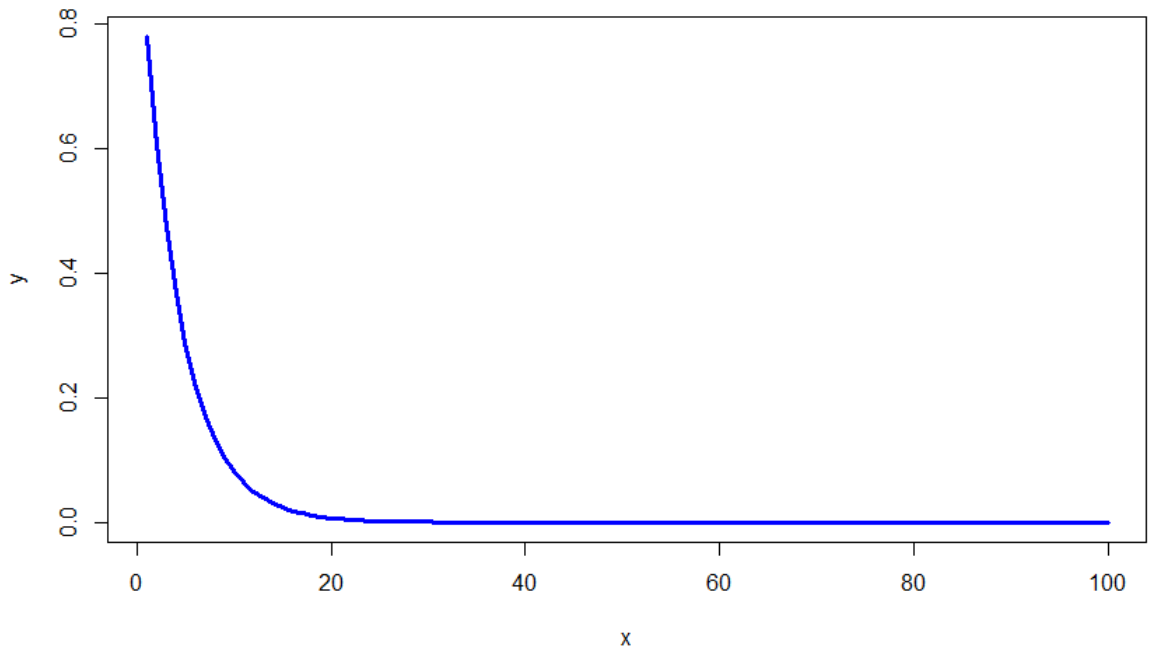

Figure 3: exponential distribution

Mathematically the power law, exponential and log-normal distribution can be made into a linear graph by logging it to any base which isn't 1. Most commonly the base used is either 10, 2 or *e*, and the relationship is still true regardless of this (https://en.wikipedia.org/wiki/Log-normal_distribution, December 2016). The difference between the uses of each base is the

resultant gradient of the straight line. Since within literature (Cowie et al., 1995; Fossen, 1996; Pickering et al., 1995; Turcotte, 1989) the quoted exponent results (table 1) the base 10 was used it makes our results comparable to also do the same (Franklin, 2013; Sleight, 2001; Davis and Simpson, 1986; Ackermann et al., 2001; Soliva and Schultz, 2008). This leaves the straight-line equation in the form of $y = mc + c$ to be $\log y = \log(m)\, x + \log c$ when the x-axes remains linear and the y-axes values are logged.

A third possible distribution is a log-normal distribution.

Equation 3: $$\boldsymbol{y = \frac{1}{x\sqrt{2\pi\sigma^2}} e^{\frac{-(\ln x - \mu)^2}{\sqrt{2\sigma^2}}}}$$

Log-normally distributed data have a peak about a point, which unlike a normal distribution is skewed heavily towards the left of the data (smaller values). This indicates a small amount of very small values which then increases very quickly in quantity to a peak. After this peak the values drop off more gradually than they had increased, figure 4. This will plot as a straight-line on a log against linear plot (Franklin, 2013), and like the exponential distribution although mathematically defined by a natural logarithm in geology is defined by a logarithm with base 10 (Franklin, 2013; Sleight, 2001; Davis and Simpson, 1986; Ackermann et al., 2001; Soliva and Schultz, 2008; McCaffrey et al., 2003).

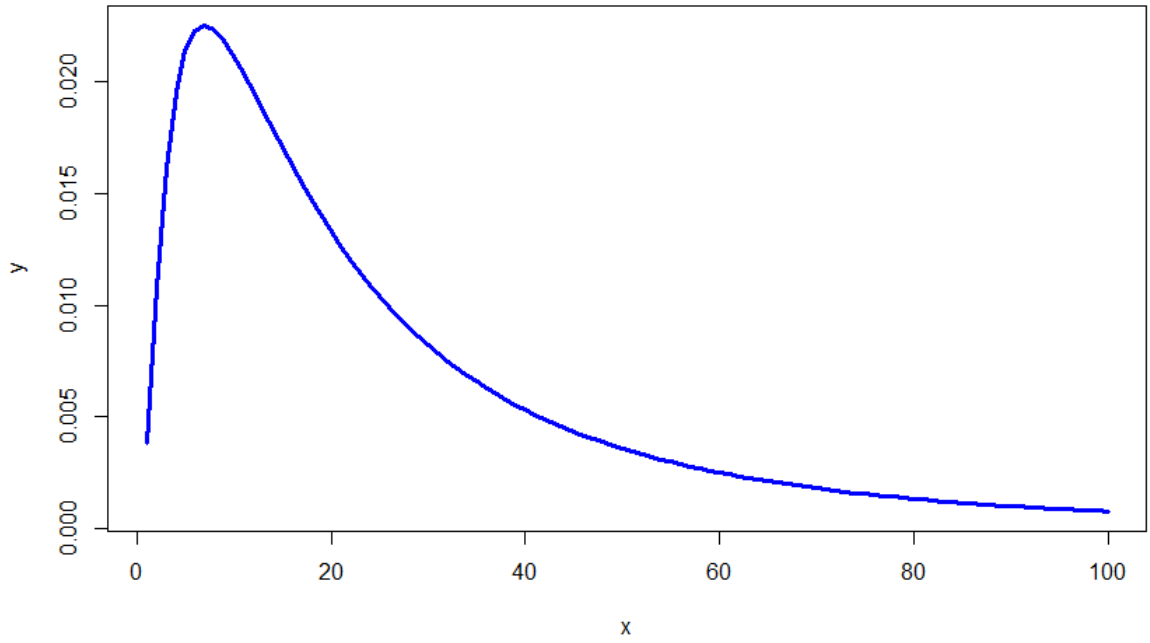

Figure 4: log-normal graph

If an object x is log-normally distributed then $y = \log(x)$ has a normally distribution (https://en.wikipedia.org/wiki/Log-normal_distribution, November 2015) and will satisfy a straight-line equation in the form of $y = m \log x + c$ when values on the x-axes are logged, and values on the y-axes remain linear.

1.4 Fault-propagation folding

In this study, we take fault-related folding or fault-propagation folding to be the folding that forms above fault blocks bounded by normal unlinked faults (Withjack et al., 1989, 1990). Fault-related folding has been primarily explored by analogue modelling experiments and tri-shear models, although some observations of fault-propagation folds have been made from outcrop and seismic data. Such as Smørbukk and Smørbukk South hydrocarbon fields, Halten Terrace, Mid-Norway (Corfield and Sharpe, 2000), and the Suez Rift, Egypt (Jackson et al., 2006). Seismic observations have led to the conclusion that many of the folds in question arise from dip changes

of the underlying faults (Suppe, 1983), or the transfer of fault slip to fold displacement (Suppe and Medwedeff, 1984; Jamison, 1987; Erslev, 1991).

Mechanical stratigraphy, as described by Ferrill et al., (2006) exerts the main control on deformation style across a different range of scales. In application to faulting and fault-related folding when the tipline of a fault plane enters a bed with different mechanical properties it will display different degrees of folding. As with any regime, over time the mechanical properties will change whether that means the deformation was short-lived and over a short time period ceases, if it deforms slowly over time, or if it is reactivated etc. As a result of this change over time the resultant fault-related folding can be varied Ferrill et al., (2006) outline the idea that fault-related folding is the preferential deformation style when a fault tip moves upwards into an incompetent stratigraphic unit. This is exemplified in the Trans Pecos region of west Texas where a fault deformed in a competent stratigraphic unit made up of mudstones and grainstones moves upwards into incompetent stratigraphic units dominated by silty and clayey mudstones (Ferrill et al., 2006).

Experiments carried out by Withjack et al (1990) looked into the effects of dip angle on the resultant fault-related fold. They proposed that forced folds are more likely to develop if underlying normal faults are steeply dipping and if detachments and/or thick ductile (incompetent) units are present to decouple the folded strata from underlying faulted strata and basement (Stearns, 1978; Laubscher, 1982; Patton, 1984; Withjack et al., 1988, 1989). Their experiment involved aluminium fault blocks which acted as the fault blocks, where the sloping sides of the boxes represent the normal faults, sedimentary cover was represented by clay. They conducted three experiments varying the sloping sides of the boxes at 60° for experiment one, 75° for experiment two and 45° for experiment three. A fourth experiment was conducted with sloping sides at 60°, but with three horizontal layers of clay each roughly 2.5cm with the middle

layer separated from the adjacent layers with double sheets of acetate to mimic detachments that completely decouple the adjacent sedimentary layers (Withjack et al.1990).

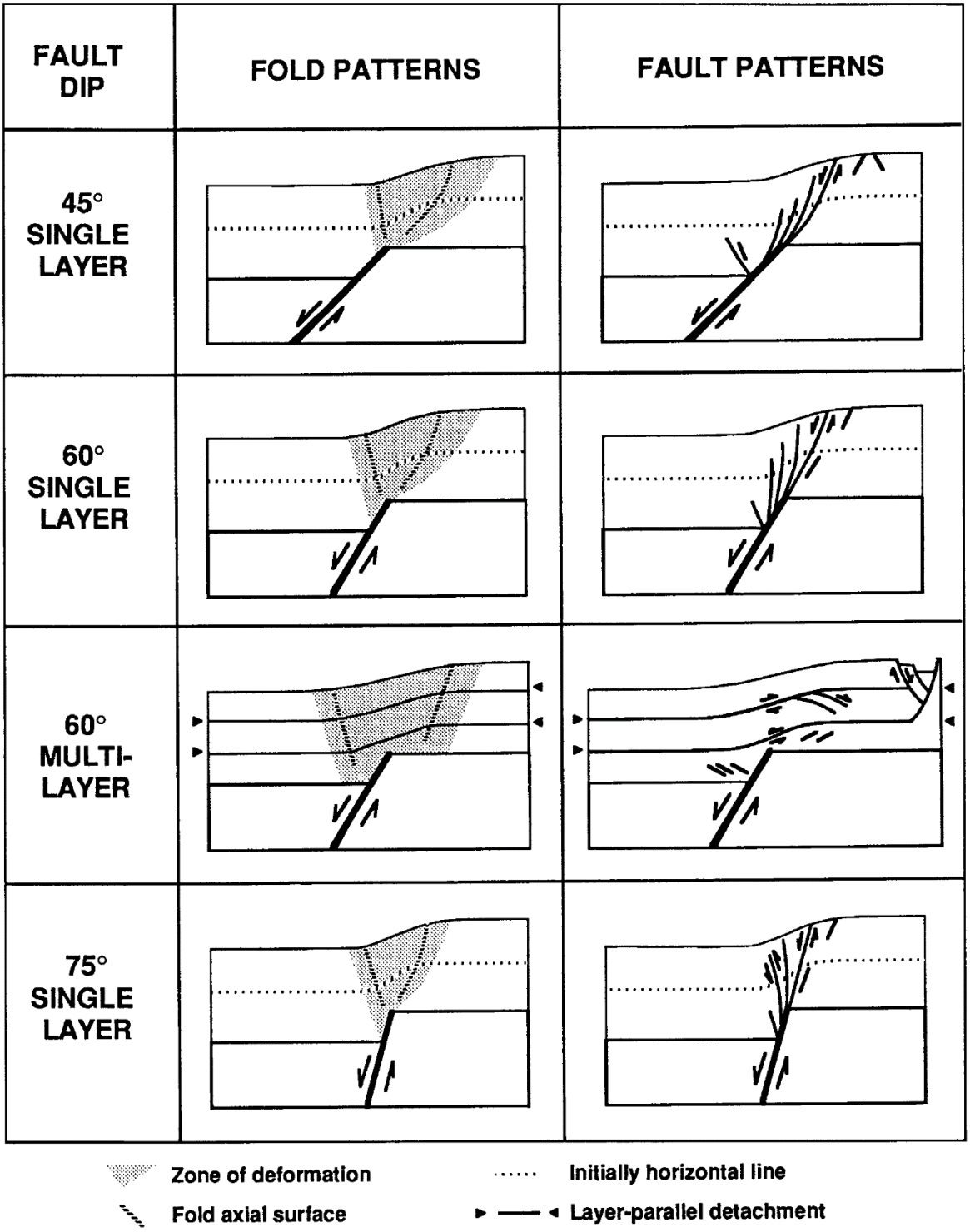

Figure 5: a diagram highlighting the results of the fault-related folding and faulting results from the four experiments carried out by Withjack et al., (1990)

They found that for experiment one approximately 2cm of displacement occurred on the master fault before the fault-related fold development ceased. Experiment two experienced more than 2.5cm before development ceased and experiment three found only 1.5cm of displacement before development ceased. In the case of experiment 4 where the adjacent layers were completely decoupled, the primary deformation mechanism was layer-parallel slip on the acetate detachments.

As described by Withjack et al., (1990) when the master fault is gently dipping the fold width is greater and limb dip less, when the master fault is steeply dipping the fold width is less and limb dips are greater. As a result of this the secondary fault patterns become dependent on the dip of the master fault. Their experiments have shown that if the dip of the master fault is less than 60° the secondary faults are low-angle causing fracturing after a small amount of slip, if the dip is greater than 60° the secondary faults are high-angle causing fracturing after a larger amount of slip. This is supported by field and seismic observations which have been made showing that fault-related folds are most likely to develop if underlying faults are high-angle, and unlikely to develop if under lying faults are low-angle.

The relationship between the evolution of the underlying fault and the resultant fold shape is of great interest for a number of reasons; an understanding of this relationship can help in hydrocarbon exploration, to seismic risk evaluation and fault mechanics. In addition, these folds which form at the tipline of the faults are often the only exposed evidence available of the nature of the underlying fault (Hardy and Allmendinger, 2011).

1.5 Thesis Overview

Chapter 2: This chapter provides a brief geological introduction to the four study areas looked at in this project; the Gulf of Mexico, the Gulf of Gabès, Inner Moray Firth and Gullfaks. Looking at their deformation style, tectonic development as well as their stratigraphy

Chapter 3: Introduction to the methodology used to model the seismic data in both TrapTester and Petrel for one-dimensional and two-dimensional data collection. This is followed by an introduction to the techniques used to assess the type of distribution exhibited within each data set, considering those used previously and attempts made to use R in order to automate the process and consider parts of the data as separate populations.

Chapter 4: This chapter validates the methodology used by comparing the results gained in this project to those already published for the same Gullfaks data set by Fossen and Rørnes. Using a combination of depth maps and depth converted values in TrapTester

Chapter 5: This chapter presents the results gained from the modelling and analysis of; the Gulf of Mexico, the Gulf of Gabès and Inner Moray Firth data sets. As well as considering the comparison between other methods and similar code developed by Clauset et al (2009).

Chapter 6: This chapter discusses the strengths and weaknesses of the results and the methodology implemented

Chapter 7: This chapter draws together the results gained and literature read into an overall conclusion

2. Study areas

2.1 Gulf of Mexico study area

2.1.1 Introduction

The depth-migrated 3D seismic dataset from the Gulf of Mexico study area covers part of the West Cameron oil field and is located approximately 60 miles south of Lake Charles, Louisiana (Bell et al. 1970). The field is characterised by an EW striking and NS dipping fault system which can be seen in a depth map and cross-section in figure 6 and 7 below.

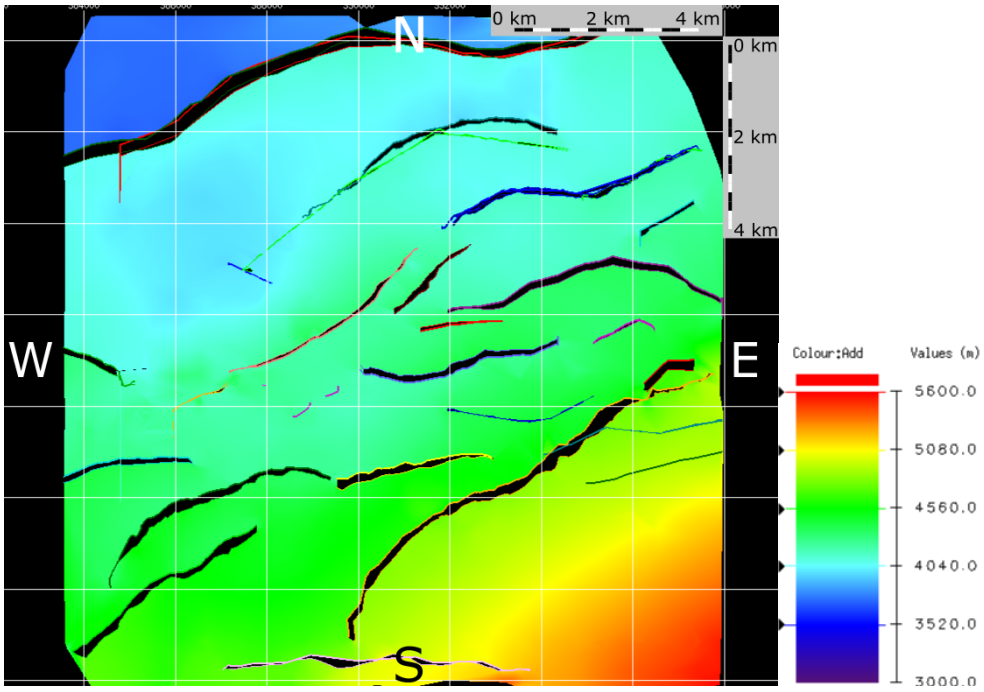

Figure 6: Early Miocene horizon showing the fault polygons of the fault system, and legend

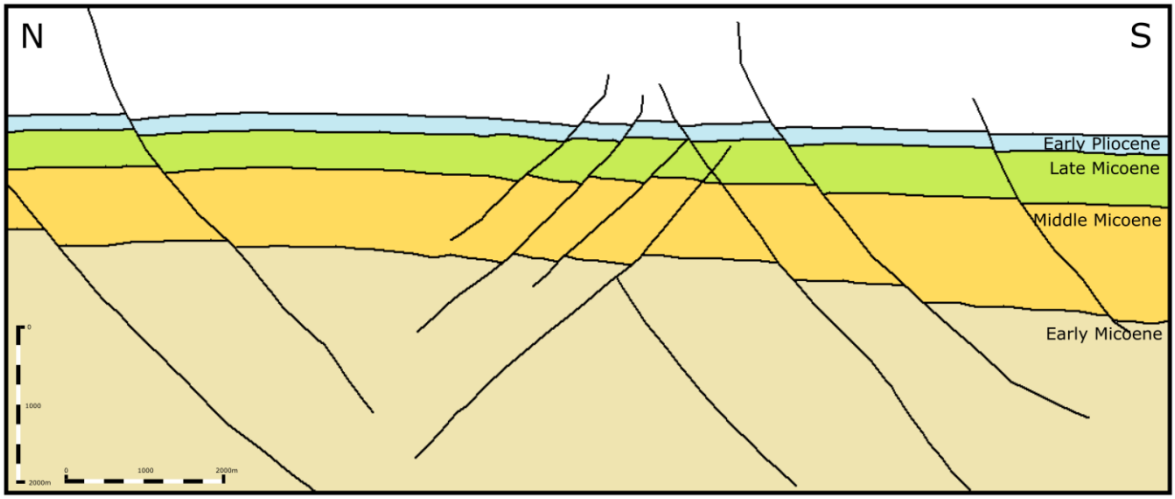

Figure 7: cross-section from the Gulf of Mexico highlighting four different horizons and the fault system through these

The cross-sections in figures 8, 9 and 10 show the fault system moving from the west to the east of the system, from these cross-sections it is clear that the deformation throughout the field remains consistent throughout. The throw on the faults appears to decrease upwards in line with the understanding that throw propagates from a maximum at the centre of a fault (Childs et al., 2003). Throughout figures 8, 9 and 10 the faulting throughout the fields doesn't appear to change much, this indicates that throughout the basin there is little variation in deformation. Figure 6 is a map of the Early Miocene horizon from the area showing the general fault pattern. This supports the consistency of deformation style in figures 8, 9 and 10 as the major fault system is clear in map view.

The schematic cross-section (figure 7) illustrates the Early, Middle and Late Miocene and the Early Pliocene horizons that have been mapped and studied in order to characterise the population of fault throws and fault-related fold amplitudes. This process will be explained in detail in chapter 3.2.1. Figure 12 is a stratigraphic column showing the regional stratigraphy of the Gulf of Mexico, and also a smaller stratigraphic column (figure 13) detailing the stratigraphy of the study area in more detail.

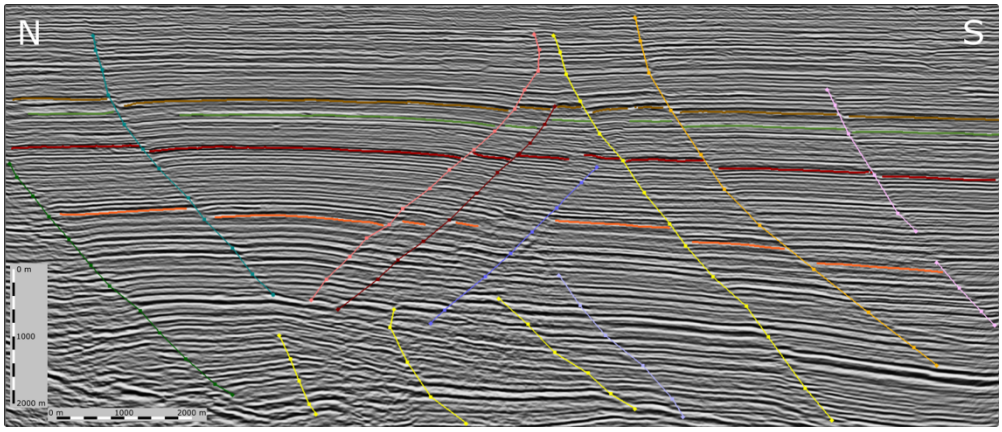

Figure 8: cross-section through the Gulf of Mexico data set showing the mapped horizons (see figure 9) and picked faults (west)

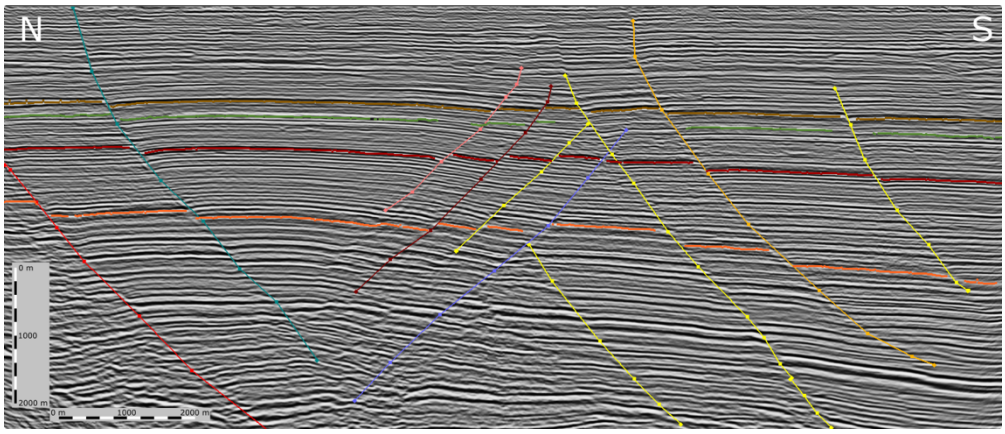

Figure 9: cross-section through the Gulf of Mexico data set (middle)

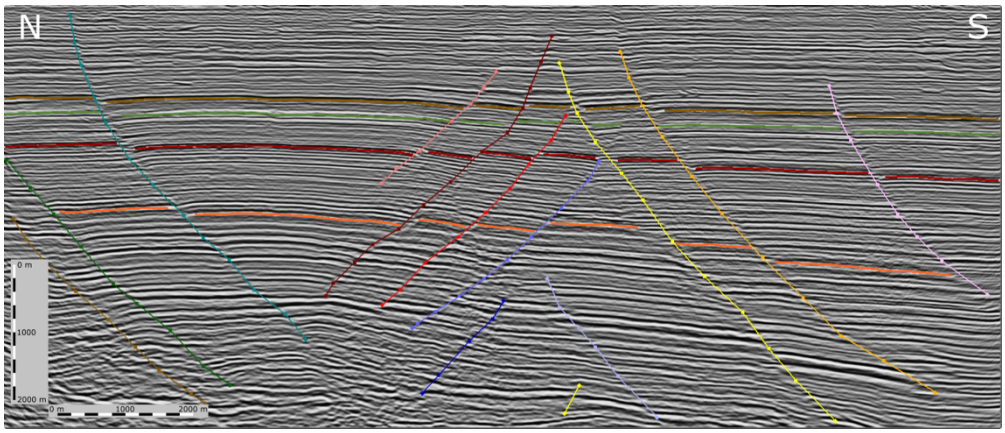

Figure 10: cross-section through the Gulf of Mexico data set (middle)

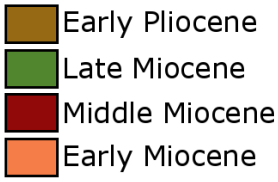

Figure 11: accompanying legend to the cross-sections in figure 8, 9 and 10

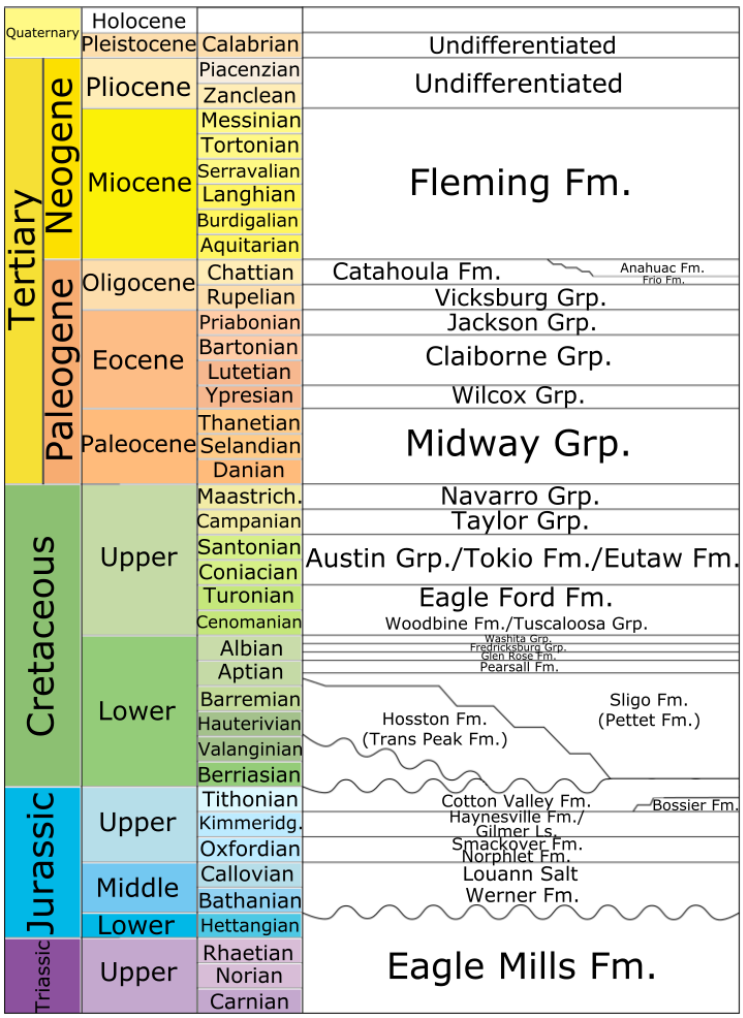

Figure 12: stratigraphic column for the Gulf of Mexico field (Chowdhury and Turco, 2006)

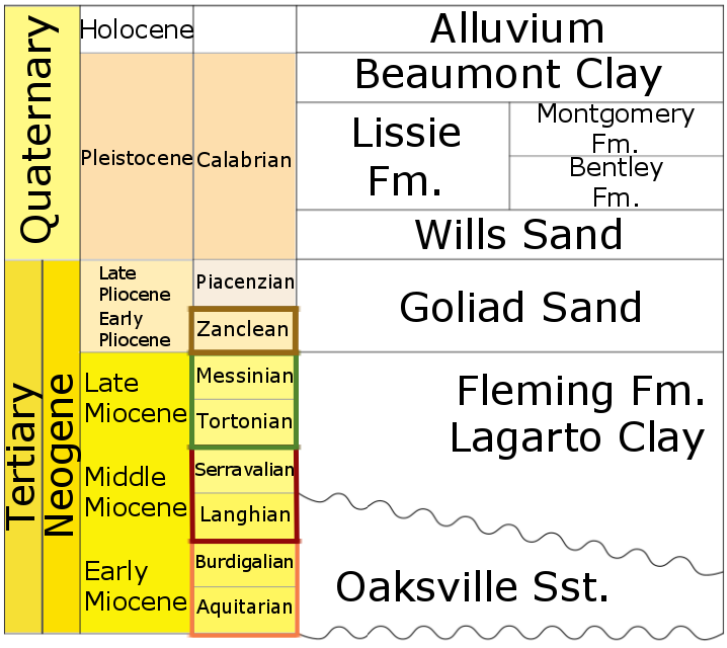

Figure 13: stratigraphic column for the specific horizons which the study has focused on (Chowdhury and Turco, 2006)

2.1.2. Geological history

The Gulf of Mexico was formed during the late Triassic as a result of lithospheric thinning associated with the breakup of Pangaea, and the opening of the North Atlantic Ocean (Goldthwait, 1991; Salvador, 1991, Byerly, 1991; Hosman and Weiss, 1991). The majority of the igneous activity is thought to have occurred during the late Cretaceous and Oligocene-Miocene periods (Bylerly, 1991) and it has been proposed that these processes may have had some control on the thermal uplift history of the basin.

Around the edge of the basin the local structures are formed largely by gravity acting on the thick sediment sections which have been deposited on atypically pressured shale or salt. These atypically pressured shales and salts have then become mobilised, due to their buoyancy, above the rigid basement to produce salt-flow structures and growth faults (Nelson, 1991). These growth faults are often referred to as listric-normal faults as they have an extension component (Nelson, 1991). The fault system within the Gulf of Mexico can generally be described as being dominated by gravity-driven normal faulting. These fault systems can be seen on an Early Miocene age depth map from the 3D seismic survey area, figure 6.

2.1.3 Stratigraphy and sedimentology of the faulted section

The sedimentary sequence imaged within the West Cameron 3D seismic dataset is mainly of early Miocene to early Pliocene age. The overlying Quaternary sediments above this succession have also been affected by the fault-related folding. The Gulf of Mexico is largely dominated by muddy sediments, which may be incompetent and particularly susceptible to folding (Ferrill et al., 2007).

More specifically the Miocene series contains the Oakville Sandstone and the Fleming formation which are formed from terrigenous clastic sediments with interbedded sand and clays (Baker, 1979). The Oakville Sandstone uncomformably overlies the Catahoula Formation and is uncomformably overlain by the Lagarto Clay of the Fleming Formation (figure 13) (Chowdhury and Turco, 2006). The Fleming Formation can be identified by its greater percentage of clay (Baker, 1979).

The Pliocene series are more arenaceous and interbedded than the underlying Miocene series. The lower part of the Goliad Formation contains course-grained sediments, including cobbles, clay balls and wood fragments (Hosman, 1996), moving into the upper part of the Goliad Formation there are finer grained sands which are cemented with calcium carbonate (Hosman, 1996).

Within the Pleistocene series the dominant subdivisions of this system are the Lissie Formation and Beaumont Clay. The Lissie Formation which is made up of reddish, orange and grey fine- to course grained crossbedded sands. These sands are more fine-grained with fewer conglomerates than the underlying Goliad Sand (Price, 1934). The Beaumont Clay which is comprised of poorly bedded, marly clay interbedded with sand (Sellards et al., 1932). There is also the Montgomery and Bentley Formations which are of equivalent age to the Lissie Formation, but are often included within the Beaumont Clay (Baker and Dale, 1961).

2.2. Gulf of Gabès study area

2.2.1. Introduction

The time-migrated 3D seismic survey from the Gulf of Gabès study area is situated over the Miskar gas field, off the NE coast of Tunisia. It consists of a NW-SE striking fault system with high angle dips which vary between NE-dipping and SW-dipping; this can be seen in a depth map and in cross-section in figure 14 and 15 below.

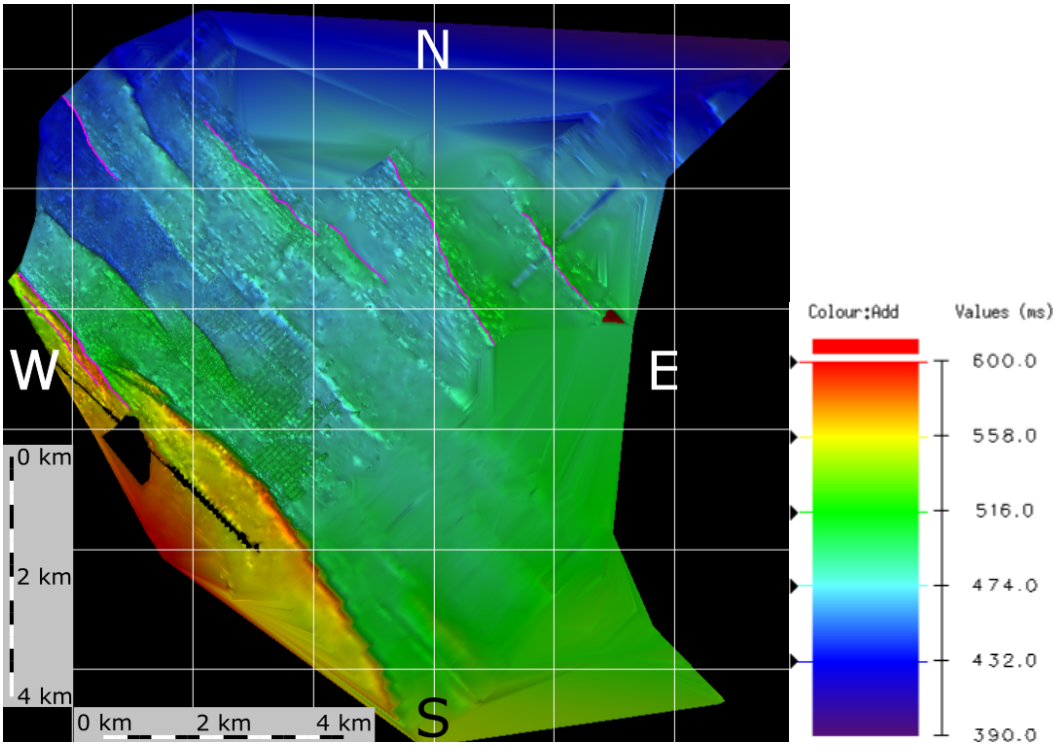

Figure 14: h2 horizon showing the fault polygons of the fault system and legend

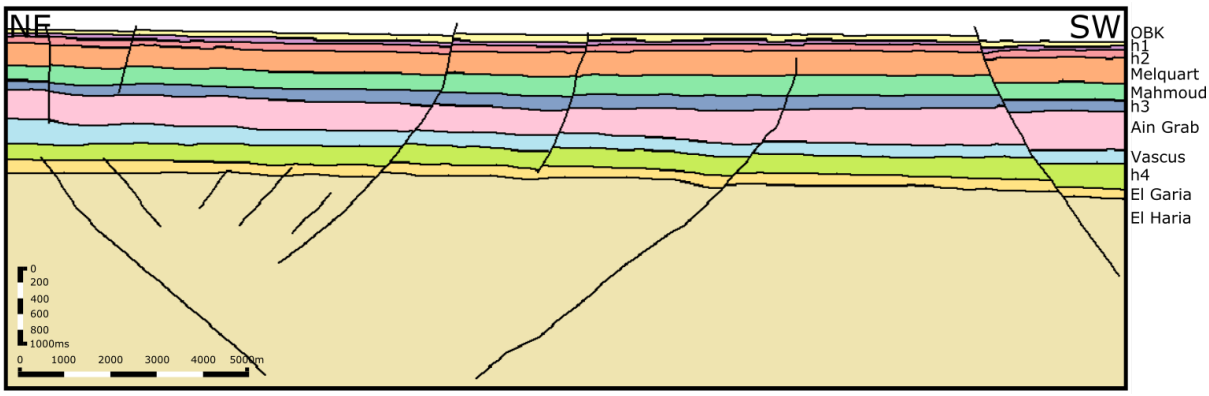

Figure 15: cross-section from the Gulf of Gabès highlighting four different horizons and the studied fault system

The cross-sections in figures 16, 17 and 18 highlight the change in the fault system moving from SE to NW. Figure 16 in the south east of the fault system is comprised of just a few SW- and NE-dipping faults which are short and occur at depth with only one fault interacting with the upper horizons. Figure 17 is much more laterally extensive and the faults are much longer and interact with horizons at depth and nearer the surface. Throw decreases upwards (Childs et al., 2003), and dip increases upwards exhibiting a higher angle at depth. Figure 18, like figure 16 is less laterally extensive however the faults extend to a much greater depth as in figure 17. Similarly between all figures 16, 17 and 18 there is a combination between SW-dipping and NW-dipping faults.

Figure 14 shows a map of a horizon h2 in the area showing the general fault pattern, illustrating the horizons that have been focused on. Figure 20 is a stratigraphic column illustrating the regional stratigraphy.

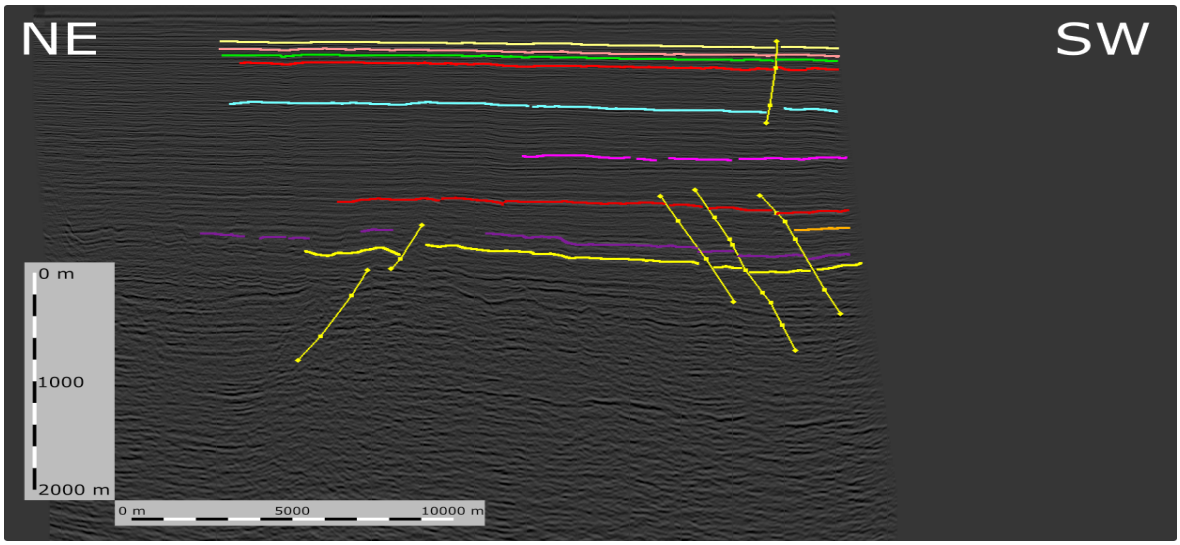

Figure 16: cross section through the Gulf of Gabès data set (south east)

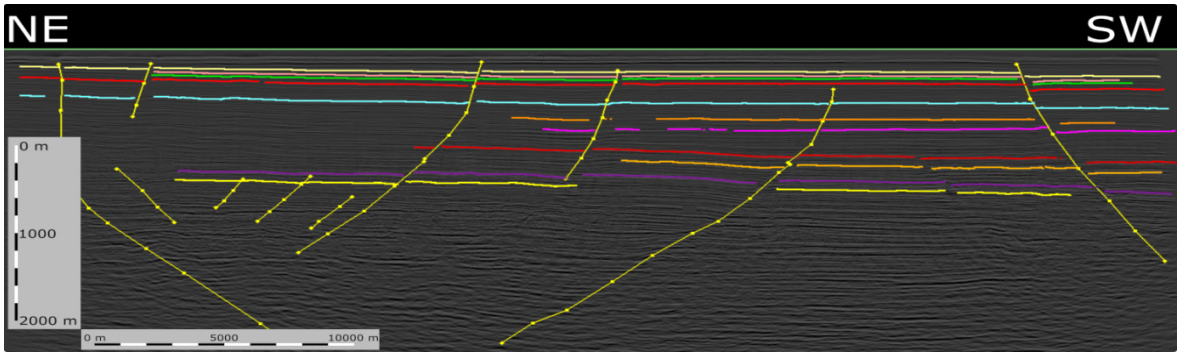

Figure 17: cross-sections through the Gulf of Gabès data set (middle)

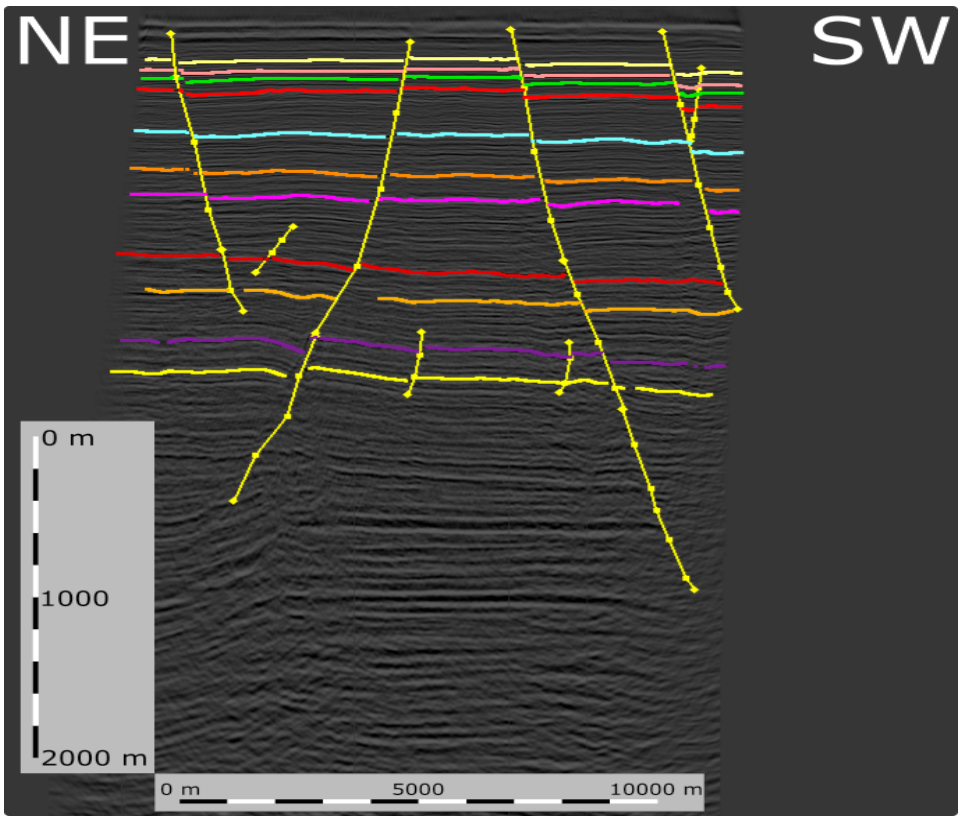

Figure 18: cross-section through the Gulf of Gabès data set (north west)

Figure 19: accompanying legend to the cross-sections in figures 16, 17 and 18

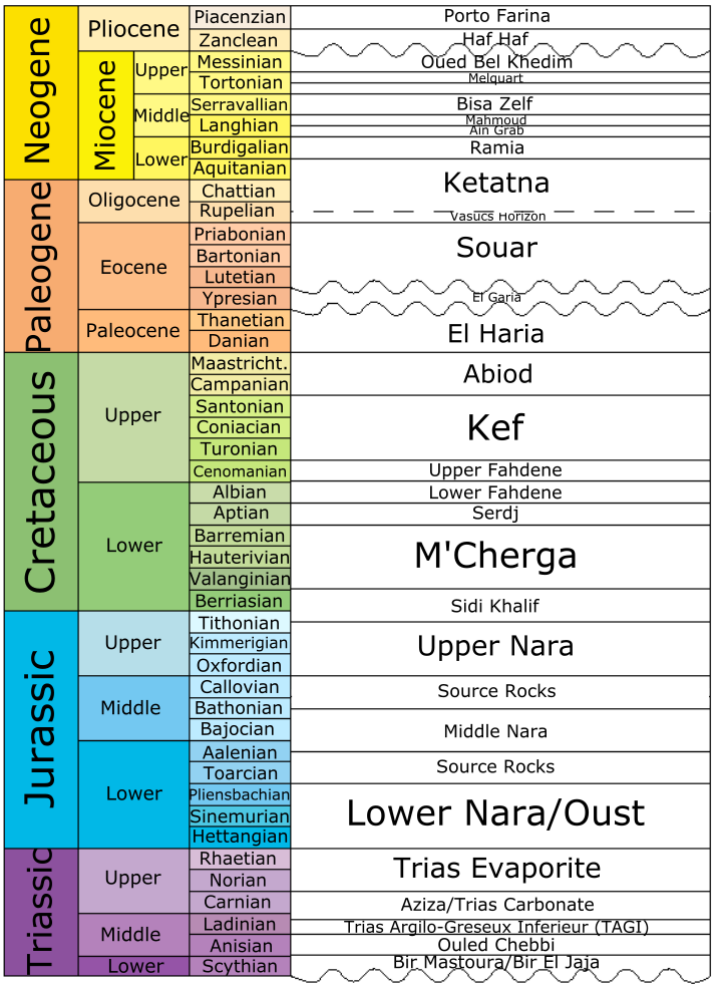

Figure 20: stratigraphic column for the Gulf of Gabès field (Klett, 2001)

2.2.2 Geological history

The Pelagian Province coincides with offshore east-central Tunisia and northern Libya in which the Gulf of Gabès resides. The area is structurally bounded by normal faults which separate the Mesozoic fault basin farther west from eastern Tunisia (Bobier et al., 1991). The faults are oriented NW-SE and the alternating horst and grabens separated by normal faults make up the major structural style at the time of the Cambrian to Carboniferous.

During the Carboniferous, Laurasia collided with Gondwana which resulted in folding, uplift and erosion of older Palaeozoic sections (Ailey et al., 1971; Burollet et al., 1978; Boote et al., 1998).

During the late Carboniferous and Permian, the opening of the Tethyan Seaway (Guiraud, 1998) resulted in rift basins and grabens forming along the northern margin of the African plate.

Moving into the Triassic and early Jurassic, extension and subsidence continued (Morgan et al., 1998) at this time the N-S trending normal faults and E-W trending transfer faults developed (Ouali, 1985; Morgan et al., 1998).

In the late Cretaceous the African plate continued to drift northward and this has continued until present (Morgan et al., 1998). Dextral shearing occurred as a result of shearing between the African and European plates, resulting in a complex horst and graben system in which the associated fault displacements and uplift of horst blocks controlled sedimentation (Morgan et al., 1998).

2.2.3 Stratigraphy and sedimentology of the faulted section

The stratigraphic record of the Gulf of Gabès can be seen in figure 20 and is described in more detail below.

The rocks from the Triassic can be separated into two main intervals consisting of a lower clastic interval and upper evaporite interval (Bishop et al., 1975). The lower interval is made up of the Bir El Jaja, Ouled Chebbi and Trias Argillo-Greseux Inferieur Formations which are comprised of sandstone and mudstone. The upper interval is interbedded with anhydrite, salt and dolostone (Busson, 1976; Bishop, 1975).

The upper Jurassic moving into the early Cretaceous contains the Nara, Sidi Khalif and M'Cherga Formations. These are composed of limestone, dolostone, marl, micrite and mudstone with some interbedded sandstone and shale within these formations (Bishop, 1975; Salaj, 1978).

The Lower Fahdene Formation, which is comprised of limestone, dolostone, sandstone, mudstone, marl and some evaporates (Burollet et al., 1978; Salaj, 1978). The Upper Fahdene Formation deposits are made up of limestone, dolostone and bioclastic rocks (Burollet et al., 1978; Bishop, 1988).

The sediments overlying the Fahdene Formation are mudstone, limestone and marl (Turonian to Campanian) (Bishop et al., 1975; Salaj, 1978). Followed by the Abiod Formation (Campanian to Maastrichtian, late Cretaceous), which is formed of chalky limestone, micrite and marl (Burollet et al., 1978; Salaj, 1978; Bishop, 1975). Overlying this is the El Haria Formation (Danian to Thanetian) which is a grey, brown or black mudstone containing some thin limestone beds in the lower part (Burollet, 1976b; Bishop, 1975).

Overlying the El Haria Formation is the El Garia whose sediments are dominated by evaporates, dolomitic rocks, glauconitic and phosphatic beds (Burollet et al., 1978; Bishop, 1988).

Continuing upwards into the middle and upper Eocene the rocks are mudstone and limestone and make up the Souar Formation (Bishop, 1988). The Vascus horizon unconformity overlies the Souar Formation and is made up of mudstone interbedded with fine grained sandstone (Bishop, 1975; Burollet et al., 1978; Hammuda et al., 1991).

Above this in the lower Miocene is the Ketatna Formation made up of limestone (Schwap, 1995). The upper Miocene is made up of four separate units; the transgressive limestone (Aïn Grab Formation), marls (Mahmoud Formation), sandy sequence (Bisa Zelf Formation) and lagoonal and brackish-water sediments (Messinion Oued Bel Khedim) (Burollet et al., 1978; Salaj, 1978).

Thus, in contrast to the Gulf of Mexico, the faulted Upper Cretaceous to Cenozoic succession in the Gulf of Gabès is dominated by limestone and mudstone.

2.3 Inner Moray Firth study area

2.3.1 Introduction

The time-migrated 3D seismic survey from the Inner Moray Firth study overlies the Beatrice oil field (Stevens, 1991) and is situated off the NE coast of Scotland. It consists of a largely SW-NE striking and NW-SE dipping fault system which can be seen in depth map (figure 21) and seismic cross-section (figures 22, 23 and 24) below.

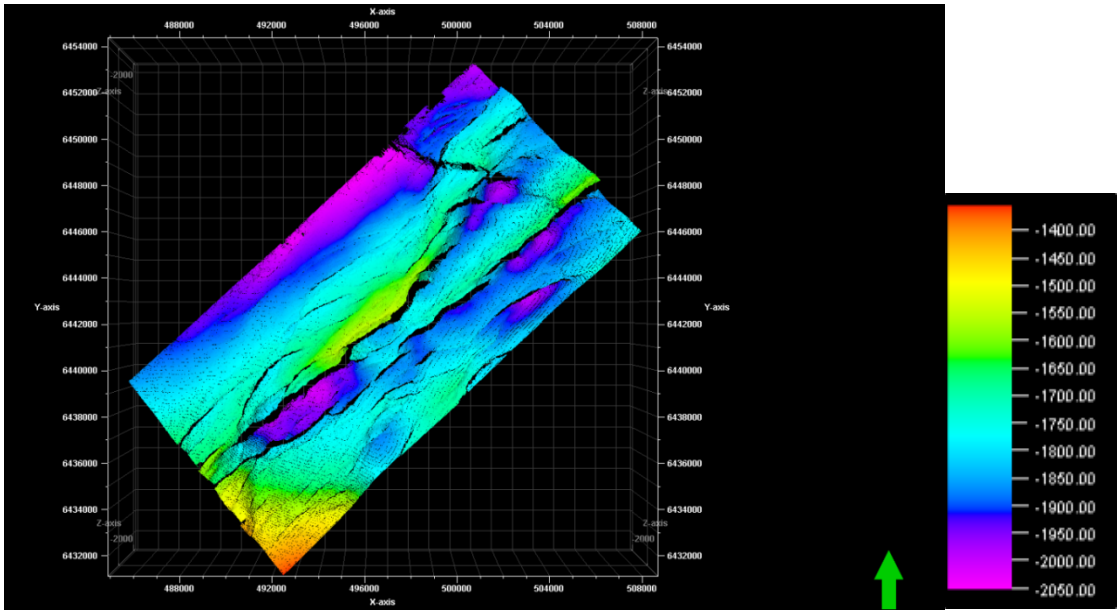

Figure 21: horizon (h1) of the Inner Moray Firth field indicating the major fault systems, scale is measured in TWTT (ms)

The cross-sections in figure 22, 23 and 24 show the major fault structures in the area, with the cross-sections moving from SW to NE. Figure 22 a combination of NW-dipping and SE-dipping faults with the throw decreasing upwards, and the dip angle remains consistent throughout the fault length. In figure 23 the fault system is NW-dipping with throw decreasing upwards. Unlike the previous cross-section there is some variation in dip-angle with it decreasing upwards. Figure 24 shows a NW-dipping fault system with throw decreasing upwards. In comparison to figure 22 and 24 there is significantly more overall deformation in figure 23.

The mapped horizon in figure 21 shows the major fault system which consists of major SW-NE striking faults with minor faults exhibiting the same striking trend either side of this. A more detailed stratigraphy of these horizons will be discussed below and can be seen in figure 26. Figure 27 also shows a schematic cross-section of the central area of the fault populations.

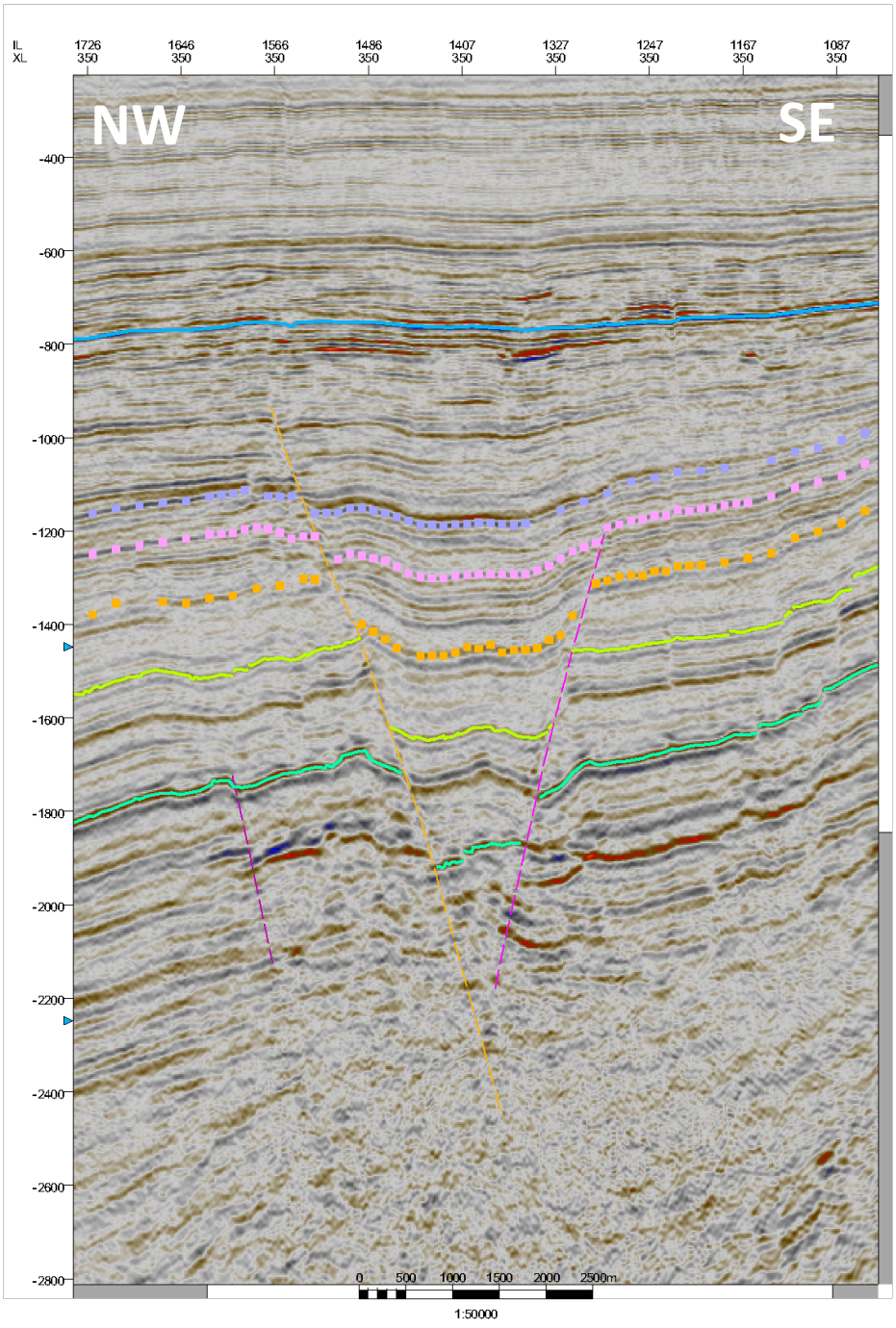

Figure 22: seismic cross-section (south east), scale is measured in TWTT (ms)

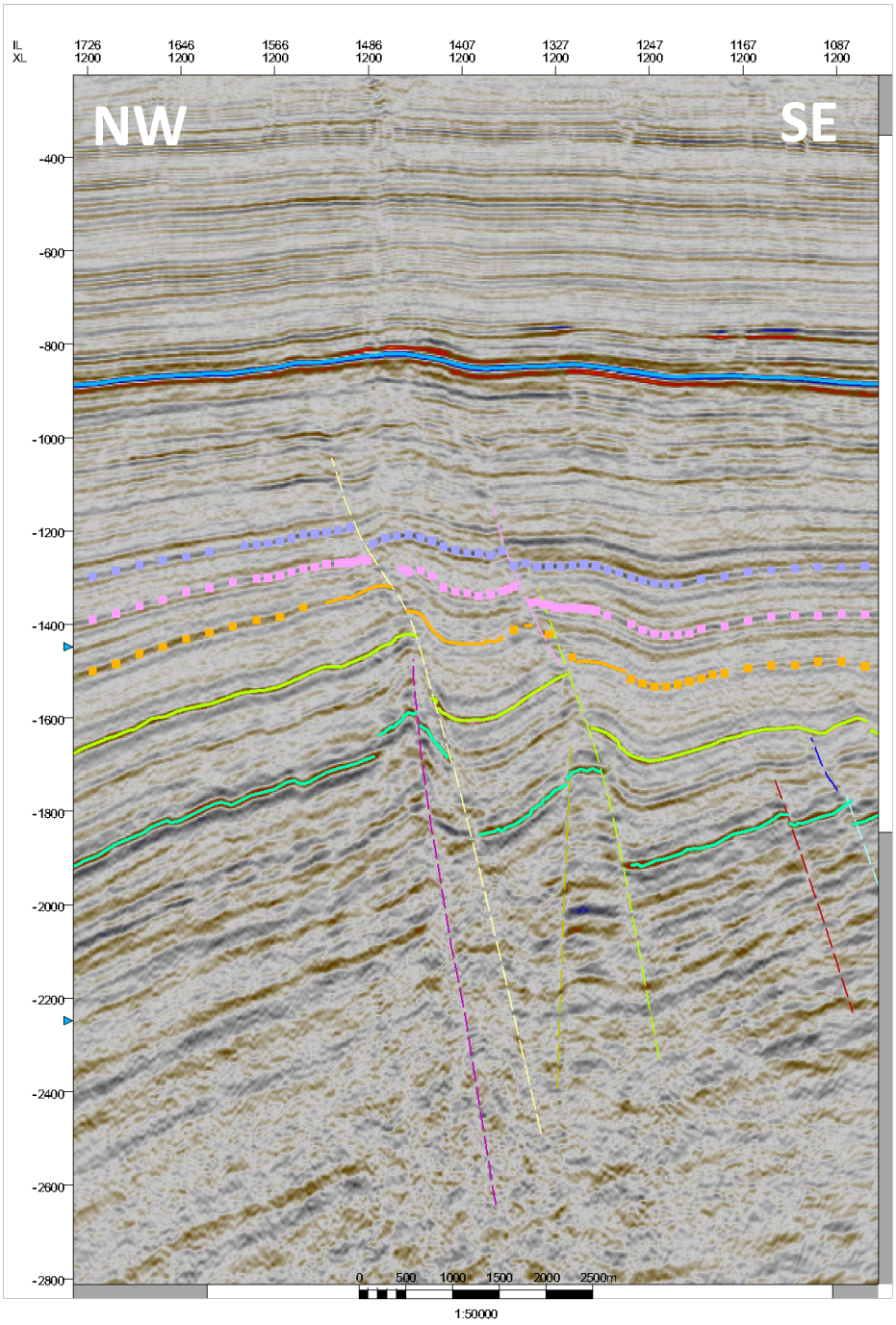

Figure 23: seismic cross section (middle), scale is measured in TWTT (ms)

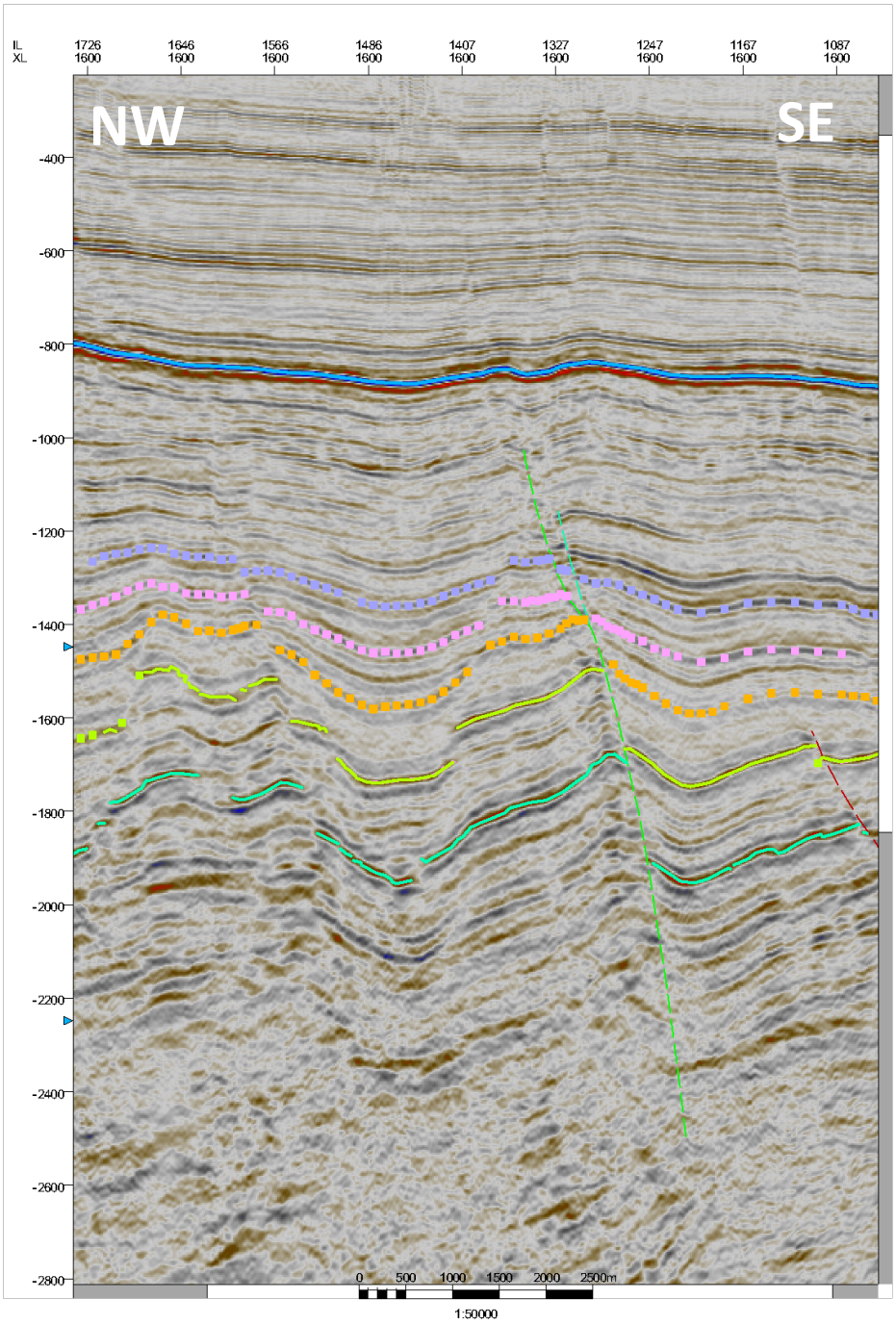

Figure 24: seismic cross-section (north west), scale is measured in TWTT (ms)

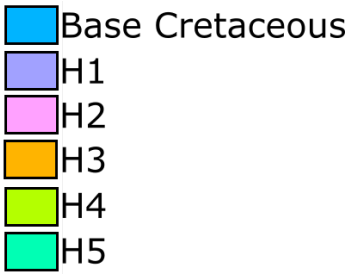

Figure 25: legend for the cross-sections in figures 22, 23 and 24 where the horizons are strong reflectors interpreted below the Cretaceous time period between the Devonian and Jurassic

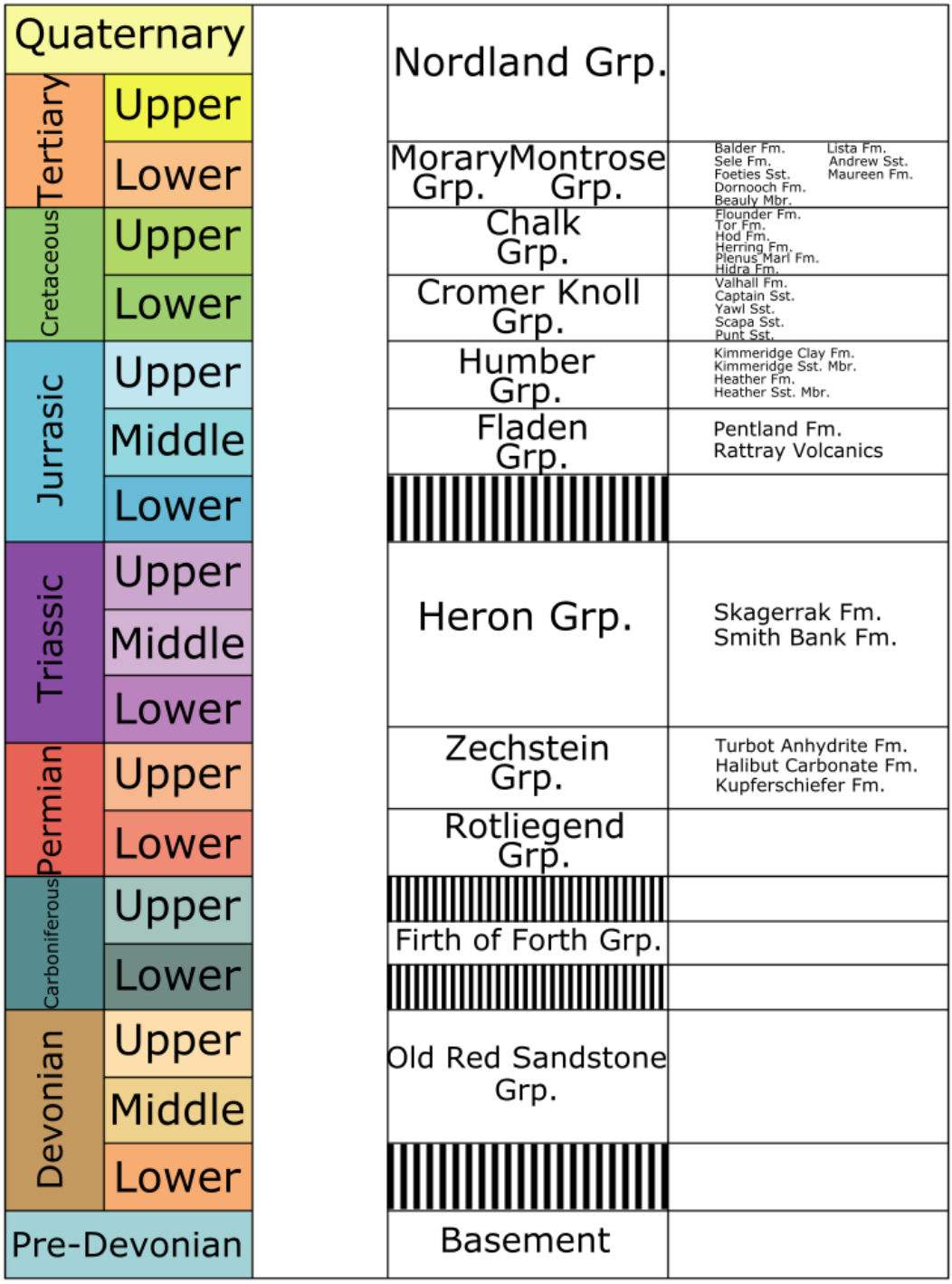

Figure 26: stratigraphic column (Roberts et al., 1990)

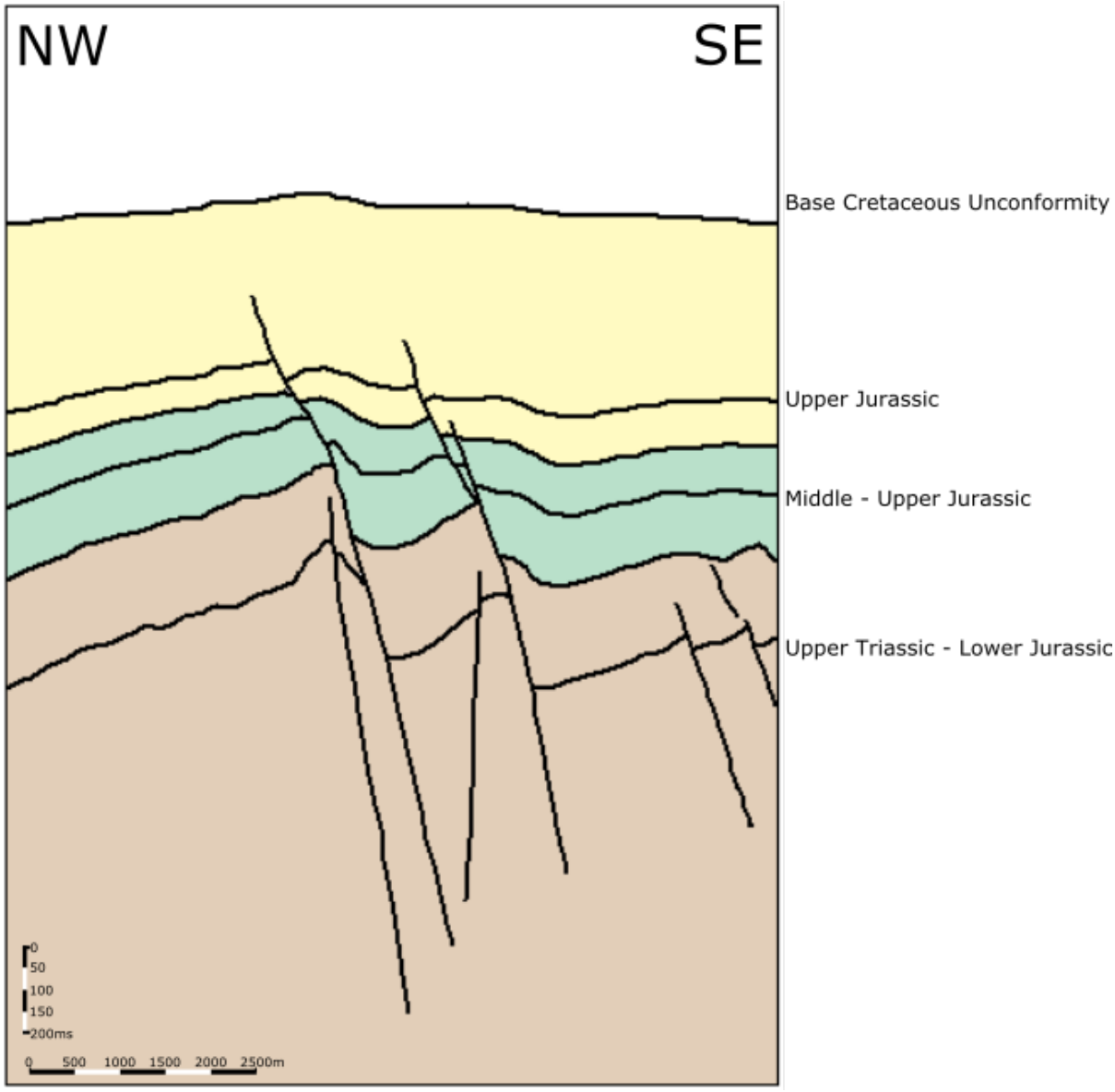

Figure 27: schematic cross-section of the Inner Moray Firth field

2.3.2 Geological history

The previously accepted kinematic model for how this basin was formed suggests that it opened as a result of cumulative 8km dextral displacement on the Great Glen Fault between the Permian and the Quaternary. The majority of this displacement is thought to have occurred during the Jurassic and early Cretaceous (McQuillan et al., 1982; Barr, 1985). This model implies that only faults trending approximately ESE-WNW will have evolved as a dip-slip component of displacement (perpendicular to the Great Glen Fault) (Roberts et al., 1990).

More recent research shows that during the Upper Jurassic-Early Cretaceous faults were accommodated by an extensional episode which concluded in the opening of the North Sea rift system (Ziegler, 1990; Thomson and Underhill, 1993; Davies et al, 2001). It has previously been proposed that the Inner Moray Firth Basin opened as a result of transtensional deformation (Roberts et al., 1990). However there is no evidence for oblique displacement, previous studies suggest that the area is dominated by dip-slip displacement (Underhill, 1991; Davies et al, 2001; Long and Imber, 2010). The strike-slip deformation was not associated with the Inner Moray Firth but the Great Glen Fault. Within the Late Cretaceous there was post-rift subsidence and sedimentation which occurred regionally and was followed by Cenozoic uplift and reactivation of some of the faults. These faults demonstrate a small amount of post-Cretaceous reactivation which was indicated by small-scale folding of the Base Cretaceous horizon, however there is no evidence of large inversion structures affecting the geometries of the pre-inversion folds.

The basin is bounded by the Wick Fault in the north, Great Glen and Helmsdale Faults in the west, the Banff Fault in the south and it opens up to the east into the Witch Ground and Buchan Graben (Roberts et al., 1990). Within the basin, it has been subdivided into graben and half-grabens which have been separated by structurally higher horsts or footwall highs, it is important to note that these structures are all interlinked (Roberts et al., 1990).

Despite the interlinked nature of the structures, the Inner Moray Firth differs in one very important way compared to the other major North Sea graben; with the use of gravity modelling, Donato and Tully (1981) have shown that below the Viking, Central and Outer Moray Firth Graben the crust is thinned such that these basins are isostatically compensated for by low-density sedimentary fill. The Inner Moray Firth on the other hand demonstrates a negative gravity anomaly suggesting that it overlies unthinned crust and is therefore isostatically uncompensated.

2.3.3 Stratigraphy and sedimentology of the faulted section

The Inner Moray Firth sedimentary record indicates the basement is pre-Devonian, with the Devonian then making up the Old Red Sandstone Group. Moving into the Carboniferous, there is the Firth of Forth Group which can be seen in the stratigraphic column in figure 26.

The Rotliegend Group sandstones are contained in the lower Permian. Red-bed facies overly this group uncomformably and are in turn overlain my carbonates, evaporates, mudstones and sandstones of the Zechstein Group. The Zechstein Group can be separated into the Kupferschiefer, Halibut Carbonate and Turbot Anhydrite Formation (Roberts et al., 1990).

The Triassic contains the Heron Group, of which the Smith Bank and Skagerakk Formation exist. The offshore Triassic of the Moray Firth comprises dominantly fluvial sediments which belong to the Smith Bank Formation. This formation is made up of sandstones and shales; they are capped throughout much of the basin by a siliceous limestone of the Statfield Cherty Rock (Frostick et al., 1988).

The Jurassic can be divided into two intervals: the clastic-dominated middle/lower Jurassic and the argillaceous upper Jurassic. The middle/lower provides the reservoir for the Beatrice Oilfield and the upper the seal (Linsley et al., 1980). The sediments of the middle/lower Jurassic are not extensive throughout the Inner Moray Firth whereas the upper Jurassic sediments are. The middle/lower Jurassic contains the Fladen Group which consists of the Pentland Formation and Rattray Volcanics. The upper Jurassic contains the Humber Group which is made up of the Kimmeridge Clay and Heather Formation, and the Kimmerige and Heather Sandstone Member.

These stratigraphic units have been shown to be mechanically incompetent making them susceptible to be deformed by fault-related folding as a result of the underlying faults. This folded area had been previously thought to have occurred as a result of differential compaction (Thomson and Underhill, 1993). However work by Lapadat et al., (2016) has shown that while it isn't possible to exclude compaction entirely it is most likely a secondary deformation style since the hanging wall folds don't display characteristics which can be attributed to this deformation.

The lower Cretaceous contains the Cromer Knoll Group which is made up of the Valhall Formation, Captain, Yawl, Scapa and Punt Sandstone. These appear as interbedded sandstones and mudstones, where the sandstone parts have been interpreted as turbidites deposited in submarine fans (Hancock, 1984).

The upper Cretaceous and Paleocene, although stratigraphically distinct, were deposited in the same environment within a prograding delta, starting with chalky sediments in the upper Cretaceous moving into sandy sediments in the Paleocene (Roberts et al., 1990). These chalky sediments are of the Chalk Group which consists of the Flounder, Tor, Hod, Herring, Plenus Marl and Hidra Formation. The Paleocene (lower Tertiary) contains the Morary and Montrose Group. The Moray Group is made up of the Balder, Sele and Dornooch Formation, the Foeities Sandstone and the Beauly Member. The Montrose Group contains the Lista and Maureen Formation and the Andrew Sandstone. Overlying these formations is the Nordland Grp in the upper Tertiary and Quaternary.

2.4. Gullfaks study area

2.4.1. Introduction

The time-migrated 3D seismic survey across the Gullfaks oil and gas field is situated off the west coast of Norway. It consists of a N-S striking, and W- and E-dipping fault system is shown in depth map (figure 28) cross-section (figure 29 and 30) below. The time-migrated seismic survey was used to characterise the main structural styles within the Gullfaks area; however, the quantitative analysis of the fault populations described in the following chapters was carried out using Statoil's depth maps of key horizons, available via the Norwegian University of Science and Technology website (http://www.ipt.ntnu.no/gullfaks/).

Unlike the previous study areas, the depth map has been taken at a greater depth since this area will not be used for studying the fault-related folds but as a comparison of methods with the comparisons being made between the Top Etive Horizon.

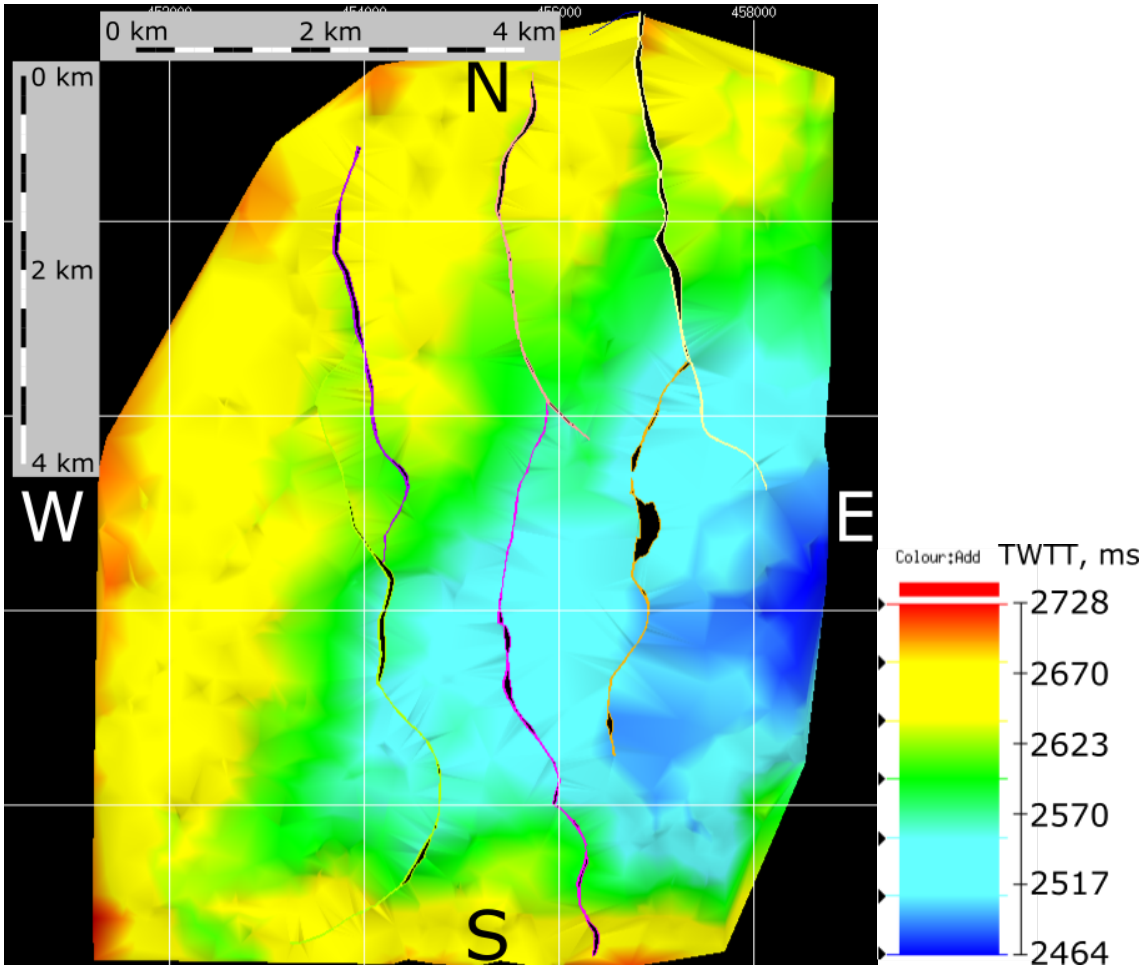

Figure 28: Top Etive horizon showing the fault polygons of the fault system, legend for figure

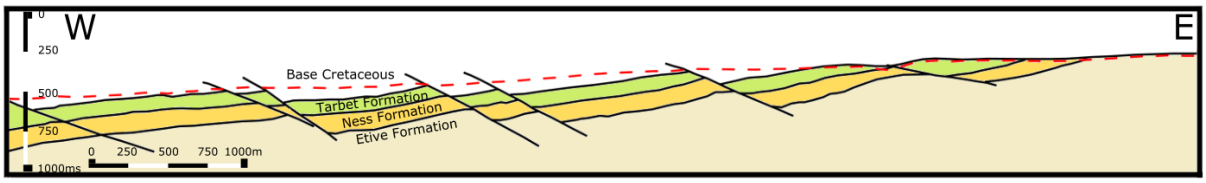

Figure 29: cross-section from the Gullfaks Field highlighting four different horizons and the fault system through these

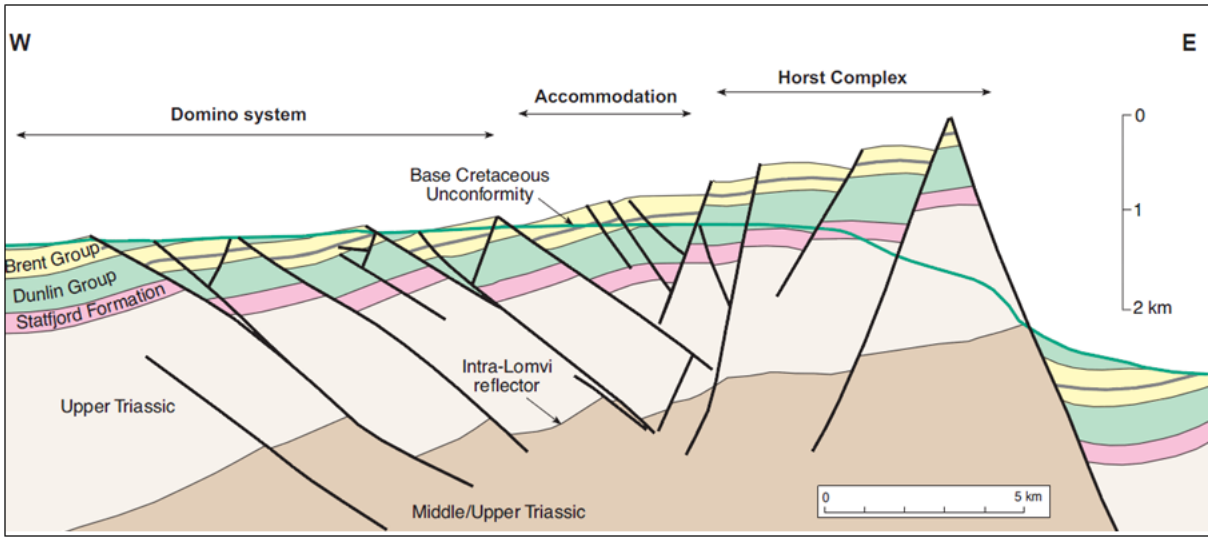

Figure 30: Schematic cross-section of the whole Gullfaks field highlighting the three different zones; Domino Zone, Accommodation Zone and the Horst Complex (Husmo et al, 2003)

The cross-sections in figure 31, 32, 33 and 34 show the major fault systems in the area, with the cross-sections moving from south to north, as well as a schematic cross-section of the whole area geology. Between figures 31, 32, 33 and 34 the style of faulting remains consistent in both dip direction and angle with only small variations. There's a strongly E-dipping fault system occurring at a low angle throughout the cross-sections. Unlike the fault throw in the previous geological areas, throw does not decrease upwards but appears to remain largely consistent throughout the horizons. However, the length of the faults in this population compared to the previous geological areas are considerably shorter. This could mean that throw occurring at a horizon deeper than has been modelled may have a much larger throw.

The seismic data covers the Domino Fault System and a small portion of the Accommodation Zone which will be described in more detail below. Figure 28 shows the Top Etive horizon where the fault polygons highlight the fault system. A more detailed stratigraphy of these horizons is included below along with a stratigraphic column in figure 36, as well as a more detailed stratigraphic column of the Brent Group in figure 37.

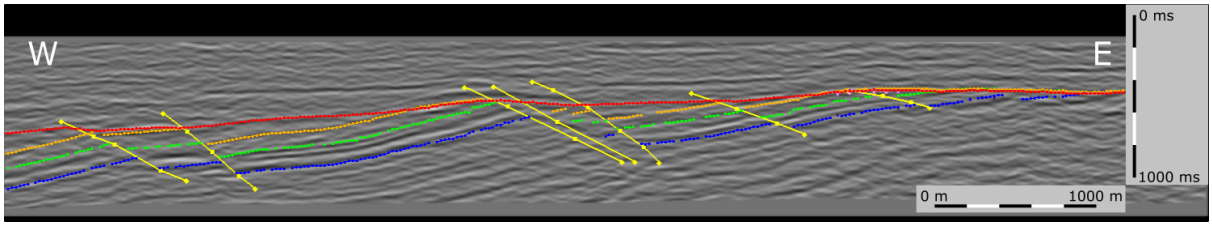

Figure 31: : cross-section through the Gullfaks Field (south)

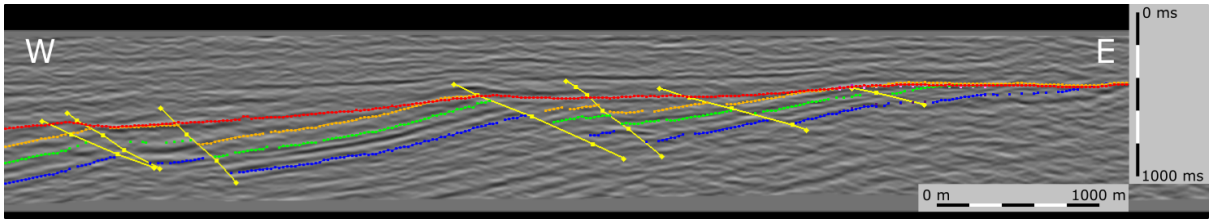

Figure 32: cross-section through the Gullfaks Field (south middle)

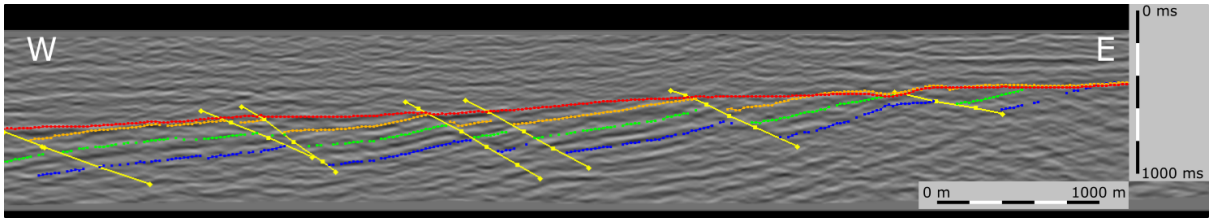

Figure 33: cross-section through the Gullfaks Field (middle north)

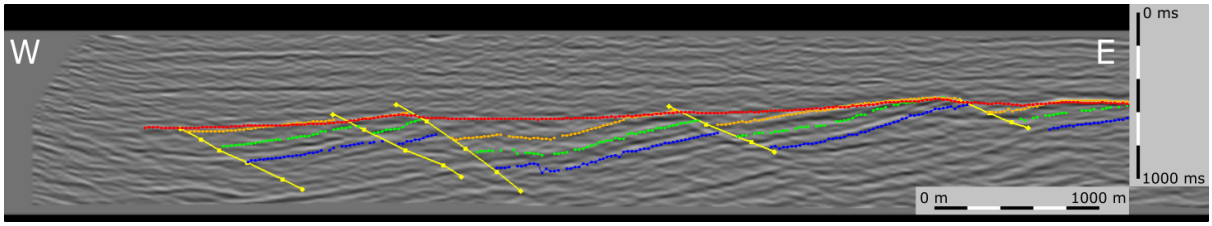

Figure 34: cross-section through the Gullfaks Field (north)

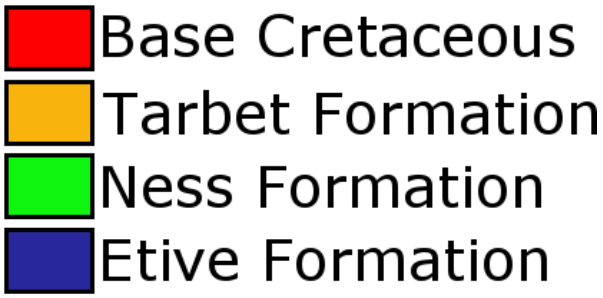

Figure 35: accompanying legend to the cross-sections in figures 31, 32, 33 and 34

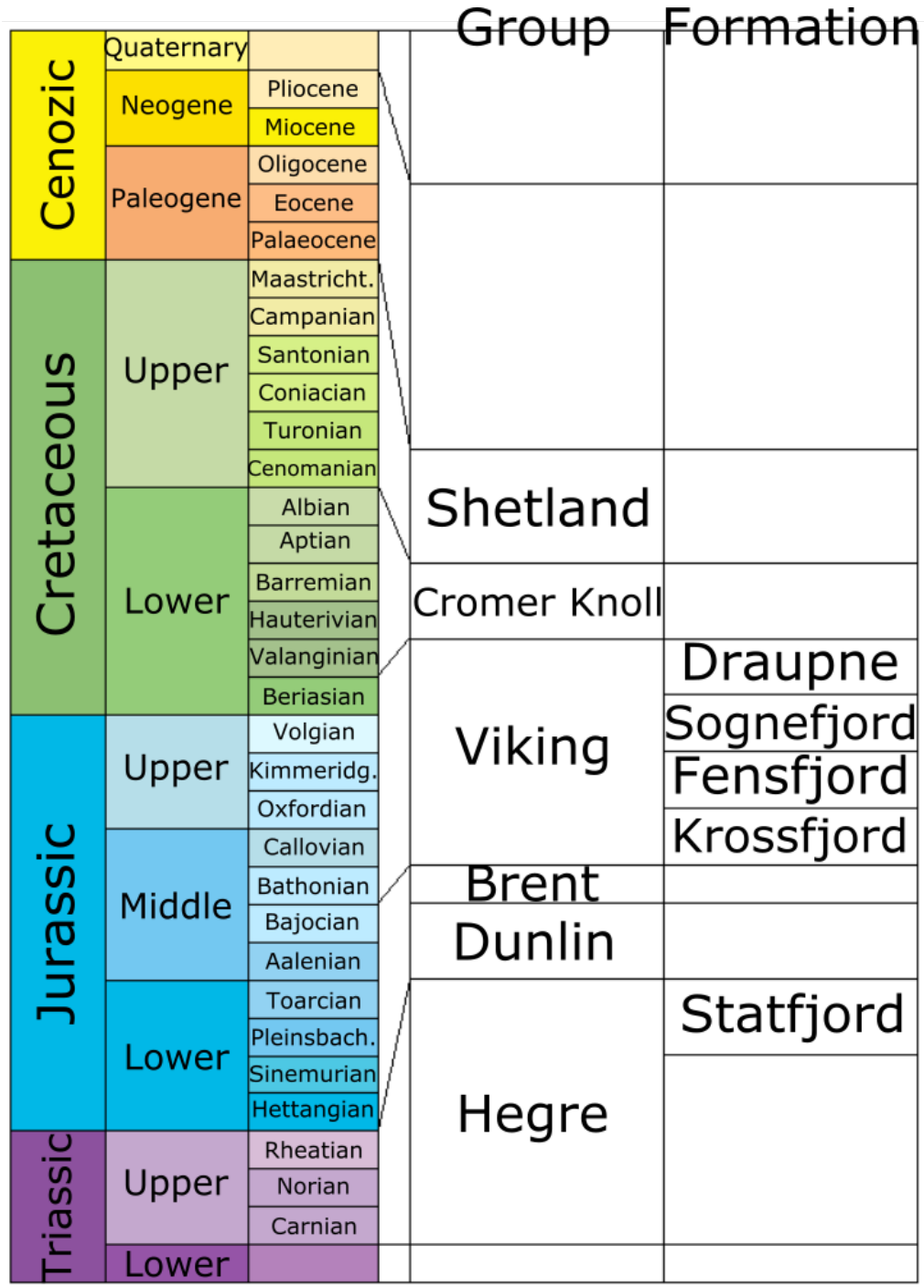

Figure 36: stratigraphic column of the Gullfaks Field (Hesthammer and Fossen, 2001)

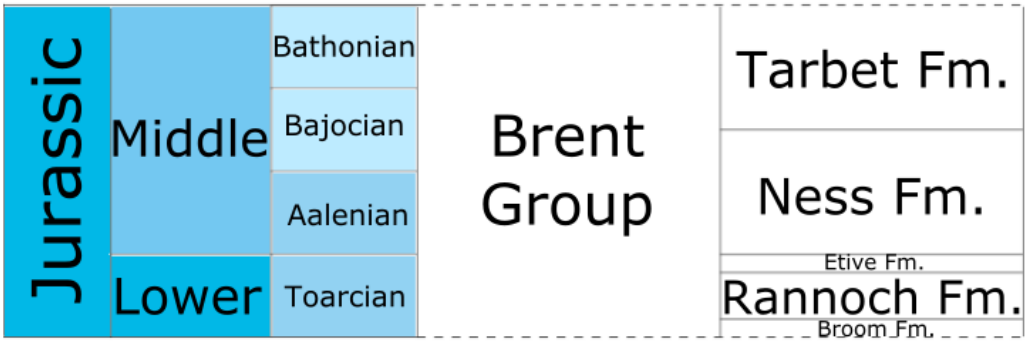

Figure 37: detailed stratigraphic column of the Brent Group (Helland-Hansen et al., 1992)

2.4.2 Geological history

The early structure of much of the North Sea region was formed in three main convergent tectonic episodes (McKerrow et al., 2000) For the Gullfaks Field the two main events affecting the underlying basement rocks were the Caledonian and Variscan orogenies (Evans et al., 2003).

During the late Jurassic to early Cretaceous there was further extension with the tilting of fault blocks adjacent to the Central and Viking Graben. These fault blocks make up the majority of the hydrocarbon-bearing formations in the North Sea. The final major event was a period of uplift in the Mesozoic followed by tectonic inversion of former sedimentary basins during the Cenozoic basins across NW Europe (Glennie et al., 1998).

The structures in the Gullfaks area can be separated into three structural domains: a western Domino-style fault system with east-dipping faults and west-dipping strata, a heavily eroded horst complex with steep faults, and a transitional Accommodation Zone (Hesthammer and Fossen, 2001). These can be seen in schematic cross-section in figure 30 (Husmo et al., 2003).

The west-dipping domino faults comprise the majority of the survey area and exhibit displacements of up to 500m, with the faults in the system dipping at a very low angle of 25-30° towards the east. There are a number of E-W trending minor faults with offsets of less than 50m, these compartmentalise the domino fault blocks. It is believed that these relate to deformation as a result of slip and make up the internal structure of the domino block (Fossen and Rørnes, 1996).

The horst complex to the east consists of faults which are displaced along a much steeper dip compared to the Domino system of about 60°. The Accommodation Zone is bound by both these

structural blocks to the east and to the west. It itself is described as a collapsed anticline with a west-dipping interlimb and is made up of largely minor faults with no consistent trend in strike or dip (Hesthammer and Fossen, 2001).

These fault systems can be seen on a depth map of a given horizon for the seismic data, figure 28 shows the fault polygons outlining the fault system at the Top Etive horizons.

2.4.3. Stratigraphy and sedimentology

The general sedimentology of the area can be described as clastic, and this is detailed below with referenced to figure 36 and 37. The upper Triassic contains the Hegre Group; the sediments in this group are made up of interbedded sandstones, claystones and shales. Overlying this, between the Rhaetian and Sinnemurian, are alluvial sandstones making up the Statfjord Formation. Above is the Sinemurian-Toarcian period which is comprised of marine clay- and siltstones as part of the Amundsen Formation, next is the Cook Formation comprised of regressive marine silty claystones, muddy sandstones and sand. The final formation before the Brent Group is the Drak Formation which is formed of marine shales and siltstones (Hesthammer and Fossen, 2001).

The Brent Group makes up the focus of this study area and is comprised of five formations which are as follows figure 37.

The first of the formations is the Broom Formation which is made up of mudstones and shales, interbedded with thin layers of coarse sandstone and gravel beds. The thin sandstone beds are

commonly carbonate cemented and do not interact with the overlying Rannoch Formation (Helland-Hansen et al., 1992).

The Rannoch Formation stratigraphy is comprised of an overall upward-coarsening sequence of sandstone (Helland-Hansen et al., 1992). Above this lies the Etive Formation which is a medium-course-grained upward fining sandstone sequence (Helland-Hansen et al., 1992).

The Ness Formation is distinguished from the Etive Formation by the first occurrence of a coal bed above clean sands (Tollefsen et al., 1992). The Ness Formation is often divided into an upper and lower unit; where the lower unit consists of interbedded coals, mudstones and sandstones, and the upper is dominated by silt- or claystone with coal deposits (Helland-Hansen et al., 1992). Between the lower and upper Ness there are upward-coarsening sandstones which are proposed to be of a good reservoir quality (Helland-Hansen et al., 1992).

The Tarbet Formation which is controlled purely by a marine environment, and made up of shales, siltstones and coal beds to medium-to-coarse-grained sands (Helland-Hansen et al., 1992).

3. Methodology

3.1 Introduction

The methodologies implemented in the research undertaken were developed from the previous works of Yielding et al., (1996), Watterson et al., (1996), Nicol et al., (1996) and Fossen and Rørnes (1996). One-dimensional multiline surveys were used predominantly, to sample fault-displacement (throw) and fold amplitude populations, but fault-length was investigated using two-dimensional (horizon based) sampling methods. The data were taken from the Gulf of Mexico, Gulf of Gabès, Inner Moray Firth and Gullfaks, the geological settings have been described in chapter 2. Data were acquired from 3D seismic reflection surveys interpreted in TrapTester for the one-dimensional surveys and Petrel for the two-dimensional surveys.

3.2 One-dimensional sampling of fault throw or fold amplitude

3.2.1 Fault interpretation using 3D seismic reflection data

The majority of the data were modelled in TrapTester, which is a structural analysis toolkit provided by Badley Geoscience. It has been primarily used for fault throw and fold amplitude analysis of three out of four three-dimensional seismic data sets (Gulf of Mexico (depth converted), Gulf of Gabés (two-way travel time) and Gullfaks (two-way travel time)).

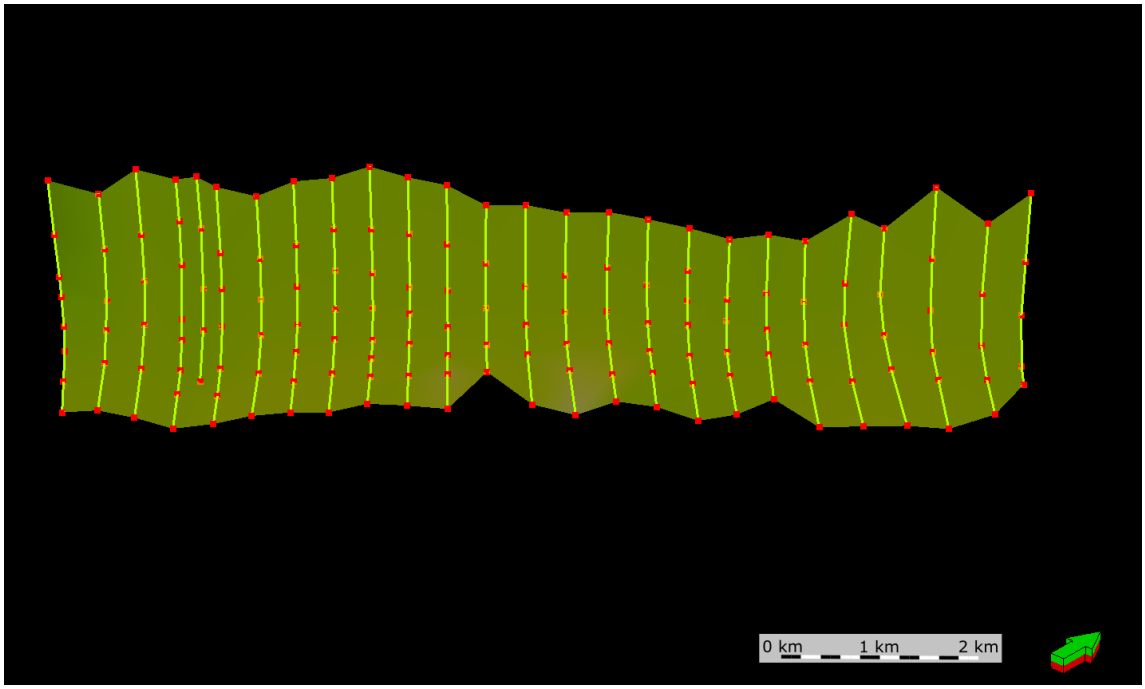

Figure 38: interpreted fault sticks made into a fault plane

Once the 3D seismic reflection data had been imported into TrapTester, the next step was to interpret fault sticks by adding a cross-section and moving this through the seismic volume at regular intervals (figure 38). The fault segments were added to the data by using the tool "Pick Fault" which can trace the line of the fault on the cross-section. In TrapTester this appears as a yellow line until it is "assigned" to a specific fault plane, where it changes colour to the colour of its assigned fault. The intervals which the cross-sections are moved by can be made larger or smaller depending on the level of precision required from the data. The intervals used were variable depending on the size of the fault plane, and the resolution of the seismic data. This was determined based largely on the size of the seismic volume, and keeping a constant spacing between each fault segment i.e. the density of fault segments for each fault remained the same throughout. After this point additional fault segments can be added if the program is still unable to make accurate interpolations between them. This is used as a measure of resolution for the seismic data. The seismic data are generally orientated such that the rows (in-lines) intersect the strike of the fault planes orthogonally, and the columns (cross-lines) run parallel to the strike of the fault planes.

Once all the fault segments have been interpreted, the fault segments can be compared by unloading the active cross-section. In many cases it is then possible to identify major faults by looking at the fault segments from above and picking out the alignments of fault sticks, which define clear trends. The relevant fault segments can be highlighted and assigned to a new fault, a new fault will then form out of the selected fault segments.

For added precision a time-slice (or depth-slice) can be loaded parallel to the survey datum. This time slice will highlight variations in reflectivity (e.g. dimming or brightening) and breaks in reflectors where there is fault present, and therefore provide an accurate method to see which fault segments belong to which fault planes. By moving the time-slice it is possible to assess the vertical extent of the fault plane to ensure all fault segments are added to the fault plane to maximise the amount of data and improve the accuracy.

The next step is to create horizons which will generate fault polygons and eventually fault throws or fold amplitudes (Freeman, et al. 1990). These will generate the data sets from which the scaling distributions can be analysed. Horizon mapping was done by identifying particularly bright, continuous reflectors, which can be tracked throughout the entire seismic data set.

Having identified these reflectors, if not already provided, they needed to be modelled throughout the seismic data by selecting the “Pick Horizon” tool. Again, similar to the fault segments the horizons are created in more or less detail by varying the interval size between the rows and columns. Unlike the fault segments, it is necessary to use both the row and column cross-sections to produce the most accurate and complete horizon possible. A triangular mesh can be generated automatically to fill in the gaps of the horizon grid. However, for this mesh to be

accurate enough interpretation has to already been have been completed or TrapTester is likely to make incorrect interpolations across the grid.

Having completed this for all required horizons and by assigning all fault segments to a fault plane, the resultant throw can be modelled. TrapTester calculates this by taking the difference between the horizons in the footwall and hanging wall of the fault plane, and by also taking into account the dip of the fault in question (figure 46).

As there are number of horizons which have been modelled, the throw can be calculated across all of these. This is done by a fault polygon being created on the fault plane for every horizon which has been modelled which the fault plane intersects. The fault polygon projects the horizon in question onto the fault plane such that there is a line representing the footwall cut-off (i.e. the intersection between the horizon and the footwall side of the fault plane), and one representing the hanging wall cut-off.

The perfect fault polygon would be a smooth line in both the footwall and hanging wall and each would remain in its respective position depending on if it is a normal or thrust fault system. It is often the case that there is not enough horizon data with respect to the size of the fault causing the fault polygon to not be as accurate as is desirable. To remedy this problem, the horizon grid can be refined, with a higher density grid around the fault plane. The patch size can also be changed such that horizon data is included closer to or further away from the fault plane. Despite these measures it's sometimes the case that the fault polygon still doesn't reflect the horizon that it is fitting, at this point it is possible to edit the fault polygon by hand as long as it stays true to the horizon it is modelling i.e. not made smoother in places where it is not.

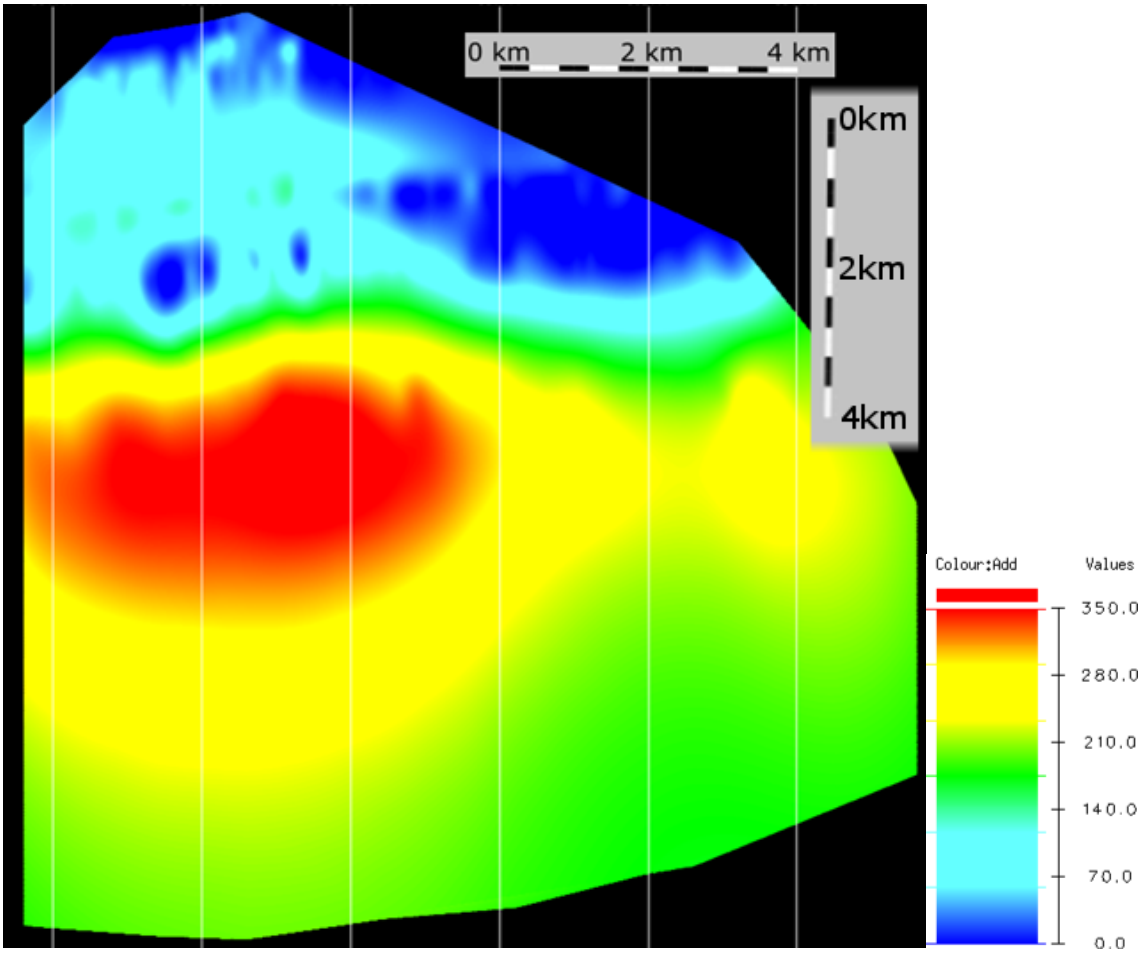

Figure 39: throw projected onto a fault plane in strike projection view with scale bar values in meters (i.e. looking directly onto the surface of the fault plane)

After creating the fault polygons for each horizon and fault plane the resultant throw can be projected onto the surface of the fault plane (figure 39). The expected result of this consists of a throw maximum (bullseye) positioned near the centre of the fault (e.g. Walsh and Watterson, 1989; Kim and Sanderson, 2005; Childs et al., 2003). Throw decreases away from the throw maximum with respect to distance, so the throw minimum should be recorded by the tipline of the fault plane. Ideally, the tipline represents the zero throw contour. From where a fault first forms, the subsequent growth is outwards of this point. This results in high upwards displacement gradients, in which the throw decreases rapidly upwards from the centre of the fault (Childs et al., 2003).

3.2.2 Multiline sampling fault throw or fold amplitude

One-dimensional multiline sampling involves taking a cross-section as close to orthogonal as possible to the strike of a given fault. This enables the throw to be measured between the horizon in the footwall and hanging-wall of the given fault segment. Throw values can be exported automatically by setting the increments with which the sample lines will be set, i.e. every 5m, 10m, 100m etc.

One is then able to select the specific fault and specific horizon for which you want to export the throw values for. This process can be done *en masse* for all faults which intersect a horizon or be carried out for each individual fault and horizon. It is therefore possible to extract and plot the fault throw data against distance along each sample line on a graph, and hence identify where along the fault the maximum throw occurs. However, for this research the overall throw values are more significant than that of the individual throw on each horizon, so the throw values can largely be exported *en masse*.

If the sampled fault throw (or fold amplitude) data are drawn from a power law population, one-dimensional multiline sampling should yield a power law exponent value somewhere between -0.4 to -1.0 (Nicol et al., 1996; see Chapter 1). This is the expected value for one-dimensional data taken from a seismic survey; however a different range of values can be expected for data acquired by a different method (table 1, chapter 1).

For collection of the fold amplitude data similar methods were used to those carried out in the fault collection. At and above the upper tipline of each fault, reflectors can be identified which exhibit fault-related folding (figure 40, 41, 42, 43 and 44), these reflectors generally exhibited the largest amount of folding nearest the tipline and the fold amplitude decreased the further the

horizon was above the tipline. This is in a similar way to the fault throw amplitude at the centre of the fault and the throw decreasing away from this.

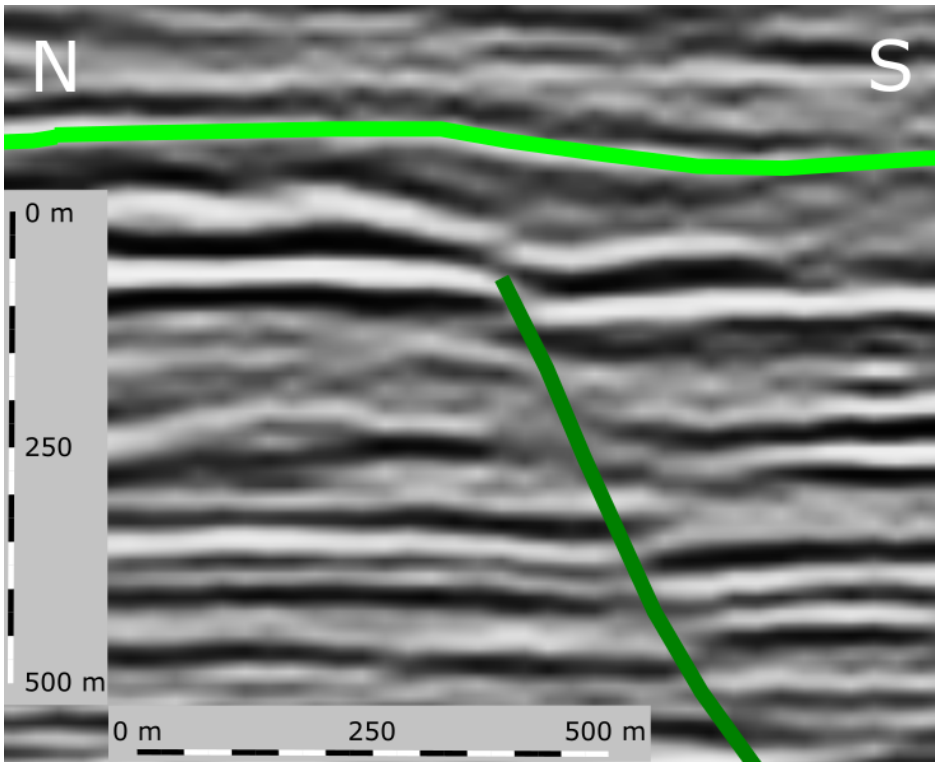

Figure 40: this figure is from the end of the fault plane where the underlying fault hasn't broken through the stratigraphic unit (Gulf of Mexico data set)

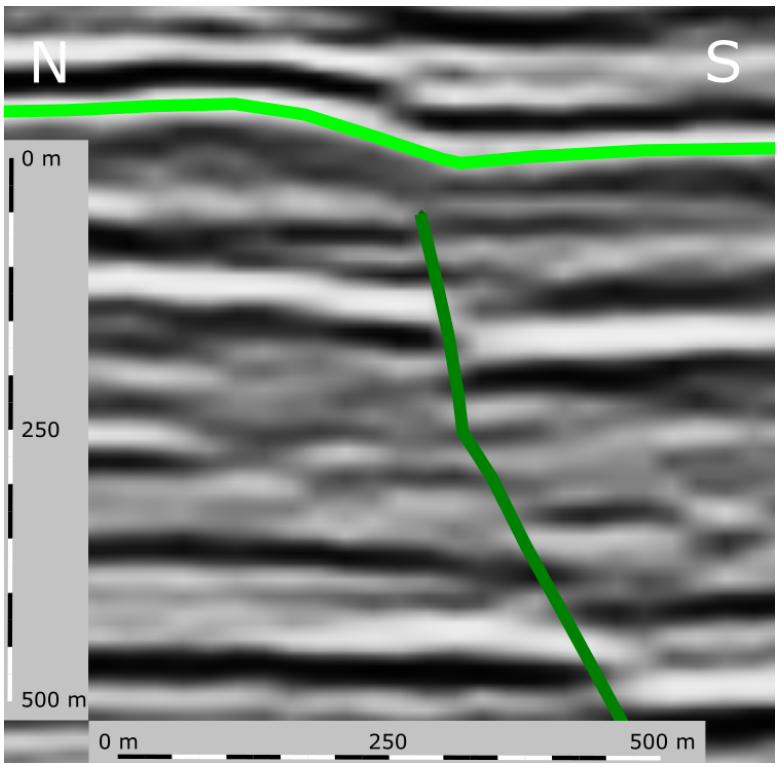

Figure 41: this is the same horizon and fault segment but moving along the strike of the fault plane. This shows a fault-related fold which has propagated into the stratigraphic sequence from the underlying fault from the fault cutting higher due to growth moving

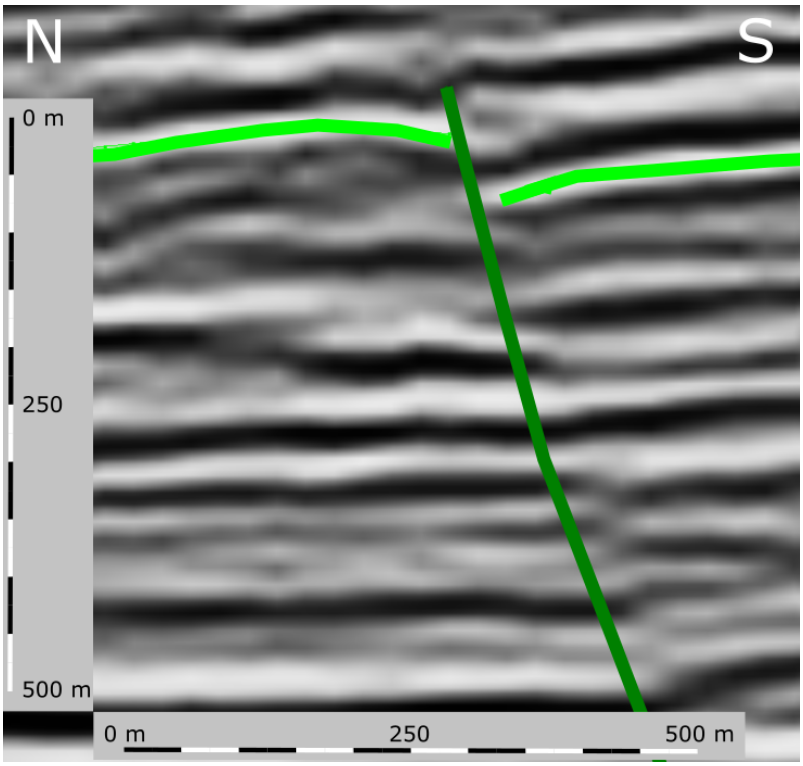

Figure 42: this figure is from further along the strike towards the centre where the underlying fault has broken through the stratigraphic unit causing it to fault (Gulf of Mexico data set)

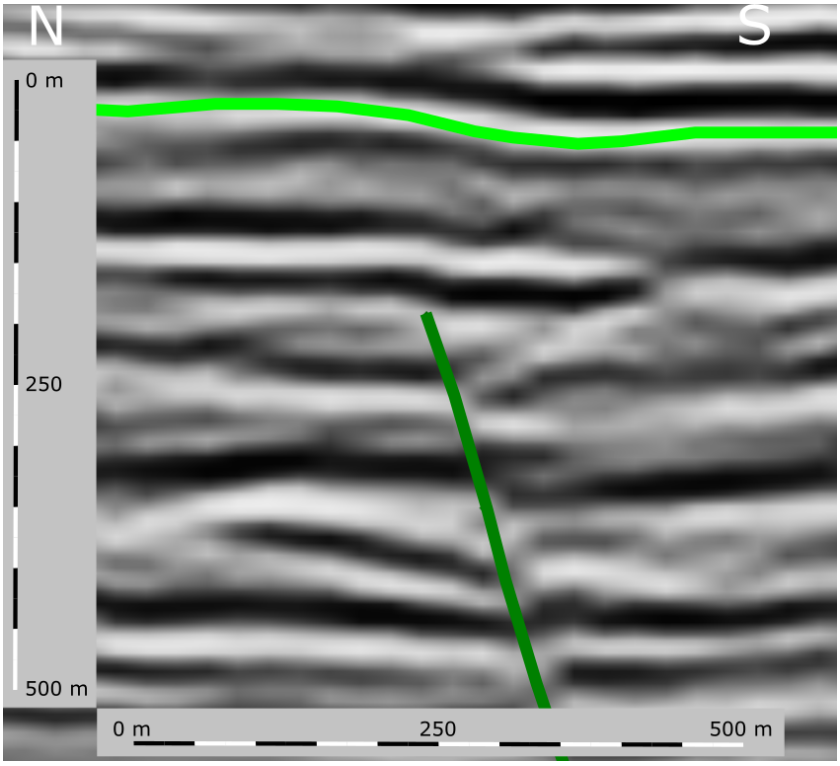

Figure 43: is taken further along the strike of the fault plane away from the centre, here there is a fault-related fold which has been propagated into the stratigraphic unit (Gulf of Mexico data set)

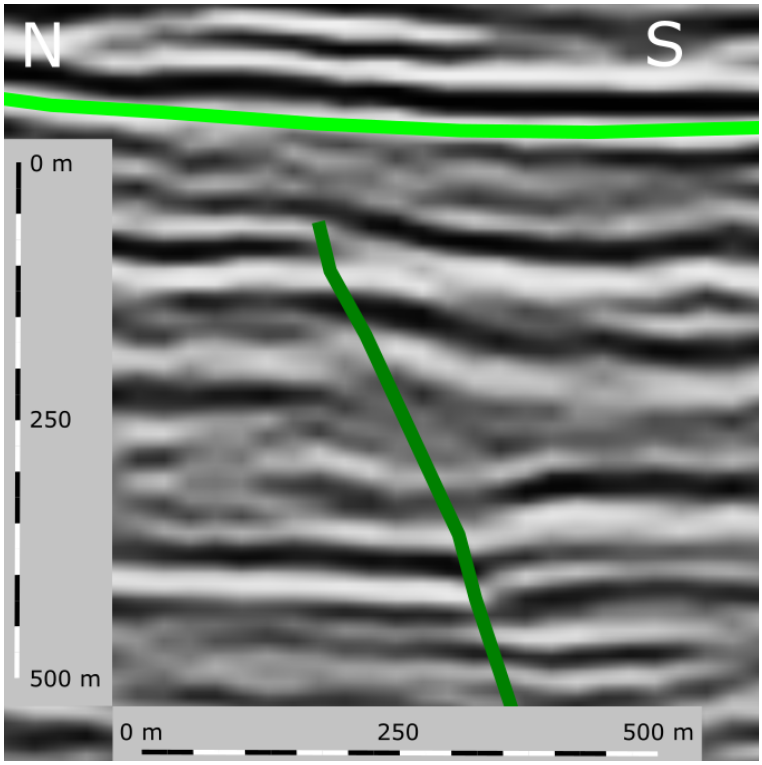

Figure 44: this has reached the end of the fault plane moving along the strike and the overlying stratigraphic is undeformed by the underlying fault (Gulf of Mexico data set)

Since in seismic cross-section it was evident that the folding existed in these areas, the fault-related folding horizons were extended beyond the vertical tipline of the fault plane. Figures 40, 41, 42, 43 and 44 show the development of the fault-related fold moving laterally through the seismic section across one fault plane from the Gulf of Mexico. Figures 40 and 44 demonstrate an undeformed stratigraphic unit overlying a fault segment, the figures are taken from opposite ends of the strike of the same fault plane. Moving along the strike of the fault plane towards the centre of the fault (figures 41 and 43) the underlying fault segment has propagated upwards and formed a fault-related fold in the interpreted horizon. The final figure 44 was taken through the centre of the strike of the fault plane and shows the interpreted horizon to be faulted by the underlying fault plane.

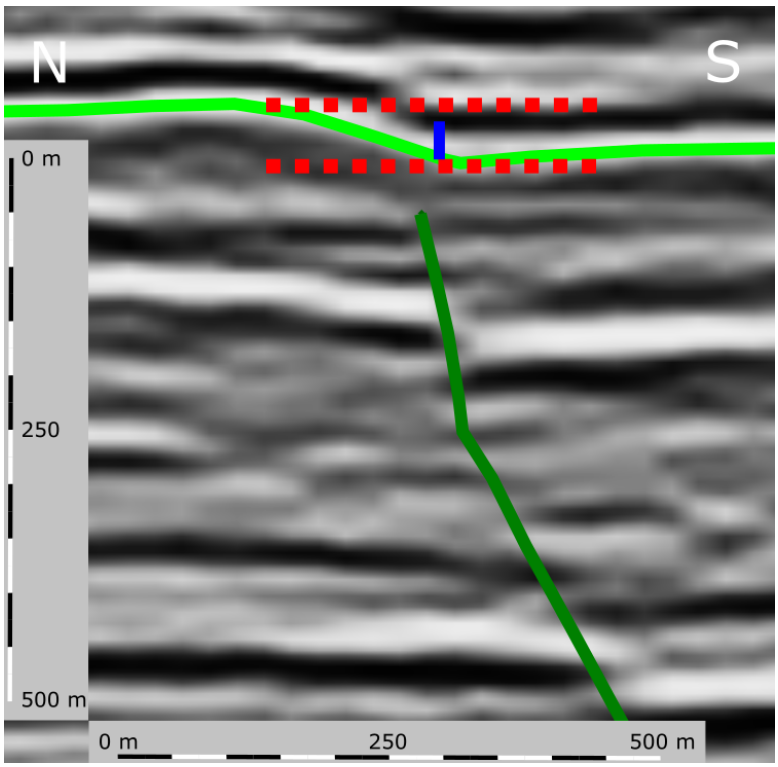

Figure 45: schematic depiction of how and where the fold amplitude measurement was taken

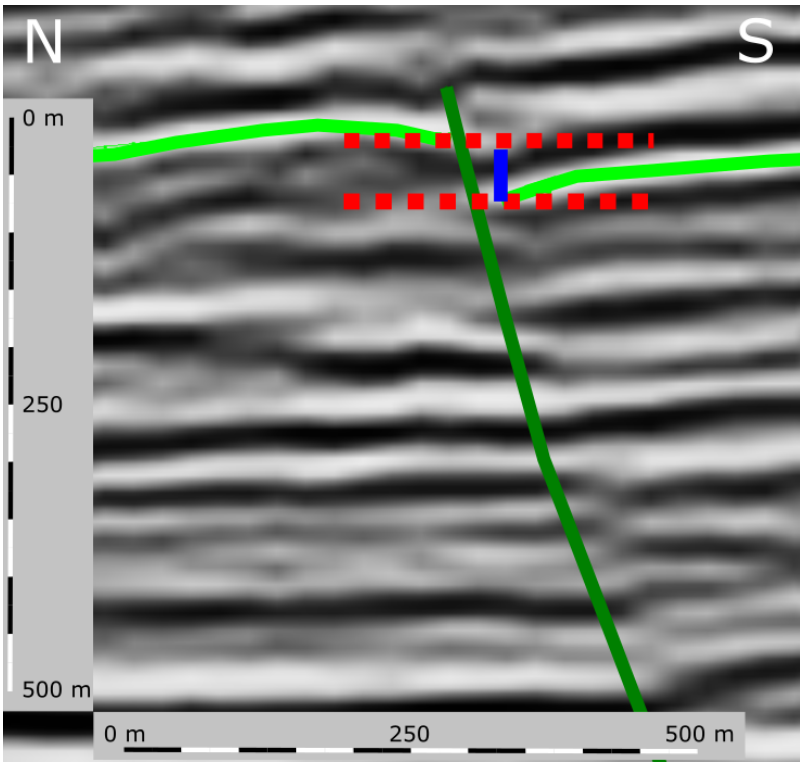

Figure 46: schematic depiction of how and where the fault throw measurement was taken

These horizons were modelled in the same way that they were for the other horizons regarding the throw, but extended only locally above the fault plane tipline. TrapTester is designed for fault

analysis and does not have the ability to export fold amplitude values (figure 45) in the same way that it can for fault throw (figure 46). As a result, the fold amplitude values were measured by hand using the "Measure" tool in TrapTester, this measurement was taken equivalent to where throw is measured. Figures 45 and 46 highlight the distance that was measured; the lines in red extend horizontally from the interpreted horizon and the blue line represents the distance that was measured for each of the measurements. In order to be consistent with the collection of fault throw values, the fold amplitudes were measured at the same interval along the same lines as the throw values were taken.

Having collected both datasets seismic noise (non-interpretable signals recorded by seismometers which mostly consist of surface waves) needed to be accounted for which was picked up in the automated export of the fault throw values, as well as for the seismic resolution of the data. This is generally accepted to be between 10-30m (Yielding et al., 1996). This was set at 10m in order to not impose too many boundaries on the data, so any value which was less than 10m in both the fault and fold data was not analysed. It was felt that setting the value to be 30m would be likely to not include real values of fault throw as opposed to seismic noise. It is important to note however that this value will be variable based on the quality of the seismic data at hand and could be reduced to as little as 4m.

3.3 Two-dimensional sampling of fault length data from the Inner Moray Firth study area

Petrel was used to sample two-dimensional, fault length data from selected time slices and mapped horizons within the Inner Moray Firth 3D seismic reflection data set. The fault planes and horizons were modelled in the same way as for the other seismic data sets in TrapTester (section 3.2.1). However the fault-size measured for this data set was fault-length not fault-throw, as a

result of this the data was acquired in a different way. As described above, particular attention was paid to identifying and mapping fault tiplines.

3.3.1 Sampling fault and fold length data on timeslices and mapped horizons

Fault lengths were measured by hand in Petrel. To do this a similar technique was used as in TrapTester, using a “Measure” tool. Instead of taking a cross-section through the seismic data, a time slice was taken through the data. This meant that fault-length could be measured directly along the time-slice, in the same way that the vertical cross-sections are in the same plane as the fault-throw. It was set up to move up or down by an increment of 100ms (data was in two-way travel time). This was kept the same for every fault and folded horizon. The length of the fault was then measured from each extreme where it intersected the time slice.

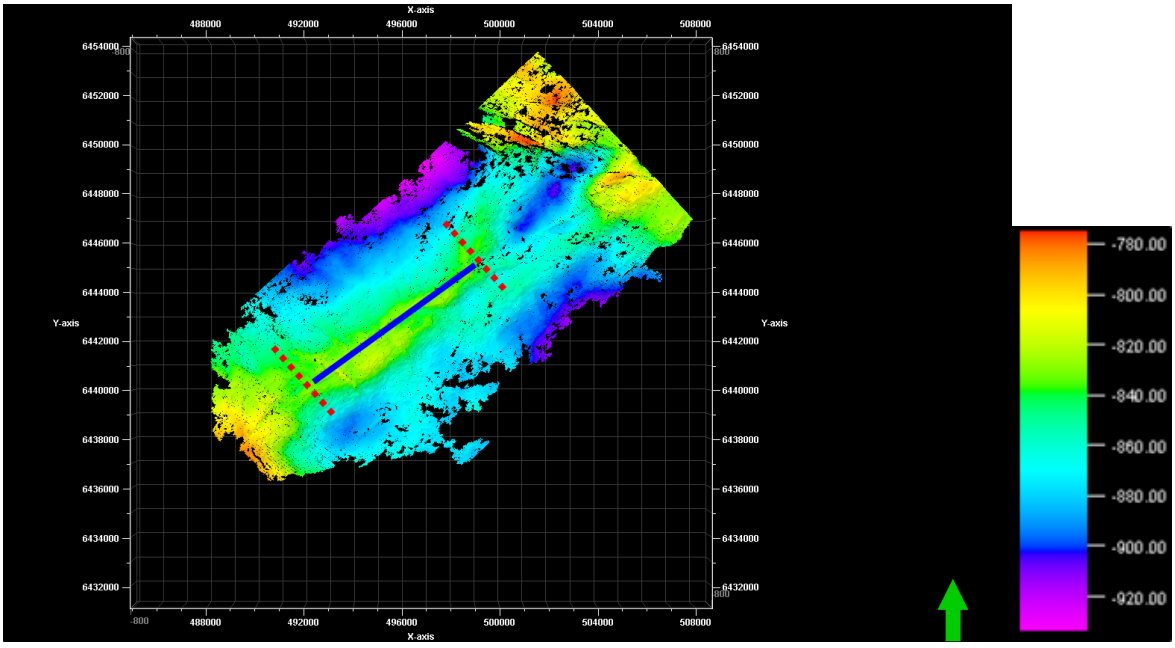

Figure 47: shows the bounds of where the fold length was measured using a depth projection on the interpreted horizon and measuring between the highest contours (TWTT, ms)

In order to measure the fold-length (fold length axial trace), a two-way travel time contours, highlighted using an appropriate colour bar, were imposed on the horizon to identify where the

topographic highs were, and then use this to guide the measurement of the fold length. Unlike the fault plane, a folded horizon is far more continuous and becomes less distinct until it can be considered that the folding has ceased. This point was taken to be a significant flattening out of the topography by noting where the colour of the depth projection changed and became constant as it extended away from the folded area.

In the case of faults, or folds, length data that are drawn from a power-law population and sampled in this manner, would expect to be described by a power-law exponent value somewhere in the range of -1.1 to -2.0 (Yielding et al., 1996). Usually this would be +1.0 on the exponent value from the one-dimensional multiline seismic survey described above.

Fault and fold lengths all surpass the seismic resolution of the data so all values could be analysed. Fault lengths however are subject to censoring and truncation effects (3.4.1). Given the large lengths of the faults it was considered that these effects would not be significant overall and the same effect would have been had on each fault length therefore being equal throughout the fault plane.

3.4 Data analysis

3.4.1 Preliminary analysis using Excel

Having sampled the fault throw and fold amplitude and/or fault length and fold length populations from all the study areas, a rudimentary analysis was carried out in Excel to assess any obvious scaling laws which might be apparent in the data sets. The data were plotted to test for power law, exponential and log-normal distributions. This was achieved by plotting the data on a

log-log axes, log-linear axes and linear-log axes, respectively, for each distribution. This is an accepted method throughout geological literature (Franklin, 2015; Sleight, 2003), and a log base 10 logarithm is used in place of a natural logarithm since it is accepted within geology that events and scaling are governed by base 10 and not base *e*. Cowie et al., 1995; Turcotte, 1989; Fossen, 1996 and Pickering et al., 1995 all use log to the base 10 to acquire their results, this makes it possible to equate exponent values of results since the exponent will vary depending on the log base used.

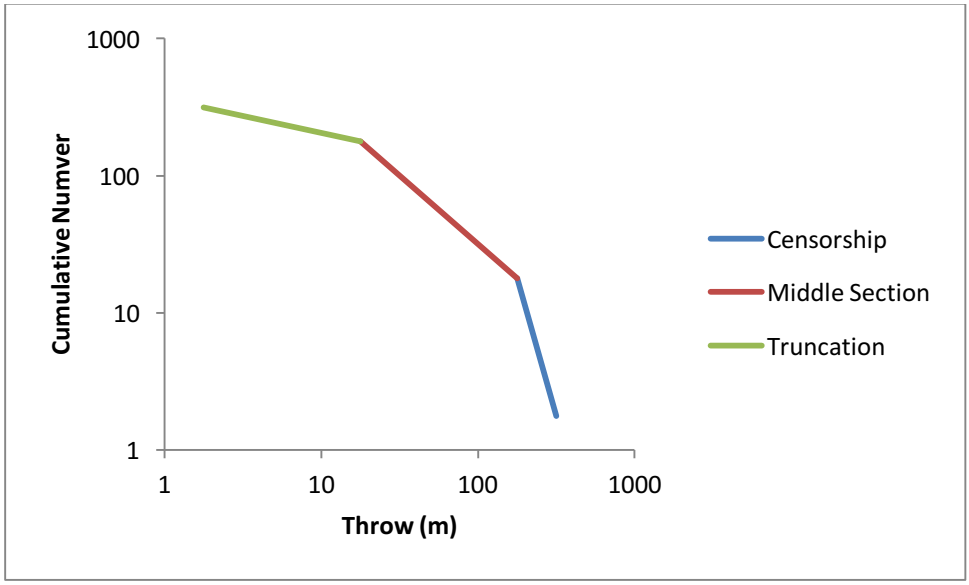

Figure 48: figure highlighting each of the three segments, truncation, middle section that the distribution is commonly thought to be contained in, and censorship. The y-axis is cumulative number and x-axis is fault-size. They are plotted as arbitrary values in order to show the characteristic shapes, this is the shape that should be observed on a log graph.

In each of these cases, if the data plotted follow a straight line graph then it would generally be accepted to follow that respective scaling distribution, and the exponent would be found from the gradient of the straight line section. This technique is reflected in previous published studies, notably Yielding et al., (1996), Watterson et al., (1996), Nicol et al., (1996) and Fossen and Rørnes (1996). These graphs should form a characteristic appearance with a sub-horizontal left-hand segment which indicates a lack of observations below the limit of seismic resolution (truncation) (figure 48). A moderately-dipping middle segment which denotes the distribution fit and is where

the exponent can be calculated (figure 48). Finally a steeply-dipping right-hand segment which indicates a lack of sampling and does not form a representative sample of the population at the higher throw or fold values (censoring) (figure 48) (Needham et al., 1996; Pickering et al., 1995).

3.4.2 Statistical analysis of data distribution using R

R is a programming language which caters for statistical computation, and is supported by graphics. R was used to implement statistical tests of the goodness-of-fit of the sampled data to the different theoretical distributions.

Clauset et al (2009) introduced the idea of using R to generate a synthetic power-law data set from x_{min} and α of a real data set. Where x_{min} represents the smallest value which belongs to the distribution being tested, and α represents the exponent value of the tested distribution. Their paper centres around testing the goodness-of-fit between the real dataset and the synthetic power law distribution (using a Kolmogorov-Smirnov test) (chapter 3.4.2.3), but also touches on fits to exponential and log-normal distributions, and also provides the relevant code for this (http://tuvalu.santafe.edu/~aaronc/powerlaws/, January 2016). The power law fitting method used is maximum-likelihood fitting which is combined with goodness-of-fit tests in order to quantify the fit between the empirical and observed data.

Whilst providing a rigorous, objective methodology to identify the best fitting distribution, the method of Clauset et al., (2009) has a major problem which prohibits the use of it for this research, and other commonly used geological datasets. In particular, they have made the assumption that α (the power law exponent value) will always be greater or equal to 1. However, it has been established previously that for a one-dimensional multiline sampling survey the

expected exponent value will be between -0.4 to -1.0, which is less than 1 (Nicol et al., 1996). As a result of this limitation, the method and also code produced by Clauset et al., (2009) is strictly valid only for two-dimensional datasets – but not the one-dimensional multiline samples. An alternative method to test the goodness-of-fit between real datasets and theoretical distributions has therefore been developed, in collaboration with Dr Camila Caiado (Department of Mathematical Sciences, Durham University). Dr Camila Caiado wrote the base for the code, for both the Kolmogorov-Smirnov and Anderson-Darling test testing the power law. This was then built upon to test for the other distributions and also to vary the way in which the exponent value was gained. This intention is that the new method should provide a more objective approach to, and build upon, the more established methods of estimating best-fits to straight line segments, described by Yielding et al., (1996), Watterson et al., (1996), Nicol et al., (1996), and Fossen and Rørnes (1996) and others.

The code that was developed had two variants: first, sub-sampling the cumulative frequency distribution using an incremental increase in window size; and second, sub-sampling cumulative frequency distributions using a moving window. The goodness-of-fit (chapter 3.4.2.5) between sub-samples and theoretical (e.g. power law) distributions were tested using the Kolmogorov-Smirnov (http://www.rdocumentation.org/ "Kolmogorov-Smirnov Tests", January 2016) and Anderson-Darling Tests (http://www.rdocumentation.org/ "kSamples, Anderson-Darling Test", February 2016). These variant are described below. However, the basic code varies by only a small amount for each of the respective statistical tests. The code for the incremental window and the moving window is presented in Appendix 1.

3.4.2.1 Incremental window method

The incremental window method starts with a given window size which provides a sub-sample of the entire data set and tested for a power law (or other) distribution, and then the window size is increased and a larger sample of the data is obtained and tested. This is repeated until the window has been incrementally increased such that the entire data set has been included. A diagrammatic representation is show below in figure 49, as well as the included code in Appendix 1 and a flowchart showing how this works (figure 118).

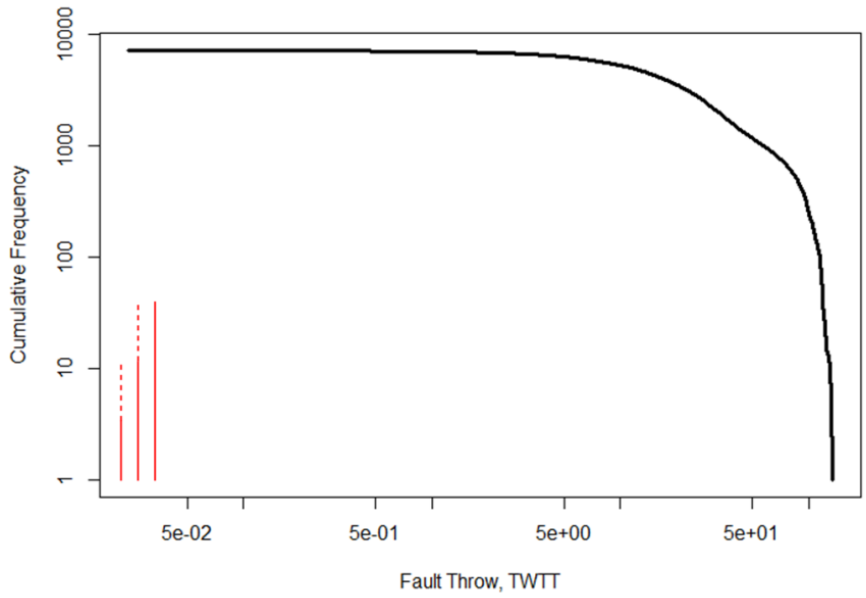

Figure 49: illustrates how the incremental window works. Starting with the red line on the left and increasing by the amount indicated by the dashed red line and so on. This process is repeated until the window spans the entirety of the data set until the length of the red line is equal to the number of data points (data from the Gulf of Mexico).

This method commonly shows a good fit at the start when the window size only tests a small number of data points. It becomes a worse fit as it includes an increasing amount of data as the window size increases (figure 49).

3.4.2.2 Moving window method

The moving window method uses a window of a given size to sub-sample the entire data set, and it moves along the data set at a given spacing i.e. is shifted by a set amount each time. There is a diagrammatic representation show below in figure 50, as well as the code included in Appendix 1 and a flowchart showing how this works (figure 50).

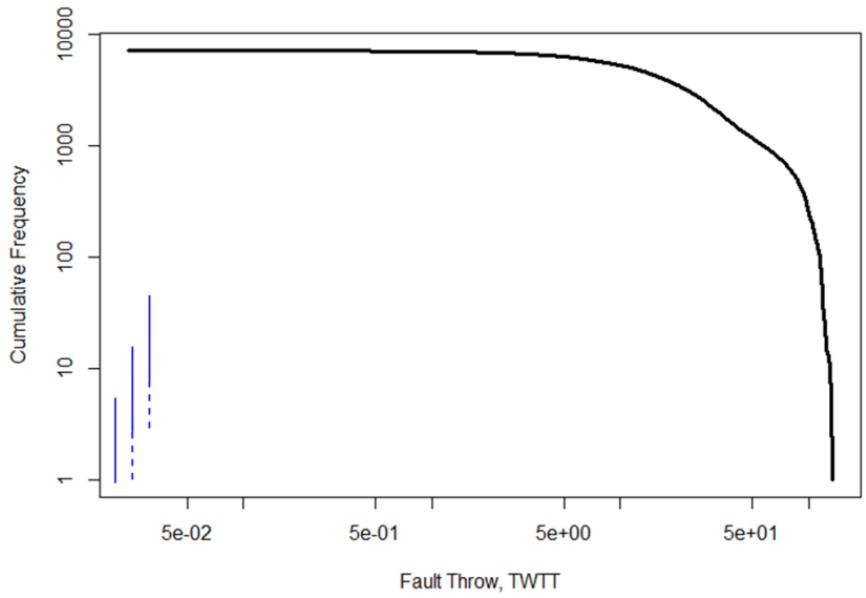

Figure 50: illustrates how the moving window works. Starting with the blue line on the left and shifting upwards by the amount indicated by the dashed blue line and so on. This process is carried out for the entirety of the data set until the blue line has moved across all of the data points (data from the Gulf of Mexico).

Tests indicate that this method is able to highlight different parts of the cumulative frequency distribution where the data are not described by a power law (or other) distribution. This is a useful property because previous authors have suggested that an overall fault population generally contains a number of smaller fault populations that can be scaled Yielding et al., (1996), Watterson et al., (1996), Nicol et al., (1996) and Fossen and Rørnes (1996). These points at which there is a discontinuity in the overall population are here termed “break points”, and are defined as the point at which the p-value (a level of significance which represents the probability of a given event occurring) changes significantly enough such that data no longer is described by the scaling distribution in question.

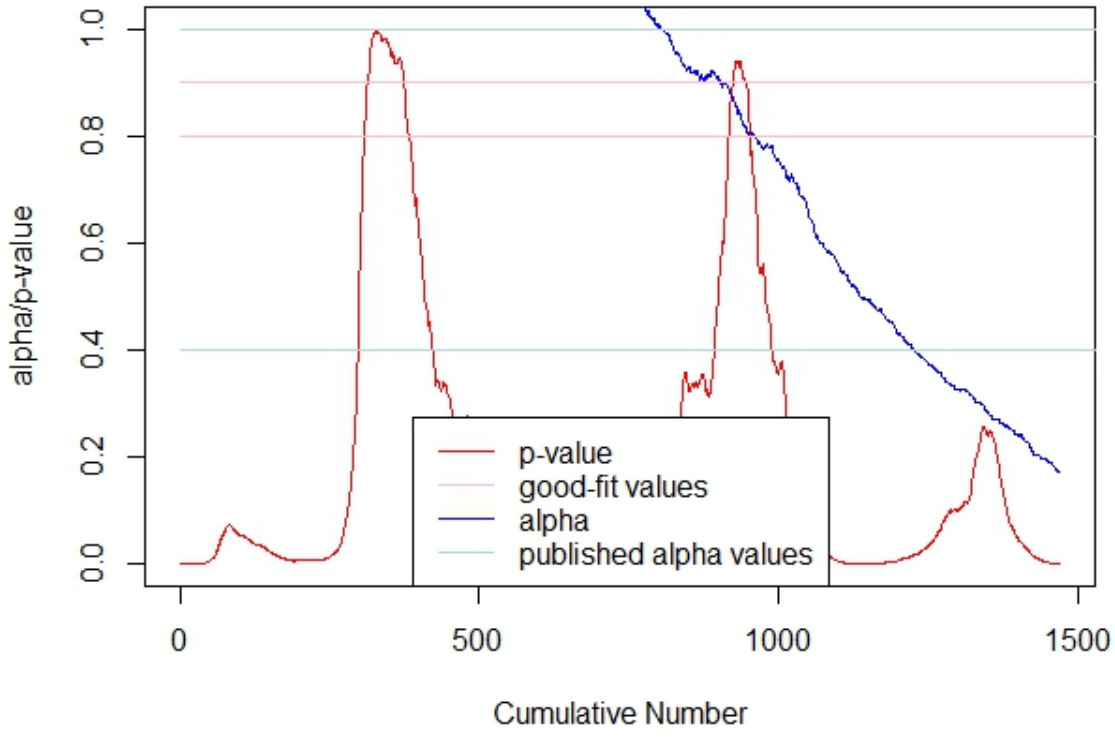

Figure 51: shows the p-value and alpha value, given the exponent plots is a negative number it has been inversed for the needs of this figure so it is clear where the values overlap. The blue line is the p-value and the horizontal lines indicate the 0.8 and 0.9 points at which a fit is accepted, and the red line is the exponent value (alpha) with the horizontal lines set at 0.4 and 1.0 (Nicol et al., 1996)

The benefit of this approach is that it is possible to identify the individual and numerous points on the cumulative frequency curve at which the data fit a given theoretical scaling distribution, and can then overlay several different p-values for different distributions over each other (figure 51). By doing this, regimes can be identified where different distributions dominate, or areas where they all appear to dominate and so hypothesise different reasons for why this may occur. To quantify the goodness-of-fit of the scaling distributions, Kolmogorov-Smirnov and Anderson-Darling tests have been used.

3.4.2.3 Kolmogorov-Smirnov test

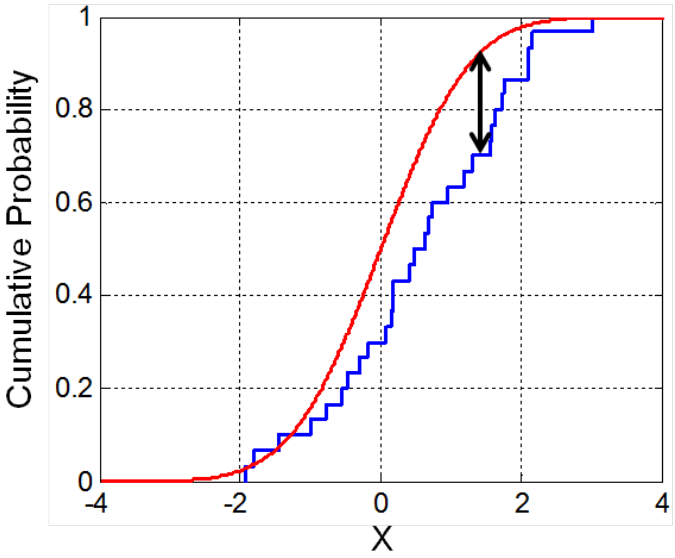

Figure 52: diagrammatic representation of how both the Kolmogorov-Smirnov and Anderson-Darling calculate the goodness-of-fit (see text for explanation)

Figure 52 is a graphical representation of the process carried out by the Kolmogorov-Smirnov test (and also Anderson-Darling test). The red line represents the true data set, and the blue line the synthetic data set generated for comparison. The Kolmogorov-Smirnov test (and also Anderson-Darling test) produces its goodness-of-fit p-value by taking the difference between the two lines and generating a critical value, which is the distance between the two data sets in the Kolmogorov-Smirnov and Anderson-Darling Tests described in this chapter and chapter 3.4.2.4. How the blue line (synthetic data) is generated varies between the Kolmogorov-Smirnov and Anderson-Darling test.

For our use of the Kolmogorov-Smirnov and Anderson-Darling test we generated our own synthetic dataset based on the mean value of each of the windows that the code ran over. The exact way in which this was done can be seen in Appendix 1.

The Kolmogorov-Smirnov test is a nonparametric (not based on parameterised probability distributions) test. It is used for continuous, one-dimensional probability distributions to test their equality and is used to compare a given sample (e.g. the sampled fault or fold size measurements) with a reference distribution (e.g. power law distribution). A one-dimensional probability distribution is univariate (includes just one variable). In the case of this study the variable is either the fault throw or fold amplitude. The Kolmogorov-Smirnov test works by quantifying the distance (figure 52) between the empirical data set and the synthetic data set.

Quantifying the distance between the empirical and synthetic distributions enables the null distribution of the statistic to be calculated. This is calculated under the null hypothesis and assumes that the empirical sample is drawn from the reference distribution (i.e. power law, exponential or log-normal), or that both the empirical and synthetic are drawn from the same sample distribution. This two-sample Kolmogorov-Smirnov test is generally regarded as one of the most useful and widely applied nonparametric methods for the comparison of two samples. It is both sensitive to the differences in shape and location of the empirical and reference cumulative distribution functions. As a result, it is influenced less by any assumptions where the empirical and reference samples are drawn from, and so deals with each sample independently of any other distribution assumptions.

The Kolmogorov-Smirnov test can be modified in order to serve as a goodness-of-fit test. The goodness-of-fit of a statistical model is a method by which to describe how well it describes a set of given observations. The measure of goodness-of-fit is typically defined as the discrepancy between empirical values and the reference values expected under the model in question. In the case of the Kolmogorov-Smirnov test this is the distance between the red and blue line depicted in figure 52. These measures are used in statistical hypothesis testing to test whether two samples are drawn from the same distribution.

In R the Kolmogorov-Smirnov is executed as shown below (http://www.rdocumentation.org/ "Kolmogorov-Smirnov Tests", January 2016).

```
> ks.test(x, y, …, alternative = c("two.sided", "less", "greater"),
exact = NULL)
```

- `x`; a numeric vector of data values
- `y`; a numeric vector of data values, or a character string naming a cumulative distribution i.e. `pnorm`
- …; parameters of the distribution specified (as a character string) by `y`
- `alternative`; indicates the alternative hypothesis and must be one of `"two.sided"` (default), `"less"`, or `"greater"`
    - `two.sided`; specify that the null hypothesis is equal to the hypothesised distribution
    - `less`; specify that the null hypothesis is less than the hypothesised distribution
    - `greater`; specify that the null hypothesis is greater than the hypothesised distribution
- `exact`; `NULL` or a logical indicating whether an exact p-value should be computed

The code defines `x` and `y` to be numeric vectors, empirical data and the other derived mathematically from this data set. The code uses a `two.sided` test which tests whether the data sets are drawn from the same continuous distribution.

The Kolmogorov-Smirnov statistic can be mathematically described (below) for a cumulative distribution function $F(x)$ (https://en.wikipedia.org/wiki/Kolmogorov%E2%80%93Smirnov_test, January 2016).

Equation 4: $$\boldsymbol{D_n = sup_x|F_n(x) - F(x)|}$$

Where sup_x is the supremum (the smallest value that is greater than or equal to each of a given set or subset of values) of the set of distances. $F_n(x)$ and $F(x)$ are the values in each of the empirical and reference distributions, and D_n is the Kolmogorov-Smirnov statistic. Where n goes to infinity, it is almost certain than D_n will converge to 0.

The goodness-of-fit test for the Kolmogorov-Smirnov test is made up of the critical values of the Kolmogorov-Smirnov distribution. The null hypothesis is rejected if;

Equation 5: $$\boldsymbol{\sqrt{n}D_n > K_\alpha}$$

For level α. Where K_α is found from,

Equation 6: $$\boldsymbol{Pr(K \leq K_\alpha) = 1 - \alpha}$$

Where K is the values in the Kolmogorov-Distribution, K_α are the critical values and Pr is an abbreviation for probability. Which is the probability that K is less than or equal to K_α is equal to 1 minus α, i.e. if the alpha level is 20% (0.2) then the probability that K is less than or equal to K_α must be 80% (0.8). The asymptotic power of this test is 1, i.e. a value greater than 1 cannot be returned since it is a value of probability and values greater than 1 is not numerically viable.

The description above is for the one-sample case, and the start point of the Kolmogorov-Smirnov test. The code implements the two-sample Kolmogorov-Smirnov test, as the data are not from a known distribution. The previously described test was a one-sample test and compared a given data set to a reference distribution i.e. power law, exponential or log-normal. A two-sample test on the other hand tests whether two underlying one-dimensional probability distributions are drawn from the same distribution, or if they differ i.e. whether our empirical and synthetically generated data sets are from the same distribution. For the two-sample case, the Kolmogorov-Smirnov statistics varies as follows;

Equation 7: $$D_{n,n'} = sup_x \left| F_{1,n}(x) - F_{2,n'}(x) \right|$$

This is comparable to the Kolmogorov-Smirnov statistic quoted previously for a one-dimensional case, however $F_{1,n}(x)$ and $F_{2,n'}(x)$ represent two samples of which neither descend directly from a known distribution. Here the null hypothesis is rejected at level α if,

Equation 8: $$D_{n,n'} > c(\alpha)\sqrt{\frac{(n+n')}{(nn')}}$$

3.4.2.4 Anderson-Darling test

The Anderson-Darling test (figure 52), like the Kolmogorov-Smirnov test is a statistical test of whether a given sample is drawn from a given probability distribution. In its most simple form it assumes that there are no parameters (nonparametric) to be estimated in the distribution being tested. This means that the test and its critical values are distribution free, and are not bound by any assumptions (https://en.wikipedia.org/wiki/Anderson%E2%80%93Darling_test, February 2016).

With respect to whether a given distribution satisfactorily describes a data set the Anderson-Darling test is regarded as one of the most powerful statistical tools for measuring any departures from normality.

The code uses a k-sample Anderson-Darling test which tests whether several collections of observations can be modelled as coming from a single population. However, the distribution function does not have to be specified i.e. the Anderson-Darling test is able to test the observations of two data sets which are not generated from any single distribution.

The Anderson-Darling test works in a similar way to the Kolmogorov-Smirnov test but uses more rigorous mathematics to calculate the distance between the data sets in question. The distance between $F_n(x)$ and $F(x)$ is given by

(https://en.wikipedia.org/wiki/Anderson%E2%80%93Darling_test, February 2016);

Equation 9: $$\boldsymbol{n \int_{-\infty}^{\infty} (F_n(x) - F(x))^2 w(x) dF(x)}$$

where $w(x)$ is the weighting function, which describes where more weight is placed throughout the data set i.e. more weight in the tails, middle portion or equally weighted throughout the data set. However, the Anderson-Darling test is based on the distance described below which varies as a function of the data $F(x)$,

Equation 10: $$\boldsymbol{A = n \int_{-\infty}^{\infty} \frac{(F_n(x) - F(x))^2}{F(x)(1-F(x))} dF(x)}$$

This equation is satisfied when, $w(x) = [F(x)(1 - F(x))]^{-1}$, meaning that the Anderson-Darling test puts more value on the observations made in the tails of the distribution.

The code carries out a nonparametric k-sample test which is based on the Anderson-Darling measure of agreement between distributions, described above. This assesses whether a number of random samples which have possibly different sample sizes may have been drawn from the same distribution, where this distribution is often unspecified.

The k-samples test computes a p-value from either an asymptotic distribution, simulated distribution or (limited) exact distribution. These can all be carried out under randomisation, with or without ties, or conditionally under random sampling from populations given the observed tie pattern. This just means that the k-samples test is able to compute the p-value under a variety of situations, and can be adjusted to treat the data sets being tested in different ways.

The k-sample test uses the Anderson-Darling criterion to assess the hypothesis that k independent samples with samples sizes $n_1, \ldots n_k$ arise from a common unspecified distribution function $F(x)$. Testing is carried out conditionally given the observed tie pattern.

The k-samples Anderson-Darling test in .R is described at (http://www.rdocumentation.org/ "kSamples, Anderson-Darling Test", February 2016), where it is located in `library(kSamples)`.

```
> ad.test(…, data = NULL, method = c("asymptotic", "simulated",
"exact"), dist = FALSE, Nsim = 10000)
```

- `…`; a formula `y~g` where `y` contains the pooled sample values and `g` is a factor (of same length as `y`) with levels identifying the samples to which the elements of `y` belong
- `data`; an optional data from providing the variables in formula `y~g`
- `method;`
- `dist; FALSE` (default), if `TRUE` the simulated or fully enumerated vectors `null.dist1`, `null.dist2` are returned for the respective test statistic versions. Otherwise, `NULL` is returned when `dist=TRUE` then `Nsim<-min(Nsim, 1e8)`, to limit object size
- `Nsim; 10000` (default), number of simulated sample splits to use. It is only used when `method = "simulated"`, or when `method = "exact"` reverts to `method = "simulated"`

If AD represents the Anderson-Darling criterion for k-samples, then its standardised test statistic is,

Equation 11: $$\boldsymbol{T.AD} = \frac{(\boldsymbol{AD}-\boldsymbol{\mu})}{\boldsymbol{\sigma}}$$

Where $\mu = k - 1$ being the mean and σ the standard deviation of AD. This statistic is then carried out for each of the data sets involved in order to test the hypothesis that the samples are drawn from the same unspecified continuous distribution function, $F(x)$.

3.4.2.5 Goodness-of-fit

Both the Kolmogorov-Smirnov and Anderson-Darling tests described above have been implemented in the incremental and moving window functions in order to test and quantify the goodness-of-fit. The p-value, which each of these tests returns in R, is a probability measure for whether a number of data sets are equal or not equal to data set to which they are proposed to originate.

For example, if a synthetic power law dataset based on the parameters (for this project these are x_{min} and α) from the experimentally acquired data is used, the code can calculate the probability of whether these originate from the same distribution. Statistically the highest probability score is 1, meaning that for a value of 1 the empirical data set is derived from the same distribution as the experimental data set. 0.8 is generally taken to be an accepted level of confidence; so any value returned which is greater or equal to 0.8 signifies that the empirical and experimental data fit the distribution that is being tested (C. Caiado, personal communication, 2016).

The code was also developed so that the exponent value for each window was also estimated. This exponent can be plotted with the p-value and can identify the areas where it is believed the distribution is a good fit, but also the expected exponent value at this point (figure 51). As a result of this it is possible to identify areas that are likely to be geologically significant as a power law. For example, a portion of the graph where the p-value produced for a power law fit exceeds the 0.8 mark, and in the same portion of the graph also produces an exponent within the expected range.

In order to test the main hypothesis underlying this study the goodness-of-fit analysis can be performed for both the fault and fold data for a given data set and identify whether the tested distributions which dominate are similar or not.

3.5 Comparison with the Clauset et al. (2009) code

By carrying out a two-dimensional sampling of fault and fold length in the Inner Moray Firth study area, the code produced by Clauset et al., (2009) can be used alongside the code developed for this project. The Clauset et al., (2009) code can now be used under the assumption that alpha (the exponent) will be larger than 1, unlike the situation for one-dimensional multiline sampling method. The expected exponent value for this two-dimensional survey should be in the range of -1.1 to -2.0 (Yielding et al., 1996) for a power law distribution.

The statistical analysis developed in this study enabled a comparison of the results with those produced by the Clauset et al., (2009) methods. This enables consistency of both codes to be assessed, and makes an easy comparison between this code and the developed code for this project.

However, the analysis methods vary in one potentially significant aspect. The Clauset et al., (2009) method assumes the whole of the data to be one population, whereas the method developed in this study takes into account that the data could belong to several populations. This means that comparisons cannot be made directly between the results of the two methods without making adjustments.

In the original paper by Clauset et al., (2009) a number of non-geological data sets were used in order to test the code which they had developed. The data sets comprised continuous and discrete sets, as well as a mix of data sets controlled by power law and other distributions. The data sets compared from the Clauset et al., (2009) paper were: the number of customers affected in electrical blackouts in the United States between 1984 and 2002 (Newman, 2005), the human population of cities in the United States in the 2000 Census (http://tuvalu.santafe.edu/~aaronc/powerlaws/data.htm, June 2016), the size in acres of wildfires occurring on United States federal land between 1986 and 1996 (Newman, 2005) , peak gamma-ray intensity of solar flares between 1980 and 1989 (Newman, 2005), the number of links to web sites found in a 1997 web crawl of about 200 million web pages (Broder et al., 2000) and the frequencies of occurrence of United States family names in the 1990 census (http://tuvalu.santafe.edu/~aaronc/powerlaws/data.htm, June 2016) . These data sets were proposed to have a mix of distributions.

As most of these data sets are readily available to the public, they provide a powerful test of the statistical methods and a mechanism to gain insight into the functionality of their statistical codes. This enables the results to be compared between the project code and their code when carried out on the same data sets.

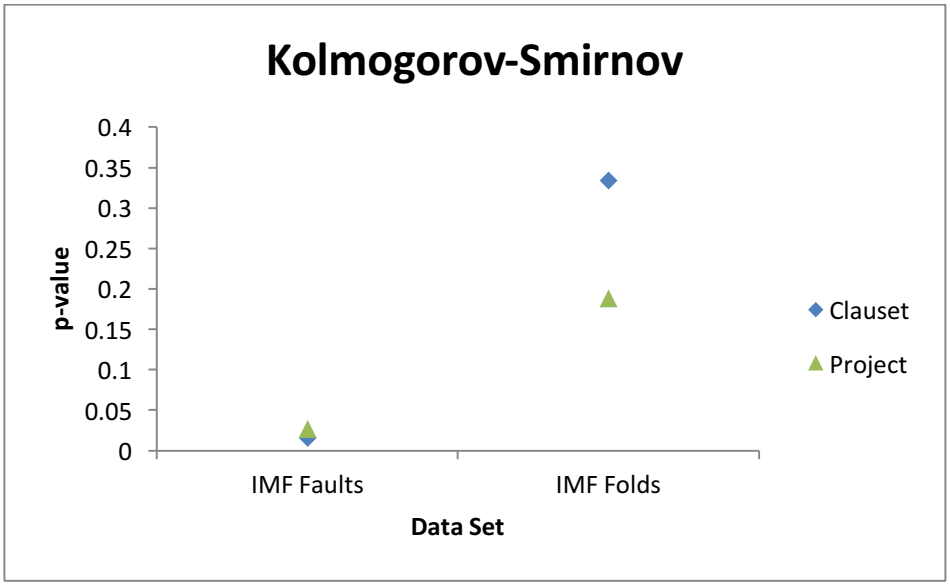

Figure 53: Inner Moray Firth fault data and fold data comparison of p-values

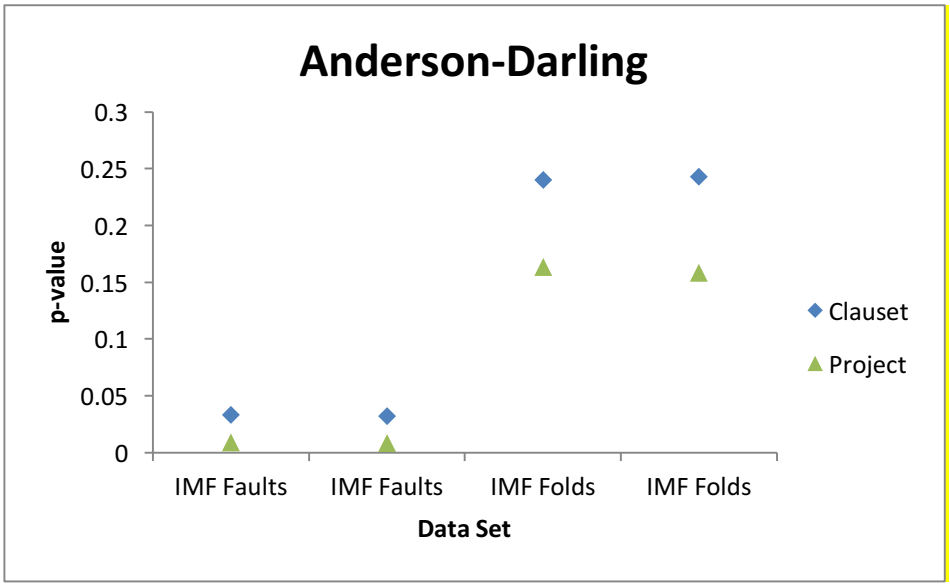

Figure 54: Inner Moray Firth fault data and fold data comparison of p-values

The results of the Kolmogorov-Smirnov test demonstrate agreement between the Clauset and project code. For the Anderson-Darling test the same trend continues with the project and Clauset code forming a good agreement.

4. Repeatability and method testing using data from the Gullfaks study area

4.1 Introduction

The first aim of this chapter is to test the repeatability of the one-dimensional multiline sampling method by comparing previously published fault throw data from the Gullfaks area with fault throw data I have extracted from Statoil's horizon depth maps. Fossen and Rørnes published a paper in 1995 entitled "Properties of fault populations in the Gullfaks Field, northern North Sea". In this paper they estimated the power law exponent of a number of different fault populations within the Gullfaks Field, using: EW sample lines across the entire depth map, EW and NS lines across the entire depth map, EW lines from the Domino Area, EW lines across the NS striking faults, EW lines across the NS striking intra-block faults, EW lines across the NNE-SSW striking faults, and NS lines across the EW striking faults.

The second aim of this chapter is to assess the methodology described in this project, and to also validate these methods by comparing the results in this paper against those that have been published. This will be achieved by comparing the fault throw data obtained for the Statfjord horizon by Fossen and Rørnes to fault throw data obtained from Statoil depth maps.

4.2. Extracting fault throw data from the Statoil depth maps

ArcMap was used to "GeoReference" Statoil's Statfjord depth map in figure 55, which also has the distinct deformation zones highlighted. This allowed the accurate addition of EW and NS sample lines across the map, exactly as Fossen and Rørnes did for their study (figure 56 and 57). There were 64 EW lines spaced at 200m intervals for a total length of 510km, and 24 NS lines spaced at 437.5m for a total width of 240km.

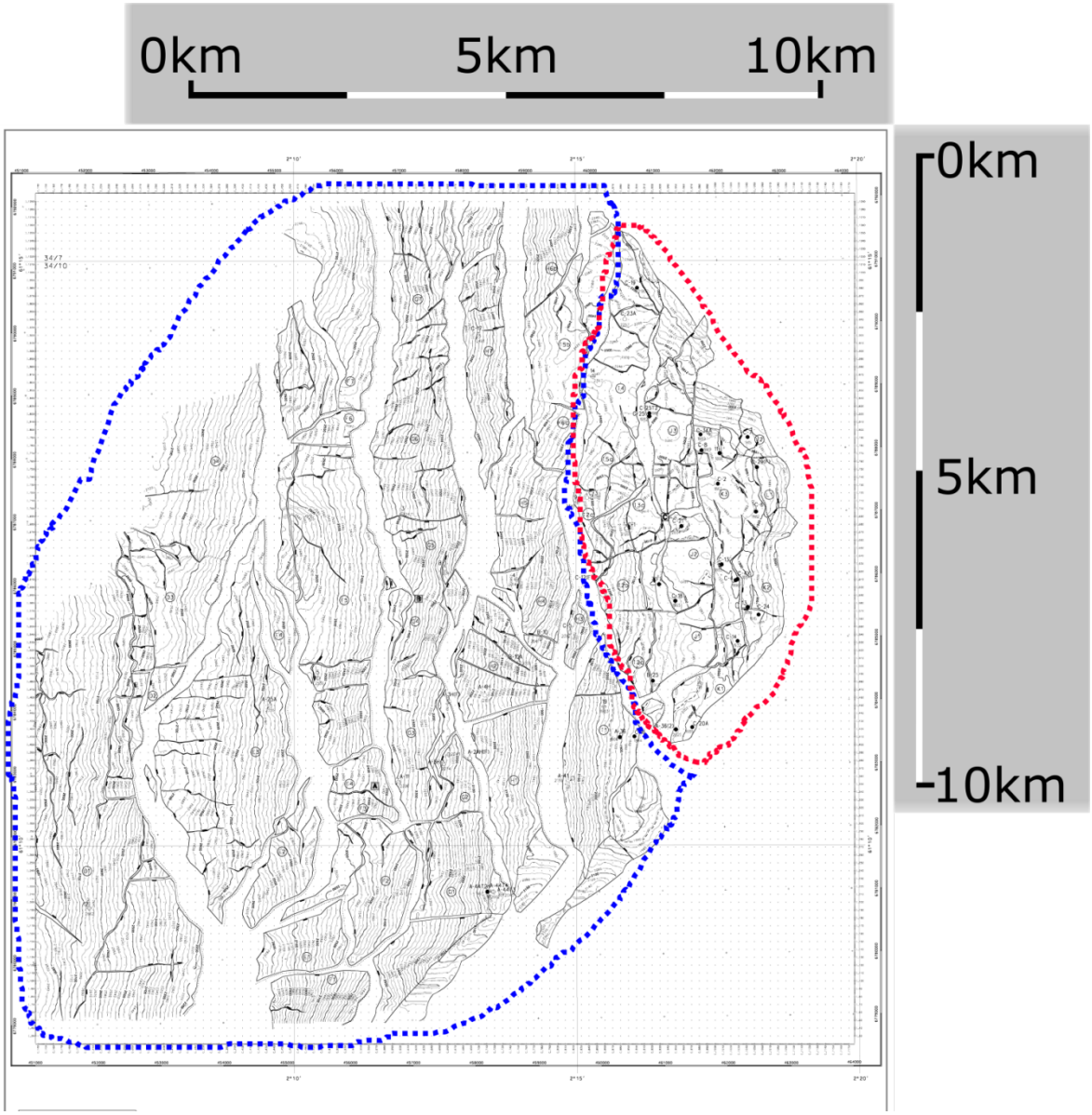

Figure 55: a depth map of the Statfjord horizon showing the fault systems, the area circled in blue represents the Domino Zone and the are circled in red represents the Accommodation zone

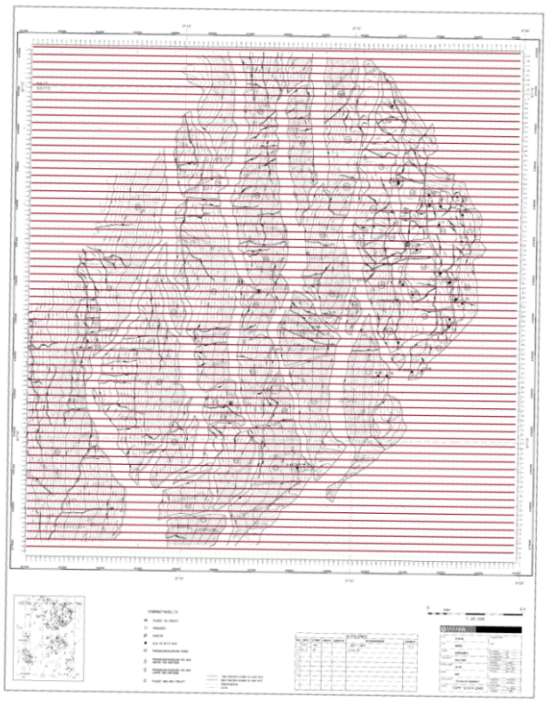

Figure 56: EW lines on the Statoil depth map for the Statfjord Horizon georeferenced in ArcMap

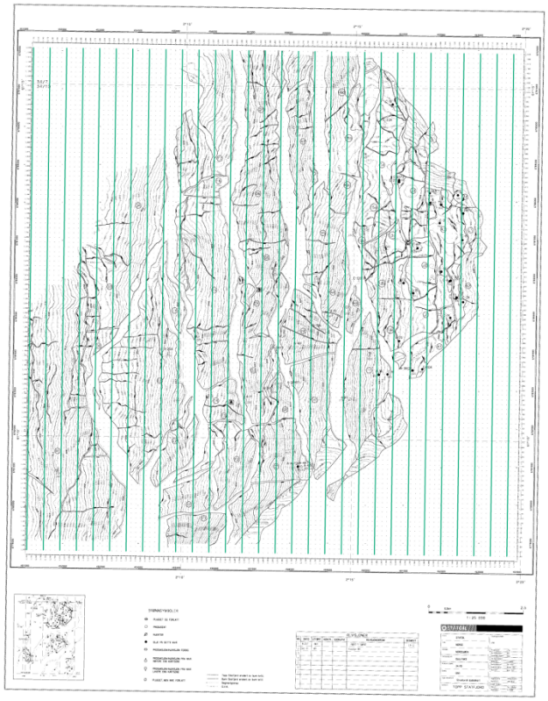

Figure 57: NS lines on the Statoil depth map for the Statfjord Horizon georeferenced in ArcMap

Having done this, the fault throw data set was acquired by going along each line and measuring the throw over each fault that the line intersects. The depth maps were contoured to 20m

meaning that for faults with an offset of less than 20m could only be measured as 20m. As a result of this it is likely that their throw has been over-estimated due to the limited precision. The effect of this contouring can be seen in the results reported later in this chapter.

This process was repeated for each of the fault populations described by Fossen and Rørnes (EW lines, EW and NS lines, NS striking faults major fault in the Domino Zone (DZ), NS striking intrablock faults DZ, NNE-SSW striking faults DZ, EW striking faults DZ and all fault in the Domino Zone) using the same EW and/or NS lines that they used.

The major fault system and many of the minor faults in this region strike NS, because of this the EW lines form a more comprehensive data set for throw values compared to the NS lines as they intersect the fault plane orthogonal to the strike. Whereas the NS lines run parallel to the strike and do not necessarily intersect the faults hanging wall and footwall. Some of the faults have a slight curvature in their strike so the NS lines intersect the hanging wall of the same fault plane twice without crossing the footwall. This does not produce a value and contributes to a small number of faults being provided by the NS lines.

The values from the Fossen and Rørnes paper were digitised using (http://arohatgi.info/WebPlotDigitizer/app/, April 2016) and these were plotted against the values collected from the depth map to visually compare the data. After doing this visual comparison, the data sets acquired from the depth maps were analysed in order to compare the raw data and to test the difference in methods between calculating the power law exponent.

The data sets were plotted together on the same axis to visually analyse where they are similar and where they are not. The results of this can be seen in figures 62a, b, c, d,e, f and g later figures in the chapter.

There were four different methods implemented in order to calculate the power law exponent. The first method was to calculate the gradient manually from the straight line segment of the data plotted on log-log axis, this was done using the same upper and lower cut-offs in throw value that Fossen and Rørnes imposed on their data. The second method was to repeat the first method but it was calculated without any imposed boundaries. The gradient was manually calculated using the following equation;

Equation 12: $$\alpha = \frac{dy}{dx} = \frac{\log y_1 - \log y_2}{\log x_1 - \log x_2}$$

The third method was to evaluate the data in R. using the boundaries imposed by Fossen and Rørnes, and finally evaluating the data in R. without these boundaries. This was carried using

Equation 13: $$\log y = \log C - \alpha \log (x)$$

Re-arranged for α(this equation satisfies a straight line), this was implemented in the code developed for this project in order to calculate the gradient at the point at which the p-value was highest.

After doing this for the Statfjord Horizon it was necessary to repeat the process for the Etive Horizon depth map in figure 58, with the distinct deformation zones highlighted. The method described above was implemented in the exact same way and the map was "GeoReferenced" in ArcMap and the EW and NS sample lines added (figure 59 and 60). These data were compared to the results collected from TrapTester (the main methodology of this project); the seismic data in TrapTester were modelled in the way described in chapter 3.2.1. The same sample line spacing (64 EW lines spaced at 200m intervals for a total length of 510km, and 24 NS lines spaced at

437.5m for a total width of 240km) was also applied in TrapTester when exporting the throw values to ensure that the data sets both arise from the same geological location, in order to most accurately compare them.

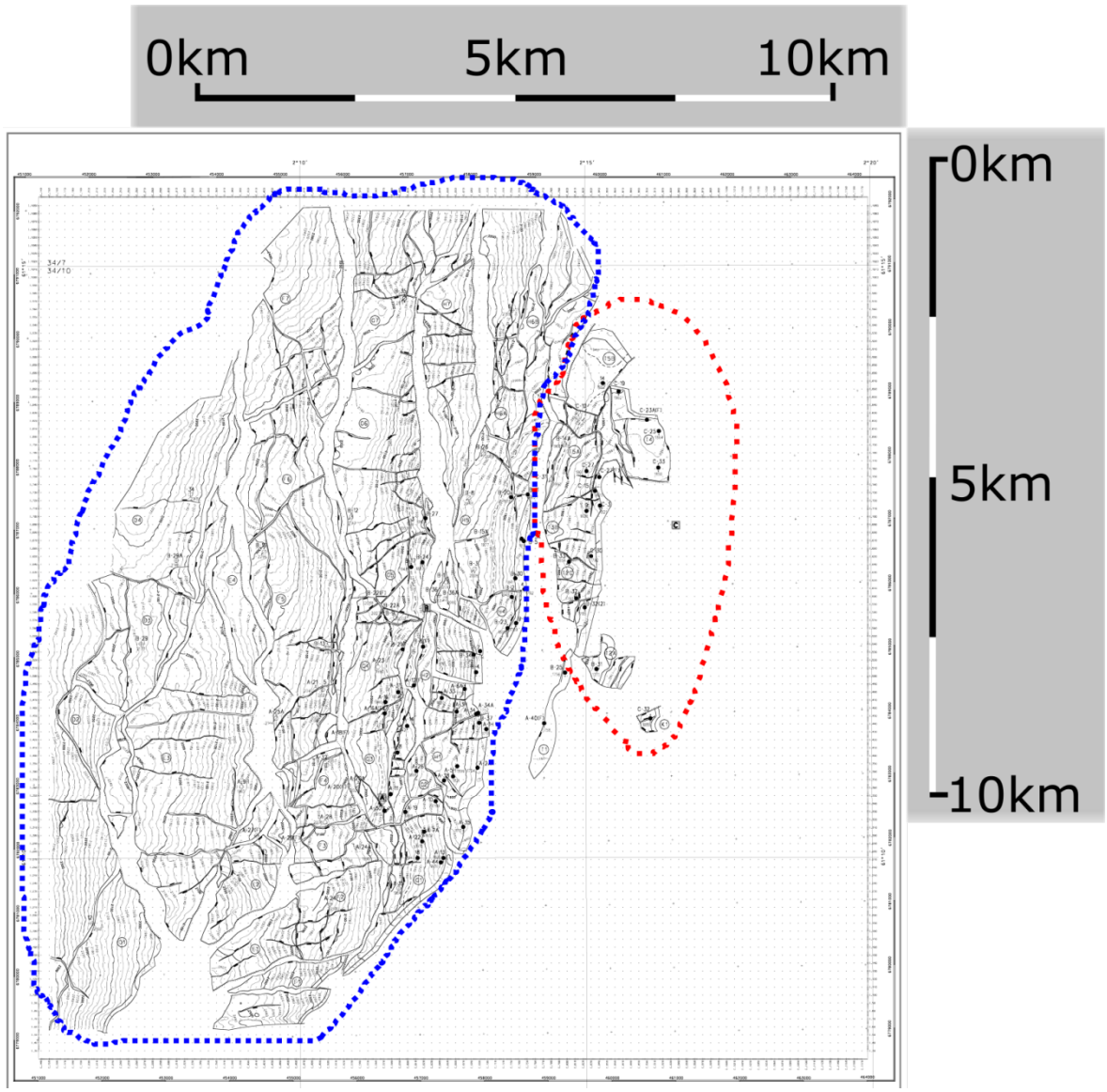

Figure 58: a depth map of the Etive horizon showing the fault systems, the area circled in blue represents the Domino Zone and the are circled in red represents the Accommodation zone

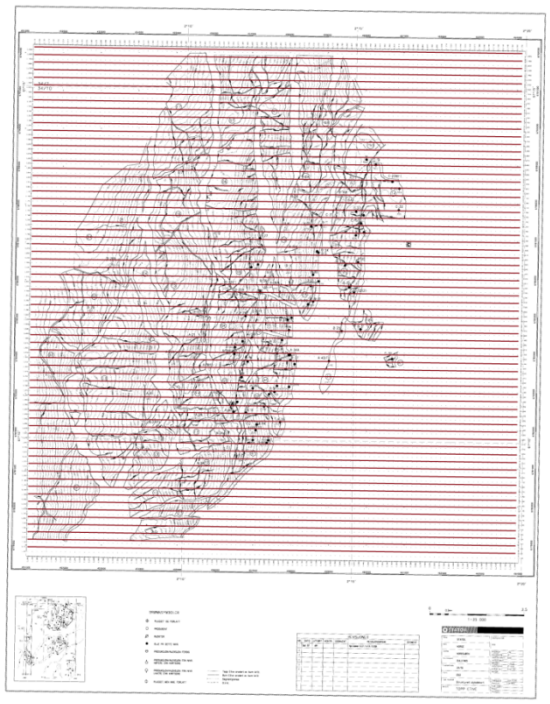

Figure 59: EW lines on the Statoil depth map for the Etive Horizon georeferenced in ArcMap

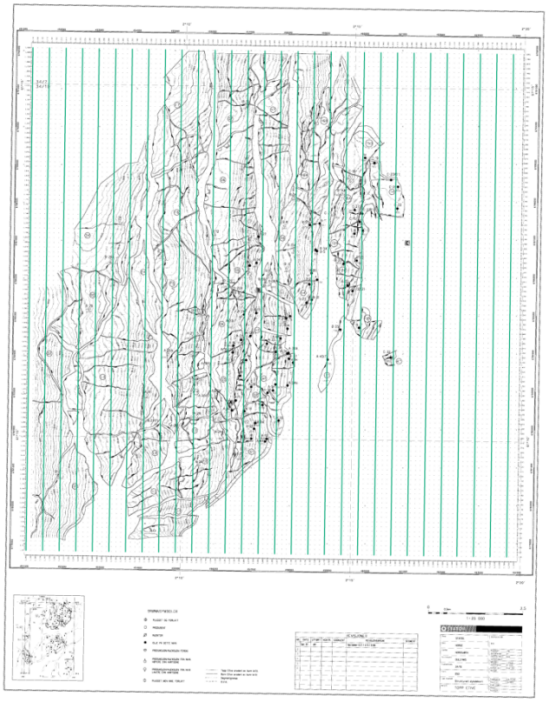

Figure 60: NS lines on the Statoil depth map for the Etive Horizon georeferenced in ArcMap

4.3 Depth conversion

Unlike the depth maps which are contoured in meters the results from TrapTester are measured in TWTT (ms). As a result of this the data acquired from TrapTester needed to be depth converted and this was carried out using the well logs provided by Statoil.

A velocity profile was established (table 2) by taking the average velocity for a given depth range from the well log data where the Etive Horizon occurs. The minimum and maximum values from each depth range were used to form the error bars on the velocity values. These were then plotted on the Vp against depth graph (figure 61) to check that they were still true to the data set. This was done in order to verify that the values used had not been influenced by an anomaly in the data occurring from a sampling error, or a disproportionately larger or smaller value as a result of a geological unconformity.

Depth Intervals, TVD (m)	Depth Point	Vp, m/s
1780-1880	1830	2315.925
1880-1980	1930	2496.573
1980-2080	2030	2713.914
2080-2180	2130	3122.555
2180-2258	2230	5084.79

Table 2: the Vp used for each depth interval with Vp taken for the lower end of the interval

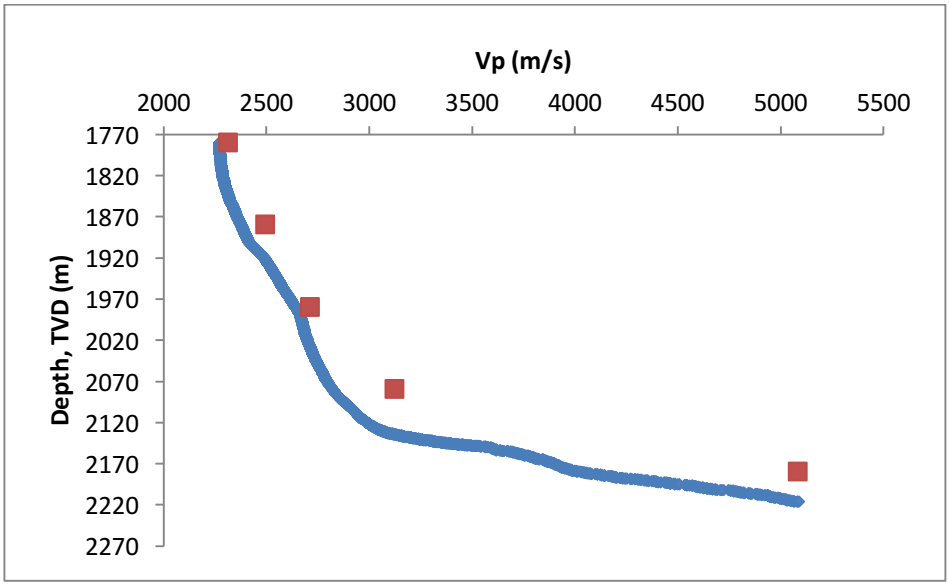

Figure 61: shows Vp against depth with the velocity profile (red) used plotted to highlight that the values used were accurate to the well logs (blue)

After forming this velocity profile the TWTT values from TrapTester were depth converted using the following equation;

Equation 14: $$D = \frac{TWTT}{2} v$$

Then every value in the velocity profile was applied to all the TWTT values exported from TrapTester. This formed a minimum, average, and maximum depth value for each point in the dataset. From these three values, the average was plotted as the main line on the graph, and the minimum and maximum were added as horizontal error bars.

Having finalised the TrapTester data set and put it in the same form as the depth map values they were plotted on the same axis (figure 65, 66 and 67) in order to compare the two data sets. This was done to validate the primary method of this project, i.e. obtaining fault throw (and fold amplitdude) data from seismic interpretations carried out in TrapTester and Petrel, the results of this are reported later in the chapter.

4.4 Spatial distribution of faulting and extension

An analysis of the spatial distribution of faults within the Gullfaks field was also carried out as a secondary method to validate and analyse the data. This method aims to measure the heterogeneity of displacement and throw for individual fractures sampled along a line (Putz-Perrier and Sanderson, 2008). It also provides a statistic that can be used to test for any significant departures from a uniform distribution.

This approach provides an additional tool to assess the consistency of the horizon maps obtained from TrapTester and Statoil. The significance of this is that if the maps are representing the same geology as each other the results from the Fossen and Rørnes data comparison will hold more significance in the validation of the methods of this paper. This survey was carried out on the Etive Horizon depth maps (figures 58, 58 and 60).

The maps were “Georeferenced” in ArcMaps as had been previously done for the Fossen and Rørnes. A layer was then created in ArcMaps which consisted of three EW lines and three NS lines. When applied to the other maps this ensured that they were in the exact same position making it as accurate as possible.

The distance across each line was measured until a fault was reached. At this point a fault number, fault throw and distance across the line to the fault were recorded. This process was repeated for every EW and NS lines on each map. All these values were then added together so that there was a cumulative distance, cumulative throw and fault number for each line, following the method described by Putz-Perrier and Sanderson (2008).

These data were then plotted with cumulative distance against fault number, and cumulative distance against cumulative throw enabling all the characteristics of each line to be plotted on each graph. This also allowed for the same line of each map to be plotted on the same graph to give a direct comparison. These lines were then characterised by the description laid out in the paper from Putz-Perrier and Sanderson (2008). For the cumulative throw against cumulative distance, a low gradient suggests smaller throw vales whereas steeper slopes relate to larger throw vales, constant gradients show homogeneously distributed deformation and slopes with large steps and gradient changes represent localised deformation. For fault number against cumulative distance, a low gradient shows that faulting has occurred at low frequencies, a steep slope shows faulting which is occurring at a high frequency, a constant gradient shows homogeneous faulting, and a varying gradient relates to heterogeneously distributed faults.

Being able to characterise the throw and distribution of the faults across each of the lines surveyed made it possible to compare the throw and distribution for the same line on each map. It is then possible to compare between the same horizons and assess whether they are showing that the faults are distributed in the same way with a similar cumulative throw. For the Statfjord Horizon one of the maps used by Fossen and Rørnes were not accessible, so the spatial analysis can only be carried out for the Etive Horizon. The maps used for the Etive Horizon in this survey were the same as those used in the depth map, power law distribution method, so the results of the Putz-Perrier survey can be used to assess whether they reflect the same geology.

The results of this data comparison are reported below.

4.5 Results

4.5.1 Throw population data

The graphs of the digitised Fossen and Rørnes data plotted alongside the data from the Statoil depth maps can be seen in figures 62a, b, c, d, e, f and g shown on the next page.

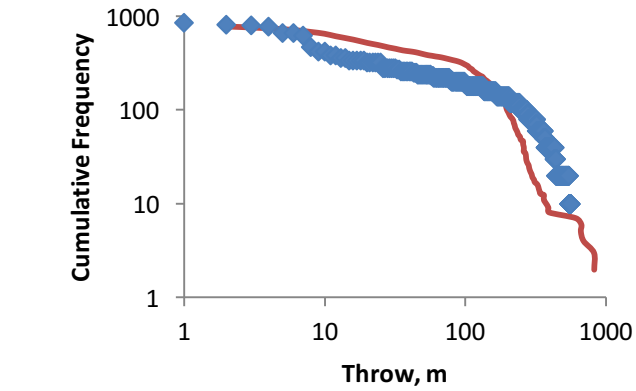

a

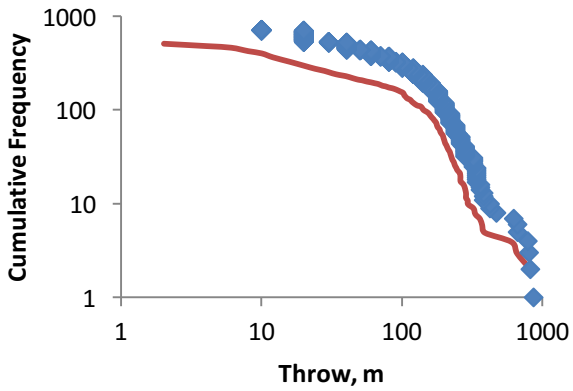

b

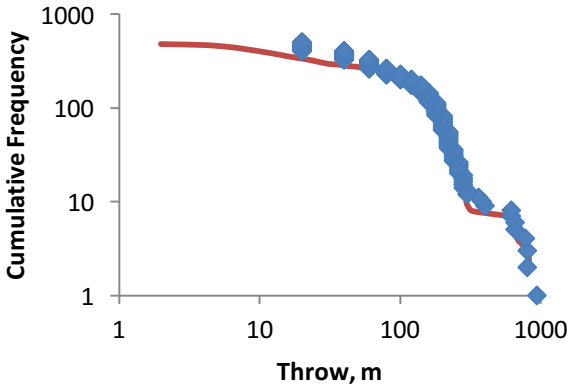

c

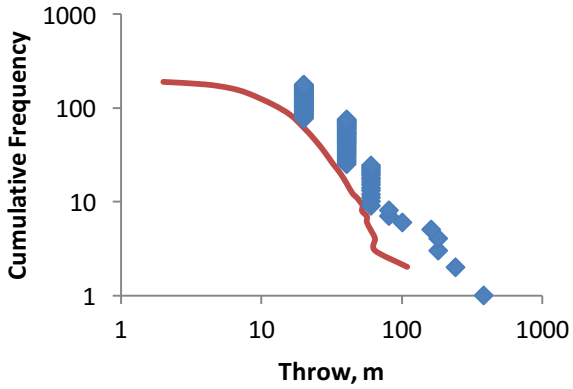

d

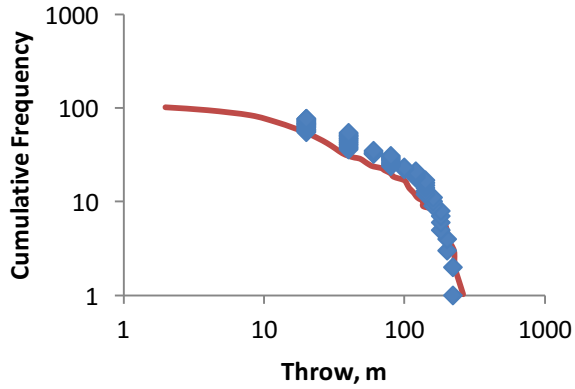

e

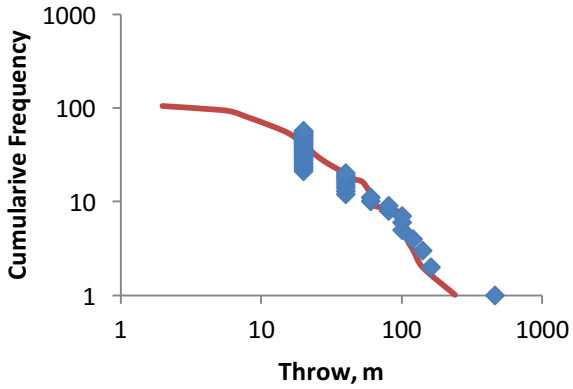

f

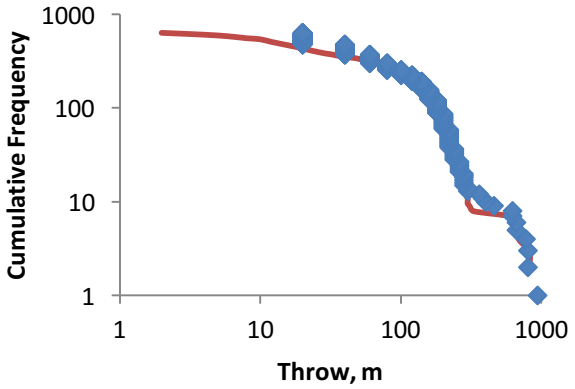

g

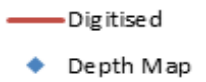

Figure 62: shows the results from our Depth Map survey compared t digitised values from Fossen and Rørnes (1995)

a: EW lines
b: EW and NS lines
c: NS striking major faults DZ
d: NS striking intrablock faults DZ
e: NNESSW striking faults DZ
f: EW striking faults DZ
g: all Domino Zone faults

The graph of the EW lines across the entire depth maps (figure 62a) shows a reasonable visual fit to the data from Fossen and Rørnes across the entire data set. In particular, the slope of the straight line segment (between ca. 10 and ca. 100m throw) is similar in both datasets. This suggests that the use of depth maps as a methodology is good when compared to results which have already been published.

Moving on to the EW and NS lines across the entire depth map (figure 62b) there is an evident deviation from the Fossen and Rørnes data and the throws on faults measured on the depth map are generally higher than the published throw values. However, the depth map data demonstrates the same overall distribution as the Fossen and Rørnes data, and the data ends at roughly the same throw value.

Figure 62c shows the results of the EW lines along the NS striking faults in the Domino Area. These results show an incredibly good fit to the Fossen and Rørnes data with only a small deviation from their data in the left-hand tail of the graph. The EW lines along the NS striking intra-block faults in the Domino Area (figure 62d) does not show a good fit to the Fossen and Rørnes data. Although the data do still mirror a similar distribution curve to that of Fossen and Rørnes the actual throw values appear to be much larger than those reported by Fossen and Rørnes. The reason why the depth map reports much larger throw values than those reported by Fossen and Rørnes in this graph is due to the intra-block faults having much smaller throw values which can only be measured at a smallest value of 20m.

When data is covering at least one order of magnitude it becomes much easier to define the populations. However in this instance the data does not cover an order of magnitude since they are intrablock faults (so therefore smaller) and the depth map is contoured at 20m resulting in

faults not being able to be read to a smaller size. As a result of this, in fault populations which would be expected to have small throw values there is a large concentration of values at 20, 40, 60m because the throw cannot be read to a small precision between these values. This can be very clearly seen in figure 62d, and it may be that if the depth map was contoured to a smaller vertical interval, the data would form a closer fit to the results of Fossen and Rørnes. On the whole this lack of range over a magnitude makes it difficult to define the fault population.

This can also be seen in figure 62f, the graph of NS lines along the EW striking faults in the Domino Area. Like the intra-block faults these form a minor fault and fracture system and do not have especially large throw values. It can be seen that there is a large concentration of values at 20 and 40m. Unlike the intra-block faults however this graph visually shows the data sets forming a closer fit to each other.

The graph of the NNE-SSW striking faults along EW lines (figure 62e), does not demonstrate this characteristic shown in the previous two graphs since there are fewer very small faults. The graph then shows a very close fit between both the data sets, with the depth map data as it has previously showing the same distribution curve as the Fossen and Rørnes data.

The final data set reports values for all faults in the Domino Area (figure 62g). Since the data set is now much larger the influence of the 20m contouring has been diminished and the effect minimised by the much larger throw values and cumulative number. The data demonstrates a very good fit to the data of Fossen and Rørnes.

There is a strong correlation between the majority of the graphs; however, one aspect which is consistent throughout is the difference in left-hand truncation between graphs. This is caused by the 20m contouring on the graphs not allowing a smaller precision to be read, and hence not allowing a tail on the left-hand side to be well-defined.

The result of this poor left-hand definition is a steepening effect on the exponent since there is a large concentration of values at 20m. These would otherwise have been part of the left-hand truncation which is missing in the graphs produced from the depth maps. This is particularly noticeable in the fault populations that only consider the intra-block or non-major faults and can be seen in figures 62d, e and f.

When fitting the best fit lines to these graphs to calculate the gradient it means there is a "pillar" of values at 20m which allow the best fit line to be rotated yet still cross a number of points as a best fit line should. If these points were spread into a tail of smaller values there would be less room for rotation of the best fit line, and for it to also still be a fit. Consequently, the exponents calculated by this method are all steepened in comparison to the Fossen and Rørnes data which does have left-hand truncation.

In summary, the use of the Statoil depth maps to mimic the methods of Fossen and Rørnes produced good results, particularly for large numbers of sampled faults with throws greater than 20m, and the depth map method at least partly validated this good comparison.

Following the initial plotting and visual comparison of the data, the exponent was calculated for each depth map data set by the methods already described. These values were then compared to the exponent values calculated by Fossen and Rørnes for their data sets. Figure 63 shows the

exponent when calculated manually and with .R using the boundaries Fossen and Rørnes imposed on the data, along with the exponents from their paper. Figure 64 shows the exponent when calculated manually and with .R without imposing any boundaries on the data, also plotted with the exponents from Fossen and Rørnes.

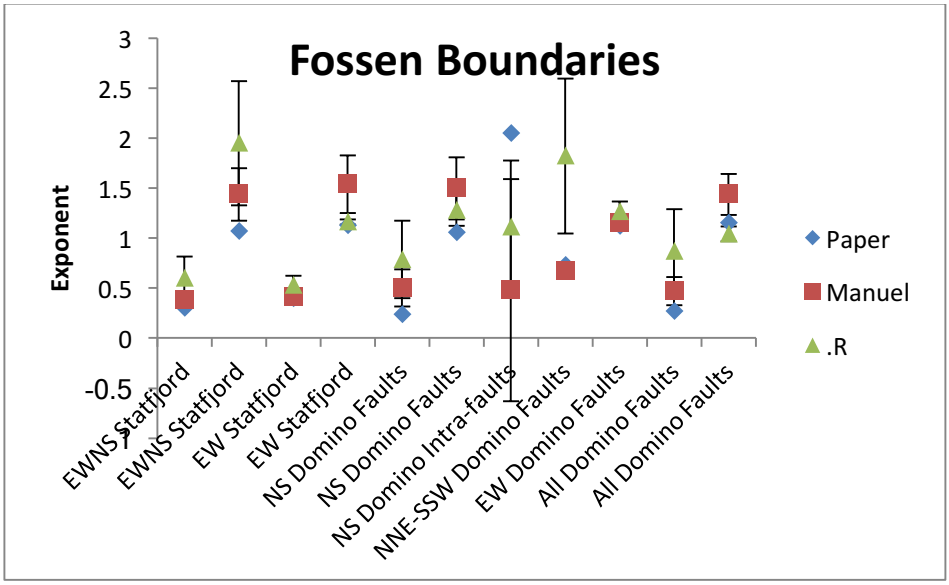

Figure 63: exponent calculated with imposed boundaries from Fossen and Rørnes. Error bar derivation explained in text

Fault Population	Boundary (cumulative number)
EW lines	100-190
EWNS lines	10-100
EWNS lines	100-190
All Domino Zone	8-90
All Domino Zone	90-190
N-S Striking Domino	8-100
N-S Striking Domino	100-190
NS Striking Intrablock Domino	20-50
NNE-SSW Striking Domino	14-100
E-W Striking Domino	18-60

Table 3: outlines the boundaries which were identified by Fossen and Rørnes

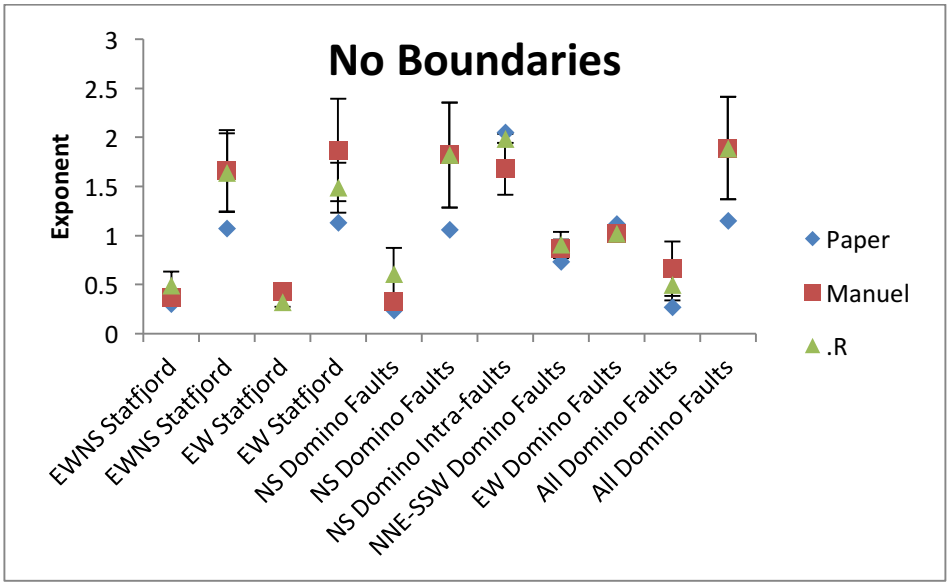

Figure 64: exponent calculated with no imposed boundaries. Error bar derivation explained in text

These exponent values have been plotted along with standard deviation error bars to highlight where and where not the exponents produced from the different methods are a good fit. The error bars were calculated by using the standard deviation from the Fossen and Rørnes exponent values and the manual values or the R values. Having calculated these values in Excel, this was made into a percentage error of the published values. As one can see, where Fossen and Rørnes identified more than one power law trend the second consistently appears to form a poorer fit than the first power law trend identified within the given fault populations.

The fault populations which Fossen and Rørnes believed to contain just one power law distribution (figure 63 and 64) show a good fit, similar to that of the first power law segment of the figures containing two distributions. However, although the NS intrablock domino faults contain only one distribution they do not show a good fit between the exponent values. This is believed to be because of the aforementioned poor definition of the left-hand truncation which is particularly evident in this fault population.

It seems that the exponent values form a better fit when no boundaries are imposed on the data. It also appears to be that the agreement between the manual and R calculated exponent values are much better than their corresponding published results (figure 63 and 64). It is most likely that the reason for this is that the manual and R values are derived from the same data set, and compared to the published exponent values which are derived from a different data set. This highlights that the exponent values are incredibly sensitive to both the method that they are derived from and also the data set, despite the close fit between the two data sets.

Fault throw data derived from depth maps of the Etive Horizon in the Gullfaks field are plotted in figures 65, 66 and 67. In these graphs the same 20m contours stop the development of left-hand truncation which causes a steepening of the gradient at this point as it causes an over estimation of the smaller fault throws. This is evident in all the graphs, in particularly the graph of the NS lines (figure 66).

The NS lines travel along the strike of the major fault systems, i.e. run parallel to the hanging wall and the footwall of the major faults therefore causing the NS lines to not measure these faults. As the major faults do not contribute a significant number of throw values the population is then dominated by minor faults. These minor faults, as has been previously stated can only be measured to a minimum of 20m resulting in over estimation of the fault throw value and a consequent steepening effect on the depth map values. As TrapTester can measure a fault throw precisely it has caused the comparison of throw values along the NS lines to not closely follow each other. There are also 40 less NS lines (24 lines) than there are EW lines (64 lines) which will also produce a smaller data set making it less likely to span at least one order of magnitude so therefore less comparable to the TrapTester data.

In figure 67 the presence of these major faults reduces the influence of the 20m contours and flattens the left-hand tail but still not in a way comparative to TrapTester. However in published works the focus of the data has been on the middle portion for which figure 67 shows a good fit between the depth map data and depth converted TrapTeste data for both the EW and NS lines.

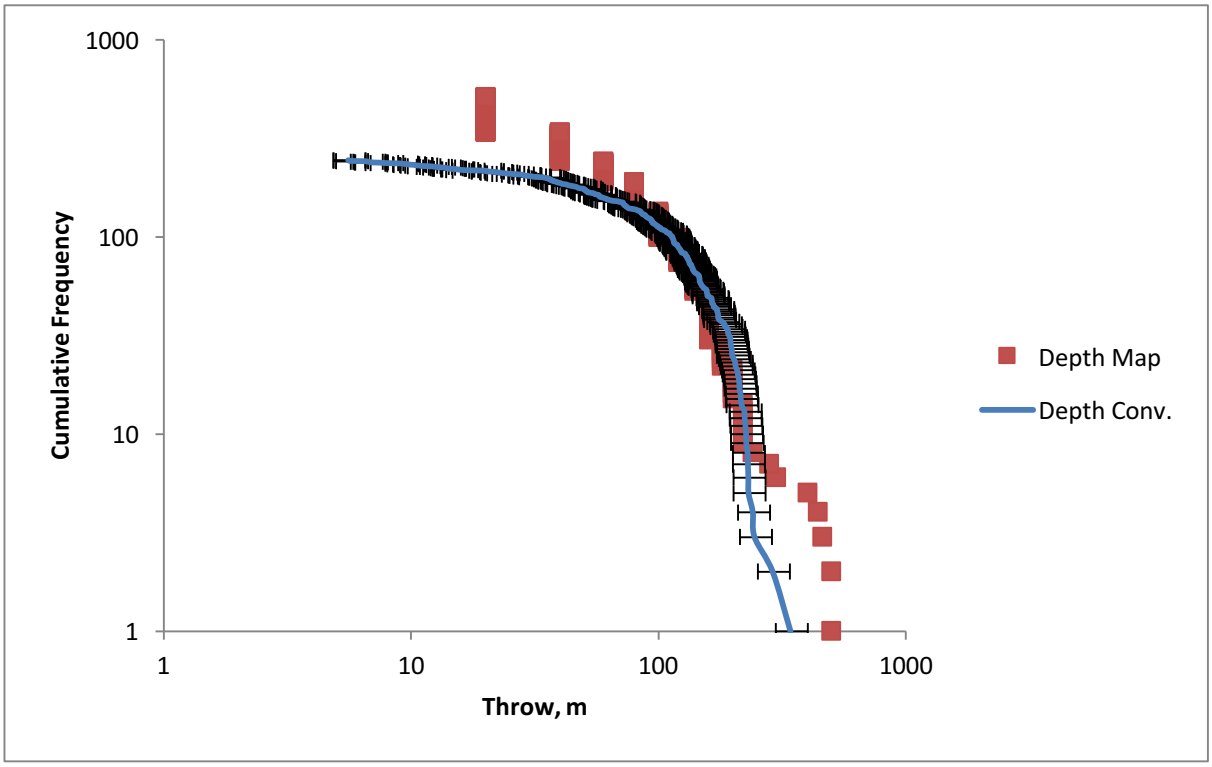

Figure 65: EW lines for the Etive horizon with depth converted values from TrapTester and values from the Statoil depth map with error bars highlighting the maximum and minimum depth which it could be given the seismic velocity data

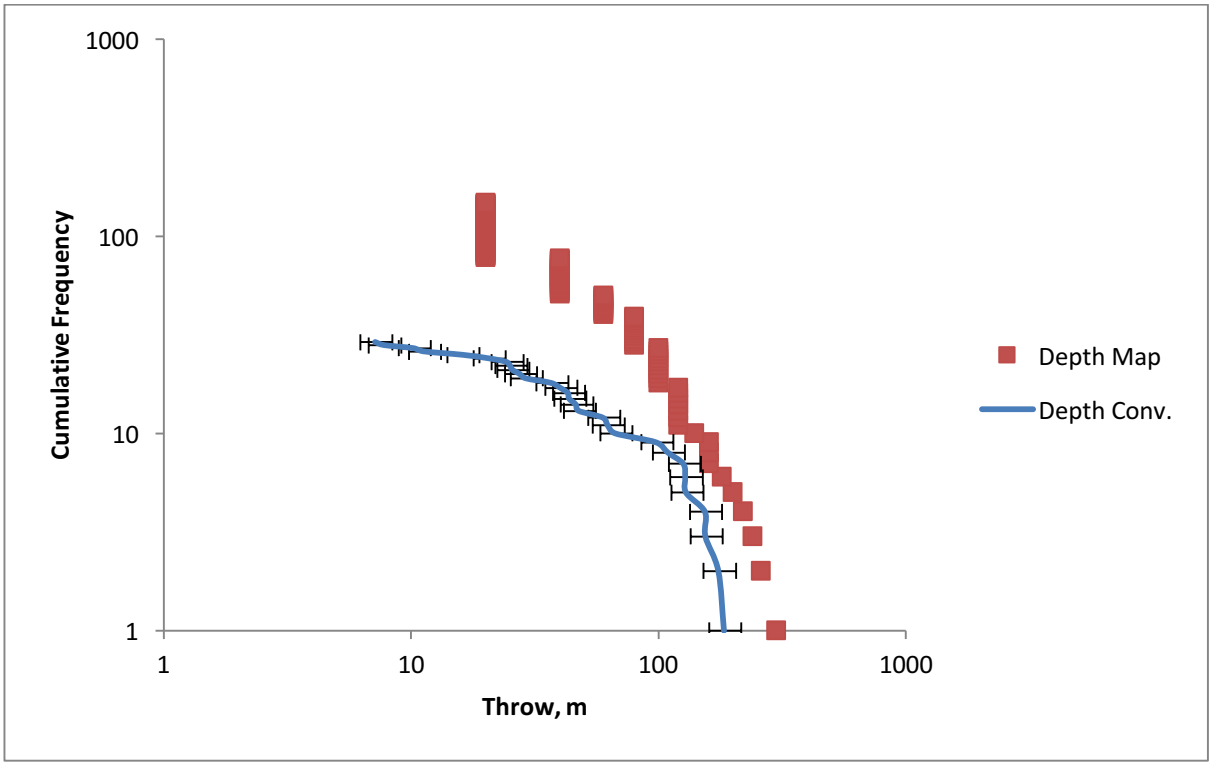

Figure 66: NS lines for the Etive horizon with depth converted values from TrapTester and values from the Statoil depth map with error bars highlighting the maximum and minimum depth which it could be given the seismic velocity data

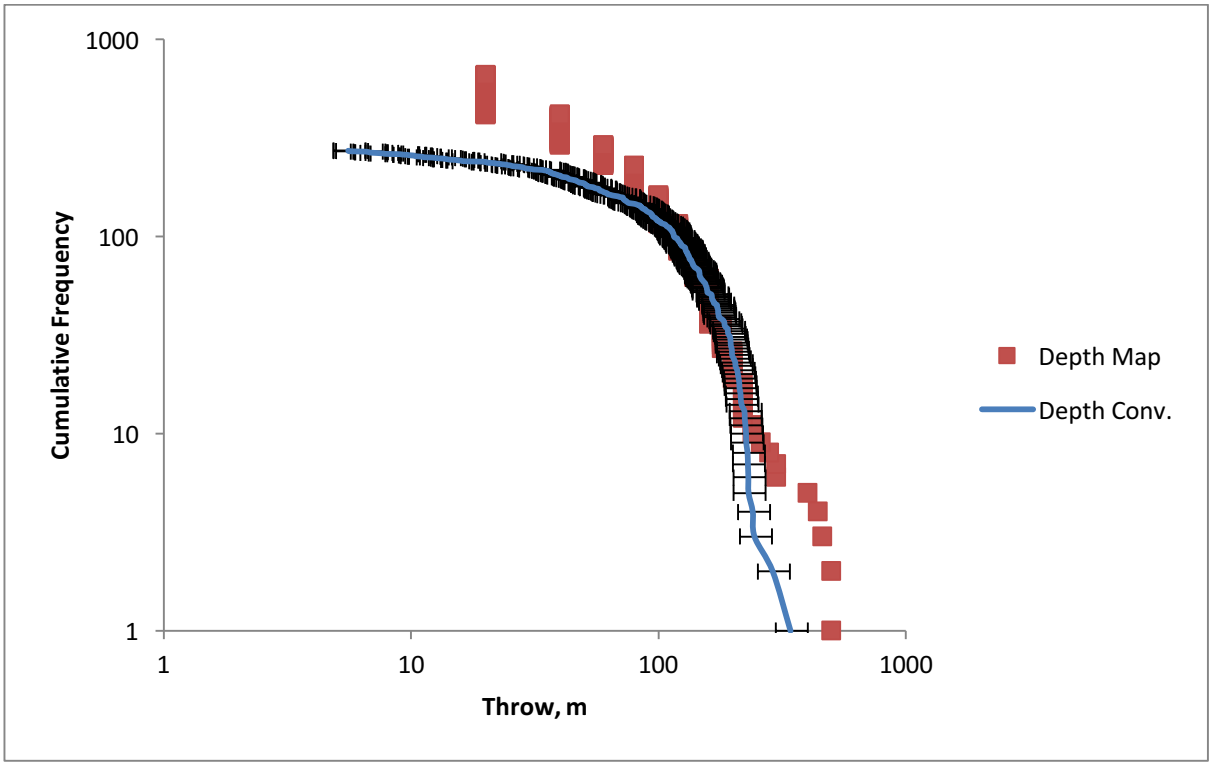

Figure 67: EW and NS lines for the Etive horizon with depth converted values from TrapTester and values from the Statoil depth map with error bars highlighting the maximum and minimum depth which it could be given the seismic velocity data

TrapTester on the other hand measures throws to a level below the seismic resolution and so includes noise in the dataset it returns. To combat this effect, the datasets have been cut off at a value of 4ms as values smaller than this are below the seismic sample interval for these data and can therefore only be considered to be noise and not part of the fault population.

The results of these graphs suggest that TrapTester can be validated as a good method despite the poor fit in the NS lines data. This is because the NS lines follow the strike of the major faults which results in a data set made up of the minor faults, because of the 20m contours on the depth maps it causes the minor fault throws to be overestimated. It is also generally felt that because of the reduced number of NS lines in comparison to the number of EW lines it is a less comparable stand-alone data set, but when combined in the EW and NS data set the influence of these overestimated smaller fault throw values and smaller data sets is not heavily observed. For the EW lines, and EW and NS lines there is a very good fit in the middle portion of the data which is the area where the relevant distributions occur it strongly supports the agreement between the two methodologies. For the EW lines (figure 65) this middle portion is between ca. 90 and ca. 300, and for the EW and NS lines (figure 67) this also falls between about ca. 90 and ca. 300. As a result of the previous validation between the Statfjord Horizon results from Fossen and Rørnes and the depth maps, validates the choice of methodology for this project because of the agreement with results acquired by different methods for the same data.

4.5.2 Spatial distribution of faults and extension

An analysis of the spatial distribution of faults and extension has been carried out for the Etive Horizon to assess whether the two fault maps (figure 68 and 69) are spatially consistent. This survey was not carried out on the Statfjord Horizon as there was no access to the map used by

Fossen and Rørnes and therefore no comparison to where the data was gathered. The results of this survey on the Etive Horizon can be seen in figures 70a, b, c, d, and e.

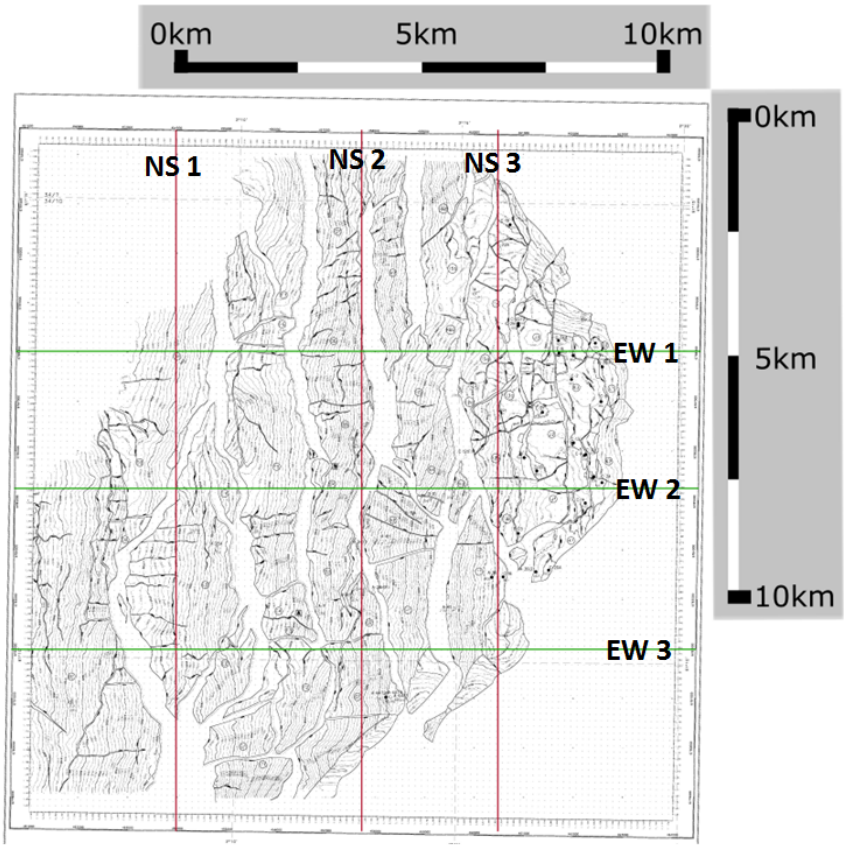

Figure 68: Etive Horizon depth map with three EW and three NS lines

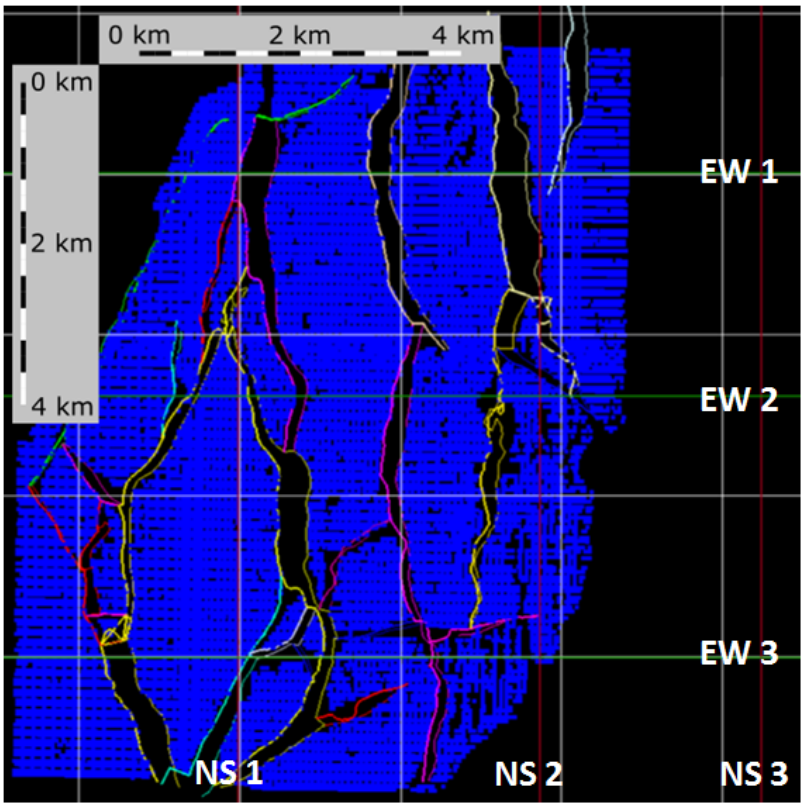

Figure 69: Etive Horizon in TraptTester with three EW and three NS lines which are positioned the same as in figure 68

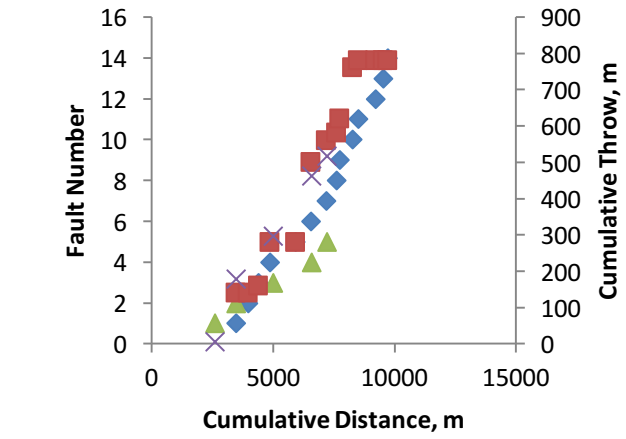

a

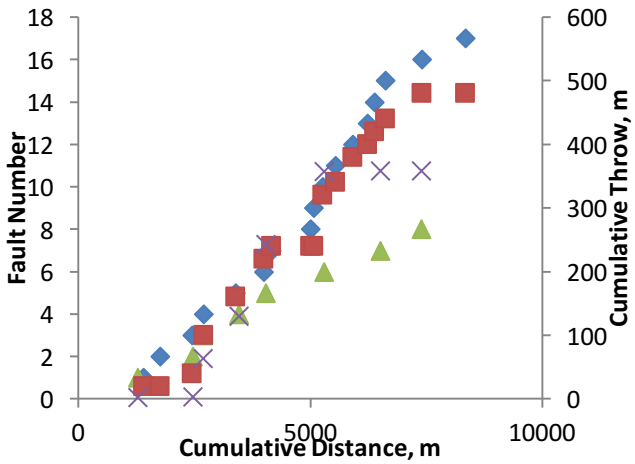

b

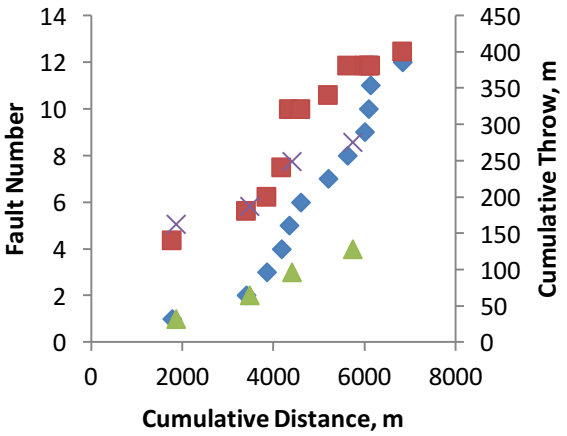

c

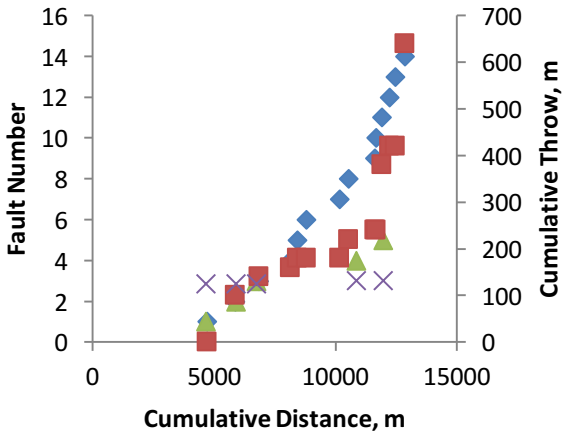

d

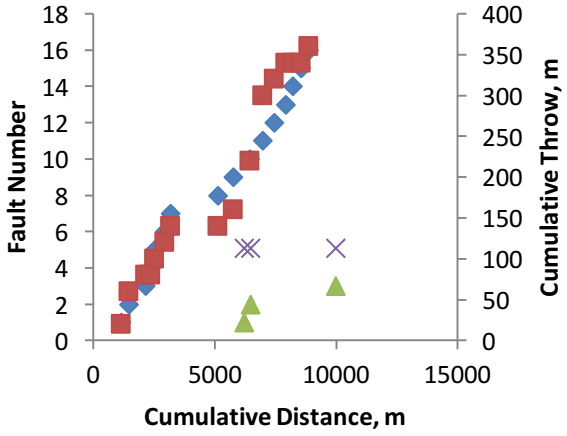

e

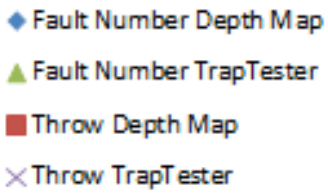

Figure 70: graphs showing the spatial distribution of faults and extension throughout the different depth maps
a: EW1
b:EW2
c: EW3
d: NS1
e: NS2

For figure 70a which represents the first EW line, this shows that the depth map line crossed relatively homogeneous faults of a constant throw with a high frequency. The TrapTester map showed faults of constant throws which were also homogeneously distributed with low frequency. The main reason for the difference in distribution is that the TrapTester data has only interpreted the major fault systems and has not interpreted all of the minor faults. Although it is able to read the throw of a fault to a higher degree of accuracy than the depth maps can there is less interpretation of minor fault and fracture systems which impacts on the frequency measure. As a result of this the frequency of fault recorded is lower, a pattern which was observed throughout the results.

The second EW line (figure 70b) shows a mixture of localised and homogeneous high frequency throw values for the depth map with evidence of a step in the data. The TrapTester data shows localised deformation at a homogeneous frequency. The last EW line (figure 70c) shows localised deformation in both the depth map and TrapTester data. However, the depth map showed high frequency fault distribution and the TrapTester faults at a low frequency. This difference in frequency distribution largely expected because of the difference in detail between maps.

The three-dimensional data in TrapTester covers a smaller area than the depth map, this can be seen in the difference between figure 70a and figure 70b. This is also a possible reason for the difference in frequencies of the faults, however the depth maps only contain data in a small portion of the area extends beyond the TrapTester data. This is the Accommodation Zone which only extends in the upper NE portion of the map and as a result of the lack of the Accommodation Zone in the TrapTester data, there are only two NS lines on which a spatial analysis can be carried out.

For the first of the NS lines (figure 70d) the depth map data are characterised as being localised deformation which is with a high frequency. The TrapTester data also has evidence of localised deformation suggesting that there is a good portion of homogeneous deformation as well. As is expected from previous explanations, these data are show lower frequency. The last line (figure 70e) shows the depth map data to come from a mixture of homogeneous and localised deformation and to be distributed at a high frequency. The TrapTester data shows localised deformation and is distributed at a low frequency.

The throw on the depth map and throw from TrapTester do not extend to the same throw value as TrapTester is comprised of fewer faults however figures 70a, b and c follow the same trend. The data for these figures are collected along NS lines where it has been previously stated are known to produce less accurate and comparable results. Similar to cumulative fault throw fault number demonstrates the same issues with the NS lines but for figures 70a, b and c the fault number lines are comparable between both maps.

The results of the spatial analysis results highlight some differences between the maps. Looking at figures 68 and 69 it can be seen that figure 68 spans a broader geographical area and includes the accommodation zone which figure 69 does not. It is also clear looking at the two maps that the depth map shows much more detail as far as the minor fault systems and fracture systems are concerned which influences the fault frequency and also cumulative throw. Overall however figure 70a and b shows there are similar deformation styles indicating that the maps are relatively consistent and are represented by the same geology.

In conclusion, this study has shown that the various methods carried out in this chapter validate TrapTester as an accurate methodology for carrying out fault throw (and, by inference, fold

amplitude) distribution analysis of other data sets. This is because of the similarities in results drawn between published results, depth maps and TrapTester itself, and tested and validated by more than one methodology.

5. Results

5.1 Introduction

Having established the validity of our approach, the results of the fault throw and fold amplitude population studies are presented in this chapter, for each of the study areas. The first section presents plots of fault throw and fold amplitude versus distance along the strike of the fault plane, for selected faults and horizons. This dataset provides an overview of the spatial distribution of distributed and discrete deformation in each study area. The second part presents histograms of fault throw and fold amplitude data, in order to summarise the fault and fold size populations in each study area. The third part analyses the data obtained from 1D sample lines and tests their fit to idealised distributions (e.g. power-law, exponential, log-normal) using the methods described in chapter 3 and implemented in R. The final part investigates 2D population data (fault length and fold length) derived from the Inner Moray Firth study area.

5.2. Throw or amplitude vs. distance plots

The fold amplitude and fault throw values were plotted against strike distance for a number of given horizons relating to a given fault plane. These graphs allowed patterns to be identified which relate to how these folds may have formed, and how they are spatially distributed around a fault plane (figure 72, 73, 74, 75, 76, 77, 78, 79 and 80).

This procedure was done for a number of horizons at different positions along the fault plane, enabling points to be identified where folding dominated, where faulting dominated, and where there was a mix of both brittle and continuous deformation. The style of deformation was most commonly seen to begin with folding adjacent to the lateral fault tip, passing along strike into faulting, and returning to folding at the opposite tip.

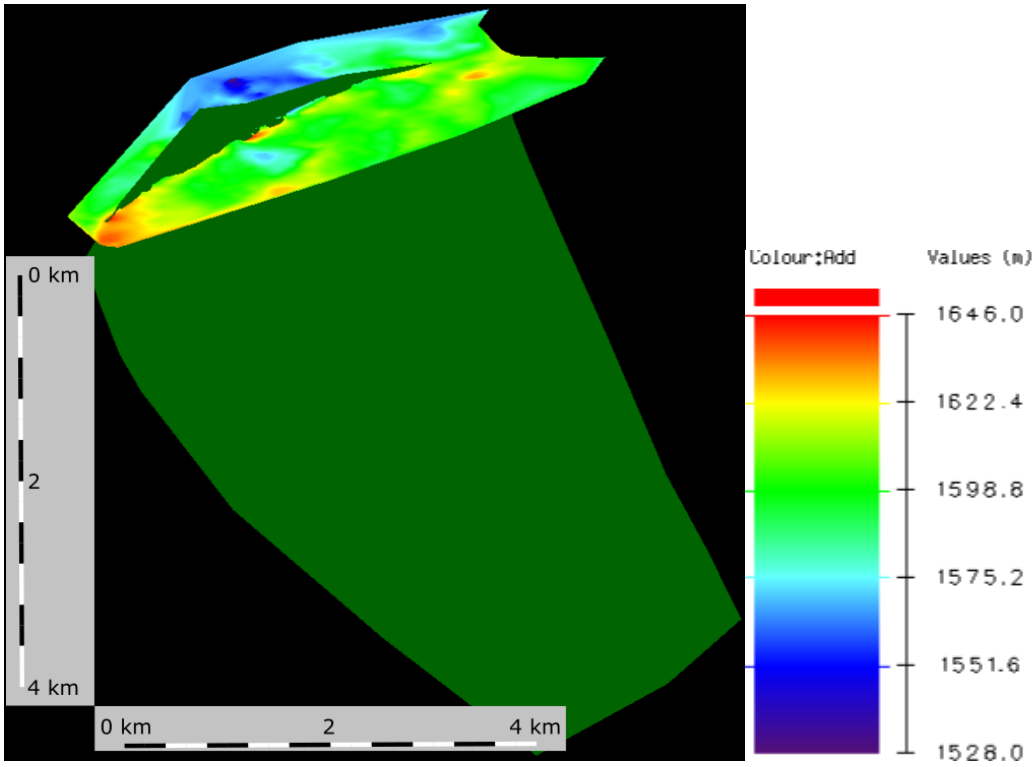

Figure 71: showing a fault plane and horizon. The horizon has had depth projected on it and it can be seen that in the hanging wall the horizon is at a shallower depth than the footwall. The fault plane is a uniform colour which doesn't represent a specific property.

This lateral variability can be seen in figure 71, where there is folding present at the lateral (vertical) tiplines of the fault plane, whereas faulting produced a significant, discrete vertical offset (throw) that predominates throughout the majority of the length of the fault plane. In figure 71 this latter region is where the fault plane has broken through, and offset, the horizon.

By initially plotting the fault throw and fold amplitude against distance along the strike of the fault plane it is possible to see the spatial distribution of fault-related folds along the fault plane. In many cases, the fold amplitude is greatest adjacent to the tip line of a fault plane. Figure 72, 73, 74, 75, 76, 77, 78, 79 and 80 shows this development for three of the fault planes involved in the study where fault throw is expressed as a blue line and fold amplitude is expressed as a red line. Figure 74 represents the results from horizon 1 on a fault in the Gulf of Mexico data set. Horizon 1 has been modelled at a greater depth than the horizons in figure 72 and 73. Figure 73 has the results from horizon 2 for the same fault plane as figure 74, but this horizon is shallower. Finally

figure 72 has the results from horizon 3 from the same fault plane and this horizon is most shallow.

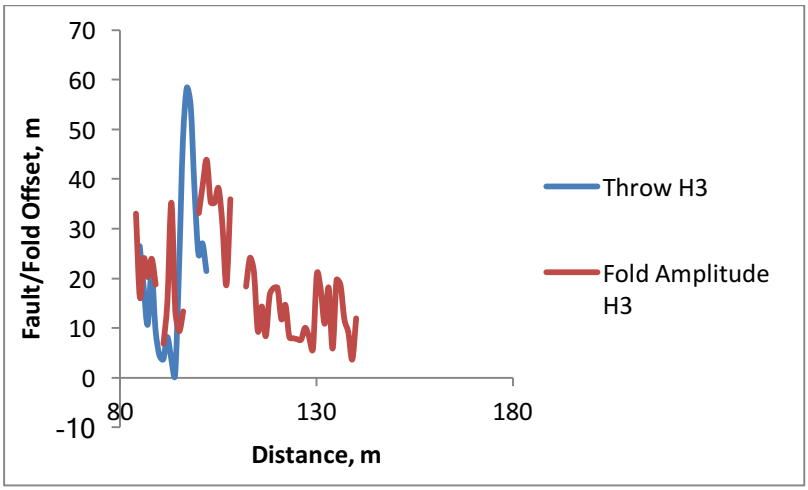

Figure 72: Fault throw and fold amplitude from horizon 3 in the Gulf of Mexico data set

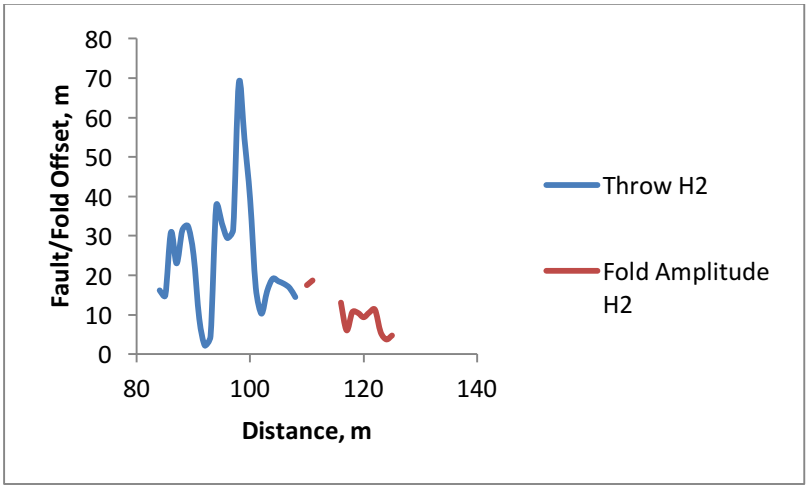

Figure 73: Fault throw and fold amplitude from horizon 2 in the Gulf of Mexico data set

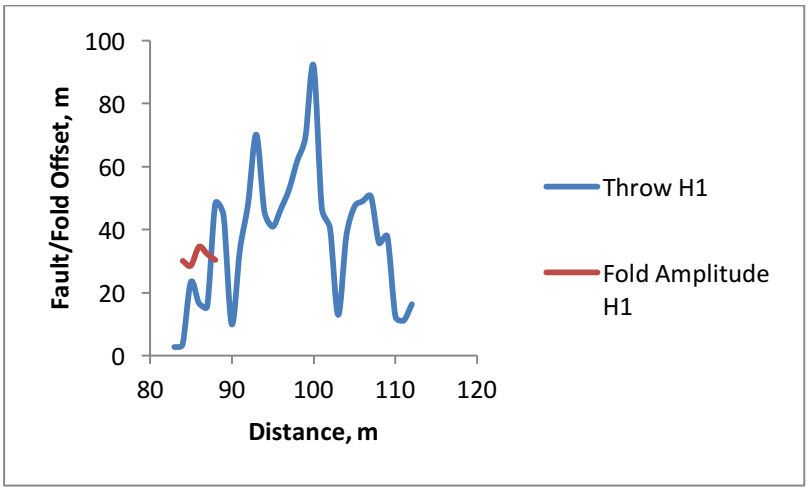

Figure 74: Fault throw and fold amplitude from horizon 1 in the Gulf of Mexico data set

In figure 74, it is possible to see at horizon 1 (H1), the horizon which is furthest from the upper tip line i.e. older in age, that the deformation is dominated by faulting. Only a small amount of folding occurs on the west of the fault plane (with west at the left-hand side of the fault, and east at the right-hand side of the fault). Moving upwards into horizon 2 (H2) (figure 73) and moving closer to the tip line of the fault plane there is a decrease in the amount of faulting and an increase in the amount of folding. This can be seen on the east side of the fault plane where the fault throw has stepped back towards the centre and fold amplitude values have taken their place. Reaching horizon 3 (H3) (figure 72) which is the horizon occurring at the tip line of the fault plane, the fault throw values have stepped back even further and occur mainly through the point at which fault throw is a maximum for the whole fault plane. The fault-related folding is now the dominant deformation style and these values have taken the place of where fault throw had previously existed.

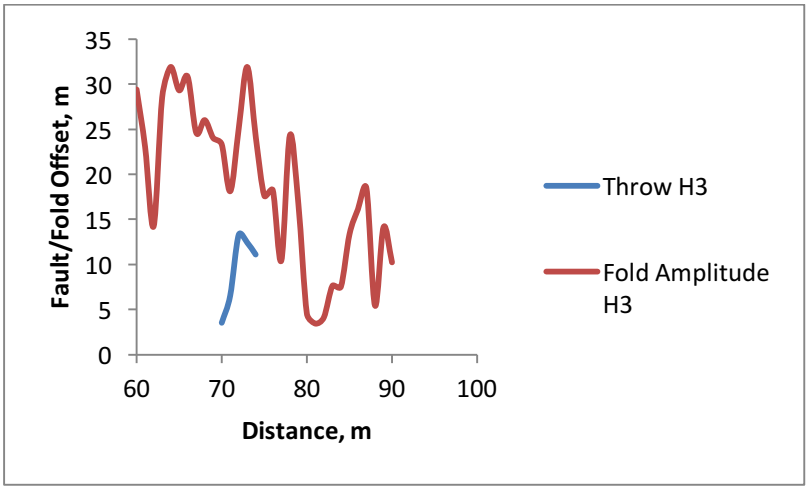

Figure 75: Fault throw and fold amplitude from horizon 3 in the Gulf of Mexico data set

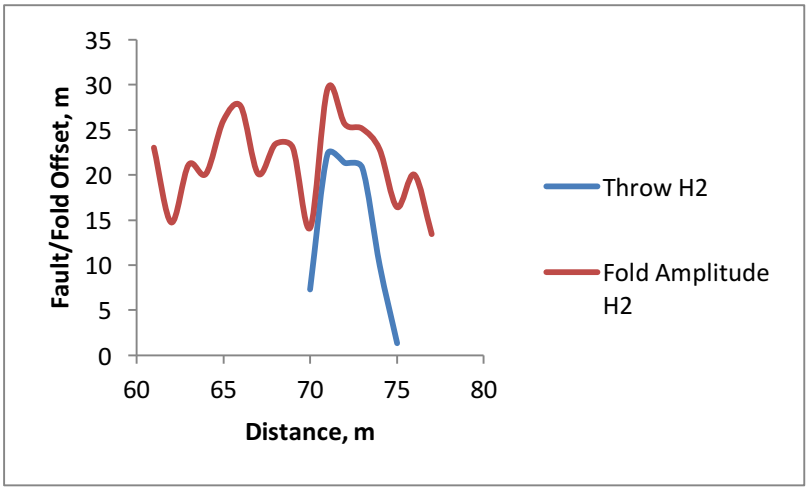

Figure 76: Fault throw and fold amplitude from horizon 2 in the Gulf of Mexico data set

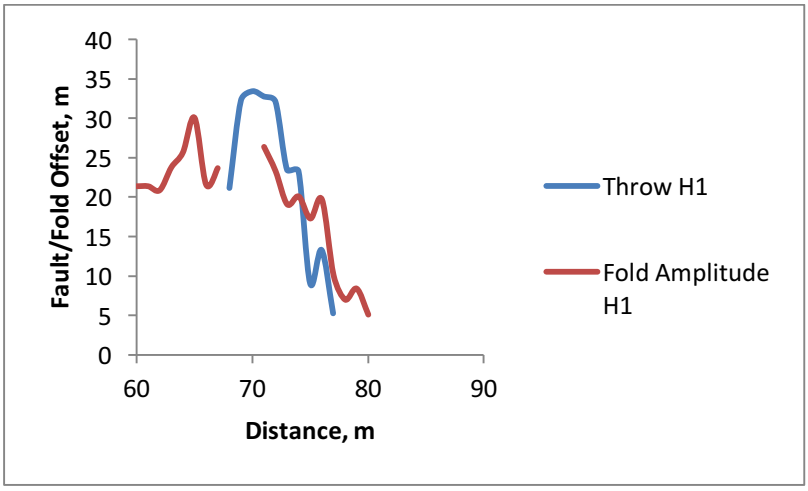

Figure 77: Fault throw and fold amplitude from horizon 1 in the Gulf of Mexico data set

Figure 75, 76 and 77 show the results from the Gulf of Mexico data set where figure 77 (horizon 1) is the deepest horizon and figure 75 (horizon 3) is the shallowest horizon. This figure shows a similar development as described above, however the fault throw recedes more equally on each side with the fold amplitude taking its place. Starting again at H1 the majority of the deformation is faulting, with some fault-related folding occurring on the left- and right-hand side of the fault plane. Moving into H2 there is the characteristic decrease in faulting as previously described, and an increase of fault-related folding further towards the centre of the fault plane. On the shallowest horizon, H3 is dominated by fault-related folding, with faulting only occurring through the maximum fault throw of the horizon which typically occurs at the centre of the fault plane.

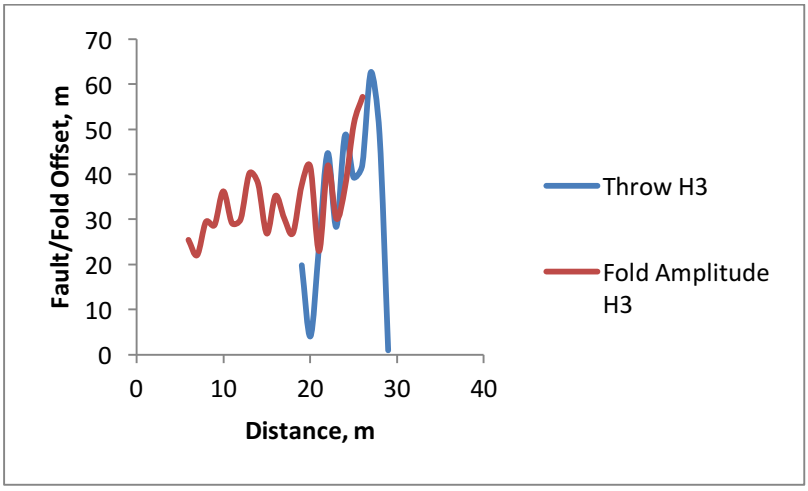

Figure 78: Fault throw and fold amplitude from horizon 3 in the Gulf of Mexico data set

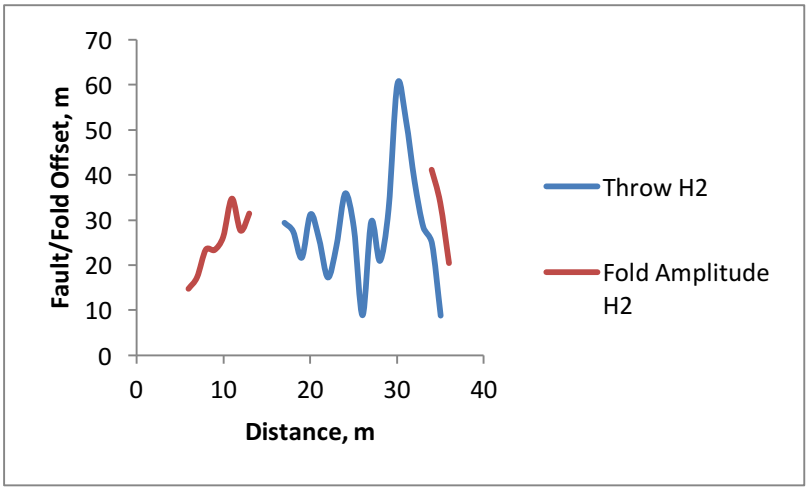

Figure 79: Fault throw and fold amplitude from horizon 2 in the Gulf of Mexico data set

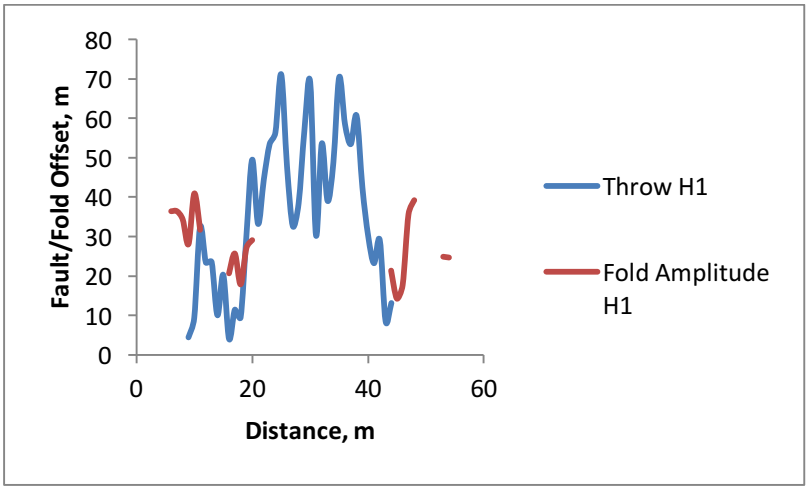

Figure 80: Fault throw and fold amplitude from horizon 1 in the Gulf of Mexico data set

The last figures, figure 78, 79 and 80 are arguably the best example of what has been described. Starting on horizon 1 (H1) fault-related folding can be observed at the western and eastern tips of the fault plane. It is clear where the fault throw maximum occurs, and this point is continued throughout the horizons in the figure. Moving upwards towards the upper tip line, H2 shows the expected decrease in the fault throw and an increase in fault-related folding, the only faulting that exists is through the fault throw maximum but most of the faulting has receded on either side of this. H3 shows that the deformation at this horizon is completely dominated by fault-related folding, with only a small amount of faulting occurring where the fault throw maximum is.

These three figures visually describe the evolution of the fault-related folding at the tip lines of the fault plane. What can also be seen in these diagrams is that the fault-related folding also occurs at the lateral tip lines on the edge of the fault plane, showing that fault-related folding is not exclusively the deformation style at the upper horizontal tip line of the fault plane (figure 72, 75 and 78). These figures also show that this is commonly where the fault-related folding starts from and as the horizon becomes shallower the fault-related folding moves in towards the centre of the fault plane until it is the main style of deformation.

It is possible that fault-related folding also occurs at the lower horizontal tip line of the fault plane. However, as a result of the decrease in seismic resolution at this depth it is not normally possible to accurately resolve the fault-related folding features to assess whether or not this deformation style continues at depth.

5.3 Qualitative analysis of fault throw and fold amplitude distributions

Histograms can be used to visually assess the distribution of sampled fault throw and fold amplitude values. This allows a comparison of how these values are distributed between fault data sets, or fold and fault data sets making it possible to assess, in a qualitative manner, whether the distribution of values are the same or not. The histograms have not been used as an indicator of a specific distribution, but as an initial indicator to show how smaller and larger values in the dataset are distributed.

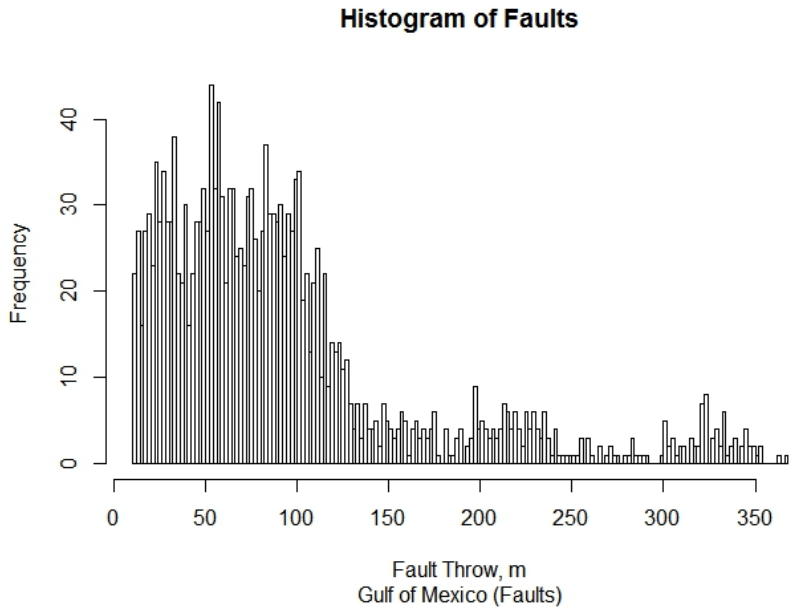

Figure 81: Gulf of Mexico faults histogram for all modelled horizons (4 horizons)

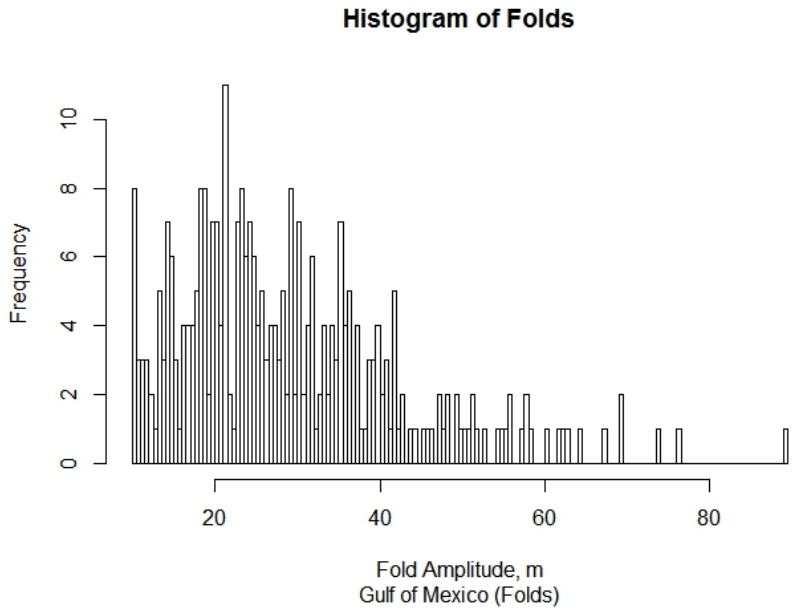

Figure 82: Gulf of Mexico folds histogram for all modelled horizons (4 horizons)

	Gulf of Mexico Fault Throw (m)	Gulf of Mexico Fold Amplitude (m)
Mean	93.10342	28.97157
Median	75.34106	25.85

Table 4: Gulf of Mexico faults and folds, mean and median

The histogram for the Gulf of Mexico fault data (figure 81) demonstrates a data set with a very large amount of smaller values which drop off quickly and continue steadily through to the larger values. In comparison to the Gulf of Mexico folds (figure 82) the histogram demonstrates a similar trend to the faults however appears to also be skewed towards the smaller values, and across the whole data set there appears to be a more even distribution of values. However, this data set is smaller and spans a shorter range of values as well. Looking at table 4 the mean and median have been used as an indicator of how skewed to the left or right the data is. For the Gulf of Mexico fault data the values are different to each showing they are skewed towards the left. For the Gulf of Mexico folds data the mean and median are also not the same demonstrating skewedness to the left, however are much nearer in range to each other than the fault data (approximately 8%). This doesn't indicate whether it fits a power law, exponential or log normal.

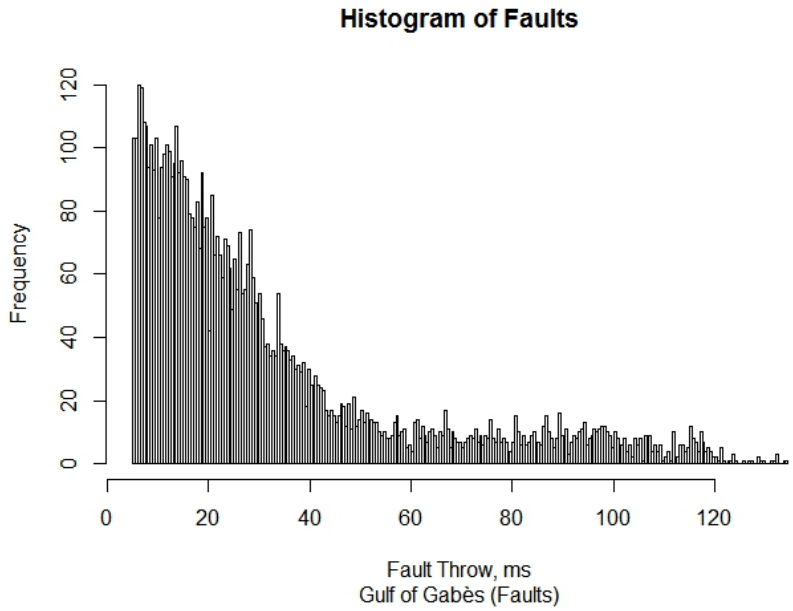

Figure 83: Gulf of Gabès faults histogram for all modelled horizons (11 horizons)

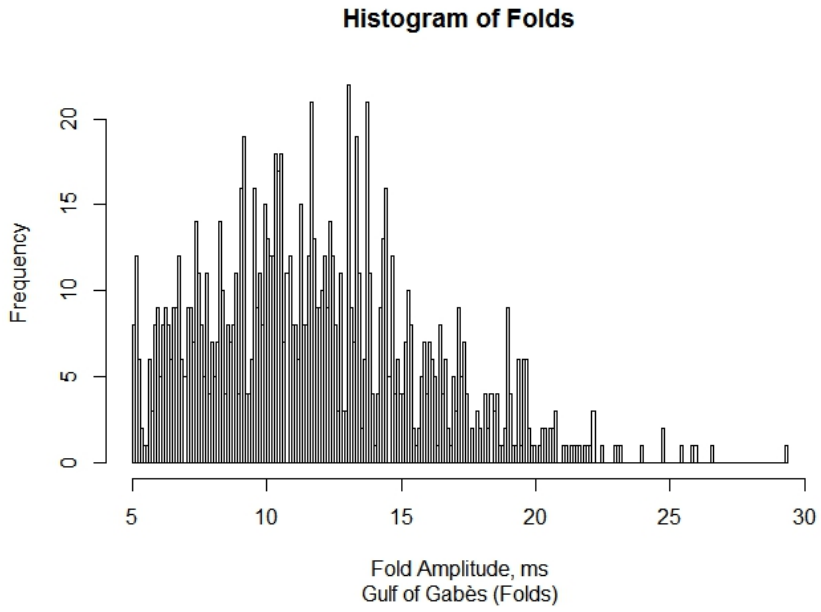

Figure 84: Gulf of Gabès folds histogram for all modelled horizons (4 horizons)

	Gulf of Gabès Fault Throw (m)	Gulf of Gabès Fold Amplitude (m)
Mean	31.99078	11.84068
Median	22.5857	11.4

Table 5: Gulf of Gabès faults and folds, mean and median

The histogram of the Gulf of Gabès fault data (figure 83) is heavily skewed towards the lower values, more so than the Gulf of Mexico data set. There is a very high concentration of smaller

values and fewer larger values. Compared to the associated folds for this data set (figure 84), the data is much less skewed and is closer to a characteristic bell shaped curve than the fault data. Unlike the Gulf of Mexico data where the difference between the mean and median for the fault and fold data was approximately 8% the difference for the Gulf of Gabès data is approximatley 25%.

Like the Gulf of Mexico fault data the Gulf of Gabès fault data shows a larger difference between the mean and median values reported (table 4) in comparision to the folds. The Gulf of Gabès fold data on the other hand reports mean and median values (table 5) which are relatively similar to each other. By looking at the histogram for the Gulf of Gabès faults it is clear however that the distribution is not very similar to the Gulf of Mexico faults. However, the Gulf of Gabès and Gulf of Mexico folds appear to be very similar, as so do the Gulf of Mexico faults which appear to be much more similar to the folds than the Gulf of Gabès faults.

When comparing the fault and fold data histograms there are strong similarities in the Gulf of Mexico results which suggest that they may follow the same distributions. However, the differences in the Gulf of Gabès histograms are a strong indication that the fault and fold data sets may not be derived from the same underlying populations.

The Inner Moray Firth data set shows a lack of data causing them to appear sparse and incomplete with no obvious trend in the data, this can also be seen in chapter 8.7.

5.4 Quantitative assessment of fault throw and fold amplitude distributions

Having collected both the fault and fold data from two one-dimensional multiline surveys it was necessary to assess them for their scaling law distributions. The figures for each data set are shown with the data plotted on linear-linear, log-log, log-linear and linear-log axes to test for linear, power law, exponential, and log-normal distributions. In each case, a straight-line segment should be observed on the graph if the dataset was drawn from a population with the corresponding distribution.

5.4.1. Gulf of Mexico

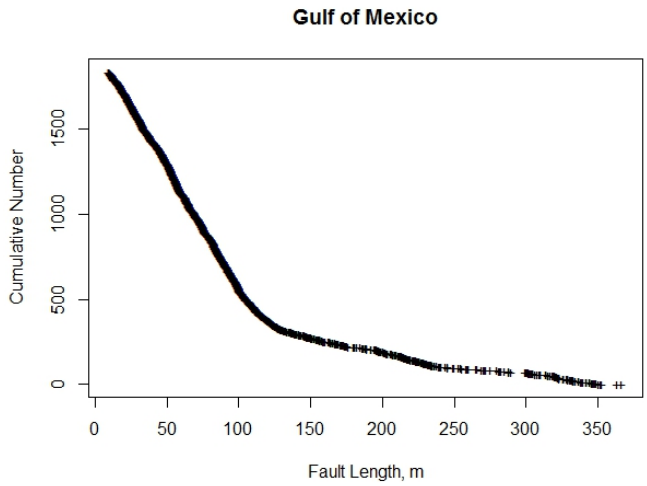

a, linear

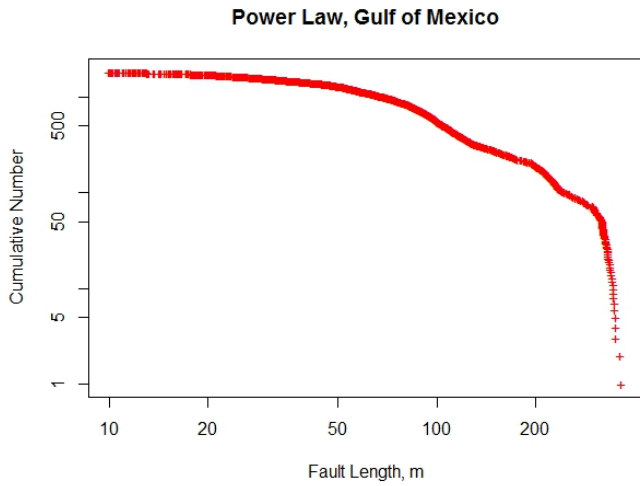

b, power law

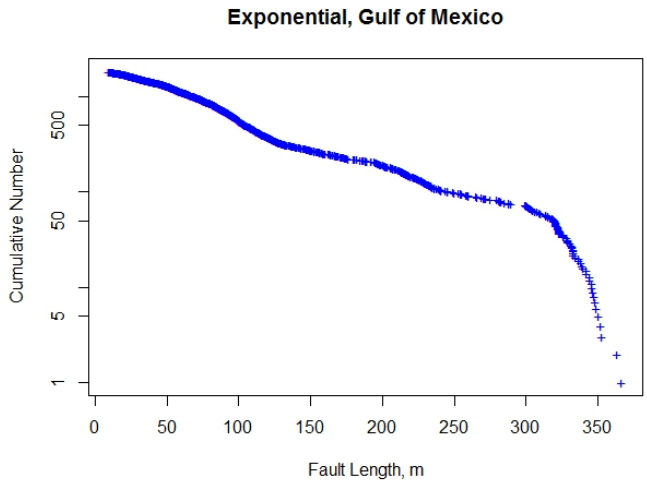

c, exponential

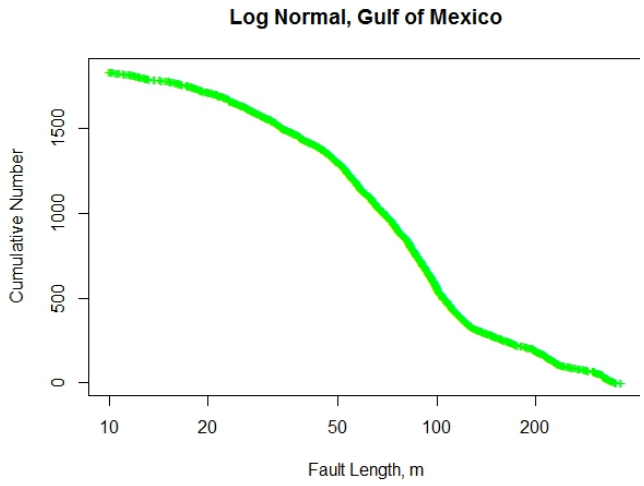

d, log normal

Figure 85: Gulf of Mexico faults distribution graphs

For the Gulf of Mexico fault data plotted on a linear plot (figure 85a) there are two distinct straight line portions of the graph with a very obvious bend in the data at about 130m. Graphically this is identifying that the majority of the data points lie between 0-130m, and from 130m onwards there are far fewer data points. This is evident in the dramatic gradient change at 130m.

For the power law distribution (figure 85b) there is an approximate straight-line segment between 50-300m. This is the classically recognised portion of the data identified by Yielding et al., (1996), Watterson et al., (1996) and Nicol et al., (1996) as being drawn from a power-law distribution. The

straight-line section is described as a moderately-dipping central segment which denotes the value of the exponent in the scaling distribution and describes the relationship between the fault throw/fold amplitude and cumulative number. On the left of this is a sub-horizontal segment indicating a lack of observation below the seismic resolution (the values are too small to be resolved by the data collection method), and on the right is a steeply dipping segment which is also not representative of the population measured (Needham et al., 1996).

Figure 85c (log-linear axes) shows a characteristic straight-line between 120-320m, and there is also the evidence of the left- and right-hand truncation. However, in comparison to the power law distribution the left-hand truncation has a much steeper gradient than that of the straight-line section; whereas the gradient steepened into the straight-line section for a power law.

The graph for the log-normal distribution (figure 85d) shows no distinct straight-line section and the majority of the graph forms a gentle curve. There is evidence of the right-hand tail which is a straight-line, but for reasons already outlined these areas are often lacking data and so are not representative of the underlying population.

From these distribution plots the data appear to show more affinity with either a power law or an exponential distribution. To test this more thoroughly the two statistical methods, the incremental (chapter 3.4.2.1) and moving window (chapter 3.4.2.2) were performed on the data. The code may be found in Appendix 1.

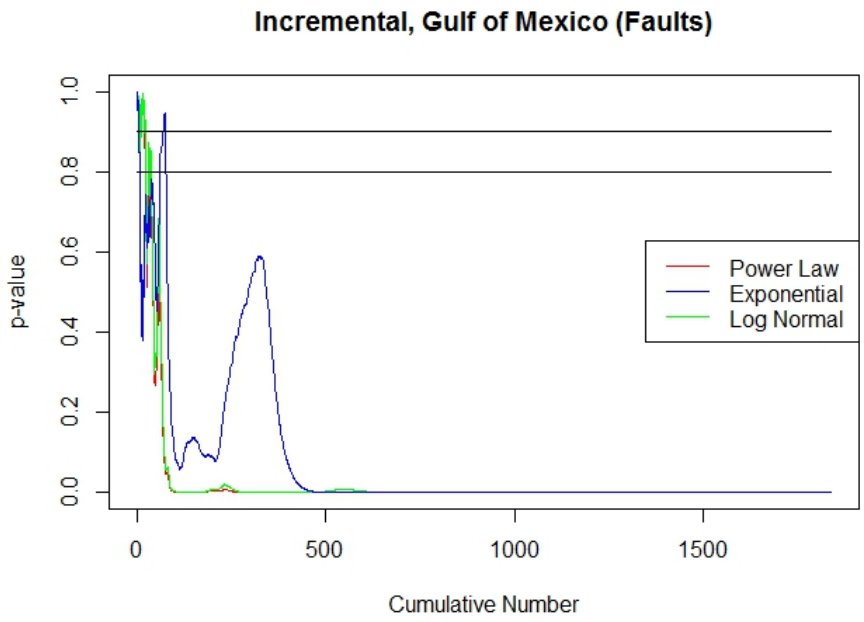

Figure 86: Incremental window with an Anderson-Darling test for the Gulf of Mexico fault data set

The results of the incremental window test (figure 86) are largely inconclusive and roughly show the same result for all of the distributions. This has been discovered as a characteristic result for the data. As a result of the incremental window, the sample size grows progressively: the initial sample size is so small that any distribution provides a good fit ($p > 0.8$). As this sample size grows it causes none of the tested distributions to be able to fit the dataset, hence the p-value flat lines at 0. As a consequence of this effect, further results from the incremental window test will not be reported below.

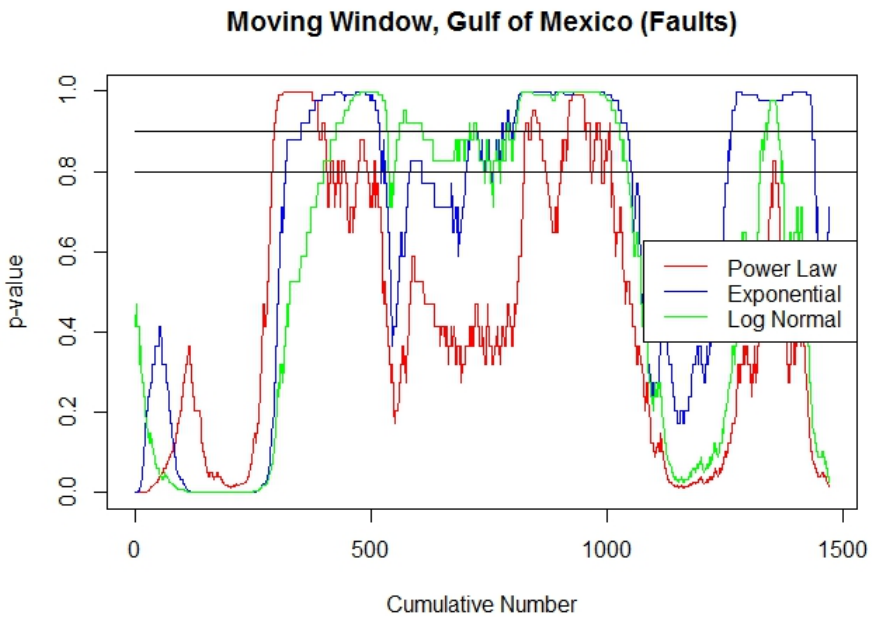

Figure 87: Moving window with a Kolmogorov-Smirnov test for the Gulf of Mexico fault data set

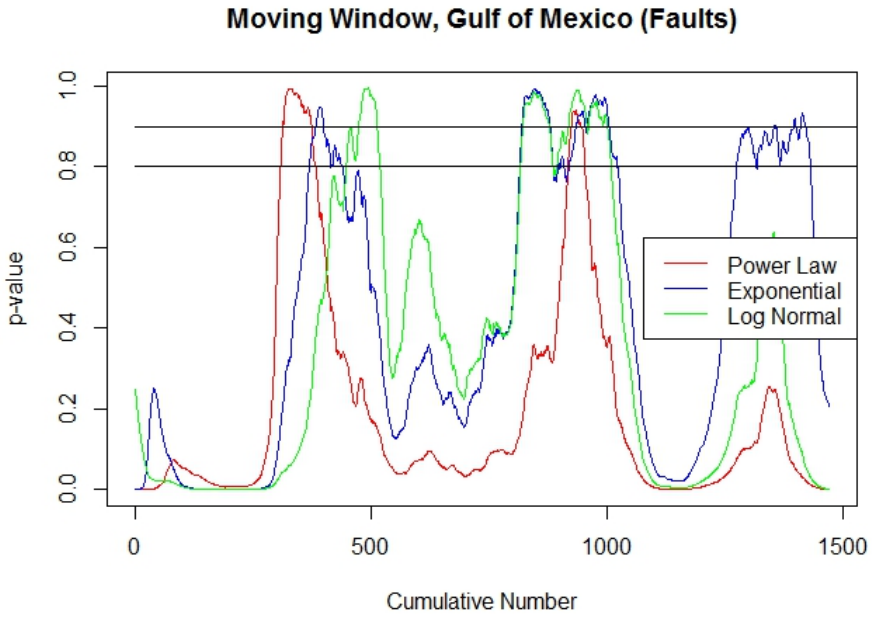

Figure 88: Moving window with an Anderson-Darling test for the Gulf of Mexico fault data set

The following tests were carried out using an Anderson-Darling k-samples test (chapter 3.4.2.4), but were also carried out using a Kolmogorov-Smirnov test (chapter 3.4.2.3) in order to compare the results from the two different methods. The Anderson-Darling and Kolmogorov-Smirnov test measure the distance between the collected data from the three-dimensional seismic volume and

a synthetic data set. The same moving window test described below was also carried out with a Kolmogorov-Smirnov test (figure 87), which can be compared to the moving window with an Anderson-Darling k-samples test (figure 88). Generally, the Kolmogorov-Smirnov test produces less smooth results, and on the whole, is not as continuous as those gained from using the Anderson-Darling test. As a result of this results will only be reported for the Anderson-Darling test.

The moving window tests appeared to produce much more useful results than the incremental window test. The moving window uses a fixed window size which moves across the data incrementally assessing the distribution at each point. The results of this test are much more beneficial in identifying areas in which some distributions dominate and others do not in comparison to the incremental window. Since the incremental window grows in size as more data is included in the window then the fit for any tested distribution quickly drops off and the test produces no good-fit for any distribution.

In figure 88 the two black lines at a p-value of 0.8 and 0.9 highlight where a good-fit is considered to exist, anything above these lines is accepted to fit the tested distribution. However, anything which falls below these lines is not accepted to fit the tested distribution. In order to carry out the moving window the size was defined as 20% of the total sample sizes i.e. for a sample size of 1000 the window size would have been 200. In chapter 6.4 different window sizes are discussed.

Figure 88 shows the results for the Gulf of Mexico fault system highlighting a number of locations where each scaling distribution dominates. It can be seen in the left- and right-hand tails of the data that no distribution is particularly fitted. This confirms the idea that within these portions the

data suffer from either truncation or censorship and leads to an unrepresentative sample of the data.

Focusing on the middle portion of the results, there are two distinct areas in which a number of the distributions are shown to fit. These exist between approximately 250-500 and 750-1000 on the cumulative number axis. At the first of these points (250-500) the fit begins as a power law distribution before a break-point (the point at which one distribution is no longer a fit, and another distribution may take its place) where an exponential distribution takes over, there is then another break-point and a log-normal distribution takes over. Between approximately 500-750 there is no presence of a good-fit, since none of the distributions break above the 0.8 p-value. The log-normal, although not over 0.8 produces the highest p-value in this area. In the second portion the log-normal distribution continues to dominate alongside an exponential distribution, the power law distribution peaks at one point however the portion is dominated by the log-normal distribution.

From the power law, exponential, and log-normal graphs there is evidence that some of the data could belong to either a power law or exponential distribution, and it appears less likely that part of the data belongs to a log-normal distribution. As previously discussed, the results of the incremental window are not a useful method and can therefore be discounted for further analyses. The moving window on the other hand provides some interesting insight into the different distributions which dominate within the Gulf of Mexico data set. On the whole, considering the earlier plotted graphs and the results of the moving window, it seems likely that the overall distribution for the Gulf of Mexico fault throw data set is exponential, with some areas being dominated by power law and log-normal distributions.

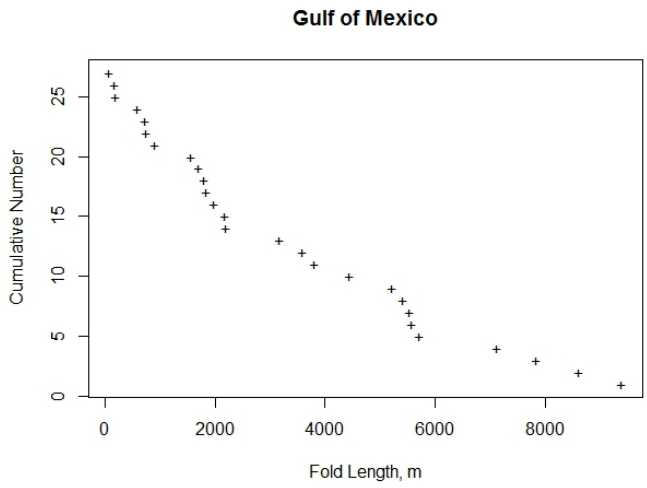

a, linear

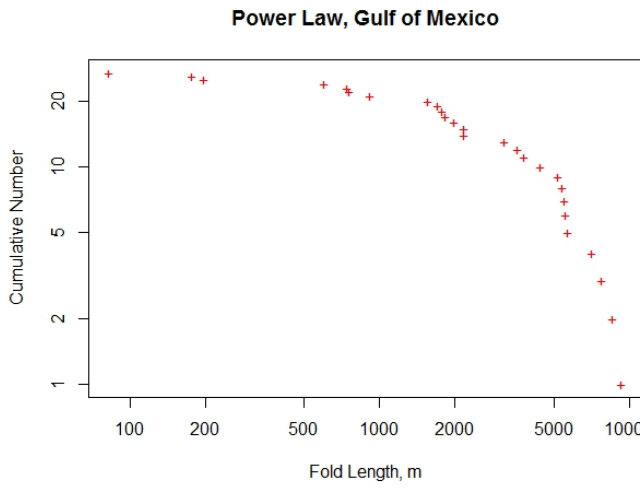

b, power law

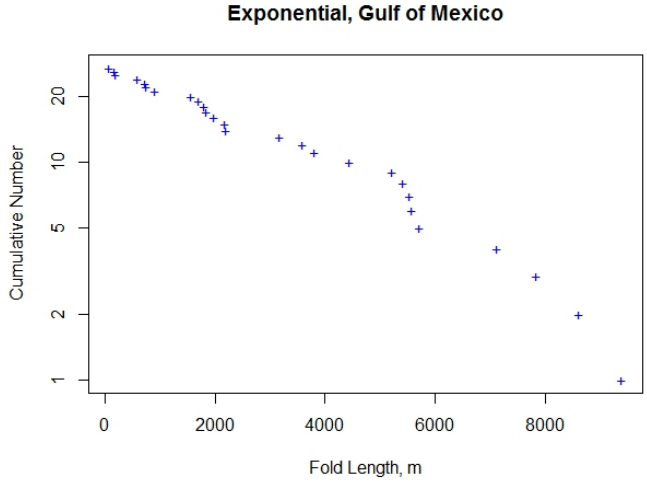

c, exponential

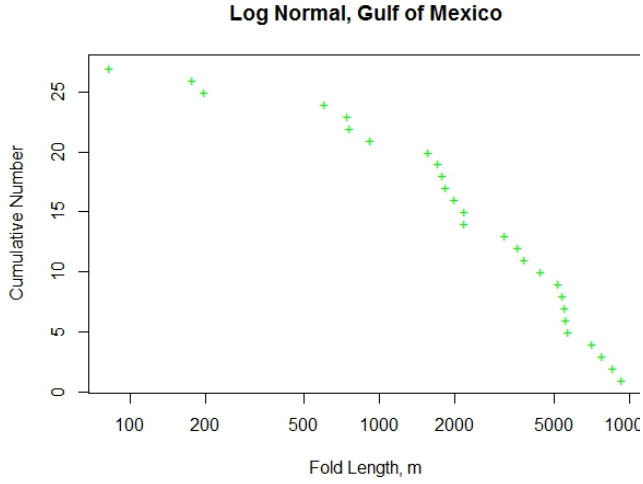

d, log normal

Figure 89: Gulf of Mexico folds distribution graph

The results of the fold data for the Gulf of Mexico, when plotted on a linear axis (figure 89a), demonstrate a smooth curve with no obvious dramatic change in gradient as was observed for the fault data. When plotted for a power law distribution (figure 89b) there is a small left-hand tail which moves gradually into a straight-line section (50-90m) for the rest of the distribution. The exponential distribution (figure 89c) plots as an almost entirely straight-line graph from 20m onwards, with a very small left-hand tail. The log normal plotted data (figure 89d) has a smaller straight-line section, between amplitudes of approximately 15-40m, however it is not hugely distinguishable between the left- and right-hand tails, showing a relatively smooth curve. These initial plots indicate that the data may satisfy an exponential distribution more so than any other, however both the power law and log-normal also have straight-line segments.

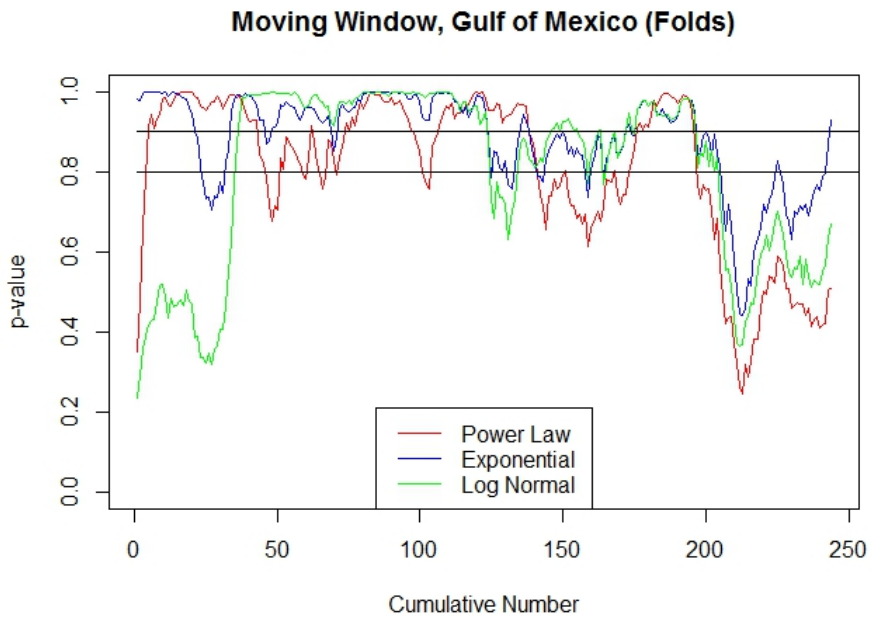

Figure 90: moving window with an Anderson-Darling test for Gulf of Mexico folds data set

The moving window (figure 90) code shows agreement with these initial findings in the distribution graphs (figure 89a, b, c, d). There is evidence of the initial left-hand tail (200-250, on the cumulative number axis) where the p-value is very low, which was consistent throughout all the previous plots. The right-hand tail (0-40) can also be seen for the power law and log-normal distribution, however it doesn't exist for the exponential which when looking at the exponential plot is expected since the straight-line extends through the rest of the data.

The middle portion of the moving window (40-200, on the cumulative number axis) results starts with a better fit to the log-normal distribution, then an exponential and power law distribution throughout approximately 40-200. Although the power law shows a poorer fit compared to the other two distributions it still gives a p-value over 0.8 suggesting that the data could fit that distribution. This continues through 40-200 on the cumulative number axis, with all the distributions increasing their p-value to largely above 0.9. Towards 200 on the cumulative number axis the power law distribution drops below the 0.8 mark whilst the exponential and log-normal stay above it. All three distributions then increase above the 0.9 mark through the middle portion

of data which has been previously viewed as the key area of the data showing that all distributions are equally probably here. This then drops off in the left-hand tail. Throughout the moving window graph there are no significant break-points between the different distributions.

Considering the distribution plots and the moving window results, the exponential distribution appears to dominate slightly more than the power law and log-normal distribution. However, it is difficult to distinguish which of the distributions best fit this data set as they often occur mutually inclusively of each other. This could be because the data does not belong to any of these distributions and belongs to another distribution. Despite this, there are still a number of places where these distributions confidently fit the data compared to the fault data which more obviously fitted one distribution better than the others.

5.4.2 Gulf of Gabès

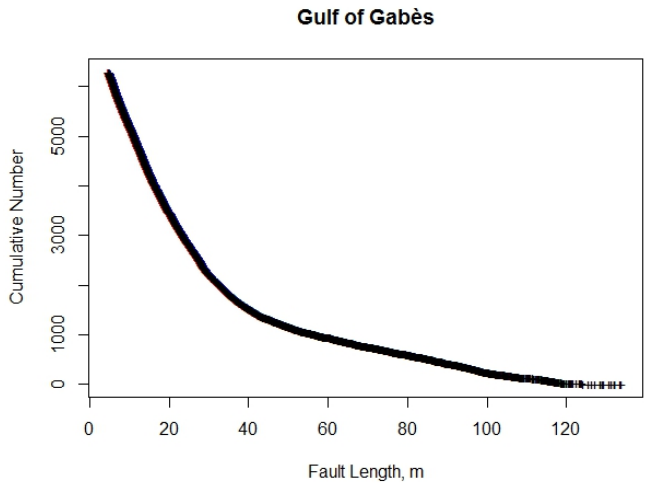

a, linear

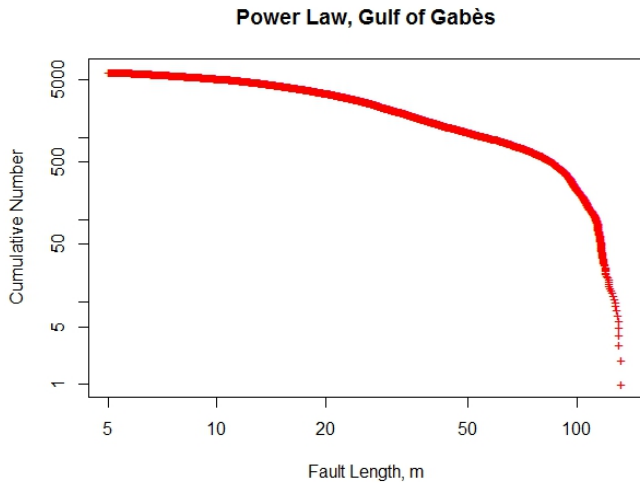

b, power law

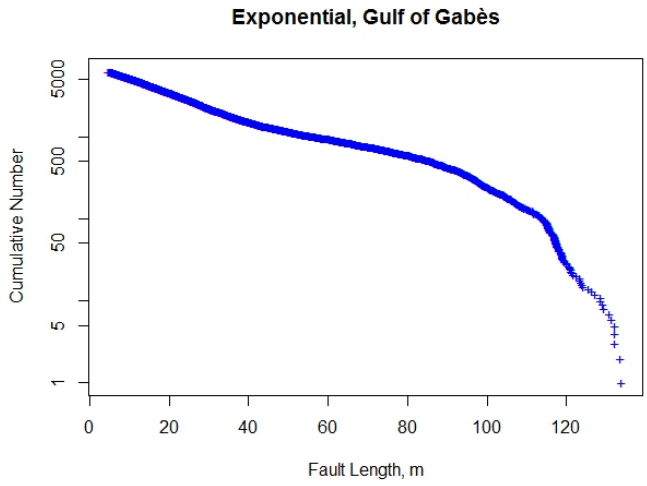

c, exponential

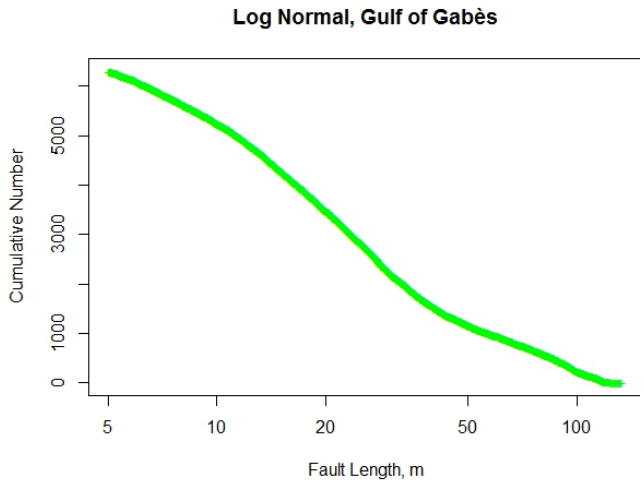

d, log normal

Figure 91: Gulf of Gabès fault throw distribution graph

The Gulf of Gabès fault data plotted on linear axis (figure 91a) demonstrate a similar shape to that of the Gulf of Mexico fault data. The bend in the data is less dramatic than the Gulf of Mexico fault data, although more dramatic than the fold data from the Gulf of Mexico. In reflection of this the data plotted for a power law distribution (figure 91b) also demonstrate this similarity in shape. There is a left- and right-hand tail which are both present in the Gulf of Mexico fault data but not in the fold data. Similar to the linear graph, the transitions from the tails into the straight-line are much less dramatic and form a smoother transition. The straight-line section of the graph occurs between approximately 15-90ms (measured in two-way travel time, important to note that since this doesn't span an order of magnitude it does make the slope more difficult to

determine), although the beginning of the straight-line section is hard to distinguish as the transition from the tail is not clearly defined.

The exponential distribution (figure 91c), like the power law distribution, mimics the shape of the results from the Gulf of Mexico but with less dramatic transitions between the tails into the straight-line section. There is a clear straight-line section between about 40-110ms, which compared to the straight-line for the power law is shifted to the right. This is also the same for the fault data in the Gulf of Mexico.

Figure 91d for the log-normal distribution has a straight-line section between about 10-40ms with a left- and right-hand tail. Again, similar to the Gulf of Mexico fault data there are similarities in the shape of the graph with less dramatic transitions between the tails and mid-section of the data.

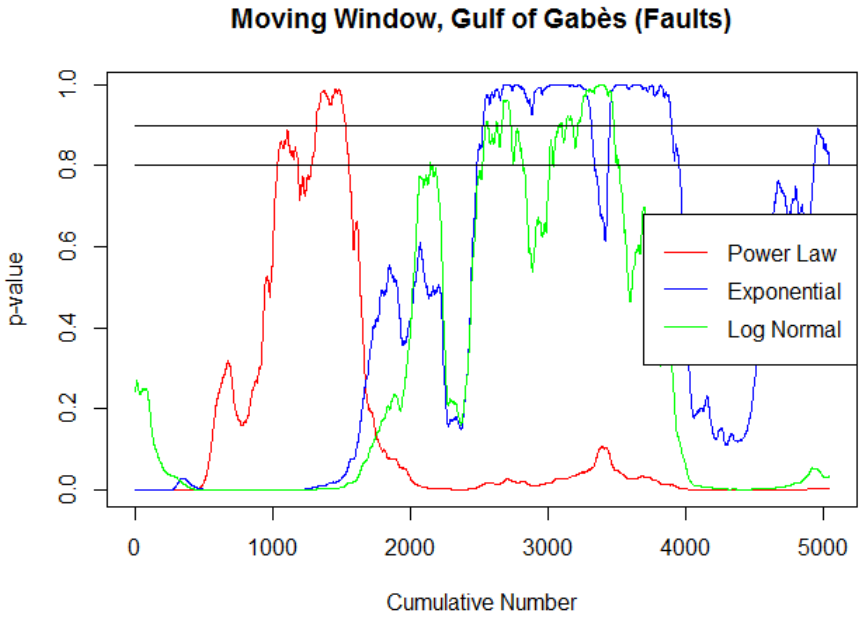

Figure 92: Moving window with an Anderson-Darling test for the Gulf of Gabès fault data set

For the moving window results (figure 92), there is a very significant drop-off of p-values in the left-hand section of the graph. The left-hand tail between 0-1000 (on the cumulative number axis) shows no distribution fit, then after 1000 for the next 500 data points there is a good power law fit whilst the exponential and log-normal distribution do not fit over this range, after this there is a break point where the power law distribution drops off for the rest of the data set. Between 1500-2500, the data doesn't show a good fit for any distribution, although the log-normal distribution just touches the 0.8 line it does not cross it. From 2500-4000 data points there is a good fit for both the exponential and log-normal distributions. The exponential distribution dominates most throughout this period with just a small, single drop off at approximately 3500. At 4000 data points there is another break point where no distribution exists, there is then just a small spike of the exponential distribution at about 4800.

In comparison to the other data sets reviewed there is a much more definite separation in distributions. Overall for this data set the exponential and log-normal distributions dominate over the power law distribution, with the exponential dominating possibly slightly better than the log-normal. On the left-hand side between about 300-1800 on the cumulative number axis the data set demonstrates a power law distribution which dominates independently of the exponential and log-normal distributions. When compared to the others, this data set appears to be much more mixed between all of the scaling distributions.

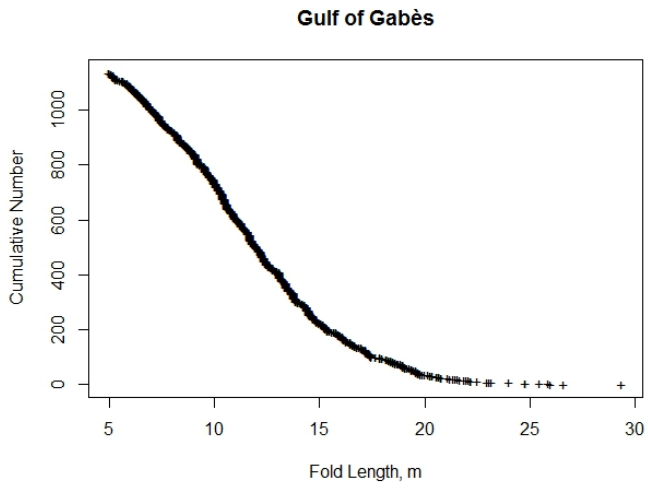

a, linear

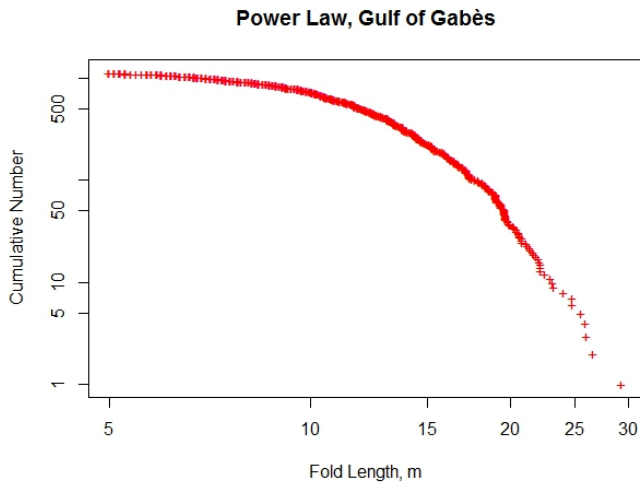

b, power law

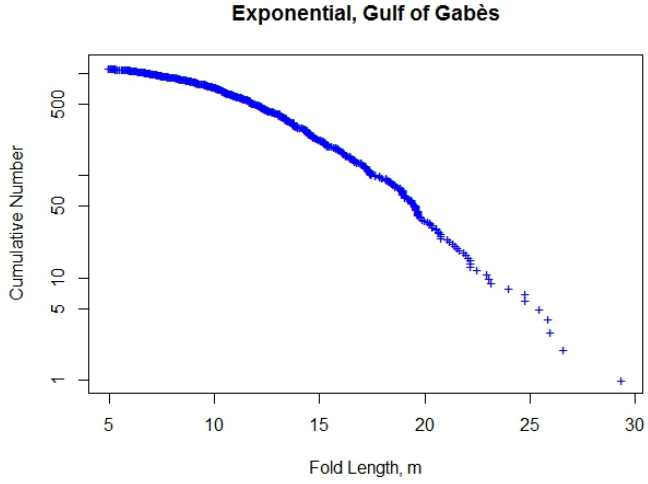

c, exponential

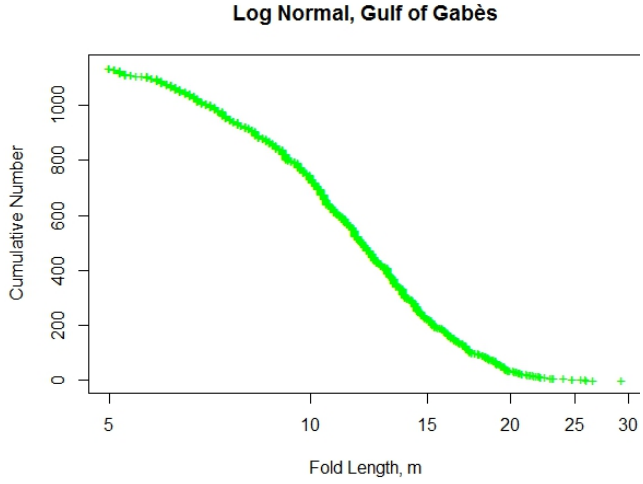

d, log normal

Figure 93: Gulf of Gabès fold amplitude distribution graphs

The associated folds from the Gulf of Gabès fault data set can be seen in figure 93a as a linear plot. Like the fault data sets (figure 85 and 91) from the Gulf of Mexico and Gulf of Gabès which exhibited similarities between the distribution plots, the fold data sets from these areas also demonstrate similarities in the distribution graphs (figure 89 and 93). Unlike the equivalent fault plot, there is no distinct bend in the data, but there is a gradual change in gradient. There is no distinct left-hand portion of the data; instead it makes up a relatively straight-line towards the lower end of the data points where it flattens to the right-hand side.

The power law graph (figure 93b) has a flat section in the left-hand tail of the graph which then steepens into a relatively straight-line for the rest of the graph at around 15ms onwards. There is no distinct right-hand tail for this data set which is also seen in the fold data of the Gulf of Mexico. The exponential graph (figure 93c) likewise mimics the shape of the exponential distribution for the Gulf of Mexico data. There is a very small left- and right-hand tail in the data but it generally forms a straight-line throughout the whole data set. The log-normal distribution (figure 93d) has a much more distinct left- and right-hand tail with a middle straight-line section at approx. 8-15ms. As has been repeated throughout the data sets so far, the log-normal distribution also mimics the shape of the fold data gathered from the Gulf of Mexico data set.

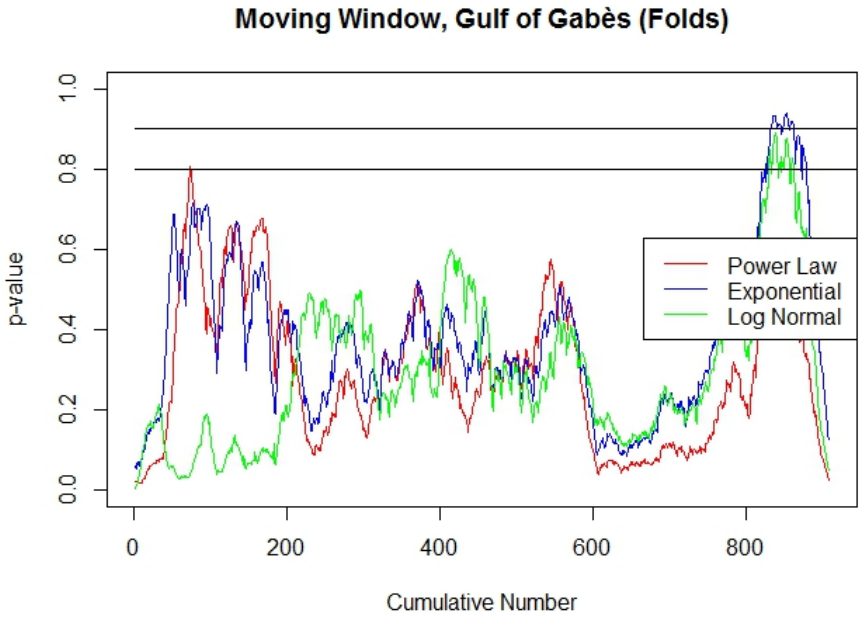

Figure 94: moving window with an Anderson-Darling test for the Gulf of Gabès fold data set

The moving window (figure 94), like the results from the Gulf of Mexico fold data does not show any great distinction between any of the distributions. They all appear to exist mutually inclusively of each other and there isn't a great deal to distinguish between each of them. Unlike the previous results where there is generally a poorer fit to the data in the tails of the data and a better fit in the middle of the data, there is a better fit at the tails and a worse fit in the middle. As well as this, there is only one point where the distribution curves produce a p-value greater than

0.8 which is in the left-hand tail of the data and is fit by the exponential and log-normal distribution. On the whole, the results of the moving window also demonstrate the curve shape, except where the log-normal varies but this difference only extends for about half the data points.

All of the distribution plots demonstrate a relatively straight-line section throughout areas with similar fold amplitudes. This is the most likely reason why the results of the moving window are similar to each other. Looking at the distribution graphs it is possible to say that although they do appear to be straight-lines they could also be gently sloped curves, this has resulted in the moving window being unable to fit any particular distribution to the data set. This makes it difficult to determine which distribution, or combination of distributions dominates throughout the data set.

	Gulf of Mexico Faults	Gulf of Mexico Folds	Gulf of Gabès Faults	Gulf of Gabès Folds
Power Law	5	7	5	2
Exponential	6	8	6	2
Log-normal	6	8	5	2

Table 6: summarises the distribution fit for each of the tested data sets where 1 represents a bad fit to the tested distribution and 10 represents a good fit to the tested distribution

5.5 Quantitative estimates of exponents

Fault and fold data sets have been gathered for each of these one-dimensional multiline surveys on the Gulf of Mexico and Gulf of Gabès. An exponent was calculated for each of these distributions. It is widely agreed that fault data sets may be described by a power law scaling distribution (Yielding et al., 1996; Watterson et al., 1996; Nicol et al., 1996; and Fossen and Rørnes 1996) however the scaling of fault-related folding has not been widely studied. As a result, most publications only provide estimates of the power law exponent values for fault data sets; it is therefore difficult to compare the results of the other distributions that were tested in this project (exponential and log-normal).

The expected exponent values for the one-dimensional multiline survey carried out for a power law lie between -0.4 and -1.0 (Nicol et al., 1996). As a result of this, only the power law exponent can be used as a validation measure of the scaling distribution. The power law was chosen because there are already published exponent results which make it possible to compare to. For a given set of results from the moving window test, if the p-value returns a good fit for a power law distribution, however the exponent value calculated over this range is not geologically possible it may be that it cannot be accepted. A value has been considered geological plausible or not by the exponent values which have been published. However, if over this range the exponent returned a geologically possible value it is likely that a power law is the dominate scaling distribution at this point.

Two methods have been used to calculate the exponent value. The first was an straight line equation method which was a re-arrangement of $y = mx + c$ for a power law gives equation 13. When this is rearranged this becomes:

Equation 15: $$\boldsymbol{m = \frac{\log y - \log c}{\log x}}$$

The second method was to carry out a simple gradient calculation on the window under consideration using equation 12.

The main difference between the two methods is that the first generates an intercept for the straight line which is fitted to each of the windows being tested in turn. The second method is a first order differential on the raw data which the window covers at the time.

It is important to note that the actual exponent is a negative number as the gradient of the data slopes downwards; this is also the case for already published results however the values are reported as positive numbers.

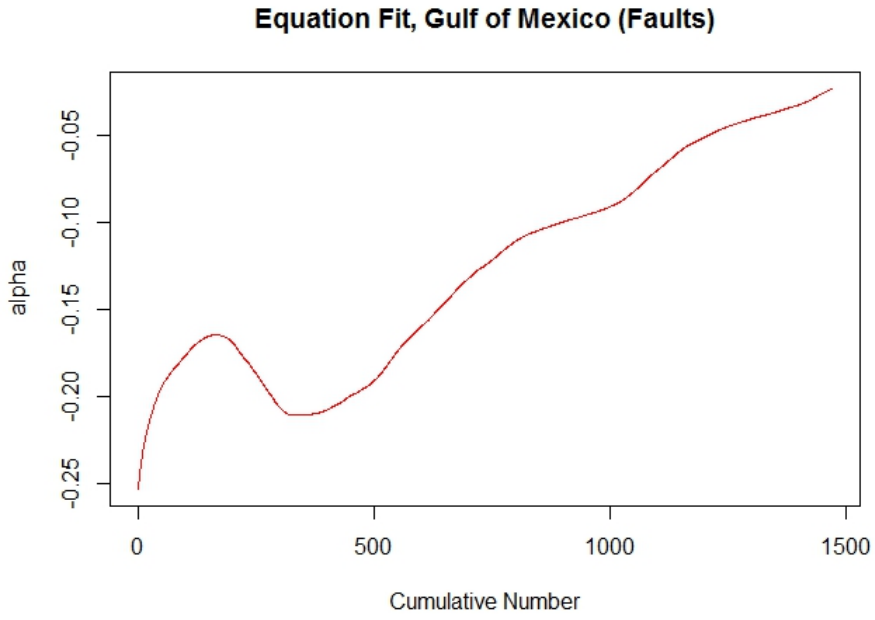

Figure 95: Straight line equation method for the Gulf of Mexico fault throw data set

The straight line equation method (figure 95) used for the Gulf of Mexico fault data does not report a value within the expected range of -0.4 – -1.0 (Nicol et al., 1996) and all the values are smaller than -0.4 where published results state the exponent to fall between, -0.4 and -1.0 (Nicol et al., 1996). This is possibly due to the use of the intercept causing the best fit line to be significantly shallower in gradient than that of the actual raw data. As a result of this the exponent calculated is not a true representation of the exponent value.

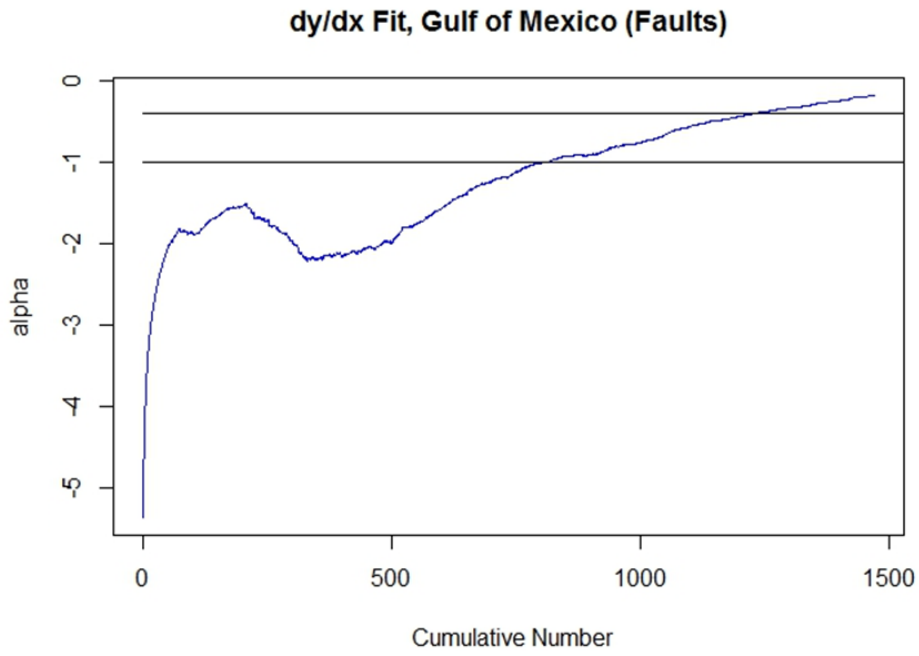

Figure 96: differential method for the Gulf of Mexico fault data set

The differential method (figure 96) produces values which fall within the expected range, this occurs between 750-1250 cumulative number. When compared to the p-value from the moving window data (figure 87) it corresponds with the first peak of where the power law data satisfies these data points. This shows that with this combination of methods it is possible to both identify where one distribution dominates, and also the exponent value at this point. Comparing this to the straight-line section of the power law distribution graph (figure 85), the data points to the exponent covers cross-over with the straight-line section between 70-300m. This therefore suggests that between these points a p-value is reported which supports a power law scaling distribution and an exponent value is also calculated which falls in the expected geological range for a data set sampled by one-dimensional multiline sampling. As a result of this it can be reported with confidence that this portion of the data is highly likely to be distributed by a power law.

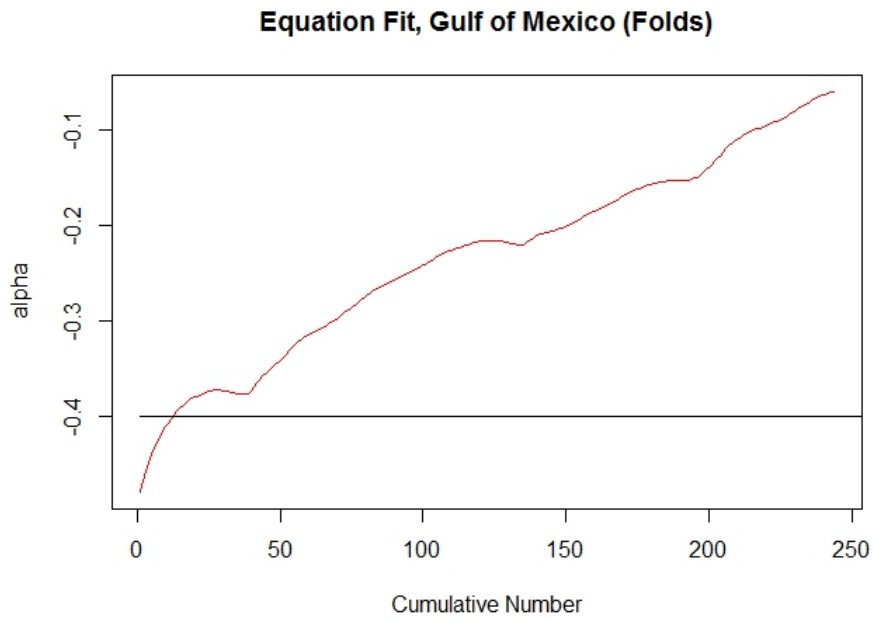

Figure 97: equation fit for the Gulf of Mexico fold data set

The Gulf of Mexico fold data set for the equation fit (figure 97) shows a very small portion of the data between about 1-20 where the exponent falls in the range expected for a power law. This is an area in the right-hand tail of the distribution fit (figure 90), which demonstrates a straight-line; however as is known from sampling errors results in the left- and right-hand tails of data sets are not commonly representative of the populations the data derives from. Despite this it is still important to assess whether the moving window results (figure 90) also verify this fit, although the power law distribution does peak slightly as it does not reach a high enough confidence level.

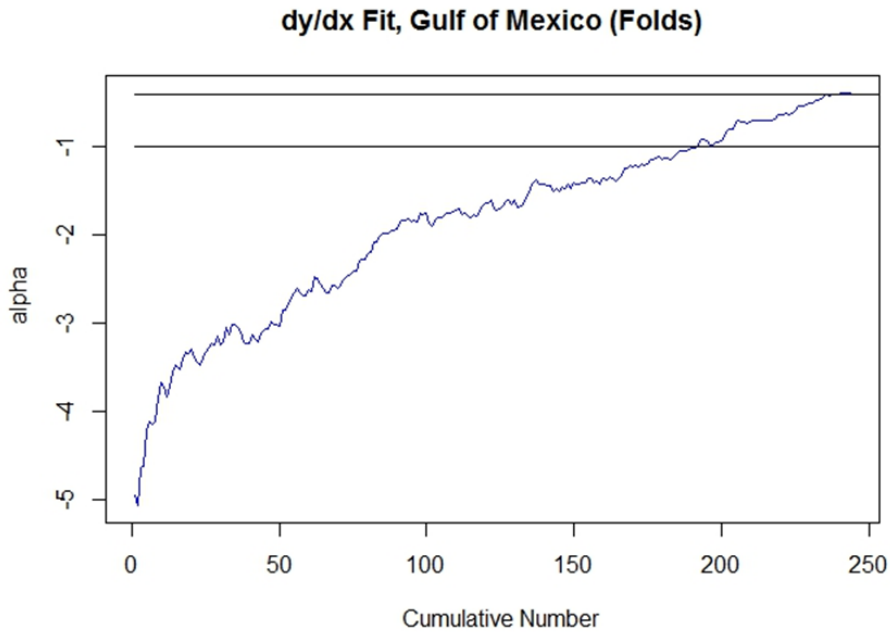

Figure 98: differential method for the Gulf of Mexico fold data set

The differential method (figure 98) produces values in the accepted range between 200-250 data points. This is in the left-hand tail of the data set and is not commonly representative of the overall data set. The power law distribution graph (figure 89b) does show a straight-line through these points which falls at the beginning of the moving window results (figure 90) where a good fit is shown despite the fact it is not likely to be representative of the population.

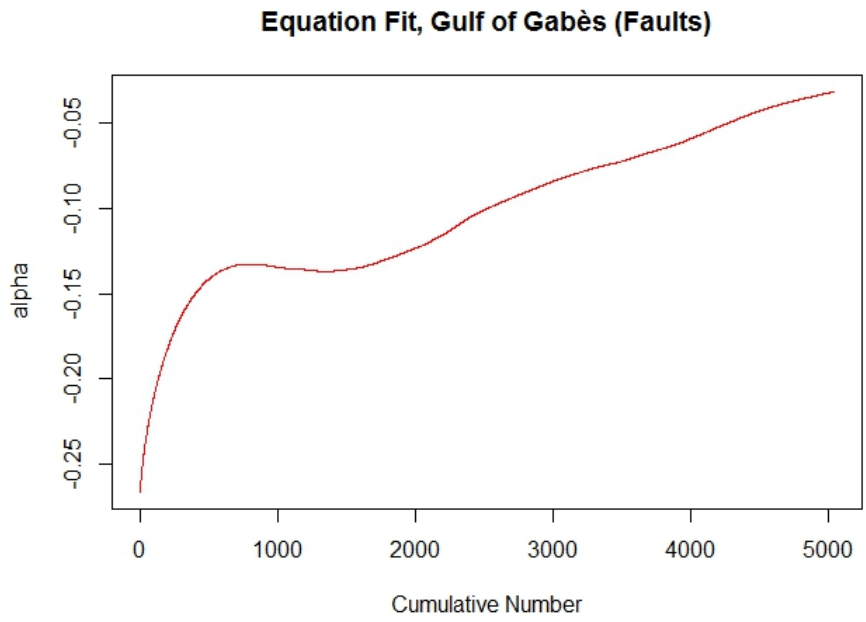

Figure 99: equation fit for the Gulf of Gabès fault data set

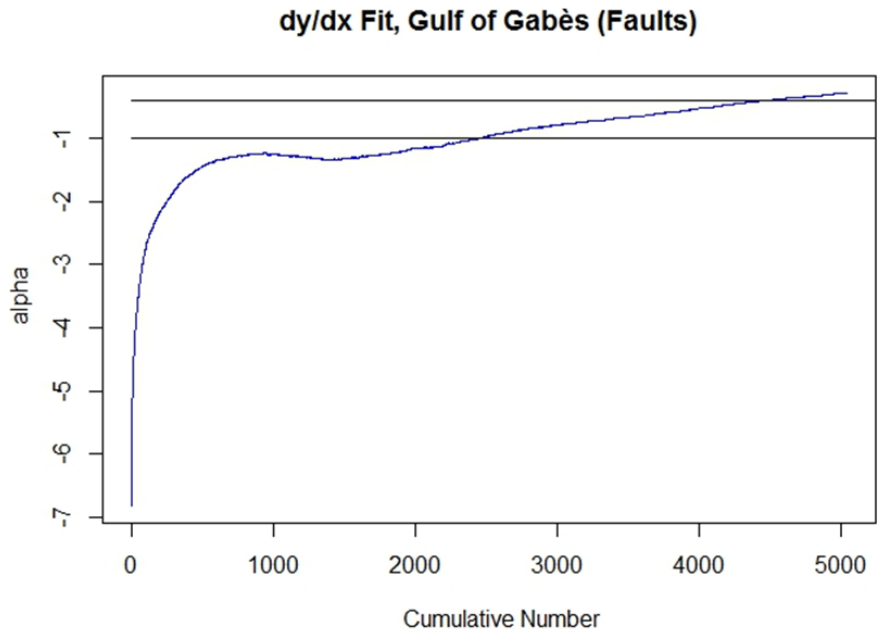

Figure 100: differential fit for the Gulf of Gabès fault data set

The Gulf of Gabès fault throw data set, as for the Gulf of Mexico data set (figure 95) produces values for the equation method which are too small compared to the values expected. In the differential method (figure 100) there is a fit for the expected values between 2500-4500 cumulative number. Like the Gulf of Mexico data set this fit for the exponent values falls at the

beginning of the straight-line section for the power law distribution curve (figure 92). This is roughly in the range of 20-90ms. When compared to the moving window results (figure 92) these confirm the presence of the first (and only) power law peak in the p-value for this distribution. As a result of this it demonstrates a geologically viable exponent value over this portion where the power law distribution fits.

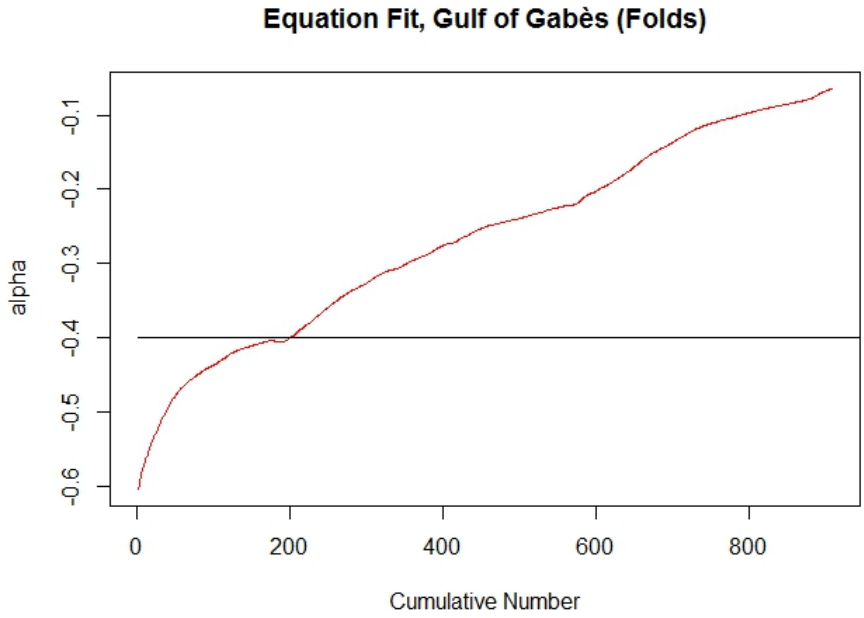

Figure 101: equation fit for the Gulf of Gabès fold data set

The Gulf of Gabès fold data set also produces values similar to those of the Gulf of Mexico fold data set. There is a very small agreement in exponent values using the equation fit (figure 101) between 1-200 data points which are in the left-hand tail of the data set. Comparing this to the moving window results (figure 94) there is a peak in the power law distribution however it only reaches a p-value where the distribution can be accepted at one point. On the whole, this portion of the data set demonstrates the highest p-value from the moving window results.

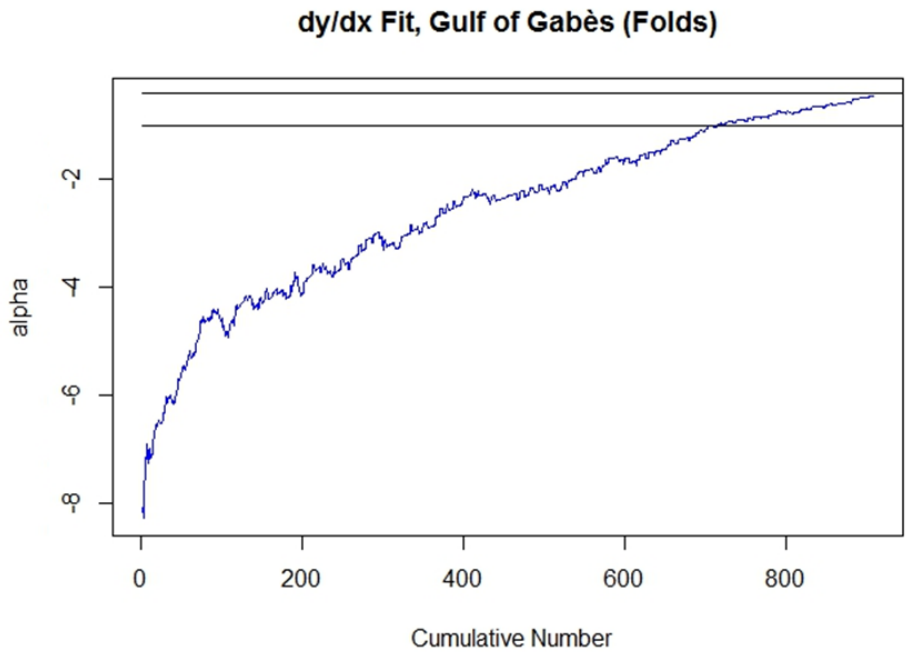

Figure 102: differential fit for the Gulf of Gabès fold data set

The differential fit (figure 102) for this data falls between approx. 700-900 data points which make up the left-hand tail of the data. Again, comparing this to the moving window results in figure 94, although the power law does not demonstrate a p-value above the 0.8 marker set for the project, it does peak in comparison to the rest of the distribution as it did in the left-hand tail of the data.

5.6 Moving window tests on smoothed datasets

The LOWESS function as explained in appendix 3 produces a smoothed version of the data set from which it was generated. Although this cannot be used to replace the raw data gathered from the one-dimensional multiline surveys they can be used as a tool to make it clearer which distribution dominates over all.

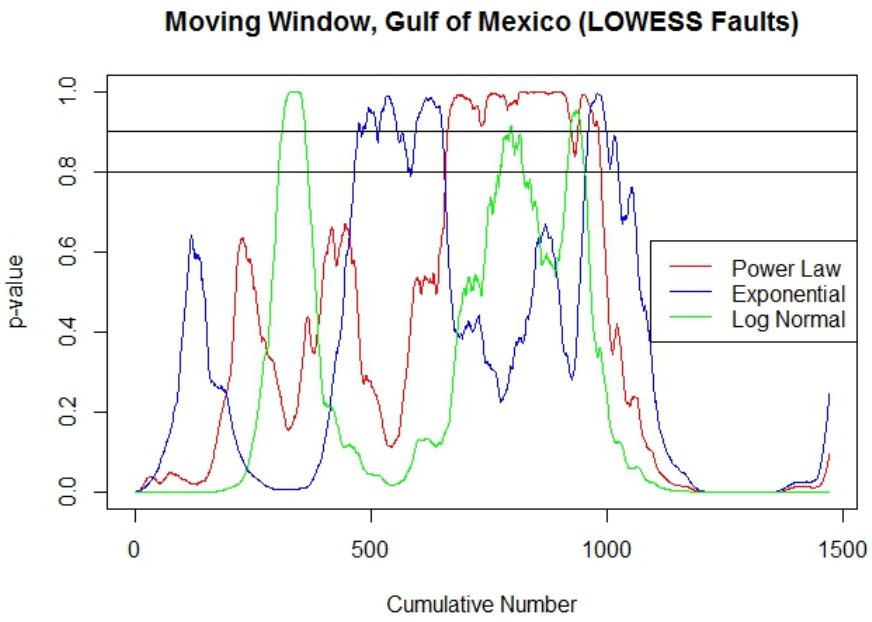

Figure 103: Gulf of Mexico faults LOWESS faults moving window

For the Gulf of Mexico faults, the LOWESS moving window results (figure 103) demonstrate the expected left- and right-hand tails where the p-values are significantly less than 0.8. The middle portion of the results between about 250-1000 data points show a good fit for a log-normal distribution, then exponential and finally power law. The power law spans most of the middle portion between approximately 600-1000; this satisfies throw values in the range of 50-160m. This range of throw values also falls between the values quoted previously (50-300m) for the straight-line segment of the power law distribution (figure 85b).

Compared to the moving window results for the raw fault data (figure 87) there are the two peaks of good fit at about 250 data points, and the second at 1000. These mark the edges of the overall section in the moving window from the LOWESS moving window (figure 103). This demonstrates that when smoothed by the LOWESS function, the data still retains its previous distribution characteristics producing results in the expected region which are geologically possible. As the LOWESS function smooths the data to a polynomial of best-fit, it could be hypothesised that the distribution which dominates in this data is the distribution that would dominate overall.

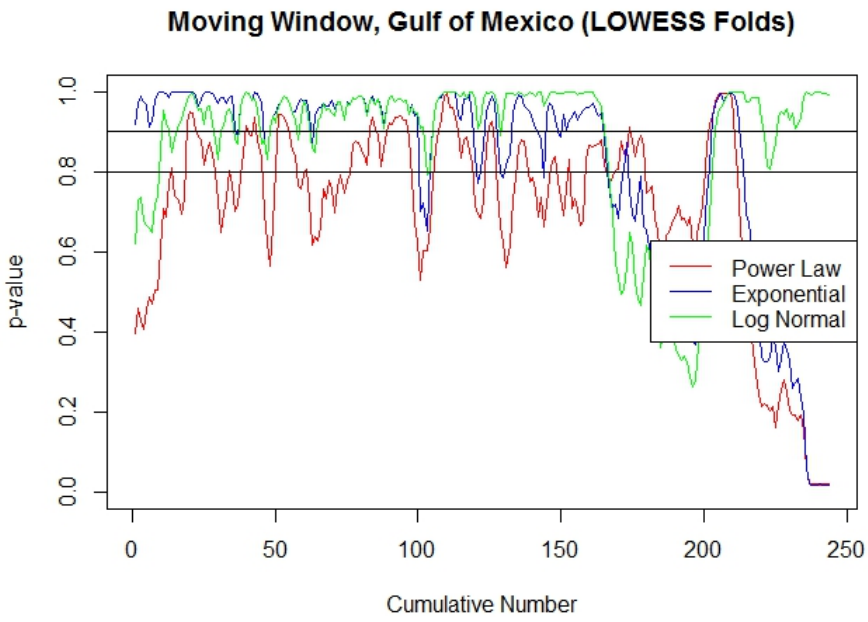

Figure 104: Gulf of Mexico folds LOWESS folds moving window

The Gulf of Mexico fold data (figure 90) initially showed a good fit for all the distributions with very little to distinguish between them. When smoothed with the LOWESS function it produces an even better fit for the data (figure 104). However, like the initial results it still is not possible to distinguish between the different distributions. Despite this, it still supports the idea that the smoothed data will provide a better fit for the data highlighting which distributions dominate. Although there is little to distinguish between the tested distributions, throughout all the distributions the p-value generally remains consistent however there are observed decreases in the p-value in range 150-200 which is within the middle portion of the data.

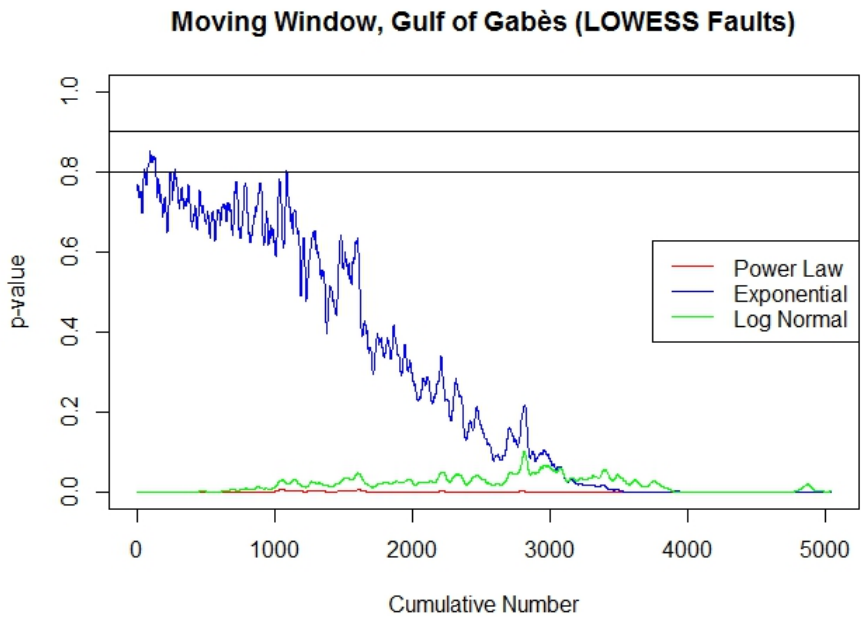

Figure 105: Gulf of Gabès faults LOWESS faults moving window

Unlike the previous examples, the moving window for the LOWESS data (figure 105) for the Gulf of Gabès does not produce smoother or similar results to that of the moving window on the raw data (figure 92). The results produced from the LOWESS data set do not appear characteristic of the moving window results generally acquired. The LOWESS data set for the Gulf of Gabès includes many very small values. When logged, these values produce `NaNs` (not a number) in the results which significantly alters the LOWESS data in comparison to the raw data ultimately making the data sets incomparable. This is the most likely cause of the uncharacteristic results, both to the expected results for the data set and also for the moving window.

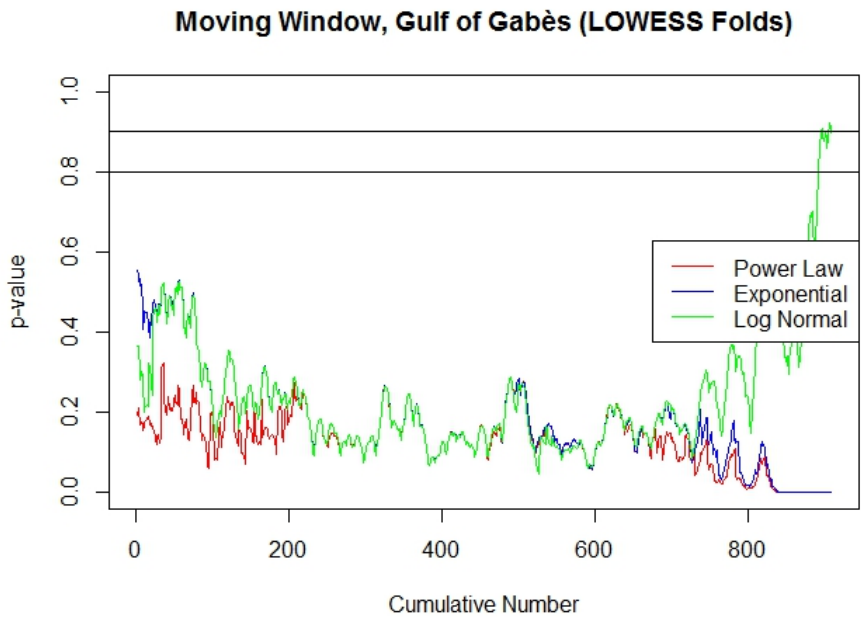

Figure 106: Gulf of Gabès faults LOWESS folds moving window

The associated folds to this data set do not suffer from this problem, and instead demonstrate results similar to what occurred in the Gulf of Mexico fold data set. In the initial moving window results for the raw data (figure 94) the distributions are indistinguishable from each other. However, unlike the Gulf of Mexico fold data where there was an improved fit for the distributions, there is a worse fit with lower p-values for the Gulf of Gabès fold data.

Although the results from the moving window on the LOWESS code (figure 106) did not always show an improvement in results, it does not necessarily suggest that there is an error or inaccuracy in the code. What it does suggest however, is that where there was not a good fit for any distribution it is likely that the data is determined by a different distribution which has not been tested by the moving window.

5.7 Analysis of two-dimensional fault length data

The same methods described above were carried out for a two-dimensional data set however it is important to note that the data sets were significantly smaller and as a result of this, these preliminary results may not be entirely representative of what would be expected from a more complete data set.

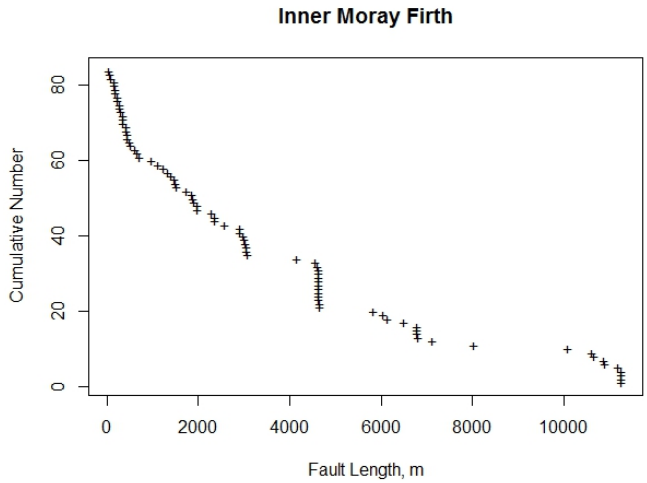

a, linear

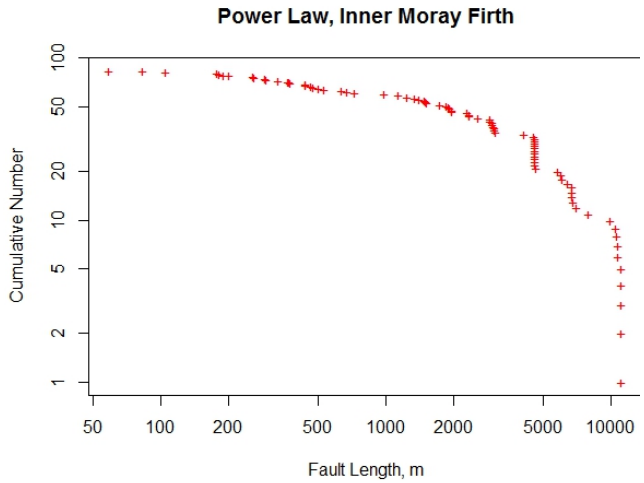

b, power law

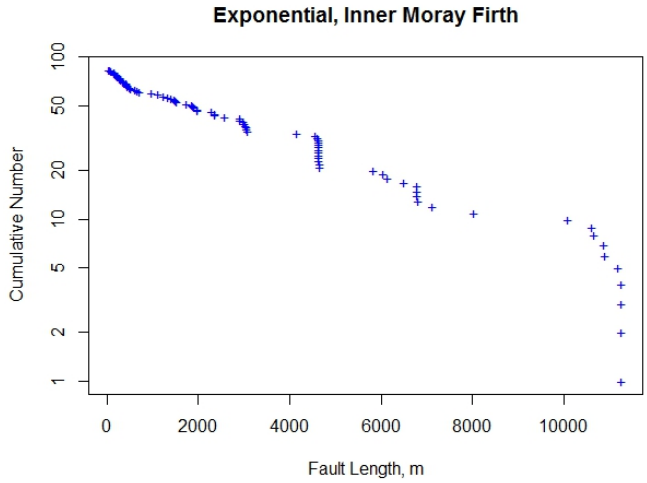

c, exponential

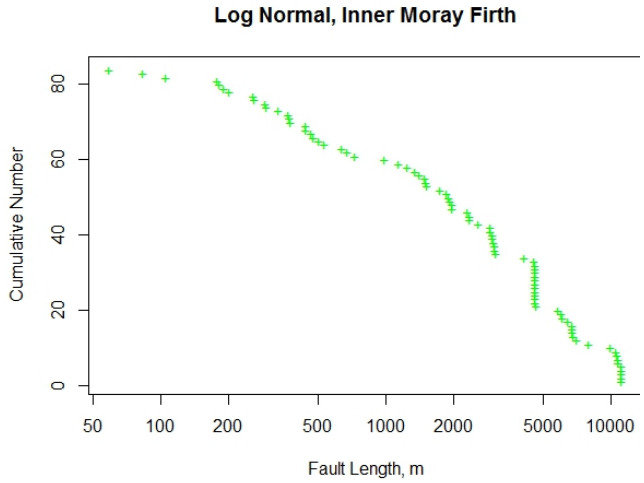

d, log normal

Figure 107: Inner Moray Firth fault distributions graph

The Inner Moray Firth fault length data were plotted on linear-linear axes (figure 107a), log-log axes (figure 107b), log-linear axes (figure 107c) and linear-log axes (figure 107d) to provide initial,

visual tests for linear, power-law exponential and log-normal distributions, respectively. The overall shape of the graphs mimic the shapes gained from the other (one-dimensional) fault data sets. Due to the lack of data points, the results are not smooth like they were previously and instead there are very large and distinctive steps in the data.

In figure 107a, the data form a gentle curve with a steep left-hand tail and a largely shallow right-hand tail. The power law graph forms a straight-line section in the range of 2000-9000m with a characteristic left- and right-hand tail either side of this. Neither the exponential nor log-normal distribution show a characteristic straight-line section that would be expected for a distribution fit which is most likely as a result of the lack of data points. However, the exponential distribution fit does demonstrate a straight-line between 1000-3000m in the left-hand tail of the data. It could be possible to extrapolate this line onwards to 9000m, however because of the steps in the data it's difficult to say for sure whether this straight-line would be an accurate observation.

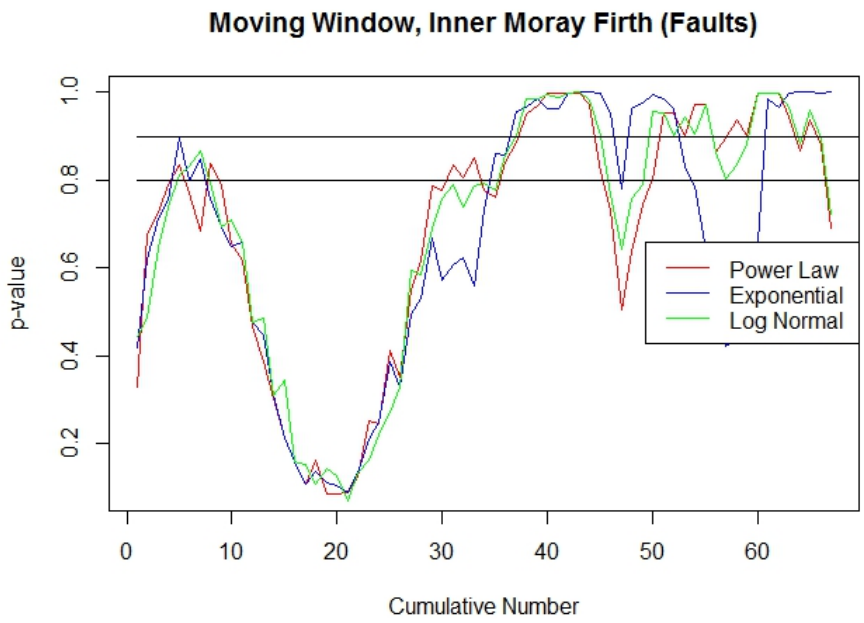

Figure 108: moving window with an Anderson-Darling test for the Inner Moray Firth faults data set

When considering the moving window results (figure 108) the first portion of the graph up to approximately 35 (on the cumulative number axis) shows no distinction between the three distributions and they form a sine like curve for one and a quarter wavelengths. During this portion of the data there are only two points which exceed 0.8, the first at 5 and the second at 30. After these points the results lie almost consistently above 0.9 with all the distributions dropping off at just before 50 and the exponential dropping off just before 60.

On the whole it would appear that the power law or log-normal distribution dominates this data set, and on the basis of the initial distributions it seems more likely to be dominated for a power law than a log-normal distribution. However as has been previously stated this data set may not be large enough to produce results which give a complete over view of the fault population.

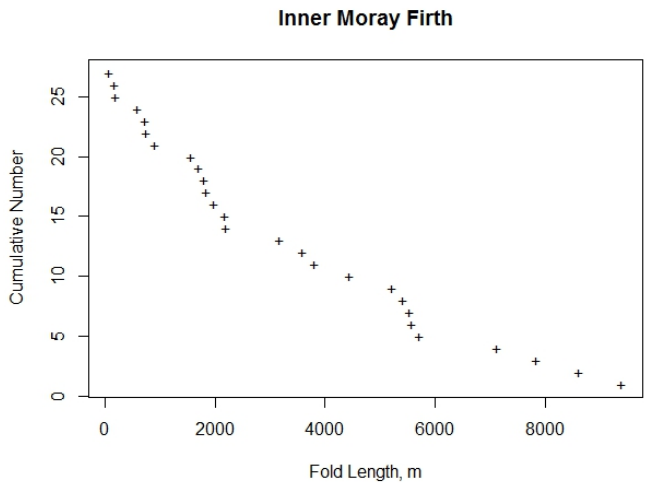

a, linear

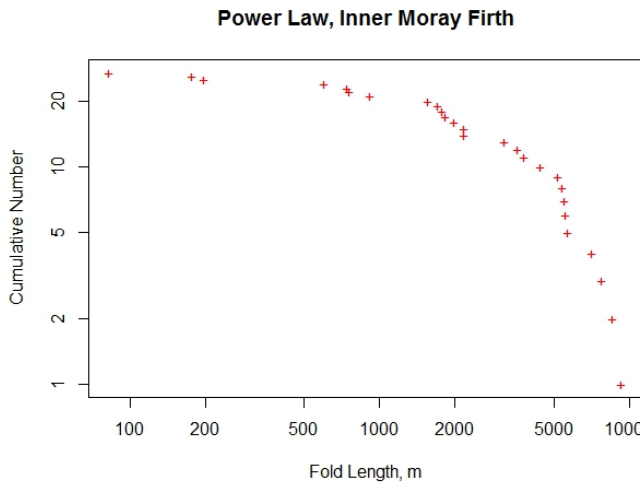

b, power law

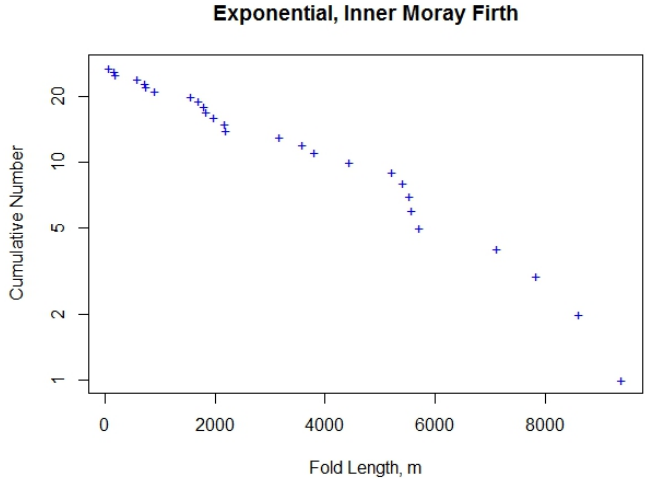

c, exponential

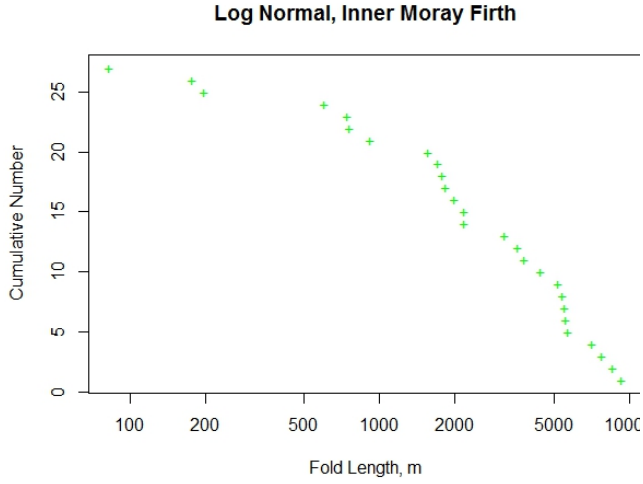

d, log normal

Figure 109: Inner Moray Firth folds distribution graph

Moving onto the fold data for this data set this problem will be further exaggerated as the data set contains even fewer data points. The linear distribution graph shows the same large steps (figure 109a) that the fault data demonstrated. As a result of this it is hard to identify a characteristic straight-line section which usually indicates a distribution fit.

The power law distribution (figure 109b) shows a gentle curve where left- and right-hand tails are visible however where a straight-line would usually be identified still forms a distinctive curve. The exponential distribution (figure 109c) appears to form a straight-line fit throughout the graph, although due to the large steps in the data it is not completely clear. The log-normal distribution

(figure 109d) like the power law graph does not have a characteristic straight-line section, but instead arguably forms two straight-lines on the left- and right-hand side of the data which can be interpreted to be extensions of the tails.

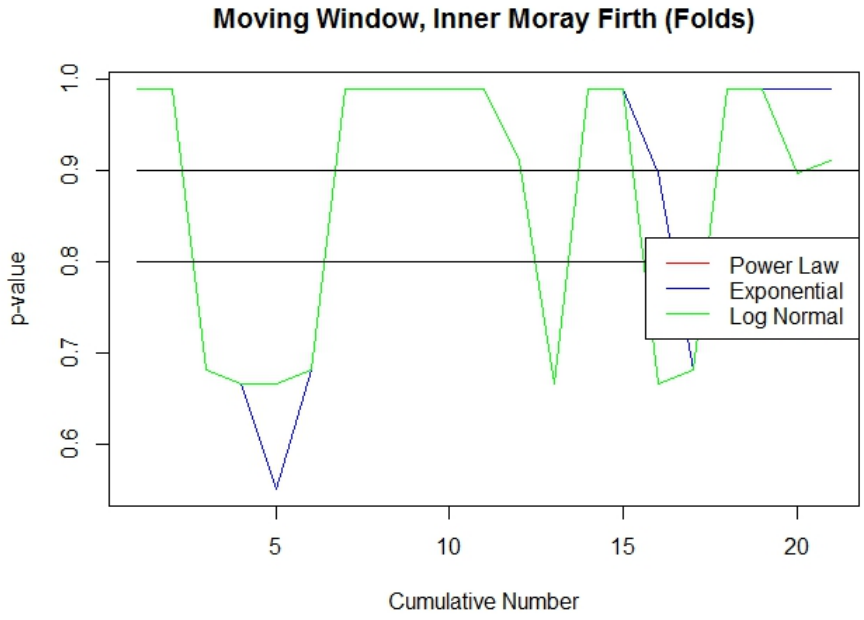

Figure 110: moving window with an Anderson-Darling test for the Inner Moray Firth folds data set

The moving window for these data, in previous examples would have been used to shed some light on the dominant distribution. However, due to the lack of data points, the results from the moving window (figure 110) are largely inconclusive. Although showing areas where distributions fit, the results do not appear as complete and rigorous as they do in other data sets and the lack of data is evident. Although not clear on the graph as the distributions are overlain, the distribution p-values lie directly over each other. Places where different distributions can be identified are where they deviate from the shared trend, but the overall results are identical for each distribution making it very difficult to identify which distribution dominates over another.

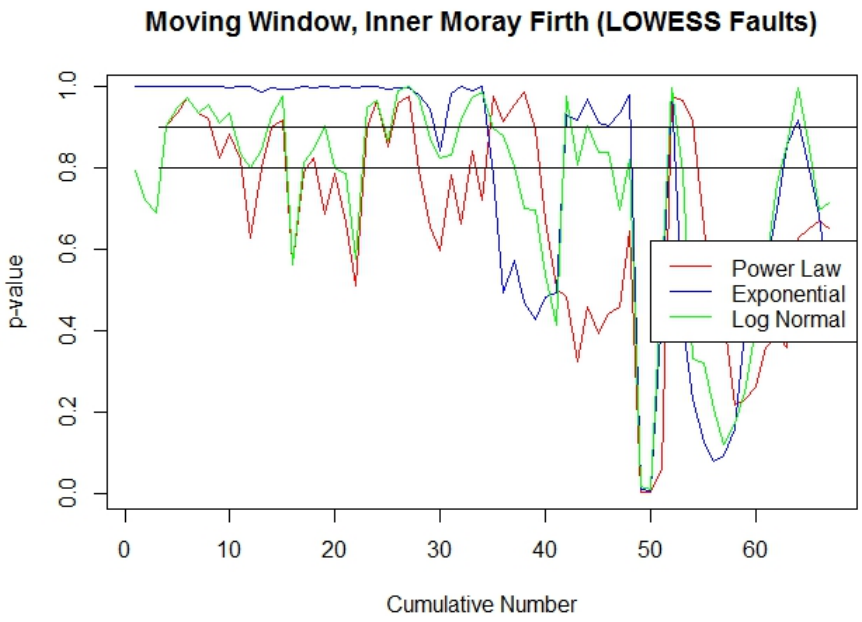

Figure 111: Inner Moray Firth fault throws LOWESS moving window

Comparing these moving window results to the results gained when using a LOWESS data set there is a vast improvement in the fault results as can be seen in the comparison of figure 108 and figure 111. From the LOWESS results it seems likely that an exponential distribution may dominate as this sits at close to 1 for the first portion of the data, it does drop off in the range 35-40 but picks back up to 50 where all of the distributions drop below the 0.8 p-value.

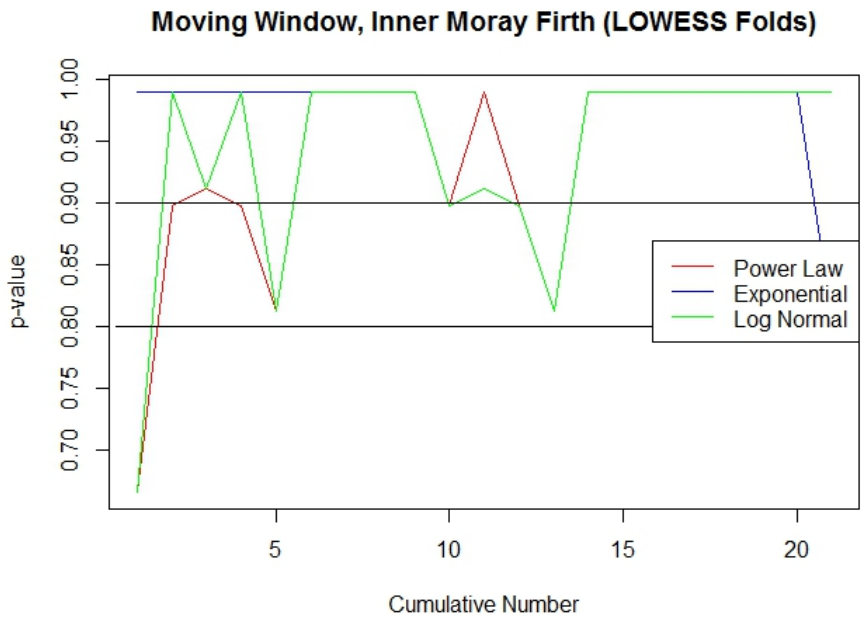

Figure 112: Inner Moray Firth folds LOWESS moving window

The comparison between the moving window results for the fold data (figure 110 and figure 112) are improved, but still appear to be dominated by the lack of data points making the results gained from this test difficult to assess as there is a lack of information.

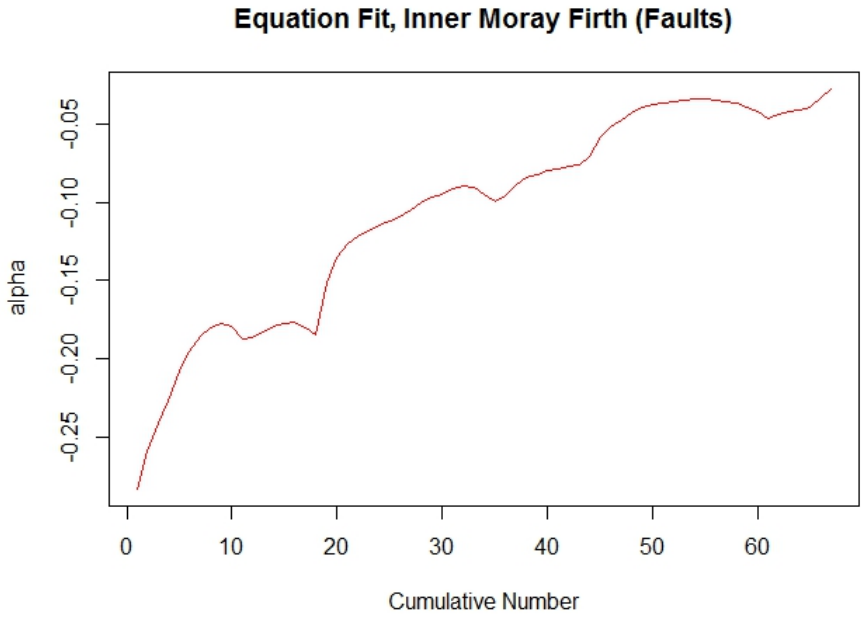

Figure 113: equation fit for the Inner Moray Firth faults data set

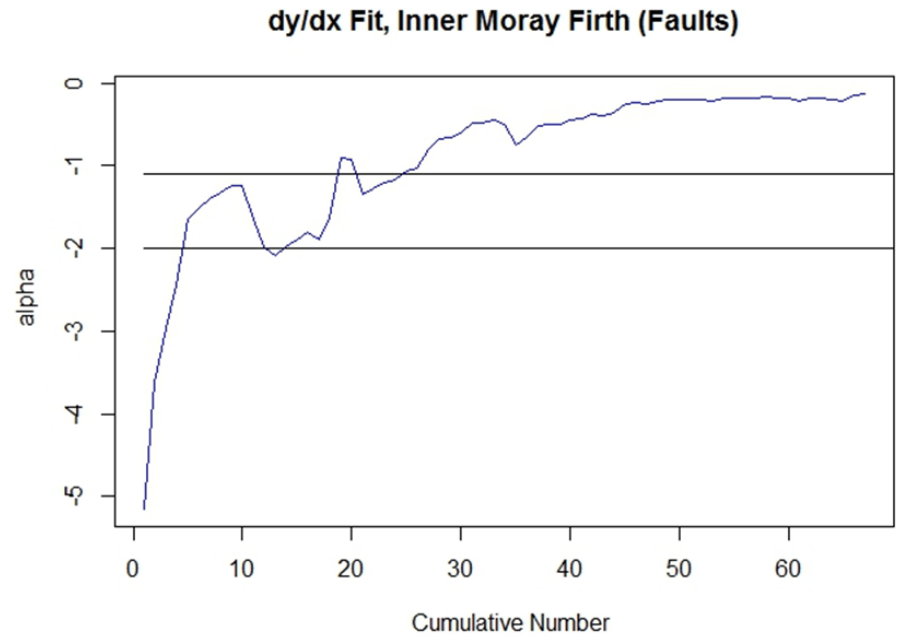

Figure 114: differential fit for the Inner Moray Firth faults data set

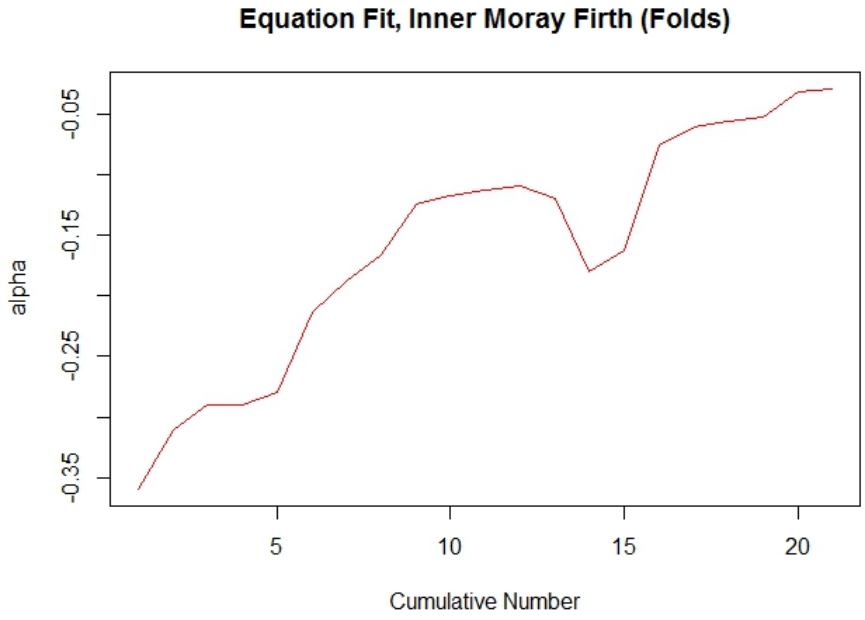

Figure 115: equation fit for the Inner Moray Firth folds data set

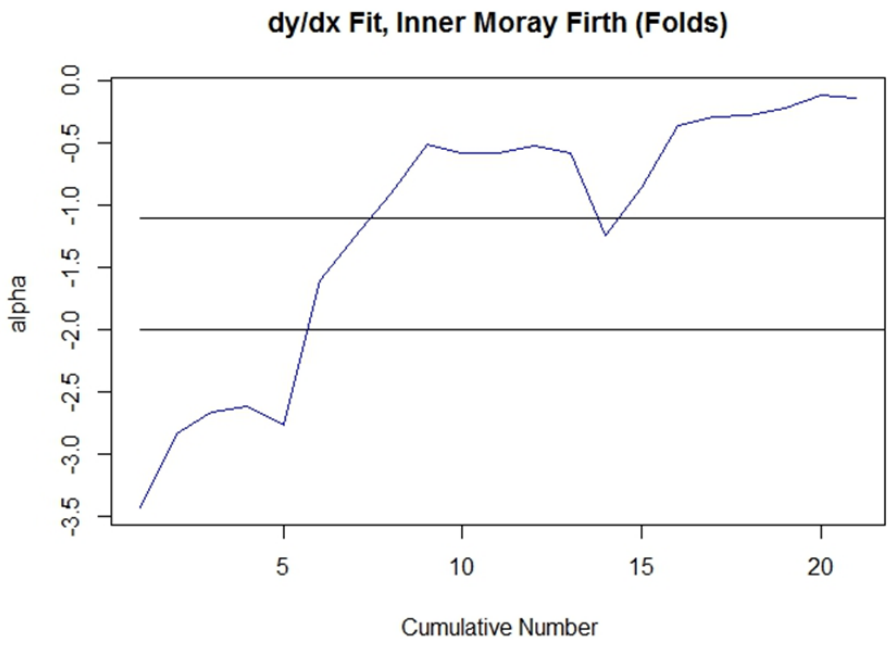

Figure 116: differential fit for the Inner Moray Firth folds data set

As with the equation fit (figure 113 and 115) in the previous examples the values produced are too small to lie in the expected values. However, the differential method (figure 114 and 116) does produce portions of the data within the range expected for a two-dimensional survey (-1.1 to -2.0).

For the fault data this falls in the range 2-20 cumulative number, which does not signify a significant power law fit in the moving window for the raw data. For the fold data this is between the values 6-8 cumulative number, which according to the moving window results does fall in line with a power law fit.

As a result of the small data sets from the Inner Moray Firth the fits assessed for each of the distributions (power law, exponential and log-normal) and for the exponent value the results must be treated with caution.

6. Discussion

The results of the Gullfaks test of methodologies show the validity of the primary data acquisition techniques used in this project, i.e. extracting fault throw and fold amplitude data along 1D sample lines in TrapTester and Petrel. The results produced indicated that there is qualitative agreement between published fault throw datasets and those gained by TrapTester (and Petrel).

6.1 One-dimensional multiline methodology and results

The results produced by the one-dimensional multiline sampling survey show consistency between the different methods used (cumulative frequency curves, moving window, exponent value and LOWESS results). The straight-line sections of the cumulative frequency graphs showed agreement with the moving window results. The range within which the well-constrained power law the exponent value occurred was as expected range for this type of survey providing further confidence in the methods. It is therefore justifiable to draw overall conclusions from the results of this investigation into scaling relationship between fault-related folds and their associated faults (table 6).

The Gulf of Mexico fault and fold data may have been derived from similar distributions, or in part from the same distribution. This is thought to be the case because of the identification of straight-line portions of the distributions curves, which could also be identified in similar places in the moving window results. Although it is difficult at this stage to assess exactly which distribution the data is derived from it is possible to assess whether they are likely to be derived from the same distribution by producing histograms. The histograms confirm the initial ideas that the data sets are distributed in a similar way as they both demonstrate the same distribution, skewed towards the left.

The Gulf of Gabès data showed a significant difference in the results produced by the cumulative frequency distribution and moving window results when treated in the same way to the Gulf of Mexico data. The histograms produced significantly different results, with the fault data being heavily skewed to the left and the fold data appearing to be closer to a normal distribution.

6.2 Two-dimensional multiline methodology and results

The analysis of the two-dimensional survey data was less comprehensive and the results are relatively inconclusive in comparison to the one-dimensional analysis. Despite a lack of data in this survey, the results are still able to give an indication that the fault and fold data are not derived from the same distribution. More data need to be analysed before definitive conclusions should be drawn. Despite this lack of data there are good indications that the use of the same methodologies used for the one-dimensional survey and the two-dimensional survey are accurate. The moving window code and the results of the histograms demonstrated the same differences and similarities between data sets.

Like the Gulf of Gabès data, it appears that the distribution graphs, moving window and histogram results from the Inner Moray Firth data set are derived from different distributions for the faults and fault-related folds. However, these histogram results identified the folds to be skewed to the left and the faults to be more normally distributed.

It is important to note the similarities in the distribution curves for the faults and the folds regardless of the data set they belong to. There is a strong correlation between curve shapes in

the fault data, and this was mirrored in the curve shape for the fold data. This is largely noted throughout all of the data sets.

The same can be said for the results of the moving window. Although the corresponding results were not identical, there is a clear distinction between results produced by faults and those produced by folds. The fault results generally showed portions in which only one of the distributions dominated over another, there was also some evidence of left- and right-hand tails as well as the middle portion of the data where the distribution is classically thought to fit. The fold data on the other hand showed very little distinction between the distributions as the curves, followed almost exactly the same lines as the others.

6.3 Scaling law distribution similarities between fault-related folds and their associated faults

The faults in the Gulf of Mexico data dip at an angle around 60° on average, according to Withjack et al., 1990 faults propagating at this angle can be expected to produce fault-related folds which don't fail after only a small amount of slip. As well as this the overall sedimentology of the Gulf of Mexico, especially in the areas where fault-related folding will occur are ductile which will preferentially promote folding instead of faulting. It is not possible to determine the bed thickness at this time, however the evidence so far suggests that where folding Is the preferential form of deformation the faults and fault-related folds may be distributed in the same way.

The faults in the Gulf of Gabès data dip at an angle around 70-80° on average. Similarly, to the Gulf of Mexico this angle of faulting is experimentally known to produce fault-related folds (Withjack et al., 1990). Compared to the Gulf of Mexico however this dip angle can experience a

larger amount of slip before the fault-related fold faults. Unlike the Gulf of Mexico however the overall sedimentology of the Gulf of Gabès, especially in the areas where fault-related folding will occur is brittle which will preferentially promote faulting regardless of the dip angle of the faults.

Considering the dip angle and sedimentology of the Inner Moray Firth the faults dip around 70° which allows fault-related folds to propagate (Withjack et al., 1990), and the lithology is a mix of brittle and ductile materials which are generally unconsolidated. This means that the sediments are more able to deform by ductile deformation than a purely brittle substance would be able to. As a result of this it can be assumed that fault-related folds should be able to propagate. Given the evidence form the Gulf of Mexico and Gulf of Gabès one would expect that the fault-related folds would be distributed in a similar way to their underlying faults. However more data is needed for these data sets before any conclusions can be made.

The results from the histograms suggest that the data sets are distributed by two different distributions and so it could be that where folding is not the preferential deformation mechanism the faults and fault-related folds will not be distributed in the same way. It may also be possible to suggest that between the dip angle and sedimentology the sedimentology is a more dominant control on how the fault-related folds are distributed with respect to their underlying faults.

From this it appears that fault-related folds do not necessarily follow the same distribution as their associated faults. From the results derived, there was only one instance where the faults and fault-related folds may potentially share the same scaling distribution (Gulf of Mexico) although it would require further investigation to fully assess this similarity in distribution. It was clear from the Gulf of Gabès results that the fault-related folds did not follow the same distribution as their associated faults.

Overall, the results gained from the fault-related folds appear not to be a product of any of the tested distributions (i.e. power law, exponential or log-normal) but may be derived from a different distribution. Some of the reasons for these differences are likely to reside within the effect of local sedimentology and dip angle of the fault population.

6.3.1 Fault-related fold development and reasons for distribution scaling law differences

Folds are heavily controlled by the lithology in which they deform. If the lithology is dominated by brittle rock then this limits the maximum fold amplitude that can be reached (Ferrill et al., 2006; Stearns, 1978; Laubscher, 1982; Patton, 1984; Withjack et al., 1988, 1989). Brittle lithologies favour faulting as a deformation style and will only allow for small folds to deform before they fracture and folding ceases. The consequence of this rheological behaviour is a large amount of very small fold amplitude values can be measured meaning that there will be very few larger values, if any.

On the other hand, a less competent, more “ductile” lithology (such as shale or evaporite) will encourage fault-related fold propagation and allow much larger fold amplitudes before faulting takes over and folding ceases (Ferrill et al., 2006; Stearns, 1978; Laubscher, 1982; Patton, 1984; Withjack et al., 1988, 1989). This will result in a much more even distribution of fold amplitude values ranging from small values where fault-related folding has just begun, to much larger values just before a fault-related fold is faulted.

As well as the surrounding lithology, fault-related folding is heavily controlled by the bed thickness. A thicker bed will accommodate more folding before the fault propagates through it. A thinner bed will be unable to accommodate as much folding, and will cease at lower fold amplitudes than a thicker bed. Based on seismic observations, it can be assumed that within individual study areas, bed (or, more precisely, reflector) thickness will remain constant and will not suffer from a significant amount of localised difference in bed thickness.

The dip angle of the underlying faults has a significant influence on the fold amplitude. It has been shown (Withjack et al., 1990) that if faults dip at high angles large fold amplitude can be propagated through it before the folding ceases. If the faults dip at low angles then only small fold amplitudes can be achieved before folding ceases.

A result of this behaviour is that fault-propagation folds will reach a certain amplitude beyond which they cannot increase further in size (unless subsequently modified by fault-bend folding; Lăpădat et al., 2016), and are more restricted than the faults. A fold will reach a point where it will no longer be able to deform under ductile deformation. At this point it will fault as the stress/strain on it has reached a point large enough to deform the rock by brittle deformation. Folds are also constrained by the overburden. A fault on the other hand, once the stress/strain on it has deformed the rock by brittle deformation, the throw on the fault is then primarily constrained by the mechanical properties of the wall rock (Watterson, 1986; Barnett et al., 1987). Generally, a fault is much less throw limited than a fold is amplitude limited.

Furthermore, a fault-related fold population deformed by faults dipping at a low angle and in a brittle lithology will demonstrate a significantly different distribution to a fault-related fold population deformed by faults dipping at a high angle within a more ductile lithology. In

comparison to the distribution of the related fault system it is likely that in some situations the scaling distributions are the same. This will not be the case for all populations and each will need to be considered independently of the associated fault populations or another fault-related fold population.

6.3.2 Faults distributed by a power law?

What can also be considered from the previously presented results is whether faults actually follow a power law distribution as is currently widely accepted (Yielding et al., 1996; Watterson et al., 1996; Nicol et al., 1996; and Fossen and Rørnes, 1996). It is believed that populations are generally formed of many sub-populations, which follow a power law distribution. However, results from the moving window graphs and distribution graphs suggest that these sub-populations may be distributed by a power law distribution, but are also likely to be controlled by other distributions such as an exponential or log-normal.

6.4 Impact of window size in the moving window test and code sensitivity

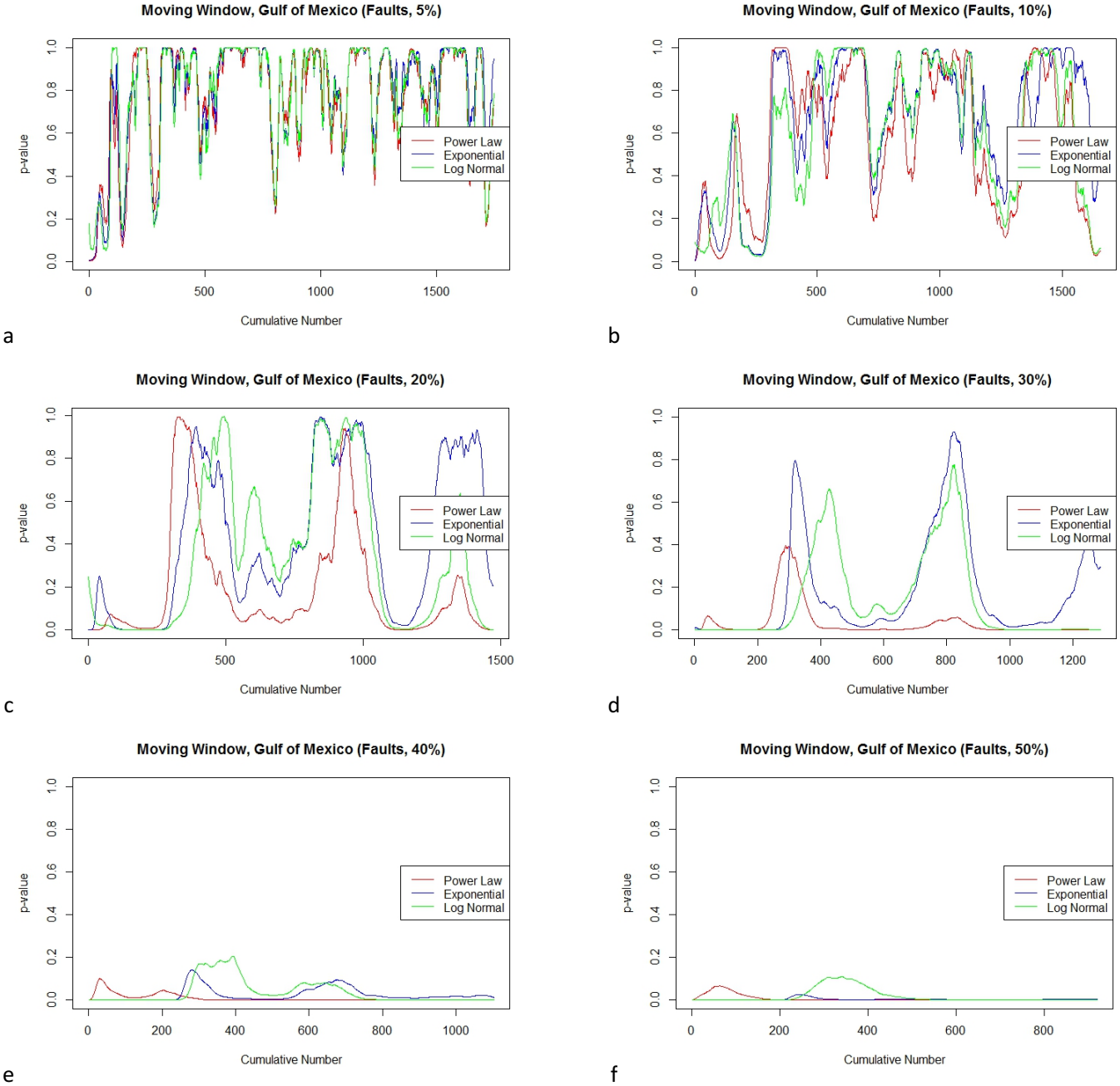

Figure 117: graphs illustrating the impact that a different window size in the moving window will have on the results (data set used is the Gulf of Mexico) a; window size 5% of data points b; 10% c; 20% d; 30% e; 40% f; 50%

Another controlling factor on the results produced from the moving window test, is the size of the window which is set. Figure 117 below illustrates the results gained when the window size is progressively changed from 5% to 50% of the size of the data set. For example if the size of the data set were 100 the 5% window would include 5 points and the 50% window would include 50 points.

A very small window size will demonstrate a very good fit for all distributions tested as can be seen in figure 117a. This is similar to the results of the incremental window in the left-hand tail where the window size was too small for it to be effectively assessed. Similarly, a window size which is very large such as in figure 117f the data will not fit any distribution especially well, this was also noted in the incremental window when it contained a large portion of the data. When the window size is set at 30% (figure 117d), 40% (figure 117e) and 50% (figure 117f) it appears that this is quite large and the data are unable to be accurately assessed. It equally appears that a window size of 5% (figure 117a) and 10% (figure 117b) is too small and results do not show any significant separation between the tested distributions.

When selecting the correct window size it is also necessary to ensure that the window size used covers at least one order of magnitude in order that the exponent can be established more accurately. In selecting the correct window size you must consider whether or not the window size will be spanning a sufficient amount of data, as well as if the data that it covers occupy at least an order of magnitude. This will therefore vary depending upon the sample size and also the order of magnitudes with which the data spans. It may be that in situations where it is a sparse data set with values spanning a large number of orders of magnitude that this method will not work. This was the basis for how the window size was selected, although for the Inner Moray Firth an issue was posed by the lack of data in it.

Although a window size of 20% has been used throughout the study it may have been appropriate to use a different window size for the Inner Moray Firth data set. Although with this data set it may have been appropriate to analyse it in a different way. It may also be better to use a range of window sizes on a study so that the variation on the results can be viewed to see if there is a

distribution which fits consistently over a different range of window sizes where other distributions may have dropped off when the window size increased.

As well as the sensitivity to the size of the window the areas where the distributions overlap in the results needs to be addressed. It is most likely that in these situations the synthetic dataset generated by each distribution is a good-fit to the actual data set because of the exponent value implemented by each distribution in each fit. Therefore consideration should be given to the exponent values at each point on the graph and consider whether these are values which in terms of geology make sense.

6.5 Further work

In future, a database based on lithology and fault dip angle could be investigated to identify whether certain deformation styles are likely to produce fault-related folds with distinctive distributions. It is also clear looking at figure 117 that the window size has a significant effect on the results produced and this could be studied to find the optimum window size, without compromising on the results produced with under or over assessment.

7. Conclusions

The project code which has been implemented in this study has taken a statistical approach to assessing the scaling law distributions of fault and fault-related fold populations. This has been achieved by introducing the method of a moving window which scans over smaller portions of the data shifting along until the whole data set has been assessed. The benefit that this has is that the scaling distribution can be assessed in more detail throughout the data set, instead of trying to assess the data set as a whole. The ability to do so has proved invaluable in being able to assess the individual scaling properties of the data. It has also enabled the comparison between other scaling law distributions providing a visual representation for where certain distributions dominate over others.

This research was carried out in order to identify and assess the scaling properties of fault-related folds and their associated faults. This was thought necessary in order to determine whether the underlying fault population distribution governs the distribution of the overlying fault-related folds, developed as a consequence of the underlying faults.

At this stage of the research it can be assumed that the fault throw populations studied are comprised of a number of different distributions. However, from the analysis of the fault data, evidence of power law distributions can be found throughout the data. These findings correspond to, and strengthen the conclusions of Yielding et al., (1996), Watterson et al., (1996), Nicol et al., (1996) and Fossen and Rørnes (1996) that fault populations do satisfy a power law distribution. However, it is also necessary to highlight that there was an obvious presence of other distributions that were tested (exponential and log-normal). It could be that there is evidence of other distributions which were not tested.

Characterising fault-related fold data distributions is complex as there are a number of controlling factors on the size to which the fold amplitude can reach; such as, fault dip angle, bed thickness , lithology, and competence and more. When a tipline of a fault plane enters a bed with different mechanical properties it will display different degrees of folding. The consequence of this is that every fault-related fold population has to be assessed independently of any other in order to more accurately evaluate the scaling distribution.

Over time it may be possible, and would be beneficial, to build a knowledge base of what can be expected in different lithologies, bedding thicknesses and underlying fault dips in order to carry out preliminary characterisation of these data sets. However as with the fault data, it is not currently possible to say whether they fit a certain distribution as the controlling distribution will be widely variable throughout data sets, and between different data sets.

Therefore, it is possible to conclude that scaling distribution of fault-related folds are not necessarily dependent on the same scaling law properties as their associated faults. It is clear that they will be distributed independently of the underlying fault populations, but as an influence of their physical properties and the surrounding lithology.

Despite this, it should be possible to characterise the distribution of the fault-related fold populations by further development of the code in order to test more distributions. It may be necessary to produce a data frame in order to gain a complete understanding of this. Allowing knowledge of fault-related fold geometry to be fuller understood enables the possible implications of this research to come to light. On further study, it may become apparent that certain distributions dominate within fault-related fold populations developed in similar lithological settings and underlying fault dip-angle. Or it may become apparent that of the

mentioned controlling factors there are some which control the resultant distribution by more than others do.

It was previously stated that the ability to identify these scaling properties provided a powerful tool for predicting a variety of geological structures. It also enables fault growth prediction and extrapolation of fault sizes which exist below the resolution of seismic reflection data. In addition to the prediction of natural fault growth this can be applied to non-geologic processes which interact with the subsurface, such as mining or fracking, in order to predict the consequence faulting or resultant fault-related folding that could occur as a result of this.

As with any regime, over time the mechanical properties of the area will change and as a result so too will the fault-related folding. The results of this research are significant since it helps in the development of an in depth understanding of this relationship is important since these folds which form at the tipline of the faults are often the only exposed evidence available of the nature of the underlying fault. Therefore, a further developed understanding of this relationship can help in hydrocarbon exploration, to seismic risk evaluation and the fault mechanics.

Appendix 1

```
> xdata=as.vector(t(read.csv("GoMfaults.csv")))
> xrange=1:length(xdata)
> log_xdata=log(xdata, base=10)
> log_xrange=log(xrange, base=10)
```

A1.1 Incremental window code

A1.1.2 Kolmogorov-Smirnov Test

```
> n_size=100
> quick_pl_ks=function(n_size,log_xrange,log_xdata){
+ ly100=log_xrange[1:n_size]
+ lx100=log_xdata[1:n_size]
+ df100=data.frame(lx=lx100,ly=ly100)
+ l1=lm(ly~lx,data=df100)
+ pred100=data.frame(lx=mean(lx100))
+ predy=predict(l1,pred100)
+ preda=(log(predy)-log(l1$coefficients[1]))/mean(lx100)
+ f1=ks.test(df100$ly,fitted(l1))
+ return(c(preda,f1$p.value))
+ }
```

A1.1.3 Anderson-Darling Test

```
> n_size=100
> quick_pl_ad_ks=function(n_size,log_xrange,log_xdata){
+ ly100=log_xrange[1:n_size]
+ lx100=log_xdata[1:n_size]
+ df100=data.frame(lx=lx100,ly=ly100)
+ l1=lm(ly~lx,data=df100)
+ sl1=summary(l1)
```

```
+ pred100=data.frame(lx=mean(lx100))
+ predy=predict(l1,pred100)
+ preda=(max(df100[2])-min(df100[2]))/(min(df100[1])-max(df100[1]))
+ f1=ad.test(df100$ly,fitted(l1))
+ return(c(preda,f1$ad[1,3],sl1$r.squared))
+ }
```

A1.2 Moving window code

A1.2.1 Kolmogorov-Smirnov Test

```
> sh=0.2*length(xdata)
> quick_pl_ks_mw=function(a,b,log_xrange,log_xdata){
+ ly100=log_xrange[a:b]
+ lx100=log_xdata[a:b]
+ df100=data.frame(lx=lx100,ly=ly100)
+ l1=lm(ly~lx,data=df100)
+ pred100=data.frame(lx=mean(lx100))
+ predy=predict(l1,pred100)
+ preda=(log(predy)-log(l1$coefficients[1]))/mean(lx100)
+ f1=ks.test(df100$ly,fitted(l1))
+ return(c(preda,f1$p.value))
+ }
```

A1.2.3 Anderson-Darling Test

```
> sh=0.2*length(xdata)
> quick_pl_ad_mw=function(a,b,log_xrange,log_xdata){
+ ly100=log_xrange[a:b]
+ lx100=log_xdata[a:b]
+ df100=data.frame(lx=lx100,ly=ly100)
+ l1=lm(ly~lx,data=df100)
+ sl1=summary(l1)
```

```
+ preda=(max(df100[2])-min(df100[2]))/(min(df100[1])-max(df100[1]))
+ f1=ad.test(df100$ly,fitted(l1))
+ return(c(preda,f1$ad[1,3],sl1$r.squared))
+ }
```

A1.3 Functions to run code

A1.3.1 Incremental window

A1.3.1.1 Power law function

```
> test_out_inc=sapply(1:length(xdata),function(i){quick_pl_ad_ks(i,log_x
range,log_xdata)})
```

A1.3.1.2 Log-normal function

```
> test_out_inc_ln=sapply(1:length(xdata), function(i){quick_pl_ad_ks(i,
xrange, log_xdata)})
```

A1.3.1.3 Exponential function

```
> test_out_inc_exp=sapply(1:length(xdata), function(i){quick_pl_ad_ks(i,
log_xrange, xdata)})
```

A1.3.2 Moving window

A1.3.2.1 Power law function

```
> test_out_mov=sapply(1:(length(xdata)-
sh),function(i){quick_pl_ad_mw(i,i+sh,log_xrange,log_xdata)})
```

A1.3.2.2 Log-normal function

```
> test_out_mov_ln=sapply(1:(length(xdata)-
sh),function(i){quick_pl_ad_mw(i,i+sh,xrange,log_xdata)})
```

A1.3.2.3 Exponential function

```
> test_out_mov_exp=sapply(1:(length(xdata)-
sh),function(i){quick_pl_ad_mw(i,i+sh, log_xrange, xdata)})
```

A1.4 Plotting code

A1.4.1 Alpha

```
> plot(test_out_mov[1,], type="l", col="red", ylab="alpha",
xlab="Cumulative Number", ylim=c(0,1))
> lines(test_out_mov_exp[1,], col="blue")
> lines(test_out_mov_ln[1,], col="green")
> title(main="WINDOW CODE, DATA SET")
> legend("right", legend=c("Power Law","Exponential", "Log Normal"),
col=c("red","blue","green"), lty=c(1,1))
```

A1.4.2 P-value

```
> plot(test_out_mov[2,], type="l", col="red", ylab="p-value",
xlab="Cumulative Number", ylim=c(0,1))
> lines(test_out_mov_exp[2,], col="blue")
> lines(test_out_mov_ln[2,], col="green")
> lines(xrange,rep(0.8,length(xrange)))
```

```
> lines(xrange,rep(0.9,length(xrange)))
> title(main="WINDOW CODE, DATA SET")
> legend("right", legend=c("Power Law","Exponential", "Log Normal"),
col=c("red","blue","green"), lty=c(1,1))
```

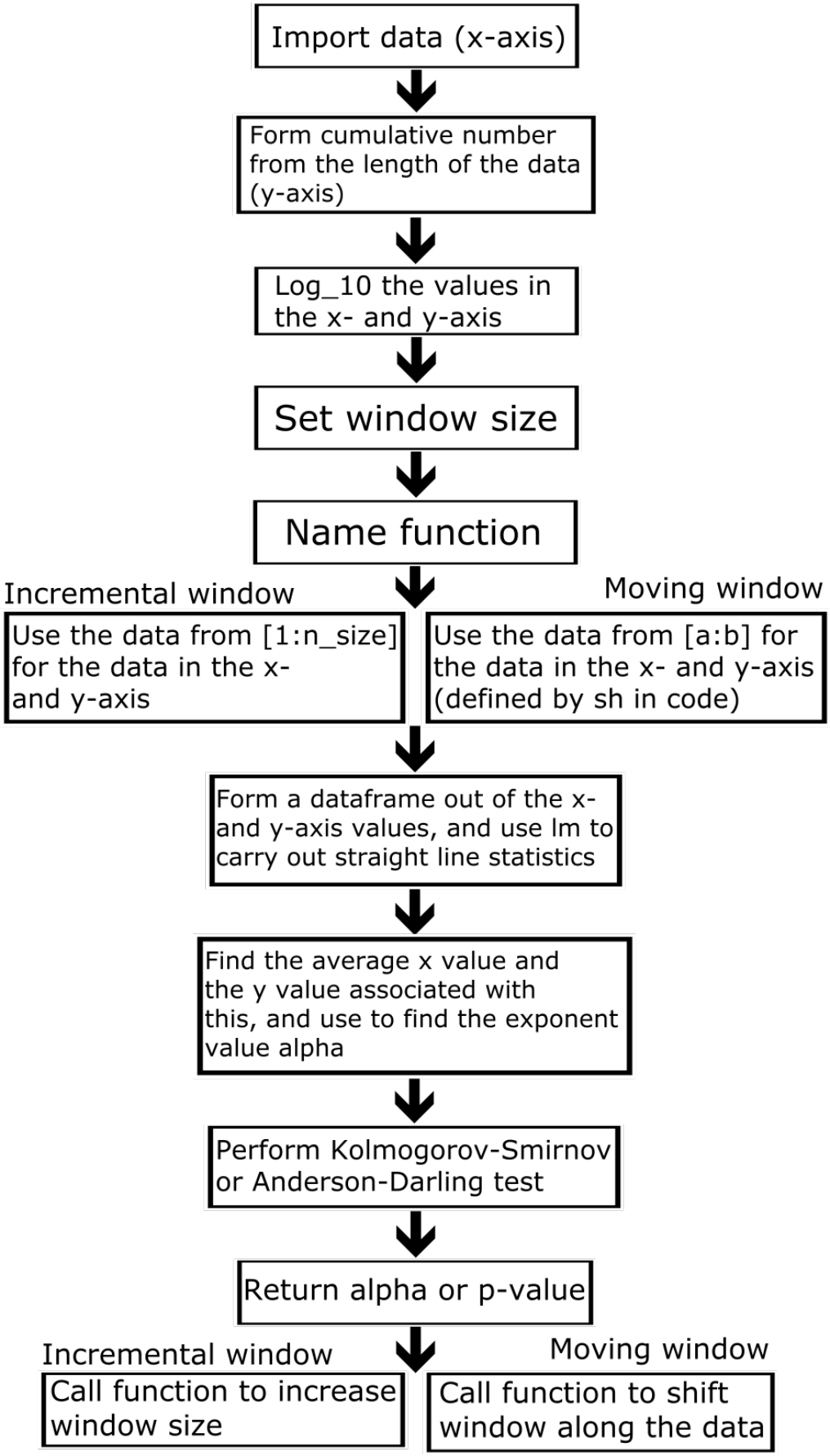

Figure 118: Flowchart showing how the code works

Appendix 2

A2.1 Comparison of methods developed in this study with those of Clauset et al. (2009)

Having two-dimensional data sets enables the use of code from Clauset et al (2009). This comparison was carried out for seven data sets quoted in the paper by Clauset et al (2009) for both Kolmogorov-Smirnov and Anderson-Darling tests. These data sets were run through the Clauset code, in addition to the code produced for this project. Below is a graph of the results for the Kolmogorov-Smirnov (figure 119) and Anderson-Darling test (figure 120).

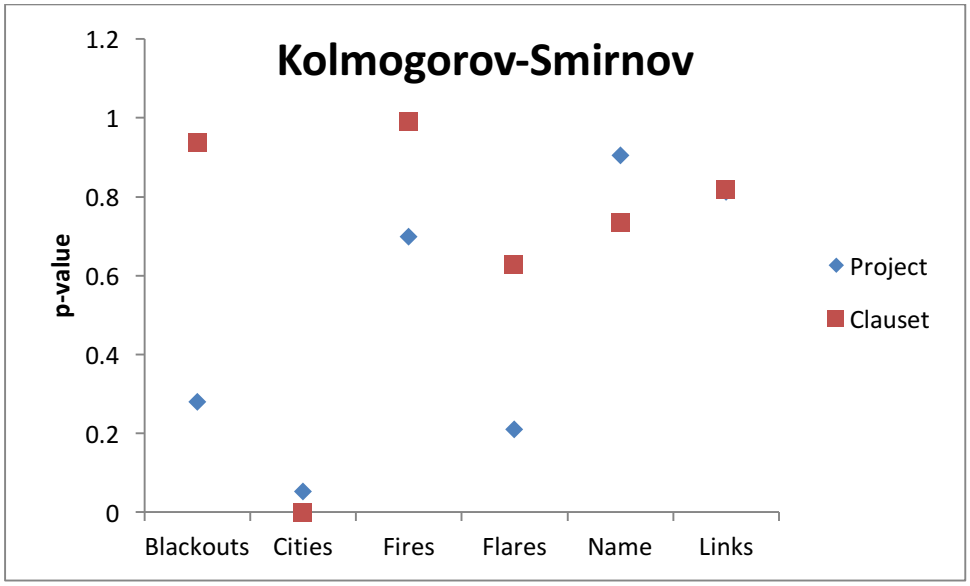

Figure 119: Kolmogorov-Smirnov test with arbitrary data sets

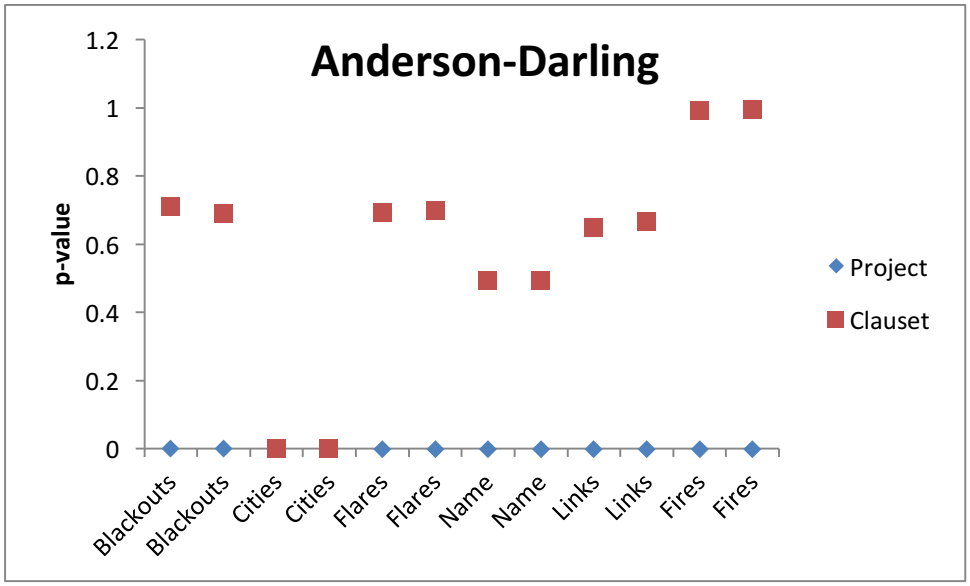

Figure 120: Anderson-Darling test with arbitrary data sets

The results of the Kolmogorov-Smirnov test (figure 119) show a mix of agreement between the different codes. For the first data set there is a poor agreement between the p-values for the Clauset code and the results generated for this project. The second data set on the other hand shows good agreement between the project code, and Clauset code. For the third and fourth data set there is no strong agreement between either of the codes. The Clauset code was not able to produce a value for the fires data set. The sixth data set doesn't show a good fit between the project code and the Clauset code. The final data set shows a better fit between the project and Clauset code.

For the Anderson-Darling test (figure 120) a two-sided result is produced, although in most cases each of the values are closely related to the first. The results produced by the project code all fall very close to zero, and no result could be gained for the third data set. Like the project code, the Clauset code was not able to produce a p-value on one occasion for the fifth data set.

The comparison between the project code and Clauset code showed a great deal of sensitivity in the p-value derived. The same sensitivity between methods is noted where in some data sets there were a good deal of variation in the exponent values calculated. These data sets, like the Inner Moray Firth data sets were small in comparison to other data sets used which produced results with less variation. Due to these issues in sensitivity it is necessary to consider the fact that these methods may need to be made more robust. Although the comparison of results for the distribution curves, moving window and histograms are good the results may not be repeatable with other similar methods.

A2.2 Web links to codes

Clauset et al., (2009) data sets; http://tuvalu.santafe.edu/~aaronc/powerlaws/data.htm

Clauset et al., (2009) code; http://tuvalu.santafe.edu/~aaronc/powerlaws/

A3 LOWESS

After carrying out the statistical analysis LOWESS function can be applied in R which is a locally-weighted polynomial regression, and acts to smooth the data input. Compared to classical methods like linear and nonlinear least squares regression. LOWESS builds on these providing a method to assess the situation in which classical methods are not robust enough to deal with (https://en.wikipedia.org/wiki/Local_regression, July 2016).

LOWESS performs a combination of a linear least squares regression which is often viewed to be much simpler, but with the freedom of a nonlinear regression which is commonly nonparametric. To achieve this LOWESS fits simple models to localised portions of the data in order to build up a picture of the entire data set to produce a function which best describes the determining portions of the data. It does this point by point, giving more weight to points near to the point whose response is being tested and less to points further away (https://en.wikipedia.org/wiki/Local_regression, July 2016). The thought behind this being that points surrounding the point being tested are most likely to be more simply related to each other compared to points much further away (Cleveland, 1981). The LOWESS fit finishes after the function has evaluated all the values in the data set.

The aim is to hopefully, by smoothing the data, demonstrate which of the distributions may dominate given the smoothing of the inherent noise sampled in natural populations. These noise values could affect the automated tests described previously and cause them to not represent the true distribution of the data. When noise is reduced it becomes easier to clearly indicate which distribution a data set might be long to.

Since we can't be sure that the LOWESS response has been modelled as opposed to the actual data the results from this have only been used as an indication towards what the likely distributions could be. As well as to assess whether it is in support of the actual data which is modelled.

References

Ackermann, R.V., Schlische, R.W. and Withjack, M.O., 2001. The geometric and statistical evolution of normal fault systems: an experimental study of the effects of mechanical layer thickness on scaling laws. Journal of Structural Geology, 23(11), pp.1803-1819.

Ackermann, R.V., Schlische, R.W., Patino, L.C. and Johnson, L.A., 2003. A Lagerstätte of rift-related tectonic structures from the Solite Quarry, Dan River/Danville rift basin. The great rift valleys of Pangea in eastern North America, 1, pp.118-133.

Aliev, M., Ait Laoussine, N., Avrov, V., Aleksine, G., Barouline, G., Lakov-lev, B., Korj, M., Kouvykine, J., Makarov, V., Mazanov, V. and Medvedev, E., 1971. Structures geologiques et perspectives en petrole et en gaz du Sahara Algerien. Sonatrach editions.

Allmendinger, R.W., 1998. Inverse and forward numerical modeling of trishear fault-propagation folds. *Tectonics*, *17*(4), pp.640-656.

Allmendinger, R.W., Zapata, T., Manceda, R. and Dzelalija, F., 2001. Trishear kinematic modeling of structures with examples from the NeuqueÂn Basin, Argentina. Thrust Tectonics Conference. *American Association of Petroleum Geologists, Special Publication*.

Anderson, T.W. and Darling, D.A., 1954. A test of goodness of fit. *Journal of the American statistical association*, *49*(268), pp.765-769.

Antonellini, M. and Aydin, A., 1994. Effect of faulting on fluid flow in porous sandstones: petrophysical properties. AAPG bulletin, 78(3), pp.355-377.

Baker Jr, E.T., 1995. Stratigraphic nomenclature and geologic sections of the Gulf Coastal Plain of Texas (No. 94-461). US Geological Survey; Earth Science Information Center, Open-File Reports Section [distributor],.

Baker, B.H., Mohr, P.A. and Williams, L.A.J., 1972. Geology of the eastern rift system of Africa. *Geological Society of America Special Papers*, *136*, pp.1-68.

Baker, E.T., 1977. Stratigraphic and hydrogeologic framework of part of the coastal plain of Texas (No. 77-712). US Geological Survey,.

Barnett, J.A., Mortimer, J., Rippon, J.H., Walsh, J.J. and Watterson, J., 1987. Displacement geometry in the volume containing a single normal fault. *AAPG Bulletin*, *71*(8), pp.925-937.

Barr, D., 1985. 3-D palinspastic restoration of normal faults in the Inner Moray Firth: implications for extensional basin development. Earth and Planetary Science Letters, 75(2-3), pp.191-203.

Barton, C.A. and Zoback, M.D., 1990. Self-similar distribution of macroscopic fractures at depth in crystalline rock in the Cajon Pass scientific drillhole. In Rock joints (pp. 163-170). Balkema Rotterdam.

Bell, J., Holmes, J. and Schoelen, J., 1970. West Cameron Block 180 Field: WEST CAMERON AREA OFFSHORE CAMERON PARISH, LOUISIANA.

Berg, R.R., 1976. Deformation of Mesozoic shales at Hamilton Dome, Bighorn Basin, Wyoming. AAPG Bulletin, 60(9), pp.1425-1433.

Bernard, S., Avouac, J.P., Dominguez, S. and Simoes, M., 2007. Kinematics of fault-related folding derived from a sandbox experiment. *Journal of Geophysical Research: Solid Earth*, *112*(B3).

Beutner, E.C. and Diegel, F.A., 1985. Determination of fold kinematics from syntectonic fibers in pressure shadows, Martinsburg slate, New Jersey.American Journal of Science, 285(1), pp.16-50.

Bishop, W.F., 1975. Geology of Tunisia and adjacent parts of Algeria and Libya. AAPG bulletin, 59(3), pp.413-450.

Blenkinsop, T., 1994. The fractal distribution of gold deposits: two examples from the Zimbabwe Archaean Craton. In *Fractals and Dynamic Systems in Geoscience* (pp. 247-258). Springer Berlin Heidelberg.

Bobier, C., Viguier, C., Chaari, A. and Chine, A., 1991. The post-Triassic sedimentary cover of Tunisia: seismic sequences and structure.Tectonophysics, 195(2), pp.371-410.

Bonnet, E., Bour, O., Odling, N.E., Davy, P., Main, I., Cowie, P. and Berkowitz, B., 2001. Scaling of fracture systems in geological media.Reviews of geophysics, 39(3), pp.347-383.

Boote, D.R., Clark-Lowes, D.D. and Traut, M.W., 1998. Palaeozoic petroleum systems of North Africa. Geological Society, London, Special Publications, 132(1), pp.7-68.

Bornhauser, M., 1958. Gulf coast tectonics. AAPG Bulletin, 42(2), pp.339-370.

Broder, A., Kumar, R., Maghoul, F., Raghavan, P., Rajagopalan, S., Stata, R., Tomkins, A. and Wiener, J., 2000. Graph structure in the web. *Computer networks*, *33*(1), pp.309-320.

Brown, R.N., 1980. History of exploration and discovery of Morgan, Ramadan and July oilfields, Gulf of Suez, Egypt.

Brown, W.G., 1988. Deformational style of Laramide uplifts in the Wyoming foreland. Geological Society of America Memoirs, 171, pp.1-26.

Burollet, P.F., (a) 1967. General geology of Tunisia. Guidebook to the Geology and History of Tunisia, pp.51-58.

Burollet, P.F., (b) Mugniot, J.M. and Sweeney, P., 1978. The geology of the Pelagian Block: The margins and basins off southern Tunisia and Tripolitania. In The ocean basins and margins (pp. 331-359). Springer US.

Burrough, P.A., 1981. Fractal dimensions of landscapes and other environmental data.

Burrough, P.A., 1984. The application of fractal ideas to geophysical phenomena. Bull. Inst. Math. and Applications.

Busson, G., 1967. Mesozoic of southern Tunisia. In Guidebook to the geology and history of Tunisia, Petroleum Exploration Society of Libya, Ninth Annual Field Conference (pp. 131-151).

Byerly, G. R., Igneous activity, in Salvador, A., 1991. Origin and development of the Gulf of Mexico basin. The gulf of Mexico basin, pp.389-444.

Cardozo, N., Bhalla, K., Zehnder, A.T. and Allmendinger, R.W., 2003. Mechanical models of fault propagation folds and comparison to the trishear kinematic model. *Journal of Structural Geology*, *25*(1), pp.1-18.

Cartwright, J.A., Trudgill, B.D. and Mansfield, C.S., 1995. Fault growth by segment linkage: an explanation for scatter in maximum displacement and trace length data from the Canyonlands Grabens of SE Utah. Journal of Structural Geology, 17(9), pp.1319-1326.

Childs, C., Nicol, A., Walsh, J.J. and Watterson, J., 2003. The growth and propagation of synsedimentary faults. *Journal of Structural Geology*, *25*(4), pp.633-648.

Childs, C., Walsh, J.J. and Watterson, J., 1990. A method for estimation of the density of fault displacements below the limits of seismic resolution in reservoir formations. In North Sea Oil and Gas Reservoirs—II (pp. 309-318). Springer Netherlands.

Childs, C., Watterson, J. and Walsh, J.J., 1995. Fault overlap zones within developing normal fault systems. *Journal of the Geological Society*, *152*(3), pp.535-549.

Chowdhury, A.H. and Turco, M.J., 2006. Geology of the Gulf Coast Aquifer, Texas. Texas Water Development Board Report, 365.

Clark, M.B., Brantley, S.L. and Fisher, D.M., 1995. Power-law vein-thickness distributions and positive feedback in vein growth. Geology, 23(11), pp.975-978.

Clauset, A., Shalizi, C.R. and Newman, M.E., 2009. Power-law distributions in empirical data. *SIAM review*, *51*(4), pp.661-703.

Cleveland, W.S., 1981. LOWESS: A program for smoothing scatterplots by robust locally weighted regression. The American Statistician, 35(1), p.54.

Cloos, E., 1968. Experimental analysis of Gulf Coast fracture patterns. Aapg Bulletin, 52(3), pp.420-444.

Coffield, D.Q. and Schamel, S., 1987. Kinematics of drape fold evolution over normal faults in the Gulf of Suez. Egypt (abs.): Geological Society of America Abstracts with Programs, 19, p.622.

Coffield, D.Q. and Schamel, S., 1989. Surface expression of an accommodation zone within the Gulf of Suez rift, Egypt. Geology, 17(1), pp.76-79.

Corfield, S. and Sharp, I.R., 2000. Structural style and stratigraphic architecture of fault propagation folding in extensional settings: a seismic example from the Smørbukk area, Halten Terrace, Mid-Norway. *Basin Research*, *12*(3-4), pp.329-341.

Cowie, P.A. and Scholz, C.H., 1992. Displacement-length scaling relationship for faults: data synthesis and discussion. Journal of Structural Geology, 14(10), pp.1149-1156.

Cowie, P.A. and Scholz, C.H., 1992. Growth of faults by accumulation of seismic slip. Journal of Geophysical Research: Solid Earth, 97(B7), pp.11085-11095.

Cowie, P.A. and Scholz, C.H., 1992. Physical explanation for the displacement-length relationship of faults using a post-yield fracture mechanics model. Journal of Structural Geology, 14(10), pp.1133-1148.

Cowie, P.A., Sornette, D. and Vanneste, C., 1995. Multifractal scaling properties of a growing fault population. Geophysical Journal International,122(2), pp.457-469.

Cristallini, E.O. and Allmendinger, R.W., 2001. Pseudo 3-D modeling of trishear fault-propagation folding. *Journal of Structural Geology*, *23*(12), pp.1883-1899.

Davies, R.J., Turner, J.D. and Underhill, J.R., 2001. Sequential dip-slip fault movement during rifting: a new model for the evolution of the Jurassic trilete North Sea rift system. *Petroleum Geoscience*, *7*(4), pp.371-388.

Davis, J.C. and Sampson, R.J., 1986. *Statistics and data analysis in geology* (Vol. 646). New York et al.: Wiley.

Davy, P., Le Goc, R., Darcel, C., Bour, O., De Dreuzy, J.R. and Munier, R., 2010. A likely universal model of fracture scaling and its consequence for crustal hydromechanics. Journal of Geophysical Research: Solid Earth,115(B10).

Dawers, N.H., Anders, M.H. and Scholz, C.H., 1993. Growth of normal faults: Displacement-length scaling. Geology, 21(12), pp.1107-1110.

Dee, S.J., Yielding, G., Freeman, B., Healy, D., Kusznir, N.J., Grant, N. and Ellis, P., 2007. Elastic dislocation modelling for prediction of small-scale fault and fracture network characteristics. *SPECIAL PUBLICATION-GEOLOGICAL SOCIETY OF LONDON*, *270*, p.139.

Donato, J.A. and Tully, M.C., 1981. A regional interpretation of North Sea gravity data. Petroleum geology of the continental shelf of North-West Europe, pp.65-75.

Drăgulescu, A. and Yakovenko, V.M., 2001. Exponential and power-law probability distributions of wealth and income in the United Kingdom and the United States. *Physica A: Statistical Mechanics and its Applications*, *299*(1), pp.213-221.

Ebinger, C.J., 1989. Tectonic development of the western branch of the East African rift system. *Geological Society of America Bulletin*, *101*(7), pp.885-903.

Eleuchi, H., Saidi, M., Fourati, L., Ghenima, R. and Friha, J., 2003, October. Northern Tunisia Thrust Belt–Deformation Model and Hydrocarbon Systems. In *1st North African/Mediterranean Petroleum & Geosciences Conference & Exhibition*.

Erslev, E.A. and Rogers, J.L., 1993. Basement-cover geometry of Laramide fault-propagation folds. Geological Society of America Special Papers, 280, pp.125-146.

Erslev, E.A., 1991. Trishear fault-propagation folding. *Geology*, *19*(6), pp.617-620.

Evans, D. ed., 2003. The Millennium Atlas: Petroleum Geology of the Central and Northern North Sea;[a Project of the Geological Society of London, the Geological Survey of Denmark and Greenland and the Norwegian Petroleum Society].

Ewing, T. E., 1991, Structural framework, in Salvador, A., 1991. Origin and development of the Gulf of Mexico basin. The gulf of Mexico basin, pp.389-444.

Feibel, C.S., 2011. A geological history of the Turkana Basin. *Evolutionary Anthropology: Issues, News, and Reviews*, *20*(6), pp.206-216.

Ferrill, D.A., Morris, A.P. and McGinnis, R.N., 2012. Extensional fault-propagation folding in mechanically layered rocks: The case against the frictional drag mechanism. *Tectonophysics*, *576*,

pp.78-85.

Ferrill, D.A., Morris, A.P. and Smart, K.J., 2007. Stratigraphic control on extensional fault propagation folding: Big Brushy Canyon monocline, Sierra del Carmen, Texas. *Geological Society, London, Special Publications*,*292*(1), pp.203-217.

Flook, A.G., 1979. The characterization of textural and structural profiles by the automated measurement of their fractal dimensions. 2nd European Symp. Particle Characterization, pp.591-599.

Fossen, H. and Hesthammer, J., 1998. Structural geology of the Gullfaks field, northern North Sea. *Special publication-Geological Society of London*, *127*, pp.231-262.

Fossen, H. and Rørnes, A., 1996. Properties of fault populations in the Gullfaks Field, northern North Sea. Journal of Structural Geology, 18(2), pp.179-190.

Franklin, B. and Samuel, G., 2013. *Characterising fracture systems within upfaulted basement highs in the Hebridean Islands: an onshore analogue for the Clair Field* (Doctoral dissertation, Durham University).

Freeman, B., Yielding, G., Badley, M. 1990, Fault correlation during seismic interpretation, First Break, v.8, no. 3, DOI: 10.3997/1365-2397.1990006

Frostick, L., Reid, I., JARVIS, J.T. and Eardley, H., 1988. Triassic sediments of the Inner Moray Firth, Scotland: early rift deposits. Journal of the Geological Society, 145(2), pp.235-248.

Galloway, W.E., Bebout, D.G., Fisher, W.L., Dunlap, J.B., Jr., Cabrera-Castro, R., Lugo-Rivera, J.E., and Scott, T.M., Cenozoic, in Salvador, A., 1991. Origin and development of the Gulf of Mexico basin. The gulf of Mexico basin, pp. 245–324.

Garfunkel, Z. and Barṭov, Y., 1977. The tectonics of the Suez rift. Geological survey of Israel.

Gauthier, B.D.M. and Lake, S.D., 1993. Probabilistic modeling of faults below the limit of seismic resolution in Pelican Field, North Sea, offshore United Kingdom. AAPG Bulletin, 77(5), pp.761-777.

Gillespie, P.A., Howard, C.B., Walsh, J.J. and Watterson, J., 1993. Measurement and characterisation of spatial distributions of fractures.Tectonophysics, 226(1-4), pp.113-141.

Gillespie, P.A., Walsh, J.J., Watterson, J., Bonson, C.G. and Manzocchi, T., 2001. Scaling relationships of joint and vein arrays from The Burren, Co. Clare, Ireland. Journal of Structural Geology, 23(2), pp.183-201.

Gillespie, P.A., Walsh, J.T. and Watterson, J., 1992. Limitations of dimension and displacement data

from single faults and the consequences for data analysis and interpretation. Journal of Structural Geology, 14(10), pp.1157-1172.

Glennie, K. W., 1998, Petroleum geology of the North Sea: basic concepts and recent advances: Oxford, Blackwell Science, XVI, 636 s. p.

Glennie, K.W., 1984. Introduction to the petroleum geology of the North Sea.

Glennie, K.W., 2009. Petroleum Geology of the North Sea: Basic concepts and recent advances. John Wiley & Sons.

Goldthwaite, D., 1991. Central Gulf Coast stratigraphy.

Goudie, A.S., 2005. The drainage of Africa since the Cretaceous.*Geomorphology*, *67*(3), pp.437-456.

Gross, M.R. and Engelder, T., 1995. Strain accommodated by brittle failure in adjacent units of the Monterey Formation, USA: scale effects and evidence for uniform displacement boundary conditions. Journal of Structural Geology, 17(9), pp.1303-1318.

Gross, M.R., 1995. Fracture partitioning: Failure mode as a function of lithology in the Monterey Formation of coastal California. Geological Society of America Bulletin, 107(7), pp.779-792.

Gross, M.R., Becker, A. and Gutiérrez-Alonso, G., 1997. Transfer of displacement from multiple slip zones to a major detachment in an extensional regime: Example from the Dead Sea rift, Israel. Geological Society of America Bulletin, 109(8), pp.1021-1035.

Gross, M.R., Gutie, G., Bai, T., Wacker, M.A., Collinsworth, K.B. and Behl, R.J., 1997. Influence of mechanical stratigraphy and kinematics on fault scaling relations. Journal of Structural Geology, 19(2), pp.171-183.

Grubb, H.F., 1998. Summary of hydrology of the regional aquifer systems, Gulf Coastal Plain, south-central United States (Vol. 1416). USGPO.

Gudmundsson, A., 1987. Geometry, formation and development of tectonic fractures on the Reykjanes Peninsula, southwest Iceland. Tectonophysics,139(3-4), pp.295-308.

Guerriero, V., Iannace, A., Mazzoli, S., Parente, M., Vitale, S. and Giorgioni, M., 2010. Quantifying uncertainties in multi-scale studies of fractured reservoir analogues: Implemented statistical analysis of scan line data from carbonate rocks. Journal of Structural Geology, 32(9), pp.1271-1278.

Guiraud, R., 1998. Mesozoic rifting and basin inversion along the northern African Tethyan margin: an overview. Geological Society, London, Special Publications, 132(1), pp.217-229.

Hackley, P.C., 2012. Geologic assessment of undiscovered conventional oil and gas resources--Middle Eocene Claiborne Group, United States part of the Gulf of Mexico Basin (No. 2012-1144). US Geological Survey.

Halbouty, M.T., 1979. Salt Domes, Gulf Region, United States & Mexico. Gulf Pub Co.

Hammuda, O.S., Van Hinte, J.E. and Nederbragt, S., 1991. Geohistory analysis mapping in the central and southern Tarabulus Basin, northwest offshore of Libya. The geology of Libya: Amsterdam, Elsevier, pp.1657-1680.

Hardy, S. and Allmendinger, R.W., 2011. Trishear: A review of kinematics, mechanics, and applications.

Hardy, S. and Ford, M., 1997. Numerical modeling of trishear fault propagation folding. *Tectonics*, *16*(5), pp.841-854.

Hardy, S. and McClay, K., 1999. Kinematic modelling of extensional fault-propagation folding. *Journal of Structural Geology*, *21*(7), pp.695-702.

Haynes, F.M., 1984. Vein densities in drill core, Sierrita porphyry copper deposit, Pima County, Arizona. Economic Geology, 79(4), pp.755-758.

Healy, D., Blenkinsop, T.G., Timms, N.E., Meredith, P.G., Mitchell, T.M. and Cooke, M.L., 2015. Polymodal faulting: Time for a new angle on shear failure. *Journal of Structural Geology*, *80*, pp.57-71.

Helland-Hansen, W., Ashton, M., Lømo, L. and Steel, R., 1992. Advance and retreat of the Brent delta: recent contributions to the depositional model. *Geological Society, London, Special Publications*, *61*(1), pp.109-127.

Heffer, K.J. and Bevan, T.G., 1990, January. Scaling relationships in natural fractures: data, theory, and application. In European Petroleum Conference. Society of Petroleum Engineers.

Hesthammer, J. and Fossen, H., 2001. Structural core analysis from the Gullfaks area, northern North Sea. Marine and Petroleum Geology, 18(3), pp.411-439.

Hooker, J.N., Laubach, S.E. and Marrett, R., 2014. A universal power-law scaling exponent for fracture apertures in sandstones. Geological Society of America Bulletin, 126(9-10), pp.1340-1362.

Hooker, J.N., Laubach, S.E., Gomez, L., Marrett, R., Eichhubl, P., Diaz-Tushman, K. and Pinzon, E., 2011. Fracture size, frequency, and strain in the Cambrian Eriboll Formation sandstones, NW Scotland. Scottish Journal of Geology, 47(1), pp.45-56.

Hosman, R.L. and Weiss, J.S., 1991. Geohydrologic units of the Mississippi Embayment and Texas coastal uplands aquifer systems, south-central United States (No. 1416-B).

Hubbert, M.K., 1937. Theory of scale models as applied to the study of geologic structures. Geological Society of America Bulletin, 48(10), pp.1459-1520.

Hurst, A.R., 1981. Mid Jurassic stratigraphy and facies at Brora, Sutherland.Scottish Journal of Geology, 17(3), pp.169-177.

Husmo, T., Hamar, G., Høiland, O., Johannessen, E.P., Rømuld, A., Spencer, A., Titterton, R., 2003. Lower and middle Jurassic. In: Evans, D., Graham, C., Armour, A., Bathurst, P. (Eds.), The Millennium Atlas: Petroleum Geology of the Central and Northern

Jackson, C.A.L., Gawthorpe, R.L. and Sharp, I.R., 2006. Style and sequence of deformation during extensional fault-propagation folding: examples from the Hammam Faraun and El-Qaa fault blocks, Suez Rift, Egypt. *Journal of Structural Geology*, *28*(3), pp.519-535.

Jackson, P. and Sanderson, D.J., 1992. Scaling of fault displacements from the Badajoz-Cordoba shear zone, SW Spain. Tectonophysics, 210(3), pp.179-190.

Jamison, W.R., 1987. Geometric analysis of fold development in overthrust terranes. Journal of Structural Geology, 9(2), pp.207-219.

Jin, G. and Groshong, R.H., 2006. Trishear kinematic modeling of extensional fault-propagation folding. *Journal of Structural Geology*, *28*(1), pp.170-183.

Kaye, B.H., 1978. Specification of the ruggedness and/or texture of a fine particle profile by its fractal dimension. Powder Technology, 21(1), pp.1-16.

Kaye, B.H., 2008. A random walk through fractal dimensions. John Wiley & Sons.

Keulen, N., Heilbronner, R., Stünitz, H., Boullier, A.M. and Ito, H., 2007. Grain size distributions of fault rocks: A comparison between experimentally and naturally deformed granitoids. Journal of Structural Geology, 29(8), pp.1282-1300.

Khalil, S.M. and McClay, K.R., 2002. Extensional fault-related folding, northwestern Red Sea, Egypt. *Journal of Structural Geology*, *24*(4), pp.743-762.

Kim, Y.S. and Sanderson, D.J., 2005. The relationship between displacement and length of faults: a review. Earth-Science Reviews, 68(3), pp.317-334.

King, G., 1983. The accommodation of large strains in the upper lithosphere of the earth and other solids by self-similar fault systems: the geometrical origin of b-value. *Pure and Applied Geophysics*, *121*(5-6), pp.761-815.

Klett, T.R., 2001. Total Petroleum Systems of the Pelagian Province, Tunisia, Libya, Italy, and Malta--the Bou Dabbous-Tertiary and Jurassic-Cretaceous Composite. US Department of the Interior, US Geological Survey.

Kruhl, J.H., 2013. Fractal-geometry techniques in the quantification of complex rock structures: A special view on scaling regimes, inhomogeneity and anisotropy. *Journal of Structural Geology*, *46*, pp.2-21.

Lăpădat, A., Imber, J., Yielding, G., Iacopini, D., McCaffrey, K.J., Long, J.J. and Jones, R.R., 2016, July. Occurrence and development of folding related to normal faulting within a mechanically heterogeneous sedimentary sequence: a case study from Inner Moray Firth, UK. Geological Society of London.

Laubach, S.E. and Ward, M.E., 2006. Diagenesis in porosity evolution of opening-mode fractures, Middle Triassic to Lower Jurassic La Boca formation, NE Mexico. Tectonophysics, 419(1), pp.75-97.

Laubscher, H.P., 1982. Die Südostecke des Rheingrabens—ein kinematisches und dynamisches Problem. Eclogae Geologicae Helvetiae,75(1), pp.101-116.

Ligtenberg, J.H. and Wansink, A.G., 2001. Neural network prediction of permeability in the El Garia formation, Ashtart oilfield, offshore Tunisia. *Journal of Petroleum Geology*, *24*(4), pp.389-404.

Linsley, P.N., Potter, H.C., McNab, G. and Racher, D., 1980. The Beatrice Field, Inner Moray Firth, UK North Sea.

Long, J.J. and Imber, J., 2010. Geometrically coherent continuous deformation in the volume surrounding a seismically imaged normal fault-array. *Journal of Structural Geology*, *32*(2), pp.222-234.

Long, J.J. and Imber, J., 2010. Geometrically coherent continuous deformation in the volume surrounding a seismically imaged normal fault-array. *Journal of Structural Geology*, *32*(2), pp.222-234.

Loriga, M.A., 1999. Scaling systematics of vein size: an example from the Guanajuato mining district (Central Mexico). Geological Society, London, Special Publications, 155(1), pp.57-67.

Macgregor, D.S. and Moody, R.T., 1998. Mesozoic and Cenozoic petroleum systems of North Africa. *Geological Society, London, Special Publications*, *132*(1), pp.201-216.

Marrett, R. and Allmendinger, R.W., 1990. Kinematic analysis of fault-slip data. Journal of structural

geology, 12(8), pp.973-986.

Marrett, R. and Allmendinger, R.W., 1991. Estimates of strain due to brittle faulting: sampling of fault populations. Journal of Structural Geology, 13(6), pp.735-738.

Marrett, R. and Allmendinger, R.W., 1992. Amount of extension on" small" faults: An example from the Viking graben. Geology, 20(1), pp.47-50.

Marzougui, W., Melki, F., Arfaoui, M., Houla, Y. and Zargouni, F., 2014. Major faults, salt structures and paleo-ridge at tectonic nodes in Northern Tunisia: contribution of tectonics and gravity analysis. *Arabian Journal of Geosciences*, pp.1-17.

McCaffrey, K.J.W., Sleight, J.M., Pugliese, S. and Holdsworth, R.E., 2003. Fracture formation and evolution in crystalline rocks: Insights from attribute analysis. *Geological Society, London, Special Publications*, *214*(1), pp.109-124.

McClay, K.R. and Scott, A.D., 1991. Experimental models of hangingwall deformation in ramp-flat listric extensional fault systems. *Tectonophysics*,*188*(1), pp.85-96.

McConnell, D.A., Kattenhorn, S.A. and Benner, L.M., 1997. Distribution of fault slip in outcrop-scale fault-related folds, Appalachian Mountains. *Journal of Structural Geology*, *19*(3), pp.257-267.

McConnell, R.B., 1972. Geological development of the rift system of eastern Africa. *Geological Society of America Bulletin*, *83*(9), pp.2549-2572.

McCoy, T.W., 1990. Evaluation of ground-water resources in the Lower Rio Grande Valley, Texas. Texas Water Development Board Report 316. Texas Water Commission, Austin. 1990. 48.

McQuillin, R., Donato, J.A. and Tulstrup, J., 1982. Development of basins in the Inner Moray Firth and the North Sea by crustal extension and dextral displacement of the Great Glen Fault. Earth and Planetary Science Letters,60(1), pp.127-139.

Morgan, M.A., Grocott, J. and Moody, R.T., 1998. The structural evolution of the Zaghouan-Ressas structural belt, northern Tunisia. Geological Society, London, Special Publications, 132(1), pp.405-422.

Morley, C.K., 1999. Patterns of displacement along large normal faults: implications for basin evolution and fault propagation, based on examples from east Africa. *AAPG bulletin*, *83*(4), pp.613-634.

Morley, C.K., 2002. Evolution of large normal faults: Evidence from seismic reflection data. *AAPG bulletin*, *86*(6), pp.961-978.

Needham, T., Yielding, G. and Fox, R., 1996. Fault population description and prediction using

examples from the offshore UK. Journal of Structural Geology, 18(2), pp.155-167.

Nelson, T. H., 1991, Salt tectonics and listric-normal faulting, in Salvador, A., 1991. Origin and development of the Gulf of Mexico basin. The gulf of Mexico basin, pp.389-444.

Newman, M.E., 2005. Power laws, Pareto distributions and Zipf's law.*Contemporary physics*, *46*(5), pp.323-351.

Nicol, A., Walsh, J.J., Watterson, J. and Gillespie, P.A., 1996. Fault size distributions—are they really power-law?. *Journal of Structural Geology*, *18*(2), pp.191-197.

Nicol, A., Walsh, J.J., Watterson, J. and Gillespie, P.A., 1996. Fault size distributions—are they really power-law?. Journal of Structural Geology,18(2), pp.191-197.

Ortega, O. and Marrett, R., 2000. Prediction of macrofracture properties using microfracture information, Mesaverde Group sandstones, San Juan basin, New Mexico. Journal of Structural Geology, 22(5), pp.571-588.

Ouali, J. and Tricart, P., 1985. Nouvelle interprétation de l'Axe nord—sud en Tunisie centrale: le chaînon Nara—Sidi Khalif. Terra Cognita, Strasbourg, 5, p.258.

Patton III, T.L., 1984. Normal-fault and fold development in sedimentary rocks above a pre-existing basement normal fault.

Peacock, D.C.P., 2003. Scaling of transfer zones in the British Isles. *Journal of Structural Geology*, *25*(10), pp.1561-1567.

Pickering, G., Bull, J.M. and Sanderson, D.J., 1995. Sampling power-law distributions. *Tectonophysics*, *248*(1), pp.1-20.

Pickering, G., Bull, J.M. and Sanderson, D.J., 1995. Sampling power-law distributions. Tectonophysics, 248(1), pp.1-20.

Pickering, G., Bull, J.M., Sanderson, D.J. and Harrison, P.V., 1994. Fractal fault displacements: A case study from the Moray Firth, Scotland. InFractals and dynamic systems in geoscience (pp. 105-119). Springer Berlin Heidelberg.

Pickering, K.T., 1984. The Upper Jurassic 'Boulder Beds' and related deposits: a fault-controlled submarine slope, NE Scotland. Journal of the Geological Society, 141(2), pp.357-374.

Pollard, D.D. and Segall, P., 1987. Theoretical displacements and stresses near fractures in rock: with applications to faults, joints, veins, dikes, and solution surfaces. Fracture mechanics of rock, 277(349),

pp.277-349.

Price, W.A., 1934. Lissie Formation and Beaumont Clay in South Texas: DISCUSSION. AAPG Bulletin, 18(7), pp.948-959.

Putz-Perrier, M.W. and Sanderson, D.J., 2008. The distribution of faults and fractures and their importance in accommodating extensional strain at Kimmeridge Bay, Dorset, UK. Geological Society, London, Special Publications, 299(1), pp.97-111.

Quarles Jr, M., 1953. Salt-ridge hypothesis on origin of Texas Gulf Coast type of faulting. AAPG Bulletin, 37(3), pp.489-508.

Racey, A., Bailey, H.W., Beckett, D., Gallagher, L.T., Hampton, M.J. and McQuilken, J., 2001. The petroleum geology of the early Eocene El Garia Formation, Hasdrubal field, offshore Tunisia. *Journal of Petroleum Geology*, *24*(1), pp.29-53.

Reches, Z.E., 1978. Development of monoclines: Part I. Structure of the Palisades Creek branch of the East Kaibab monocline, Grand Canyon, Arizona. Geological Society of America Memoirs, 151, pp.235-272.

Reed, W.J., 2001. The Pareto, Zipf and other power laws. *Economics Letters*, *74*(1), pp.15-19.

Roberts, A.M., Badley, M.E., Price, J.D. and Huck, I.W., 1990. The structural history of a transtensional basin: Inner Moray Firth, NE Scotland.*Journal of the Geological Society*, *147*(1), pp.87-103.

Robson, D.A., 1971. The structure of the Gulf of Suez (Clysmic) rift, with special reference to the eastern side. Journal of the Geological Society,127(3), pp.247-271.

Rogers, J.L., 1989. Structural geometry and basement kinematics of the Forellen Peak Fault, Northern Teton Range, Wyoming.

Salaj, J., 1978. The geology of the Pelagian Block: the eastern Tunisian platform. In The ocean basins and margins (pp. 361-416). Springer US.

Salvador, A., 1991. Origin and development of the Gulf of Mexico basin. The gulf of Mexico basin, pp.389-444.

Salvini, F. and Storti, F., 2001. The distribution of deformation in parallel fault-related folds with migrating axial surfaces: comparison between fault-propagation and fault-bend folding. *Journal of Structural Geology*, *23*(1), pp.25-32.

Schlische, R.W., Young, S.S., Ackermann, R.V. and Gupta, A., 1996. Geometry and scaling relations of

a population of very small rift-related normal faults. *Geology*, *24*(8), pp.683-686.

Schlische, R.W., Young, S.S., Ackermann, R.V. and Gupta, A., 1996. Geometry and scaling relations of a population of very small rift-related normal faults. Geology, 24(8), pp.683-686.

Scholz, C.H. (a) and Cowie, P.A., 1990. Determination of geologic strain from fault slip data. Nature, 346, pp.837-839.

Schwerdtner, W.M., Rivers, T., Zeeman, B., Wang, C.C., Tsolas, J., Yang, J. and Ahmed, M., 2014. Post-convergent structures in lower parts of the 1090–1050 Ma (early-Ottawan) thrust-sheet stack, Grenville Province of Ontario, southern Canadian Shield 1. *Canadian Journal of Earth Sciences*, *51*(3), pp.243-265.

Sellards, E.H., Adkins, W.S. and Plummer, F.B., 1932. The geology of Texas, volume I, stratigraphy: University of Texas at Austin. Bulletin, 3232.

Sharp, I.R., Gawthorpe, R.L., Underhill, J.R. and Gupta, S., 2000. Fault-propagation folding in extensional settings: examples of structural style and synrift sedimentary response from the Suez rift, Sinai, Egypt. *Geological Society of America Bulletin*, *112*(12), pp.1877-1899.

Sims, D., 1993. The rheology of clay: a modeling material for geologic structures. Eos, Transactions, American Geophysical Union, 74(46), p.569.

Sjøblom, T.S., Steel, R.J., Liljedahl, T., Sauar, B.E. and Tjelland, T., 1995. Tectonic controls on Bathonian-Volgian syn-rift successions on the Visund fault block, northern North Sea. *Norwegian Petroleum Society Special Publications*, *5*, pp.325-346.

Sleight, J.M., 2001. *Fracture characteristics from two reactivated basement fault zones: examples from Norway and Shetland* (Doctoral dissertation, Durham University).

Soliva, R. and Schultz, R.A., 2008. Distributed and localized faulting in extensional settings: insight from the North Ethiopian Rift–Afar transition area. *Tectonics*, *27*(2).

Stearns, D.W., 1978. Faulting and forced folding in the Rocky Mountains foreland. Geological Society of America Memoirs, 151, pp.1-38.

Stephens, M.A., 1974. EDF statistics for goodness of fit and some comparisons. *Journal of the American statistical Association*, *69*(347), pp.730-737.

Stevens, V., 1991. The Beatrice Field, Block 11/30a, UK North Sea.*Geological Society, London, Memoirs*, *14*(1), pp.245-252.

Stone, D.S., 2009. Geologic Interpretation of Seismic Profiles, Big Horn Basin, Wyoming, Part 11: West Flank.

Storti, F., Salvini, F. and McClay, K., 1997. Fault-related folding in sandbox analogue models of thrust wedges. *Journal of Structural Geology*, *19*(3), pp.583-602.

Suppe, J. and Medwedeff, D.A., 1990. Geometry and kinematics of fault-propagation folding. Eclogae Geologicae Helvetiae, 83(3), pp.409-454.

Suppe, J., 1983. Geometry and kinematics of fault-bend folding. American Journal of science, 283(7), pp.684-721.

Suteanu, C. and Kruhl, J.H., 2002. Investigation of heterogeneous scaling intervals exemplified by sutured quartz grain boundaries. Fractals, 10(04), pp.435-449.

Thiebaud, C.E. and Robson, D.A., 1979. The geology of the area between Wadi Wardan and Wadi Gharandal, east Clysmic rift, Sinai, Egypt. Journal of Petroleum Geology, 1(4), pp.63-75.

Thomson, K. and Underhill, J.R., 1993, January. Controls on the development and evolution of structural styles in the Inner Moray Firth Basin. In *Geological Society, London, Petroleum Geology Conference series*(Vol. 4, pp. 1167-1178). Geological Society of London.

Tollefsen, S., Graue, E. and Svinddal, S., 1992, January. The Gullfaks Field development: challenges and perspectives. In European Petroleum Conference. Society of Petroleum Engineers.

Trishear: A review of kinematics, mechanics, and applications. Stuart Hardy and Richard W. Allmendinger

Trudgill, B. and Cartwright, J., 1994. Relay-ramp forms and normal-fault linkages, Canyonlands National Park, Utah. Geological Society of America Bulletin, 106(9), pp.1143-1157.

Turcotte, D.L., 1989. Fractals in geology and geophysics. In Fractals in geophysics (pp. 171-196). Birkhäuser Basel.

Underhill, J.R., 1991. Implications of Mesozoic—Recent basin development in the western Inner Moray Firth, UK. *Marine and Petroleum Geology*, *8*(3), pp.359IN1361IN7365IN13369-360IN6364IN12368IN18.

Vially, R., Letouzey, J., Benard, F., Haddadi, N., Desforges, G., Askri, H. and Boudjema, A., 1994. Basin inversion along the North African Margin. The Saharan Atlas (Algeria). Peri-Tethyan platforms: Paris, Technip, pp.79-118.

Walsh, J., Watterson, J. and Yielding, G., 1991. The importance of small-scale faulting in regional extension.

Walsh, J.J. and Watterson, J., 1987. Distributions of cumulative displacement and seismic slip on a single normal fault surface. Journal of Structural Geology, 9(8), pp.1039-1046.

Walsh, J.J. and Watterson, J., 1989. Displacement gradients on fault surfaces. *Journal of Structural Geology*, *11*(3), pp.307-316.

Walsh, J.J. and Watterson, J., 1992. Populations of faults and fault displacements and their effects on estimates of fault-related regional extension. Journal of Structural Geology, 14(6), pp.701-712.

Walsh, J.J., Watterson, J. and Yielding, G., 1994. Determination and interpretation of fault size populations: procedures and problems. North Sea Oil and Gas Reservoirs–III. Kluwer, London, pp.141-155.

Watterson, J., 1986. Fault dimensions, displacements and growth. *Pure and Applied Geophysics*, *124*(1-2), pp.365-373.

Watterson, J., Walsh, J.J., Gillespie, P.A. and Easton, S., 1996. Scaling systematics of fault sizes on a large-scale range fault map. Journal of Structural Geology, 18(2), pp.199-214.

Wescott, W.A. and Hood, W.C., 1994. Hydrocarbon generation and migration routes in the East Texas Basin. AAPG bulletin, 78(2), pp.287-306.

Wilson, T. and Paulsen, T.S., 1998. CRP-1 fracture arrays: constraints on the Neogene-Quaternary stress regime along the Transantarctic Mountains Front, Antarctica. Terra Antartica, 5(3), pp.327-335.

Withjack, M.O., Meisling, K.E. and Russell, L.R., 1988. Forced folding and basement-detached normal faulting in the Haltenbanken area, offshore Norway. AAPG Bull.;(United States), 72(CONF-880301-).

Withjack, M.O., Meisling, K.E. and Russell, L.R., 1989. Forced Folding and Basement-Detached Normal Faulting in the Haltenbanken Area, Offshore Norway: Chapter 37: North Sea and Barents Shelf.

Withjack, M.O., Olson, J. and Peterson, E., 1990. Experimental models of extensional forced folds (1). *Aapg Bulletin*, *74*(7), pp.1038-1054.

Wojtal, S.F., 1994. Fault scaling laws and the temporal evolution of fault systems. Journal of Structural Geology, 16(4), pp.603-612.

Wojtal, S.F., 1996. Changes in fault displacement populations correlated to linkage between faults. Journal of Structural Geology, 18(2), pp.265-279.

Yielding, G., Needham, T. and Jones, H., 1996. Sampling of fault populations using sub-surface data: a review. Journal of Structural Geology,18(2), pp.135-146.

Yielding, G., Walsh, J. and Watterson, J., 1992. The prediction of small-scale faulting in reservoirs. First break, 10(12), pp.449-460.

Zaïer, A., Beji-Sassi, A., Sassi, S. and Moody, R.T.J., 1998. Basin evolution and deposition during the Early Paleogene in Tunisia. *Geological Society, London, Special Publications*, *132*(1), pp.375-393.

Ziegler, P.A., 1990. Geological atlas of western and central Europe. Geological Society of London.

https://en.wikipedia.org/wiki/Log-normal_distribution, November 2015

http://tuvalu.santafe.edu/~aaronc/powerlaws/, January 2016

http://tuvalu.santafe.edu/~aaronc/powerlaws/data.htm, January 2016

http://www.rdocumentation.org/, January 2016

https://en.wikipedia.org/wiki/Anderson%E2%80%93Darling_test, March 2016

https://en.wikipedia.org/wiki/Kolmogorov%E2%80%93Smirnov_test, March 2016

http://www.ipt.ntnu.no/gullfaks/, April 2016

http://arohatgi.info/WebPlotDigitizer/app/, April 2016

https://itportal.decc.gov.uk/web_files/relinqs/p1268.pdf, July 2016

https://en.wikipedia.org/wiki/Local_regression, August 2016